# Local Dynamics of the Single-Band Hubbard Model in Infinite Dimensions via Dynamic Density-Matrix Renormalization

Dissertation
zur Erlangung des Doktorgrades
der Naturwissenschaften
der Fakultät Physik an der Technischen Universität Dortmund

vorgelegt von

**Patrick Gilbert Grete**

Juni 2010

Erster Prüfer: Prof. Dr. G.S. Uhrig
Zweiter Prüfer: Prof. Dr. F.B. Anders
Wissenschaftlicher Mitarbeiter: Dr. S. Schmitt
Leiter der Prüfungskomission: Prof. Dr. B. Spaan
Tag der Prüfung 12.07.2010

> Ideen, wie absolute Gewißheit, absolute Genauigkeit, endgültige Wahrheit und so fort, sind Erfindungen der Einbildungskraft und haben in der Wissenschaft nichts zu suchen.
>
> *(Max Born 1882-1970)* `http://www.zitate-online.de/autor/born-max/`

# Contents

**1 Introduction and Overview** **6**

**2 Strongly Correlated Electrons in Physics and their Modeling** **8**
- 2.1 Metals, Insulators and Superconductors and the Role of Strongly Correlated Electrons 8
  - 2.1.1 Introduction . . . . . . 8
  - 2.1.2 Cuprates . . . . . . 10
  - 2.1.3 Self-Energy, its Physical Meaning and Kinks in the Self-Energy . . . . . . 11
- 2.2 Modeling Strongly Correlated Electrons . . . . . . 13
  - 2.2.1 The Full Solid State Hamiltonian – General Remarks . . . . . . 13
  - 2.2.2 The Pure Electronic Hamiltonian: The Hubbard Model, its Properties and the Mott-Metal-to-Insulator Transition . . . . . . 13

**3 Treating the Mott-Transition: Dynamical Mean-Field Theory of the Single-Band Hubbard Model** **17**
- 3.1 Introduction . . . . . . 17
- 3.2 Details of the Dynamical Mean-Field Theory (DMFT) . . . . . . 18
- 3.3 Effective One-Site-Model for DMFT: The Single Impurity Anderson Model (SIAM) . . 22
  - 3.3.1 Origin of the SIAM – Historical Remarks . . . . . . 22
  - 3.3.2 Formulation of the SIAM . . . . . . 23
  - 3.3.3 Jordan-Wigner Transformation of the SIAM . . . . . . 26
  - 3.3.4 Self-Energy of the SIAM via the Q-function . . . . . . 29
- 3.4 Impurity Solvers – an Overview . . . . . . 32
  - 3.4.1 Exact Diagonalization . . . . . . 32
  - 3.4.2 Iterative Perturbation Theory . . . . . . 33
  - 3.4.3 Quantum Monte-Carlo Methods . . . . . . 34
  - 3.4.4 The Non-Crossing Approximations . . . . . . 36
  - 3.4.5 Numerical Renormalization Group Theory . . . . . . 37
  - 3.4.6 Dynamic Density-Matrix Renormalization Group Theory . . . . . . 37

**4 Density-Matrix Renormalization Group in a DMFT Framework and its Implementation** **39**
- 4.1 Main Idea and Details of the DMRG . . . . . . 40
  - 4.1.1 Density-Matrices and the Problems of Real-Space Block Renormalization – General Remarks . . . . . . 40
  - 4.1.2 The DMRG Truncation . . . . . . 41
  - 4.1.3 Finite-System DMRG Algorithm . . . . . . 44
  - 4.1.4 Local Dynamics and Dynamic DMRG . . . . . . 46
  - 4.1.5 Inhibition of Sticking to Local Minima – Adding Absent Fluctuations to the Density-Matrix . . . . . . 48
  - 4.1.6 Aspects of DMRG Theory . . . . . . 49
- 4.2 Implementation and Validation of the DMRG . . . . . . 52

4.2.1 Details of the Parallelization . . . 52
4.2.2 Assessing the Choice of Parameters . . . 53
4.2.3 Further Checks for the Asymmetric SIAM . . . 65
4.3 Deconvoluting D-DMRG Raw Data . . . 68
4.3.1 Why Convoluted Data Appears . . . 68
4.3.2 The Least Bias Ansatz . . . 69
4.3.3 Checks for Deconvoluting Asymmetric Raw Data . . . 70
4.3.4 Deconvoluting Self-Energies . . . 71
4.4 Closing the DMFT Cycle: Extraction of the Continued Fraction Coefficients . . . 73

**5 Results** **79**
5.1 Preliminaries: Spectral Densities for the Asymmetric SIAM on a Bethe Lattice . . . 80
5.2 Q-function for the Asymmetric SIAM on a Bethe Lattice . . . 83
5.3 Kinks in the Self-Energy in the DMFT Approach . . . 87
5.4 Dynamic Mean-Field Results for the Half-Filled Case . . . 92
5.4.1 Results for the Semielliptic DOS . . . 92
5.4.2 Results for the Rectangular DOS . . . 97
5.4.3 Results for the Triangular DOS . . . 108
5.5 Dynamic Mean-Field Results away from Half-Filling . . . 114
5.5.1 Introduction . . . 114
5.5.2 Local Spectral Densities for the Doped Metal . . . 115
5.5.3 Local Self-Energies for the Doped Metal . . . 120
5.5.4 Local Susceptibilities for the Doped Metal . . . 127
5.5.5 Kinks and Local Bosonic Excitations away from Half-Filling . . . 136

**6 Conclusion and Outlook** **140**
6.1 Conclusion . . . 140
6.2 Outlook . . . 141

**7 Bibliography** **142**

**A Appendix** **150**
A.1 Abstract . . . 150
A.2 Kurze Zusammenfassung . . . 150
A.3 Danksagung . . . 151
A.4 Erklärung . . . 152

# 1 Introduction and Overview

The research field of “strongly correlated electrons” is very broad representing a large part of the whole solid state physics and exhibiting a large list of phenomena on the experimental side and many models with a lot of specialized tools to solve those models on the theoretical side. Trying to structure it in order to give an introduction to and some kind of context of the present thesis about local dynamic quantities of the single band Hubbard model may follow different strategies.

Following a chronological account, one would start with the discovery of electrons by J.J. Thomson [200] in 1897 who conjectured that the electrons are responsible for the physical properties of solids. The first classical statistical calculations were done by Drude [41] in 1900 and the first quantum statistical calculations were done by Sommerfeld [189] in 1928 who gave a microscopic explanation of the specific heat and its temperature dependence in solids. Those early works considered the electrons as ideal free gases saying that the Coulomb interaction between the electrons is screened away by the electric field of the nuclei. The next obvious step was to consider weakly interacting electrons. This idea led Landau [116] in 1956 to his Fermi-liquid (FL) theory in which the same quantum numbers as in the non-interacting case are present and the interaction between the electrons leads to different masses of the particles. The further development in understanding the effect of correlated electrons led to the simplest model of correlated electrons in solids – the Hubbard model – which was independently formulated by Hubbard [85, 86, 87], Gutzwiller [77] and Kanamori [102] in 1963/1964.

Following a more experimental-phenomenological account, one would mention the different classes of compounds in which strongly correlated electrons are present and likely responsible for the found phenomenons: Vanadates (early analyses were done by Morin [141]) show a metal-to-insulator transition (MIT) and a transition from paramagnetic to anti-ferromagnetic insulators (see McWhan et al. [132] and the review of Imada [88, p.1144ff.]) as a function of pressure, temperature and doping. A MIT being caused by correlation effects was proposed by Mott [142] in 1949 and is called Mott-transition. Certain cuprates show a transition from an insulating to a superconducting phase (see Bednorz and Müller [16]) as a function of doping and temperature. Certain cobaltates also show superconductivity (see Takada et al. [198]), exhibit a MIT (see e.g. Tokura et al. [201]) and they exhibit large thermopower (see Terasaki et al. [199] and Lee et al. [118]). Certain manganites exhibit several magnetic phases (see Wollan and Koehler [227]) and colossal magnetoresistance (see Jin et al. [98]); the latter is used in contemporary computers to build hard disks with large memory density. Certain ruthenates show superconductivity (see Maeno et al. [126]) but with an unconventional pairing symmetry (see Sigrist et al. [186] and Mackenzie and Maeno [124]). At last, we mention the class of heavy-fermion systems consisting of lanthanides and actinides compounds in which correlated $f$-electrons (and not $d$-electrons like in all compounds mentioned before) lead to many interesting phenomena (see e.g. the early review of Steglich et al. [193] and the recent book by Misra [140]).

The above mentioned physical features, phases and phase-transitions can be traced back to the complex interplay of spin, charge and/or orbital degrees of freedom of several bands of electrons in the certain compounds and the crystal structure of the compounds. Although it is possible to formulate a multi-band Hamiltonian of correlated electrons describing the all needed degrees of freedom on a certain lattice at once, there are no tools at hand to adequately treat such a general model. Therefore, we have to restrict ourselves to certain phenomena which simplify the Hamiltonian and allow to use specialized tools to treat the model.

In this thesis, we analyze the single-band Hubbard model with doping by studying spectral densities of the metallic phase near the metal-to-insulator transition. Since calculating spectral densities and dynamic susceptibilities of the Hubbard model on an arbitrary lattice in any dimension is impossible, we simplify the analysis further and take up a local point of view which is the starting point for the dynamic mean-field-theory (DMFT). Although a local point of view simplifies the problem considerably, i.e. instead of the full lattice problem a local site embedded in a non-interacting bath has to be solved, the latter is still a quantum-mechanical many-body problem. Systems consisting of a local site embedded in a bath are solved by impurity solvers. Here, the impurity solver dynamical density-matrix renormalization was implemented. This sketched framework allows us to calculate static quantities and local spectral densities, self-energies and susceptibilities of good quality and high numerical resolution. Such quantities are an approximation to the spectral densities and susceptibilities of a real lattice with a single band of electrons near the metal-to-insulator transition. In particular, DMFT neglects all spatial fluctuations which gives a first insight into the physics of real compounds where spatial fluctuations are present. This thesis is organized as follows:

In chapter 2, we give an introduction to strongly correlated electrons in physics. In Sec. 2.1, we give an introduction to the phenomena of strongly correlated electrons in physics, mention some details of cuprates and explain the self-energy. In Sec. 2.2, we introduce the Hubbard model and the Mott metal-insulator transition.

In chapter 3, we give an introduction and details of the dynamic mean-field theory (DMFT) which maps the Hubbard model in infinite dimension onto the single-impurity Anderson model (SIAM). The SIAM is described in Sec. 3.3. Solving the SIAM to obtain dynamical quantities necessitates the implementation of impurity solvers. The most commonly used impurity solvers are discussed in Sec. 3.4.

One of the mentioned impurity solvers is the dynamic density-matrix renormalization (D-DMRG). The implementation of D-DMRG in a DMFT framework is described in chapter 4. The main idea of DMRG is given in Sec 4.1. How D-DMRG is implemented, the validation of this implementation and an assessment of the reached accuracy is given in Sec. 4.2. D-DMRG produces spectral densities that are convoluted with a Lorentzian and the used deconvolution algorithm is described in Sec. 4.3. It will turn out that DMFT sets up a self-consistency problem that can be illustrated as a cycle. How this cycle is closed for D-DMRG is described in Sec. 4.4.

In chapter 5, the results of this thesis are given. After presenting the results for the asymmetric SIAM embedded on a Bethe lattice in Sec. 5.1 and assessing the direct calculation of the self-energy for the SIAM via the Q-function in Sec. 5.2, we turn to the DMFT results. We present some general remarks on kinks in the real part of self-energies in DMFT in Sec. 5.3. In Sec. 5.4, we present results for the half-filled band and in Sec. 5.5 we give the results of the doped band. We end in chapter 6 with a conclusion and a short outlook pointing to open questions.

# 2 Strongly Correlated Electrons in Physics and their Modeling

Contents

**2.1 Metals, Insulators and Superconductors and the Role of Strongly Correlated Electrons . . . 8**

2.1.1 Introduction . . . 8

2.1.2 Cuprates . . . 10

2.1.3 Self-Energy, its Physical Meaning and Kinks in the Self-Energy . . . 11

**2.2 Modeling Strongly Correlated Electrons . . . 13**

2.2.1 The Full Solid State Hamiltonian – General Remarks . . . 13

2.2.2 The Pure Electronic Hamiltonian: The Hubbard Model, its Properties and the Mott-Metal-to-Insulator Transition . . . 13

2.2.2.1 The Hubbard Model . . . 14

2.2.2.2 The Mott Metal-Insulator transition . . . 15

In this chapter, we introduce the topic of strongly correlated electrons. It is divided in two sections. In the first section 2.1, we mention the most peculiar experimental phenomena of the compounds belonging to this field and focus especially on cuprates. In the second section 2.2, we present the full (non-relativistic) solid state Hamiltonian and sketch how to derive a pure electronic Hamiltonian – the Hubbard Hamiltonian – from it. Then, we introduce the concept of the Mott metal-insulator transitions and how they are described by the Hubbard model.

## 2.1 Metals, Insulators and Superconductors and the Role of Strongly Correlated Electrons

In this section, we summarize experimental phenomena that can be traced back to strongly correlated electrons. To this end, we start with short introduction in Sec. 2.1.1 and discuss cuprates afterwards in Sec. 2.1.2. The last subsection 2.1.3 is the connecting section to the modeling part in Sec. 2.2 because it deals with the self-energy. The self-energy is on the one hand introduced as a theoretical concept and on the other hand it is directly connected to observables in experiments.

### 2.1.1 Introduction

It is quite remarkable that with undergraduate quantum mechanics (atomic orbitals, Hunds rules, etc.) one can understand the whole table of elements, their basic chemical properties and even some properties of chemical compounds. For example, sodium and potassium have one $s$ electron which builds the conduction band in solids so that both are metals. If they are in compound with chlorine or oxygen, this $s$ electron is bounded by them so that such compounds are insulators.

If we then apply this simple picture to transition metal oxides (TMO), i.e. oxides of titanium, vanadium, etc., we would expect all of them to be metals since TMOs have one (or more) unbounded $d$ electron(s). However, this simple picture is wrong. Such TMOs show a very rich physics like (anti)ferromagnetism, transitions between several crystal structures, superconductivity and many more. For the physics of TMOs, it is believed that strong correlations between electrons play an important role. Let us mention the resistivity $\rho(T)$ as a function of temperature $T$. Strongly correlated solids are in general bad metals, i.e. strong on-site correlations of the $d$ electrons result in high resistivity. It is clear that below a certain temperature $T^*$ quantum effects are very important but above this temperature there should exist a simple power law $\rho \propto T^\alpha$ whose exponent $\alpha$ can be one or two. For simple metals, $T^*$ is nearly the same for all of them but for strongly correlated metals $T^*$ can range from zero to several hundred Kelvin although the only obvious electronic energy scale is the Fermi energy (which is a few eV).

A seminal work to describe phenomenologically the low energy excitations of correlated metals is Landaus Fermi-liquid (FL) theory. Starting from the non-interacting free electron gas, the question arose what physics we face if there is only small interaction between the particles. There is a very general answer to this question at least for the lowest excitations of systems with weak interactions. In particular, Landau [116] in 1956 introduced a scenario in which there exists an one-to-one correspondence between the excitations of the free and the weakly interacting system. Landau named such gases Fermi quantum liquids (FL); see also the monograph of Pines and Nozières [156]. In FL, we are faced with quasi-particles instead of electrons. The façon de parler is that the interaction dresses the bare electron and that this quantum object (electron + dressing) is the quasi-particle. This dressing is treated via the so-called self-energy (see Sec. 2.1.3 on page 11) which is an important quantity in this framework[1]. One other important quantity that can be calculated from the self-energy is the effective mass of the quasi-particle (which differs from the mass of the bare electron). This effective mass (instead of the known bare mass of the electron) determines the physical behavior of the solid like e.g. the specific heat.

One interesting feature of compounds with strongly correlated electrons is that they can undergo a metal-insulator transition (MIT) as a function of electron/hole doping or pressure. This transition at $T = 0$ is an example for a quantum-phase-transition. It was first investigated by Mott in 1949 [142] and is called Mott metal-insulator transition. A very exhaustive review on metal-insulator transitions was given by Imada et al. [88] in 1998. See also the book of Gebhard [66]. For a local treatment via dynamical mean-field theory, a treatment we also use in this thesis, see the review of Georges et al. [67].

Another feature of solids with strongly correlated electrons is that the Pauli-paramagnetism (see Ref. [184, p.285-289]), which in normal metals is independent of temperature, is (without exception) dependent on temperature. The list of not fully understood phenomena is much longer but we leave it with those comments by which we just motivate why the physics of strongly correlated electrons is given that much attention. For more insights, the reader may start with the review of Ramakrishnan from 2008 [166].

The history of strongly correlated electrons may have started with transition metal oxides but it did not end with them. For a review on TMOs, see the book of Maekawa et al. [125]. In addition to TMOs, there exists the wide field of “heavy-fermion systems”. The reader is referred to the review

---

[1] The concept of self-energy is more general and applies also to systems with non-FL behavior.

of Stewart [194] from 1984 or to the more recent book by Misra [140] on the topic of heavy-fermion systems. There also exist systems which show Non-Fermi-Liquid behavior[2], see the review by Stewart [195] in 2001. One should also mention ruthenates that are also TMO's but with 4*d* instead of 3*d* electrons. Like other TMO's, $Sr_2RuO_4$ has a superconducting phase (see Maeno et al. [126]) but it is the only known compound with Cooper-pairs exhibiting spin-triplet pairing. Spin-triplet pairing is reviewed by Mackenzie and Maeno [124]. For further reviews of ruthenates, see Ovchinnikov [152] and the corresponding section in the review of Yanase et al. [228].

In this thesis, we analyze the single-band Hubbard model near the Mott transition. Cuprates are the paradigmatic compounds that are adequately described by this model. For this reason, we mention in the next subsection some properties of cuprates.

### 2.1.2 Cuprates

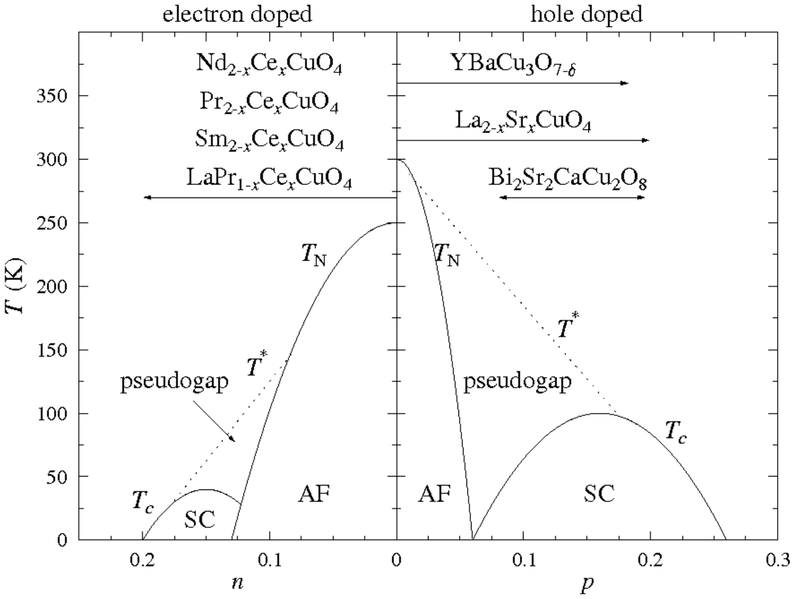

Figure 2.1: Temperature-doping phase diagram for perovskite cuprates. For discussion see text. This picture is part of the public domain (see footnote 3) and is the result of comprehensive angular resolved photoemission spectroscopy studies reviewed by Damascelli et al. [39].

Cuprates, i.e. compounds of copper and oxygen with some other cations, exhibit very rich physics. This is due to the different electronic configurations of copper, the different crystal structures and different doping. We focus here on copper perovskites. In 1986, Bednorz and Müller [16] discovered that certain cuprates have a superconducting phase with much higher transition temperatures than former BCS superconductors. This increased the scientific effort of understanding cuprates.

Without any doping, cuprates have an unpaired 3*d* electron. Due to strong correlations, this electron cannot move freely so cuprates are Mott insulators. Below a critical temperature $T_{\mathrm{N}}$ of approximately 300K, they show long-range Néel order, i.e. they are antiferromagnets. This is shown in the generic phase diagram[3] for cuprates shown in Fig. 2.1. For larger doping (note the different behavior for electron or hole doping), the Néel order is lost and the cuprate becomes a bad metal with a generic pseudogap structure in the density of states. For low enough temperature, doped cuprates undergo

---

[2] In one spatial dimension, no Fermi-liquid behavior of interacting electrons is possible which was discovered by Luttinger [123], Tomonaga [202] and Mattis and Lieb [131]; one dimensional Fermi-liquids are hence called "Luttinger liquids". See the review of Voit [213].

[3] Public domain picture; see `http://en.wikipedia.org/wiki/File:Cuphasediag.png`.

a phase transition and become superconducting. Early after the discovery of high-temperature superconductivity by Bednorz and Müller [16], Anderson [9] argued that this superconductivity is due to strongly correlated electrons. The symmetry of the electron-pairing is not $s$-wave like in ordinary superconductors but it is $3d_{x^2-y^2}$-wave; see the review of Tsuei and Kirtley [204].

Above the dotted line in Fig. 2.1 indicated by $T^*$, cuprates are said to be a "strange metal". In this region, cuprates show several special features. For instance, the resistivity is proportional to the temperature $T$ (and not to $T^2$ like in normal metals). Also the Hall coefficient is temperature dependent (in contrast to any normal metals). Varma et al. [206] in 1989 proposed an explanation for this non-FL behavior. This "strange metal" behavior can be destroyed by larger doping. However, the physical mechanism behind this behavior is still unknown, hence the name "strange metal" for this region. Also the pairing mechanism in the superconducting phase is still a matter of debate. Some argue that phonons [125, p.163] serve as the glue between the electrons. Others, like Anderson [10] in 2007, doubt that a special glue (apart from the dynamics of strong correlated electrons) is needed. In 1986, Miyake et al. [139] proposed for heavy-fermion systems that spin-fluctuations mediate the Cooper-pairing. For cuprates, Maier et al. [129] argued for a "spin-fluctuation glue" as a pairing-mechanism without phonons.

Apart from the physics of superconductivity, cuprates constitute an interesting research field because they occur also with different dimensionality. There are one-dimensional cuprate chains which show all features of a Luttinger liquid[4]; see Hase et al. [81]. There are also cuprate ladder systems. For a review on ladder systems see Alloul et al. [3], chapter two in Ref. [125] and also Schmidt and Uhrig [173] for a review of magnetic excitations of two-leg ladder cuprates.

### 2.1.3 Self-Energy, its Physical Meaning and Kinks in the Self-Energy

Self-energy is a notion stemming from classical electrodynamics [91, p.865f.]. There, it describes the effects of the interaction of the electron with its own radiation field; hence the name "self-energy". Feynman [52, 53] introduced the quantum-electrodynamic analog in his works on this topic in 1949 and Dyson [42, 43] introduced such concepts in the quantum field description of an interacting Fermi gas. In the latter, one considers the ground state of such a system and the first excitations of it via the single particle Green functions. The interested reader finds more details on this topic in standard textbooks like Fetter and Walecka [51] or Mahan [127]. Here, we focus on translation invariant systems. By comparing the single-particle Green function (see Ref. [149, p.147])

$$G_0(\omega, k) = \frac{1}{\omega - (\epsilon(k) - \mu)} \tag{2.1}$$

of a system of free fermions with the single-particle Green function (see Ref. [149, p.169])

$$G(\omega, k) = \frac{1}{\omega - (\epsilon(k) - \mu + \Sigma(\omega, k))} \tag{2.2}$$

of a system of interacting fermions, it turns out that the complex valued self-energy $\Sigma(\omega, k)$ captures (like in classical electrodynamics) the whole interaction of the fermion with all other fermions. Mathematically, the self-energy serves as an energy shift [149, p.169]. This statement reads

---

[4] See footnote 2 on page 10.

$$G(\omega,k) = G_0(\omega - \Sigma(\omega,k),k) \tag{2.3}$$

If we insert $G_0(\omega,k) = {}^1\!/_{(\omega-(\epsilon(k)-\mu))}$ in Eq. (2.2), we obtain

$$G(\omega,k) = \frac{1}{\frac{1}{G_0(\omega,k)} - \Sigma(\omega,k)} \qquad \Leftrightarrow \qquad G(\omega,k) = G_0(\omega,k) + G_0(\omega,k)\Sigma(\omega,k)G(\omega,k) \tag{2.4}$$

which is the so-called *Dyson equation*. From now on, we only consider $k$-independent systems. The self-energy determines the physical properties of the quasi-particles (see Ref. [51, p.146f.] and Ref. [149, p.169f.]). The self-energy leads to a change of the effective mass of the particles in the system. One can define the quasi-particle weight $Z$ by

$$Z := \frac{1}{1 - \frac{\partial}{\partial\omega}\Re\,\Sigma(\omega)\big|_{\omega=0}}. \tag{2.5}$$

Moreover, the real part $\Re\Sigma(\omega)$ contains the energy shift of the quasi-particle and the imaginary part $\Im\Sigma(\omega)$ introduces the life time of the quasi-particle. From this it follows why kinks in the low energy range of $\Re\Sigma$ are so important: A kink indicates an abrupt change of the quasi-particle energy shift and hence a kink could indicate e.g. a coupling of the quasi-particle to some excitations in the system. The physical origin of this excitation is not revealed by the detection of a kink. However, the discovery of a kink in $\Re\Sigma$ is a good starting point to search for any excitations in that energy range.

Via angular resolved photoemission, the self-energy and the quasi-particle peak is directly observable. Especially for high temperature superconductors, there exists a lot of such experimental works and many of them show a kink in the real part of the self-energy. In the framework of high-$T_\mathrm{c}$ superconductors, one seeks for such excitations that are responsible for the pairing of the electrons. There are mainly two camps of different opinions on that topic (see also Sec. 5.3 on page 87). One of the camps suppose that phonons are responsible for the pairing in such systems (like in conventional superconductors). The other camp supposes spin fluctuations to be responsible for the pairing. Since the kinks in $\Re\Sigma$ gives only a hint to a possibly present excitation, the main question is *which* excitations are actually present and relevant in the particular system. We mention just a few studies for an impression of the vast amount of data that has been taken for assessing the question which excitations are present. For instance, Meevasana et al. in 2007 [136] analyzed several cuprates (see Sec. 2.1.2 on page 10) and found such kinks within a range of 30-90 meV. Kinks have also been found in other superconductors like in ruthenates which are spin-triplet superconductors. Aiura et al. [2] in 2004 found kinks at ≈40 meV in $Sr_2RuO_4$ and $Sr_3Ru_2O_7$. In 2005, Iwasawa et al. [90] confirmed this kink at that energy in $Sr_2RuO_4$. In cobaltates, kinks occur at 70-100 meV which is the result of Yang et al. [229] from 2005. But not only superconductors show such kinks. For instance, manganites with their colossal magnetoresistance show kinks at 60 meV which is the result of Sun et al. [196] from 2006. For the high-$T_\mathrm{c}$ superconductors, the pairing mechanism is still a matter of debate; see e.g. the recent review of Mishchenko [138] from 2010.

We conclude from the above statements that the self-energy $\Sigma$ is a very important quantity for both theoretical and experimental investigations of strongly correlated electron systems. In particular, we saw that kinks in $\Re\Sigma$ may indicate the presence of excitations in the system that provide important information about the internal degrees of freedom of the system under consideration.

## 2.2 Modeling Strongly Correlated Electrons

In this section, we introduce the model to treat strongly correlated electrons in solids. To this end, we sketch how the Hubbard model is derived from the full Hamiltonian of a solid. Then, we introduce the first quantum phase transition, the *Mott metal-insulator transition*, that can be analyzed with the Hubbard Hamiltonian.

### 2.2.1 The Full Solid State Hamiltonian – General Remarks

In the introduction, we mentioned the versatile phenomena of compounds with strongly correlated electrons covering many kinds of ordering like spin-, charge-, orbital- or structural ordering and interesting properties of solids like superconductivity, thermopower, magnetoresistance or metal-insulator transition. Although we are far from a universal understanding of the physical mechanisms behind all those phenomena, we are confident that quantum theory provides the correct framework for all theoretical investigations of the mentioned phenomena. Solids consist of atoms which consist of a nucleus[5] and electrons. All particles have kinetic energy and all particles interact via Coulomb interaction. The non-relativistic Hamiltonian of this problem reads (see Ref. [66, p.50])

$$\mathscr{H}_{\text{solids}} = \sum_{n=1}^{N_{\text{nuc}}} \frac{\vec{P}_n^2}{2M_n} + \sum_{n=1}^{N_{\text{el}}} \frac{\vec{p}_n^{\,2}}{2m} + \frac{e^2}{2} \sum_{n \neq m=1}^{N_{\text{nuc}}} \frac{Z_n Z_m}{\left|\vec{R}_n - \vec{R}_m\right|} + \frac{e^2}{2} \sum_{i \neq j=1}^{N_{\text{el}}} \frac{1}{|\vec{r}_i - \vec{r}_j|} - e^2 \sum_{n=1}^{N_{\text{nuc}}} \sum_{i=1}^{N_{\text{el}}} \frac{Z_n}{\left|\vec{R}_n - \vec{r}_i\right|}. \quad (2.6)$$

The first term describes the kinetic energy of the $N_{\text{nuc}}$ nuclei which can have different masses $M_n$ and which are located at $\vec{R}_n$ with the atomic number $Z_n$. The second term describes the kinetic energy of the $N_{\text{el}}$ electrons with mass $m$ which are located at $\vec{r}_i$. The third term describes the interaction between the nuclei, the fourth term describes the interaction between the electrons and the last term describes the interaction between the nuclei and the electrons.

If we recall the impossibility of solving the Schrödinger equation $\mathscr{H}\psi = E\psi$ for three particles (e.g. the helium [185, p.233]), it is clear that obtaining the solution with the Hamilton operator (2.6) for realistic situations, i.e. $N_{\text{el}}, N_{\text{nuc}} \approx 10^{24}$, is a hopeless task. Even the aim to obtain a *general* approximation is hopeless which can be seen from analyzing the involved energy scales (see Gebhard [66, p.51]): The binding energy of the inner electrons is of the order of up to $10^4$ eV and we are interested in the low temperature behavior of the solids which is of the order $10^{-2} - 10^{-4}$ eV. Hence, an approximation would have to cover eight orders of magnitude and we would need a resolution of up to $10^{-8}$. Although such a solution would cover the formation of atoms (i.e. their crystal structure) and all the phenomena mentioned in the introduction, no approximation theory known to us covers such energy range or exhibits such a resolution.

### 2.2.2 The Pure Electronic Hamiltonian: The Hubbard Model, its Properties and the Mott-Metal-to-Insulator Transition

The statements of the last subsection could provoke us to refrain from a microscopic understanding of solids. However, the situation for investigations is not that bad if we concentrate on certain issues.

---

[5] We do not consider the internal structure of the nuclei, i.e. protons and neutrons or even their constituents like quarks, since this would necessitate relativistic quantum theory. All relativistic effects are neglected here.

Analyzing the energy scales lead to simplifications. Indeed, such an analysis of the involved energy scales shows that the energy scale splits into several parts. For example the masses of the electrons and the nuclei differ by several orders of magnitude so we can split the dynamics of the nuclei and electrons[6]. This implies that as a first approximation we can treat the nuclei as a static background (e.g. a fixed lattice) and the electron-nucleus interaction as an effective interaction responsible for the stability of the solid. Following this reasoning, we may construct effective single electron models (e.g. Hartree, local density approximations, ect.) for calculating the band structures of solids (see. Gebhard [66, p.79ff.]) and/or may treat the pure electronic many-particle system.

#### 2.2.2.1 The Hubbard Model

We focus on the latter, treat the pure electronic problem and we end up with the Hubbard Hamiltonian which is the simplest model of correlated electrons. The Hubbard model was introduced and first analyzed by Hubbard in 1963/1964 in a series of three articles [85, 86, 87]. The Hubbard model was independently introduced by Gutzwiller [77] and Kanamori [102] at the same time. It is noteworthy that all three authors investigated ferromagnetism and used localized Wannier functions that overlapped but they reached the Hamiltonian (and treated it) differently. Gutzwiller followed a variational approach (see e.g. the pedagogical introduction by Gebhard [66, p.111ff.]) and Kanamori used the T-matrix (see Ref. [66, p.76] for a brief comment). We do not go into details of the deduction of the model but we mention the main ingredients. We apply the previous mentioned Born-Oppenheimer approximation. Since the electrons are mainly located at the sites of the lattice, we use Wannier functions with a certain overlap to the neighboring sites. We then switch to the so-called second quantization formulation of (2.6). The overlap between neighboring sites, i.e. the integral over the overlap of the adjacent Wannier functions, translates into a hopping matrix $t_{ij}$ which we consider to be symmetric (hopping from site $i$ to site $j$ is as likely as hopping from site $j$ to site $i$). The electron-electron interaction translates into a density-density integral, i.e. an integral over the product of both Wannier-densities scaled with an $1/r$-term (where $r$ denotes the distance between the centers of both Wannier functions). This is the Coulomb $U$ parameter. For more details on the deduction see Ref. [66, p.58f.]. We end with the Hubbard Hamiltonian

$$\mathscr{H} = -\sum_{<i,j>,\sigma} t_{ij}(c^{\dagger}_{i,\sigma}c_{j,\sigma} + c^{\dagger}_{j,\sigma}c_{i,\sigma}) + U\sum_{i} n_{i,\uparrow}n_{i\downarrow} - \mu\sum_{i,\sigma} n_{i,\sigma} \tag{2.7}$$

where we added a shift of the local energies (the $\mu$ term). The parameters $t_{ij}, U, \mu$ are real valued. In addition, we restrict our investigation to $t_{ij}, U \geq 0$ because $t \geq 0$ ensures without magnetic field a minimum of the dispersion relation at the center of the Brillouin zone and $U \geq 0$ ensures repulsion between the electrons. In contrast, $\mu$ can have positive or negative values since it is the chemical potential which describes the doping of electron or holes. Other parameters are the lattice (i.e. its dimension $d$ and the number of nearest neighbors $z$) and the temperature $T$ of the system.

If we consider a bipartite lattice and $\mu = U/2$, then (2.7) exhibits particle-hole-symmetry, i.e creation and annihilation operators can be interchanged without any change of the Hamiltonian. In the following, we consider nearest neighbor hopping only, so that $t_{ij} = 0$ if $i$ and $j$ do not correspond to nearest neighbor sites and the hopping amplitude is equal between all sites. If we study a metal, we expect a spectral density with considerable spectral weight at $\omega = 0$. If the spectral density $\rho(\omega)$ has a compact support $[\omega_-, \omega_+]$, $W := |\omega_+ - \omega_-|$ is defined as the "bandwidth" which sets the relevant

---

[6] This is the well-known Born-Oppenheimer approximation; see textbooks like e.g. Schwabl [185, p.273ff.]

energy scale of the non-interacting system. For particle-hole symmetry, $|\omega_+| = |\omega_-|$ follows and one can introduce $W := 2D$ with $D$ being the relevant energy scale.

The above introduced Hubbard model is the simplest model of correlated electrons but a general solution for the whole parameter space is still unknown. In the case of a one-dimensional chain, Lieb and Wu [119] gave the analytical solution via Bethe-ansatz[7]. For an exhaustive review on the one-dimensional Hubbard model, see the book of Essler et al. [46]. For all other dimensions, only certain limiting cases can be solved exactly:

- Fermi gas limit. For $U = 0$, Hamiltonian (2.7) consists of the (shifted) hopping terms only. This Hamiltonian is diagonal in momentum space and describes an ideal Fermi gas on a certain lattice. Since all electrons can move freely, this is an ideal metal.
- Atomic limit. For $t_{ij} = 0 \ \forall i, j$, Hamiltonian (2.7) has no hopping terms. The Hubbard Hamiltonian (2.7) is diagonal in position space [85, 86]. Since all electrons are immobile, this model describes an insulator. At half-filling the spin of every electron ($N_{\mathrm{el}}$ is the number of electrons) is arbitrary so that the ground state is $2^{N_{\mathrm{el}}}$-fold degenerate. Since the spin is arbitrary, this insulating phase is paramagnetic, i.e. it exhibits no longe range order.
- Large-$U$ limit. This limit case is not exactly solvable but it leads to a model that can be treated more easily. The above mentioned $2^{N_{\mathrm{el}}}$-fold degeneracy of the atomic limit at half-filling can be lifted in second order perturbation theory. At half-filling, we obtain the Heisenberg model

  $$\mathscr{H}_{\mathrm{Heis}} = \sum_{<i,j>} J\left(\vec{S}_i\vec{S}_j + \frac{1}{4}\right) \qquad \text{with} \qquad J = \frac{4t^2}{U} > 0 \tag{2.8}$$

  with $\vec{S}_i$ being a spin[8]. This model describes an antiferromagnetic insulator. Away from half-filling, we obtain the $t-J$-model which was first derived by Spałek in 1988 [191]; see [66, p.74] and [38, p. 369f.] for a short introduction to both models. For a more comprehensive review on the $t-J$-model, see the article of Spałek [192].

#### 2.2.2.2 The Mott Metal-Insulator transition

From the above limiting cases of the Hubbard model (2.7), one can presume the existence of a metal-insulator transition in the intermediate parameter range. Since (2.7) consists of hopping hampered only by Coulomb repulsion, this presumed transition is caused by quantum fluctuations. Such a transition has been proposed by Mott [142] fourteen years before the introduction of the Hubbard model in 1963. Historically, this Mott-Metal-Insulator transition was the first *quantum-phase transition.* As mentioned above, there are two insulating phases: One without a long range order (i.e. a paramagnetic behavior) which is called the *Mott-Hubbard insulator* and one with an antiferromagnetic order which is called the *Mott-Heisenberg insulator.* The latter is a band insulator. We restrict ourselves in the following to the Mott-Hubbard insulator.

At first sight, one may suggest that we are in a lucky situation since we can solve the Hubbard model in one dimension analytically and that we hence can study the Mott transition. This statement is correct but in one dimension the Hubbard model is an insulator for every $U \neq 0$ (see Ref. [46]).

---

[7] The original ansatz by Bethe [17] solved the one-dimensional Heisenberg chain.

[8] The elements $S_i^\alpha$ (with $\alpha \in \{x, y, z\}$) of $\vec{S}_i$ obey the angular momentum algebra, i.e. $\left[S_i^\alpha, S_j^\beta\right]_- = \mathrm{i}\hbar\delta_{ij}\epsilon_{\alpha\beta\gamma}S_i^\gamma$; see also Eqs. (3.30) on page 27.

This implies that there is no correlated metal phase in one dimension at $T = 0$. In more than one dimensions, an analytical solution is not known and we have to use approximative techniques for a quantitative investigation of the Mott-Hubbard transition.

Apart from the quantitative analysis of the Mott transition, one can formulate a qualitative picture of it. There are two starting points for such a reasoning, namely the insulating or the metallic phase. The first starting point was used by Hubbard [87] and the latter starting point was used by Brinkman and Rice [30].

Hubbard [87] starts with the insulating (paramagnetic) phase where the original spectral density (with the bandwidth $W$) has split into an upper and a lower Hubbard band. Between both bands there exists an energy gap $\Delta \approx U - W$. If $U$ is decreased, the gap becomes smaller and at a certain critical interaction value $U_{\mathrm{c}1}$ both bands touch each other (i.e. the gap closes) and a transition to the metallic phase occurs. The drawback of this picture is that it cannot comprise the Fermi-liquid behavior of the metallic phase.

Brinkman and Rice [30] started with the metallic phase which they consider as a strongly renormalized Fermi-liquid. The ratio between the mass $m^*$ of the quasi-particle and the electron mass $m$ defines the quasi-particle weight $Z$ (see definition (2.5) in Sec. 2.1.3 on page 11) via

$$\frac{1}{Z} = \frac{m^*}{m}. \tag{2.9}$$

The Fermi energy $\epsilon_{\mathrm{F}}$ is also renormalized by $Z$, i.e. $\epsilon_{\mathrm{F}} \longrightarrow \epsilon_{\mathrm{F}}^* = Z\epsilon_{\mathrm{F}}$. At a certain critical Coulomb repulsion $U_{\mathrm{c}2}$, the weight $Z$ becomes zero and hence the mass $m^*$ infinite, i.e. the quasi-particles localize. This defines the transition to the insulating phase. As Brinkman and Rice pointed out, the divergency has the exponent $-1$, i.e.

$$\frac{m^*}{m} \propto \frac{1}{U_{\mathrm{c}2} - U} \overset{Z\to 0}{\longrightarrow} \infty. \tag{2.10}$$

The Brinkman-Rice-scenario adequately describes the low energy behavior, but not the high-energy features like the Hubbard bands of the correlated metals.

# 3 Treating the Mott-Transition: Dynamical Mean-Field Theory of the Single-Band Hubbard Model

Contents

**3.1 Introduction** . . . . . . . . . . . . . . . . . . . . . . . . . . . . . . . . . . . . . . . . **17**
**3.2 Details of the Dynamical Mean-Field Theory (DMFT)** . . . . . . . . . . . **18**
**3.3 Effective One-Site-Model for DMFT: The Single Impurity Anderson Model (SIAM)** . . . . . . . . . . . . . . . . . . . . . . . . . . . . . . . . . . . . . . . . **22**
  3.3.1 Origin of the SIAM – Historical Remarks . . . . . . . . . . . . . . . . . . . . . . 22
  3.3.2 Formulation of the SIAM . . . . . . . . . . . . . . . . . . . . . . . . . . . . . . . . 23
  3.3.3 Jordan-Wigner Transformation of the SIAM . . . . . . . . . . . . . . . . . . . . . 26
  3.3.4 Self-Energy of the SIAM via the Q-function . . . . . . . . . . . . . . . . . . . . . 29
**3.4 Impurity Solvers – an Overview** . . . . . . . . . . . . . . . . . . . . . . . . . **32**
  3.4.1 Exact Diagonalization . . . . . . . . . . . . . . . . . . . . . . . . . . . . . . . . . 32
  3.4.2 Iterative Perturbation Theory . . . . . . . . . . . . . . . . . . . . . . . . . . . . . 33
  3.4.3 Quantum Monte-Carlo Methods . . . . . . . . . . . . . . . . . . . . . . . . . . . . 34
  3.4.4 The Non-Crossing Approximations . . . . . . . . . . . . . . . . . . . . . . . . . . 36
  3.4.5 Numerical Renormalization Group Theory . . . . . . . . . . . . . . . . . . . . . . 37
  3.4.6 Dynamic Density-Matrix Renormalization Group Theory . . . . . . . . . . . . 37

## 3.1 Introduction

Mean-field theories (MF-theories) belong to the standard toolbox of methods to study many-body systems (classical and quantum mechanical). The first step (so-called "cavity method") in many MF-theories consists of splitting the system into a local part, the environment and the connection between both. Instead of considering the whole many-body system, one considers the local one- or few-body system embedded in an environment (often called "bath"). The local problem is treated *exactly* and the environment is treated on *average*. We restrict ourselves to cases where the local problem is an one-body problem. However, the connection to the bath may turn the problem again into a many-body system. The local site influences the environment and the environment influences the local site. This setup defines a *self-consistency problem* which entails further problems to treat the problem. However, experience shows that the MF-setup can be treated easier than the full lattice problem because only local correlations are taken into account.

One may criticize this local MF-approach as an uncontrolled approximation because no clue is given under which circumstances the negligence of any correlations but the local ones is reasonable and can be applied to a certain system. But there exists a strategy to turn the MF-approach into a controlled approximation: One tries to find a limit case when the MF-theory becomes exact. This said limit is the limit of infinite dimension/coordination number $z \to \infty$.

However, performing this limit is not straightforward because summing over infinitely many nearest neighbors of the local site for obtaining e.g. the partition function could lead to divergencies. To avoid those divergencies, one has to find a rescaling of the parameters of the model such that the limit of infinitely many nearest neighbors becomes finite (but not trivial). For a local one-body system, the limit $z \to \infty$ implies that all spatial fluctuations are neglected. In addition, MF-theories found in standard textbooks (e.g. Weiss theory of the Ising model [184, p.290]) are static in the sense that all temporal fluctuations are neglected. The so-called "dynamical mean-field theory" (DMFT), which we apply in this thesis to the Hubbard model, captures temporal fluctuations (hence the name "dynamical") and is described in the following.

## 3.2 Details of the Dynamical Mean-Field Theory (DMFT)

The model under consideration is the Hubbard model (see Sec. 2.2.2 on page 13 for further details)

$$\mathscr{H} = -\sum_{<i,j>,\sigma} t_{ij}(c^\dagger_{i,\sigma}c_{j,\sigma} + c^\dagger_{j,\sigma}c_{i,\sigma}) + U\sum_i n_{i,\uparrow}n_{i\downarrow} - \mu\sum_{i,\sigma} n_{i,\sigma}, \tag{3.1}$$

in which, for simplicity, we take $\mu = 0$ for the moment. The extension of MF-theory to incorporate temporal fluctuations at site 0 is straightforward. Instead of taking the standard action $S$ of the Hamiltonian to calculate the partition function (or any other correlation function) as an integral $Z = \int \prod_{i,\sigma} \mathrm{D}c^\dagger_{i,\sigma}\mathrm{D}c_{i,\sigma}e^S$ over Grassmann variables, one takes the effective action reading

$$S_{\text{eff}} = -\int_0^\beta \mathrm{d}\tau \int_0^\beta \mathrm{d}\tau' \sum_\sigma c^\dagger_{0,\sigma}(\tau)G_0^{-1}(\tau-\tau')c_{0,\sigma}(\tau') + U\int_0^\beta \mathrm{d}\tau n_{0,\uparrow}(\tau)n_{0,\downarrow}(\tau) \tag{3.2}$$

with imaginary time $\tau$ and $\tau'$ to calculate the partition function $Z$ (or any other correlation function). In this expression, $G_0^{-1}(\tau-\tau')$ is the analog to the effective static Weiss field. $G_0^{-1}(\tau-\tau')$ contains the effective amplitude for a fermion created on the isolated site 0 at time $\tau$ (coming from the environment) and being destroyed at time $\tau'$ (going back to the environment). Hence, temporal fluctuations are taken into account so this new MF-theory is a dynamical one and is called "dynamical mean-field theory" (DMFT). But up to now this approximation is uncontrolled. There is the need to find a scaling for the parameters of the Hamiltonian (3.1) such that the effective action (3.2) becomes exact in some limit and one has to find a way to calculate $G_0$. The latter is still a many-body problem and its solution is far from being trivial.

Metzner and Vollhardt [135] were the first authors observing that in the Hamiltonian (3.1) only the hopping terms $t_{ij}$ have to be scaled with $1/\sqrt{z}$ ($z$ being the coordination number) so that a non-trivial limit for $z \to \infty$ exists and that perturbation theory formulated via skeleton diagrams becomes completely local. In Ref. [143], Müller-Hartmann showed that also the many-particle Green functions reduce to dressed skeleton diagrams that are completely local[1]. In two subsequent articles, Müller-Hartmann [144] presented explicit perturbation calculations. In a series of three articles, Brandt and Mielsch [22, 23, 24] followed those ideas. They derived and solved the self-consistent functional

---

[1] This is called "the collapse of diagrams".

equations for the Falicov-Kimball model. They also showed how these equations can be extended to the Hubbard model. The collapse of the diagrams for the Green function of the Hubbard Hamiltonian (3.1) in infinite dimensions implies that also the proper self-energy $\Sigma$ is completely local. However, the summation of those diagrams is in general not possible. Despite this drawback, the DMFT treats the non-interacting limit ($U = 0$) and the atomic limit $t_{ij} = 0$ correctly [68]. If we are able to sum up the remaining diagrams, we have a tool at hand to quantitatively analyze the Mott-transition of the Hubbard model. For this, the dynamic mean-field-theory (DMFT) needs further ingredients. The remaining ingredients were contributed by Georges and Kotliar [67] and Jarrell [94] who observed that for the Hubbard model in the limit of $z \to \infty$ the same local dressed skeleton diagrams occur as in treating the Single-Impurity-Anderson-Model (SIAM) [8]. The SIAM is explained in Sec. 3.3 on page 22.

Let us now put the above statements into mathematical expressions. We adopt the notation from Karski et al. [105] and denote the retarded local Green function and the self-energy of the Hubbard model by capital letters $G$ and $\Sigma$ and the corresponding Green function and self-energy of the SIAM by small letters $g$ and $\sigma$. Then, the statements of Georges and Kotliar [67] and Jarrell [94] read

$$\Sigma(\omega) = \sigma(\omega) \qquad \text{if} \qquad G(\omega) = g(\omega) \tag{3.3}$$

holds. Note that this does not imply $G^0 = g^0$ (the corresponding bare $U = 0$, undressed propagators). The bare propagator $g^0(\omega)$ contains all information about the bath which yields a certain $g(\omega)$. But we do not know the certain $g^0(\omega)$ such that the corresponding $g(\omega)$ and $\sigma(\omega)$ fulfill Eqs. (3.3). Hence, we have to guess $g^0(\omega)$ and have to verify whether or not the corresponding $g(\omega)$ and $\sigma(\omega)$ match Eqs. (3.3). This is the typical self-consistency problem of all MF-theories.

To solve this problem, we need two further equations – the Dyson equations of the Hubbard model and the SIAM. The local self-energy $\Sigma(\omega)$ is the same at every site and acts as a mere energy shift in the bare propagator $G^0(\omega)$, i.e.

$$G(\omega) = G^0(\omega - \Sigma(\omega)), \tag{3.4}$$

which is the Dyson equation for the Hubbard model (see also Sec. 2.1.3 on page 11) in the DMFT approximation. Note that in the DMFT approximation no momentum dependence occurs. In the SIAM, the self-energy $\sigma(\omega)$ is local, i.e. it acts only on the impurity. With the local bare propagator $g^0(\omega)$ and the local self-energy $\sigma(\omega)$ of the impurity, $g(\omega)$ is given by the geometric series

$$g(\omega) = \sum_{m=0}^{\infty} g^0(\omega) \left(\sigma(\omega) g^0(\omega)\right)^m = \frac{g^0(\omega)}{1 - g^0(\omega)\sigma(\omega)} \qquad \Leftrightarrow \qquad \frac{1}{g(\omega)} = \frac{1}{g^0(\omega)} - \sigma(\omega). \tag{3.5}$$

The latter equation is the searched Dyson equation for the SIAM.

Now, an iterative cycle can be built to solve the self-consistency problem. We start with an initial guess for the bath $g^0(\omega)$ of the impurity, determine the continued fraction coefficients (see Sec. 4.4 on page 73) and calculate (via an impurity solver; see Sec. 3.4 on page 32) the propagator $g(\omega)$ of the SIAM. Both propagators $g(\omega)$ and $g^0(\omega)$ are used in Eq. (3.5) to obtain the self-energy $\sigma(\omega)$. We use $\sigma(\omega) = \Sigma(\omega)$ in Eq. (3.4) to obtain $G(\omega)$. Then, we use $G(\omega) = g(\omega)$ in Eq. (3.5) to obtain $g^0(\omega)$. If self-consistency is reached, we obtain the same $g^0(\omega)$ whereby we started the impurity solver. If no self-consistency is reached, we use the obtained $g^0(\omega)$ to start the impurity solver again. Note that the impurity solver used in this thesis gives $g(\omega + \mathrm{i}\eta)$ and we need a deconvolution (see Sec. 4.3 on page 68) to obtain $g(\omega)$. Altogether, this is the whole self-consistency cycle sketched in Fig. 3.1. Note that there exists no analytic proof that this iteration converges to a unique solution. But experience shows that one obtains usually a robust solution after 10-20 cycles.

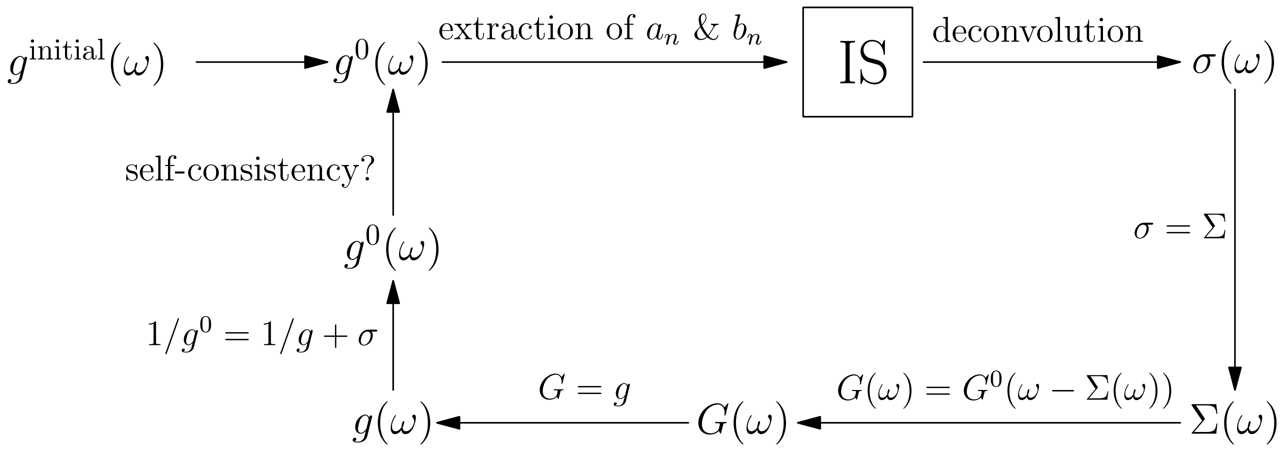

Figure 3.1: Schematic representation of the self-consistency cycle for general lattices. The box named with “IS” is the impurity solver which is the D-DMRG (see Sec. 4.1.4 on page 46) in this thesis.

The above prescription for the self-consistency cycle applies to any lattices, i.e. for any $G^0$. If $G^0$ has a semielliptic spectral density of states (DOS)

$$\rho^0(\omega) = -\frac{1}{\pi}\Im G^0(\omega) = \frac{2}{\pi D^2}\sqrt{D^2 - (\omega-\mu)^2} \tag{3.6}$$

(with $\mu$ being the shift of the position of the maximum of the semiellipse), the cycle can be simplified such that the (numerically sometimes unstable) calculation of the self-energy via Eq. (3.5) can be avoided. A semielliptic DOS is found for a Bethe lattice with infinite branching ratio [45, p.98f.]. We do not use any further feature of the Bethe lattice, hence the following statements apply to all lattices with translational symmetry with a semielliptic DOS. The simplification stems from the fact that $G^0(\omega)$ with a semielliptic DOS (3.6) has a continued fraction representation with the coefficients $a_n = \mu$ and $b_n = {}^{D^2}\!/_4$ being equal for all $n$, namely

$$G^0(\omega) = \cfrac{1}{\omega - \mu - \cfrac{D^2/4}{\omega - \mu - \cfrac{D^2/4}{\omega - \mu - \ldots}}}. \tag{3.7}$$

The bare propagator $g^0(\omega)$ of the SIAM reads

$$g^0(\omega) = \frac{1}{\omega - \mu - \Gamma(\omega)} \tag{3.8}$$

where we used the hybridization function $\Gamma(\omega)$ (see Sec. 3.3 on page 22 for further details) which itself can be written as a continued fraction

$$\Gamma(\omega) = \cfrac{V^2}{\omega - a_0 - \cfrac{\gamma_0^2}{\omega - a_1 - \cfrac{\gamma_1^2}{\omega - a_2 - ...}}} \tag{3.9}$$

in which $V$ is the hybridization of the impurity to the bath, $\gamma_i$ the hopping constants between site $i$ and $i+1$, $a_i$ the local field at site $i$ and $\mu$ the local field at the impurity site. Inserting Eq. (3.8) in the Dyson equation (3.5) of the SIAM and using the self-consistency condition $\sigma = \Sigma$, we obtain

$$\frac{1}{g(\omega)} = \omega - \mu - \Gamma(\omega) - \Sigma(\omega). \tag{3.10}$$

Then, we employ the Dyson equation (3.4) of the lattice, make use of Eq. (3.7) and obtain

$$G(\omega) = G^0(\omega - \Sigma(\omega)) = \cfrac{1}{\omega - \mu - \Sigma(\omega) - \cfrac{D^2/4}{\omega - \mu - \Sigma(\omega) - \cfrac{D^2/4}{\omega - \mu - \Sigma(\omega) - ...}}}. \tag{3.11}$$

Hence, the inverse of the propagator $G(\omega)$ reads

$$\frac{1}{G(\omega)} = \omega - \mu - \Sigma(\omega) - \cfrac{D^2/4}{\omega - \mu - \Sigma(\omega) - \cfrac{D^2/4}{\omega - \mu - \Sigma(\omega) - ...}} = \omega - \mu - \Sigma(\omega) - \frac{D^2}{4} G(\omega). \tag{3.12}$$

Now, we make use of the second self-consistency relation $G = g \leftrightarrow 1/g = 1/G$ and replace the right-hand side of Eq. (3.10) for $1/G$ in Eq. (3.12). This can be solved to obtain the hybridization function

$$\Gamma(\omega) = \frac{D^2}{4} G(\omega) \tag{3.13}$$

whereby we can calculate $g^0$ needed for verifying if self-consistency is reached via Eq. (3.8). This is a much simpler self-consistency cycle and it is depicted in Fig. 3.2.

Before we proceed, we shall recapitulate what the DMFT is able to comprise and what kind of extensions to DMFT exist. The presented DMFT applies to the single-band fermionic Hubbard model and it is exact in the non-interacting limit ($U = 0$; i.e. the metallic solution) and in the atomic limit ($t_{ij} = 0$; i.e. the insulating solution); see Georges et al. [68, p.18]. Like other MF-theories, it becomes exact in the limit of infinite spatial dimension $d$ or for infinite coordination number $z$. The DMFT is a dynamical extension of the static MF-theory because it also comprises all local temporal fluctuations at one site. It was presented here in a single-band version. However, multiple bands can also be present at a single site. Hence, it is no surprise that the same DMFT can also be used for multi-band Hubbard models (see [68, p.96] for further details).

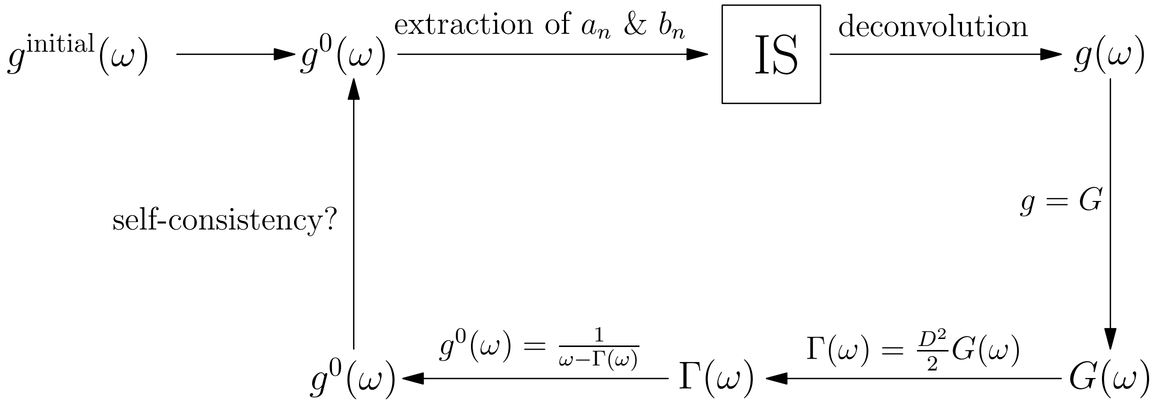

Figure 3.2: Schematic representation of the self-consistency cycle of a Bethe lattice or any lattice with translational symmetry with a semielliptic DOS (see. Eq. (3.6)). The box named with "IS" is the impurity solver which is the D-DMRG (see Sec. 4.1.4 on page 46) in this thesis.

The natural extension to this standard DMFT is to incorporate spatial fluctuations in order to capture the physics of non-local fluctuations. Such dynamic mean-field theories, so-called "quantum cluster DMFT", are more difficult to formulate (see Ref. [128] for a review). Another way for extending DMFT is to formulate a DMFT for bosons. The problem to formulate such a B-DMFT is the Bose-Einstein condensation of bosons for low temperatures. B-DMFT was set up in 2008 by Byczuk and Vollhardt [32]. Recently, Byczuk and Vollhardt extended B-DMFT to mixtures of fermions and bosons on a lattice (in order to handle such mixtures in optical lattices), the so-called BF-DMFT [33]. Optical lattices also show non-local fluctuations, but up to now no cluster BF-DMFT has been set up.

## 3.3 Effective One-Site-Model for DMFT: The Single Impurity Anderson Model (SIAM)

### 3.3.1 Origin of the SIAM – Historical Remarks

Although the Single-Impurity-Anderson Model (SIAM) [8] is nowadays often mentioned in the context of DMFT (like in this thesis), its origin stems from a different problem of solid state physics. This problem is known as the "resistivity minimum problem" meaning the difficulties in explaining the minimum of resistivity as a function of temperature in doped or impure metals. Such a minimum was first found in 1922 by Bidwell [19] who analyzed Germanium. The first exhaustive analysis of the resistivity of metals at low temperatures was done by Meissner and Voigt [133] in 1930 who showed that this minimum is a generic feature. The increase of resistivity for low temperatures was a contradiction the expected $T^5$-Bloch-law [13, p.668], i.e. the monotonous decrease of resistivity if the temperature reaches zero. It was suspected that impurities play an important role in this context. After being able to produce pure samples, it was shown by Franck et al. [55] in 1961, who analyzed copper with iron impurities, that the position of this minimum depends on the degree of purity. The theoretical explanation was given by J. Kondo [109] in 1964 who used the s-d-exchange model (the so-called Kondo model) to consider the interaction between a local magnetic moment with the conduction electrons in a third order perturbation theory analysis. The scattering between the local magnetic moment and the conduction electrons led in third order to a logarithmic contribution ($\ln(T)$) to the resistivity which increases for low temperatures explaining the existence of a minimum. This third order correction exceeds the first and second order contribution, making it necessary to consider the whole series. However, this could not be the final result because in real materials resistivity does not diverge for $T \to 0$. This problem is called the “Kondo problem”. It was Wilson [226] in 1975 who used a non-perturbative renormalization approach to finally solve the Kondo problem[2]. Afterwards, numerous investigations on Kondo-like problems were done; see the monograph of Hewson [83] for an exhaustive review.

### 3.3.2 Formulation of the SIAM

Since we are not focussing on the context of magnetic impurities, we omit the motivation of this model (see the original work [8] for this) and just mention the Hamiltonian which is

$$\mathscr{H}_{\mathrm{SIAM}} = \sum_{\sigma} \epsilon_{\mathrm{d}} n_{\mathrm{d},\sigma} + U n_{\mathrm{d},\uparrow} n_{\mathrm{d},\downarrow} + \sum_{\vec{k},\sigma} \epsilon_{\vec{k}} c^{\dagger}_{\vec{k},\sigma} c_{\vec{k},\sigma} + \sum_{\vec{k},\sigma} \left( V_{\vec{k}} d^{\dagger}_{\sigma} c_{\vec{k},\sigma} + V^{*}_{\vec{k}} c^{\dagger}_{\vec{k},\sigma} d_{\sigma} \right) . \tag{3.14}$$

It consists of conduction electrons (the $c$-operators) which are coupled by the hybridization $V$ to the impurity electron (the $d$-operator)[3]. We restrict our analysis here to a non-degenerate d-orbital. If there are two electrons in this d-orbital, their interaction is given by Coulomb repulsion $U$. The Hamiltonian (3.14) can be mapped onto the s-d model, i.e. the Kondo model, for small hybridizations $V_{\vec{k}}$ [181]. In the framework of DMFT, we need to treat the more general SIAM.

In order to investigate the SIAM via DMRG (see chapter 4 starting on page 39), it is useful to map the SIAM onto a linear chain with $N_{\mathrm{c}}$ conduction electron sites plus one impurity site. To do so, we introduce a new operator

$$c^{\dagger}_{1,\sigma} := \frac{1}{V} \sum_{\vec{k}} V_{\vec{k}} c^{\dagger}_{\vec{k},\sigma} \qquad \text{with} \qquad V^2 := \sum_{\vec{k}} \left| V_{\vec{k}} \right|^2 . \tag{3.15}$$

If we denote the Fock-vacuum state with $|0\rangle$, then the creation operator $c^{\dagger}_{1,\sigma}$ creates a localized one-electron state $|1\rangle$ at the first site of the conduction electron chain. Definition (3.15) leaves the first two terms in (3.14) unchanged and the fourth term simply changes into

$$\sum_{\vec{k},\sigma} \left( V_{\vec{k}} d^{\dagger}_{\sigma} c_{\vec{k},\sigma} + V^{*}_{\vec{k}} c^{\dagger}_{\vec{k},\sigma} d_{\sigma} \right) = \sum_{\sigma} V \left( d^{\dagger}_{\sigma} c_{1,\sigma} + c^{\dagger}_{1,\sigma} d_{\sigma} \right) \tag{3.16}$$

with a real[4] positive number $V$. In order to transform the remaining part

$$\mathscr{H}_{\mathrm{c}} = \sum_{\vec{k},\sigma} \epsilon_{\vec{k}} c^{\dagger}_{\vec{k},\sigma} c_{\vec{k},\sigma} \tag{3.17}$$

---

[2] Five years later, the Kondo problem was independently solved via exact Bethe-ansatz by Andrei [11] and by Wiegmann [225]. For a review see Ref. [12].

[3] The impurity state is named “d” for historical reasons. Anderson [8] wanted to give a model for an impurity of transition metal (3d) or rare earth (4f) type in a host metal. We keep this notion here.

[4] Note that definition (3.15) does not exclude complex valued $V = V e^{\mathrm{i}\phi}$, but this phase $\phi$ can be easily gauged away with some unitary transformation of the operators $c_{1,\sigma}$. Hence, the decision that $V$ is real does not imply a loss of generality.

of the Hamiltonian (3.14), we use Lanczos tridiagonalization implying that we obtain the sequence $|\,1\rangle$, $\mathscr{H}_\mathrm{c}\,|\,1\rangle$, $\mathscr{H}_\mathrm{c}^2\,|\,1\rangle$, …, $\mathscr{H}_\mathrm{c}^{N_\mathrm{c}-1}\,|\,1\rangle$ ($N_\mathrm{c}$ is the number of electrons in the bath) as new linear independent states from which we can construct the new basis states $|\,n\rangle$. With the first state $|\,1\rangle$ given, the next basis state $|\,2\rangle$ can be constructed via

$$|\,2\rangle = \frac{1}{\gamma_1}\left(\mathscr{H}_\mathrm{c}\,|\,1\rangle - |\,1\rangle\,\langle 1\,|\mathscr{H}_\mathrm{c}|\,1\rangle\right) \tag{3.18}$$

in which $\gamma_1 \in \mathbb{R}$ has to be chosen such that $|\,2\rangle$ is normalized[5]. The recursive Lanczos relation to get the $(n+1)$th state for $1 < n < (N_\mathrm{c}-1)$ reads

$$|\,n+1\rangle = \frac{1}{\gamma_n}\left(\mathscr{H}_\mathrm{c}\,|\,n\rangle - |\,n\rangle\,\langle n\,|\mathscr{H}_\mathrm{c}|\,n\rangle - |\,n-1\rangle\,\langle n-1\,|\mathscr{H}_\mathrm{c}|\,n\rangle\right) \tag{3.19}$$

in which $\gamma_n$ has to be chosen such that state $|\,n+1\rangle$ is normalized. By this procedure, orthonormality of all states $|\,1\rangle$ , $|2\rangle$ ,…, $|\,N_\mathrm{c}\rangle$ is guaranteed. Hence, (3.17) is transformed into a ($N_\mathrm{c}\times N_\mathrm{c}$-dimensional) tridiagonal matrix whose elements read

$$\langle m\,|\mathscr{H}_\mathrm{c}|\,n\rangle = \begin{cases} \epsilon_n & \text{if } m = n \\ \gamma_n & \text{if } m = n+1 \\ \gamma_{n-1} & \text{if } m = n-1 \\ 0 & \text{else} \end{cases} \tag{3.20}$$

in which we introduced the diagonal elements $\epsilon_n$, i.e. the energy of the $n$th conduction electron with $n \in \{1, 2, ..., N_\mathrm{c}\}$ and the hopping amplitude $\gamma_{n-1}$ between site $n-1$ and $n$ with $n \in \{1, 2, ..., N_\mathrm{c}-1\}$. Note that there are $N_\mathrm{c}-1$ bonds between $N_\mathrm{c}$ electrons on a one-dimensional chain. Thus, the SIAM Hamiltonian (3.14) reads in chain-form

$$\begin{aligned}\mathscr{H}_\mathrm{SIAM} =& \epsilon_\mathrm{d} n_{\mathrm{d},\sigma} + \sum_{i=1,\sigma}^{N_\mathrm{c}} \epsilon_i c^\dagger_{i,\sigma} c_{i,\sigma} + U n_{\mathrm{d},\uparrow} n_{\mathrm{d},\downarrow} + \\ & \sum_\sigma V\left(d^\dagger_\sigma c_{1,\sigma} + c^\dagger_{1,\sigma} d_\sigma\right) + \sum_{i=1,\sigma}^{N_\mathrm{c}-1} \gamma_i \left(c^\dagger_{i,\sigma} c_{i+1,\sigma} + c^\dagger_{i+1,\sigma} c_{i,\sigma}\right)\end{aligned} \tag{3.21}$$

which can be written even more compact

$$\mathscr{H}_\mathrm{SIAM} = \sum_{i=0,\sigma}^{N_\mathrm{c}} \epsilon_i c^\dagger_{i,\sigma} c_{i,\sigma} + U n_{0,\uparrow} n_{0,\downarrow} + \sum_{i=0,\sigma}^{N_\mathrm{c}-1} \gamma_i \left(c^\dagger_{i,\sigma} c_{i+1,\sigma} + c^\dagger_{i+1,\sigma} c_{i,\sigma}\right) \tag{3.22}$$

by identifying the impurity site d with site “0” of the chain[6]. The SIAM in chain-form is sketched in Fig. 3.3.

---

[5] The Fock-vacuum $|\,0\rangle$ is normalized by definition. The normalization of $|\,1\rangle$ is ensured by Eq. (3.15).

[6] Obviously, this implies $\epsilon_0 := \epsilon_\mathrm{d}$, $\gamma_0 := V$ and $c^{(\dagger)}_{0,\sigma} := d^{(\dagger)}_\sigma$.

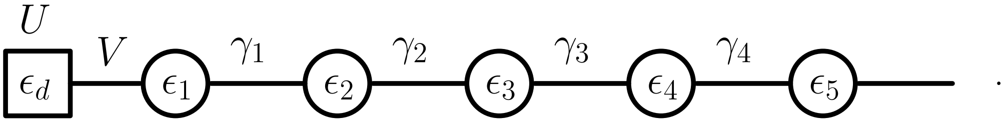

Figure 3.3: Sketch of the SIAM in chain-form described by the Hamiltonian (3.22).

In the context of DMFT, we are interested in determining the bath surrounding the impurity of the SIAM. All information of the bath, i.e. all information that are coded into the conduction electrons is comprised by the so-called *hybridization function* [212, p.47f.]

$$\Gamma(z) = V^2\Delta(z) \tag{3.23}$$

with $z := \omega + \mathrm{i}0^+$. The function $\Delta(z)$ is given [212, p.49] as a resolvent

$$\Delta(z) = \left\langle 1 \left| \frac{1}{z - \mathscr{H}_\mathrm{c}} \right| 1 \right\rangle . \tag{3.24}$$

The following facts make use of continued fractions (CFs) which may seem to occur here haphazardly. In order to dispel this impression, a lengthy remark would be necessary that point to the many distinct fields of math where CFs occur elucidating also the rich history of CFs. For a first introduction, the reader is referred to the textbook of Chihara [36]. Theoretical condensed matter physics makes use of those mathematical insights when calculating Green functions. A seminal, early review was given by Grosso and Parravicini [73] in 1985. This work influenced common textbooks on this topic like Pettifor & Weaire [155] and Viswanath [212]. We follow the line of argument of Viswanath [212, p.49f.] to compute the resolvent (3.24). Referring to Ref. [73, p.97f.], we see that $\Delta(z)$ can be written as a quotient of two Hankel determinants[7] of $[z - \mathscr{H}_\mathrm{c}]$

$$\Delta(z) = \frac{T_2(z)}{T_1(z)}. \tag{3.25}$$

We find the following recursion relation for the Hankel determinants:

$$\begin{aligned} T_i(z) &= (z - \epsilon_i)T_{i+1}(z) + \gamma_i^2 T_{i+2}(z) \qquad \text{for} \qquad i = 1, 2, ..., N_\mathrm{c} - 2 \\ T_{N_\mathrm{c}-1}(z) &= (z - \epsilon_{N_\mathrm{c}-1})T_{N_\mathrm{c}}(z) + \gamma_{N_\mathrm{c}-1}^2 \\ T_{N_\mathrm{c}}(z) &= (z - \epsilon_{N_\mathrm{c}}) \end{aligned} \tag{3.26}$$

Thus, the quotient of two subsequent Hankel determinants is given by

$$\frac{T_i(z)}{T_{i+1}(z)} = (z - \epsilon_i) + \gamma_i^2 \frac{T_{i+1}(z)}{T_{i+1}(z)}. \tag{3.27}$$

---

[7] Hankel determinants are one generalization of usual determinants of a given quadratical matrix. Given an $N \times N$-matrix, the Hankel determinant $T_n$ is given by the determinant where the first $n - 1$ rows and columns are omitted. Hence, $T_1$ is the usual determinant of a matrix.

Inserting (3.27) into (3.25) yields the continued fraction representation of $\Delta(z)$

$$\Delta(z) = \frac{T_2(z)}{T_1(z)} = \cfrac{1}{z - \epsilon_1 - \gamma_1^2 \frac{T_3(z)}{T_2(z)}} = \cfrac{1}{z - \epsilon_1 - \cfrac{\gamma_1^2}{z - \epsilon_2 - \gamma_2^2 \frac{T_4(z)}{T_3(z)}}} = \dots . \tag{3.28}$$

Hence, the hybridization function $\Gamma(z)$ can be written as a continued fraction via

$$\Gamma(z) = \cfrac{V^2}{z - \epsilon_1 - \cfrac{\gamma_1^2}{z - \epsilon_2 - \cfrac{\gamma_2^2}{z - \epsilon_3 - \dots}}} \tag{3.29}$$

wherein all degrees of freedom of the bath surrounding the impurity are given by the continued fraction coefficients $\gamma_i$ and $\epsilon_i$.

For $U = 0$, the difference between $\mathscr{H}_\mathrm{c}$ and the full Hamiltonian (3.22) is just one further site with hopping amplitude $V$. Hence, we obtain the propagator (3.8) on page 20 of the non-interacting system. The way how to calculate the full one particle propagator at $T = 0$ is given in the beginning of Sec. 4.1.4 on page 46.

### 3.3.3 Jordan-Wigner Transformation of the SIAM

After having mapped the SIAM onto a one-dimensional chain where the bath is represented by the hybridization function, we carry out one further mapping of the SIAM, namely the Jordan-Wigner (JW) transformation[8] introduced by Jordan and Wigner [99] in 1928. We do so because we want to use the finite-system DMRG algorithm (see Sec. 4.1.3) for solving the SIAM[9]. There are mainly two motivations for mapping the SIAM onto spin chains:

1. As will be explained in Sec. 4.1.6.1 on page 49, the DMRG method optimizes in a certain sense the bonds between the sites. In particular, DMRG optimizes the bonds of the active site(s) during one step in the sweeping procedure. But the DMRG sweep (see Sec. 4.1.3) stops before reaching the last site at the edges of the chain because the number of states $m$ in the truncated basis is larger than the number of states $f$ of a single site. Hence, the bonds of the first and the last sites of the chain are not optimized by DMRG. This is not a severe problem for the last sites of the chain because the bonds $\gamma_n$ converge to a limiting value $\gamma_\infty$ (see Sec. 4.4 on page 73) for $n > n_\infty$. Hence, we just have to choose an adequate chain size $N_\mathrm{c} > n_\infty + \log_f m$. In contrast, not optimizing the first bonds near the impurity site could affect the accuracy of the results adversely. After JW mapping, the impurity and the formerly first sites are located in the middle of the chain. Then the less important bonds are found at both edges of the chain. Hence, JW mapping ensures that all relevant bonds $\gamma_n$ (with $n < n_\infty$) are optimized during a DMRG sweep.

---

[8] A pedagogical article about this transformation can be found at `http://www.physics.ubc.ca/~berciu/TEACHING/PHYS503/PROJECTS/XYModel2.pdf`.

[9] In order to understand the following motivation, the reader should be familiar with DMRG (see. chapter 4 starting on page 39).

2. One DMRG step consists of adding one site and projecting the corresponding enlarged Hilbert space down to the number $m$ of kept states again. This introduces a certain truncation error. The larger the local Hilbert space is, the larger this truncation error will be. The Jordan-Wigner transformation halve the dimension of the Hilbert space of a single site and hence reduce the truncation error.

There is a third, more general, argument for the JW mapping that takes care of the different Hilbert spaces of fermions and spins. Dealing with a chain of fermions implies dealing with a fermionic Fock space which requires to keep track of long-range phases. After JW transformation, the complete Hilbert space is a direct product of local Hilbert spaces, i.e. we avoid the above mentioned difficulty of a fermionic Fock space.

A JW mapping of a system of fermions must be obtained for every possible spin orientation of the fermions separately. Since electrons can have spin up or down, the JW mapping double the size of the chain. One part, the $S$-part, correspond to the spin up fermions; the other part, the $T$-part, correspond to the spin down fermions. Both parts are coupled at the previous impurity site (which is then placed in the middle of both chains) and the previous Coulomb repulsion translates into a product of $z$-components. This is sketched in Fig. 3.4. In order to save space, the JW transformation is described only for one part of the chain.

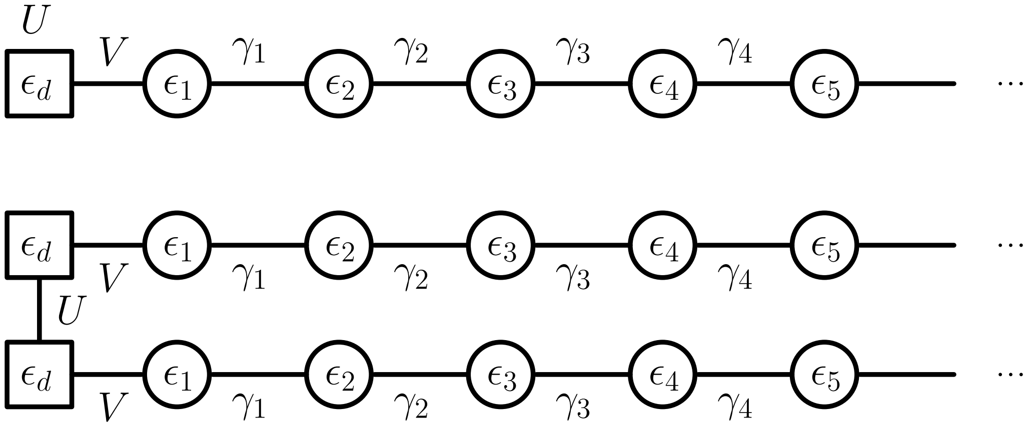

Figure 3.4: Upper part: The SIAM chain before Jordan-Wigner transformation. The local field $\epsilon_i$ ($\epsilon_0 = \epsilon_\mathrm{d}$) is present at all sites $i$. The hopping amplitude $\gamma_i$ ($\gamma_0 = V$) is present between site $i$ and $i+1$. The Coulomb repulsion $U$ is only present at the impurity site. Lower part: The SIAM chain after Jordan-Wigner transformation consists of two parts with identical parameters $U$,$\gamma_i$ and $\epsilon_i$. The two parts correspond to the two possible spin orientation of the electrons.

We introduce usual spin one-half operators $\vec{S}_i = (S_i^x, S_i^y, S_i^z)$ which obey the relations

$$\begin{aligned} \left[S_j^a, S_k^b\right] &= \mathrm{i}\epsilon_{abc} S_j^c \delta_{jk} \qquad \text{with} \qquad \{a,b,c\} = \{x,y,z\} \\ & S_j^\pm := S_j^x \pm \mathrm{i} S_j^y \\ \left[S_j^+, S_k^-\right] = 2S_j^z\delta_{jk} \qquad & [S_j^z, S_k^\pm] = \pm S_k^\pm \delta_{jk} \qquad \left(S_j^-\right)^2 = \left(S_j^+\right)^2 = 0. \end{aligned} \tag{3.30}$$

The main difference between a chain of spin one-half particles and fermions is that spins at different sites commute (i.e. exhibit a bosonic algebra) but fermions anticommute, hence we cannot directly identify spin-raising(lowering) operators with electron-creation(destruction) operators. Instead, we use

$$c_j = \exp\left(\mathrm{i}\pi \sum_{k=0}^{j-1} S_k^+ S_k^-\right) S_j^- \qquad c_j^\dagger = S_j^+ \exp\left(-\mathrm{i}\pi \sum_{k=0}^{j-1} S_k^+ S_k^-\right) \tag{3.31}$$

which is the JW transformation [99]. If $j = 0$ (the impurity site), the sum is zero and the exponential in (3.31) equals one. This implies $c_0 = S_0^-$ and $c_0^\dagger = S_0^+$. In order to transform the SIAM Hamiltonian (3.21), we need to expand the exponential in a power series to see that

$$\begin{aligned}\exp\left(\pm\mathrm{i}\pi S_j^+ S_j^-\right) &= \sum_{\ell=0}^{\infty} \frac{(\mathrm{i}\pi)^\ell \left(S_j^+ S_j^-\right)^\ell}{\ell!} = 1 + \sum_{\ell=1}^{\infty} \frac{(\mathrm{i}\pi)^\ell S_j^+ S_j^-}{\ell!} = 1 + \left(e^{\pm\mathrm{i}\pi} - 1\right) S_j^+ S_j^- \\ &= 1 - 2 S_j^+ S_j^- .\end{aligned} \tag{3.32}$$

In the second step, we used that $\left(S_j^+ S_j^-\right)$ have only the two eigenvalues zero or one. Now, we can translate the different terms in (3.21)

- $n_j = c_j^\dagger c_j = S_j^+ \exp(\mathrm{i}\pi 0) S_j^- = S_j^+ S_j^- = {}^1\!/\!_2 + S_j^z$
- $c_j^\dagger c_{j+1} = S_j^+ \exp\left(\mathrm{i}\pi S_j^+ S_j^-\right) S_{j+1}^- = S_j^+ \left(1 - 2 S_j^+ S_j^-\right) S_{j+1}^- = S_j^+ S_{j+1}^-$
- $c_{j+1}^\dagger c_j = S_{j+1}^+ \exp\left(-\mathrm{i}\pi S_j^+ S_j^-\right) S_j^- = S_{j+1}^+ \left(1 - 2 S_j^+ S_j^-\right) S_j^- = S_{j+1}^+ S_j^-$

and we obtain the SIAM Hamiltonian with JW spins reading

$$\begin{aligned}\mathscr{H}_{\mathrm{SIAM}} = \frac{U}{4} + \epsilon_{\mathrm{d}} + \sum_{i=1}^{N_{\mathrm{c}}} \epsilon_i + \left(\epsilon_{\mathrm{d}} + \frac{U}{2}\right)\left(S_0^z + T_0^z\right) + \sum_{i=1}^{N_{\mathrm{c}}} \epsilon_i \left(S_i^z + T_i^z\right) \\ + U S_0^z T_0^z + \sum_{i=0}^{N_{\mathrm{c}}-1} \left[\gamma_i \left(S_i^+ S_{i+1}^- + T_i^+ T_{i+1}^-\right) + \mathrm{h.c.}\right].\end{aligned} \tag{3.33}$$

For particle-hole-symmetry, we have to choose $\epsilon_{\mathrm{d}} = -{}^U\!/\!_2$ and $\epsilon_i = 0 \quad \forall i > 0$. In this case, the Hamiltonian (3.33) takes the simpler form

$$\mathscr{H}_{\mathrm{SIAM\ sym}} = -\frac{U}{4} + U S_0^z T_0^z + \sum_{i=0}^{N_{\mathrm{c}}-1} \left[\gamma_i \left(S_i^+ S_{i+1}^- + T_i^+ T_{i+1}^-\right) + \mathrm{h.c.}\right]. \tag{3.34}$$

### 3.3.4 Self-Energy of the SIAM via the Q-function

In the limit of infinite dimension, the dynamics of the Hubbard model is completely local and equals the dynamic of the SIAM at the impurity site. We see from the Dyson Eq. $G(\omega) = G_0(\omega - \Sigma(\omega))$ that the complete information about the dynamics is captured by the self-energy $\Sigma(\omega)$. But calculating the self-energy via Dyson Eq. (3.5) is numerically not very stable due to the involved reciprocals. Hence, it is worthwhile to think about a way to calculate the self-energy directly. One way to do so was proposed by Raas [163, p.28f.] and Raas et al. [165] in which an idea from Bulla et al. [25] was extended. We give here a short summary of Ref. [163, p.28f.].

We use the SIAM in a spin-symmetrized form and split it in three parts

$$\mathscr{H}_{\text{SIAM}} = \mathscr{H}_{\text{imp}} + \mathscr{H}_{\text{hyb}} + \mathscr{H}_{\text{bath}} \tag{3.35}$$

in which the summands are given by

$$\mathscr{H}_{\text{imp}} = U\left(n_{\mathrm{d},\uparrow} - n\right)\left(n_{\mathrm{d},\downarrow} - n\right) - \mu_0 \sum_{\sigma}\left(n_{\mathrm{d},\sigma} - n\right) \tag{3.36a}$$

$$\mathscr{H}_{\text{hyb}} = \sum_{\vec{k},\sigma} V_{\vec{k}} \left(d^\dagger_\sigma c_{\vec{k},\sigma} + \text{h.c.}\right) \tag{3.36b}$$

$$\mathscr{H}_{\text{bath}} = \sum_{\vec{k},\sigma} \epsilon_{\vec{k}} : c^\dagger_{\vec{k},\sigma} c_{\vec{k},\sigma} : \tag{3.36c}$$

and wherein $U$ is the interaction strength and $\mu_0$ the chemical potential at the impurity site, $V_{\vec{k}}$ the hybridization, $n_{\mathrm{d},\sigma} = d^\dagger_\sigma d_\sigma$ and $n := \langle n_{\mathrm{d},\sigma}\rangle$ the particle density at the impurity site. In this form, the hybridization function (3.24) $\Gamma(z)$ reads

$$\Gamma(z) = \sum_{\vec{k}} V^2_{\vec{k}} \frac{1}{z - \epsilon_{\vec{k}}} \tag{3.37}$$

whereby we can write the non-interacting local propagator

$$G_0^{-1} = z + \mu_0 - \Gamma(z). \tag{3.38}$$

Note that in the whole section we use $z = \omega + i\eta$ with $\Im z > 0$. If we know the self-energy[10] at the impurity site, we can write the full propagator as

$$G^{-1} = z + \mu_0 - \Gamma(z) - \Sigma(z) = G_0^{-1} - \Sigma(z). \tag{3.39}$$

We define the general retarded fermionic Green function (see Sec. 4.1.4 on page 46) of two operators $\mathscr{A}$ and $\mathscr{B}$ for a time-independent Hamiltonian $\mathscr{H}$ as

---

[10] In contrast to the notation during the discussion of the DMFT in Sec. 3.2 on page 18, we use here capital letters for the SIAM.

$$G_{\mathscr{A},\mathscr{B}}(z) := -i \int_0^\infty \langle 0 \,|\{\mathscr{A}(t), \mathscr{B}(0)\}|\, 0\rangle\, e^{\mathrm{i}zt}\mathrm{d}t. \tag{3.40}$$

Integration by parts yields

$$zG_{\mathscr{A},\mathscr{B}}(z) + G_{\widehat{\mathscr{L}\mathscr{A}},\mathscr{B}}(z) = \langle 0 \,|\{\mathscr{A}(0), \mathscr{B}(0)\}|\, 0\rangle \;\Leftrightarrow\; zG_{\mathscr{A},\mathscr{B}}(z) - G_{\mathscr{A},\widehat{\mathscr{L}\mathscr{B}}}(z) = \langle 0 \,|\{\mathscr{A}(0), \mathscr{B}(0)\}|\, 0\rangle \tag{3.41}$$

where $\widehat{\mathscr{L}\mathscr{X}} = (\mathscr{H}\mathscr{X} - \mathscr{X}\mathscr{H})$ is the Liouville operator[11] and where we used the invariance with respect to translation in time.

Now, we specify $\mathscr{A} = d_\sigma$ and $\mathscr{B} = d_\sigma^\dagger$ in Eq. (3.41) which yields

$$(z - \mu_0)\, G(z) - \sum_{\vec{k}} V_{\vec{k}} G_{c_{\vec{k},\sigma}(z), d_\sigma^\dagger} - U \underbrace{G_{d_\sigma\left(n_{\mathrm{d},-\sigma}\right), d_\sigma^\dagger}(z)}_{:=F(z)} = 1. \tag{3.42}$$

Then, we specify $\mathscr{A} = c_{\vec{k},\sigma}$ and $\mathscr{B} = d_\sigma^\dagger$ in (3.41) which yields

$$\left(z - \epsilon_{\vec{k}}\right) G_{c_{\vec{k},\sigma}, d_\sigma^\dagger}(z) - V_{\vec{k}} G(z) = 0. \tag{3.43}$$

Solving Eq. (3.43) for $G_{c_{\vec{k},\sigma}, d_\sigma^\dagger}(z)$ and inserting this solution in Eq. (3.42) yields

$$(z + \mu_0 - \Gamma(z))\, G(z) - UF(z) = 1. \tag{3.44}$$

Comparing (3.44) with (3.39) yields the expression for the self-energy

$$\Sigma(z) = U\frac{F(z)}{G(z)} \tag{3.45}$$

which is the result of Bulla et al. [25]. But to employ this formula, we still need to calculate $F(z)$ *and* $G(z)$. To overcome this, we choose $\mathscr{A} = d_\sigma \left(n_{\mathrm{d},-\sigma} - n\right)$ and $\mathscr{B} = d_\sigma^\dagger$ in Eq. (3.41) which yields

$$(z + \mu_0)\, F(z) - UQ(z) - \sum_{\vec{k}} V_{\vec{k}} G_{d_\sigma\left(n_{\mathrm{d},-\sigma} - n\right), c_{\vec{k},\sigma}^\dagger} = 0 \tag{3.46}$$

in which we introduced the $Q$-function

$$Q(z) := G_{d_\sigma\left(n_{\mathrm{d},-\sigma} - n\right), d_\sigma^\dagger\left(n_{\mathrm{d},-\sigma} - n\right)}(z) = -i \int_0^\infty \left\langle 0 \left| \left\{ d_\sigma \left(n_{\mathrm{d},-\sigma} - n\right), d_\sigma^\dagger \left(n_{\mathrm{d},-\sigma} - n\right) \right\} \right| 0 \right\rangle e^{\mathrm{i}zt}\mathrm{d}z. \tag{3.47}$$

---

[11] Since this operator maps an operator onto another operator, the Liouville operator $\widehat{\mathscr{L}}$ is sometimes called a "super-operator". We do not adopt this notation because it lacks mathematical rigor and we do not need to discuss the mathematical details of more general mappings than operators. If this were the case, we would refer to the mathematically rigorous notions of "functors" (for mappings as an analog to operators) and morphisms (for structures); see Ref. [130, p.26f.].

Next, we use Eq. (3.41) with $\mathscr{A} = d_\sigma \left(n_{\mathrm{d},-\sigma} - n\right)$ and $\mathscr{B} = c^\dagger_{\vec{k},\sigma}$ which yields

$$\left(z - \epsilon_{\vec{k}}\right) G_{d_\sigma \left(n_{\mathrm{d},-\sigma} - n\right), c^\dagger_{\vec{k},\sigma}}(z) - V_{\vec{k}} F(z) = 0. \tag{3.48}$$

Solving this Eq. for $G_{d_\sigma \left(n_{\mathrm{d},-\sigma} - n\right), c^\dagger_{\vec{k},\sigma}}(z)$ and inserting this into Eq. (3.46) yields

$$\left(z + \mu_0 - \Gamma(z)\right) F(z) - UQ(z) = 0 \tag{3.49}$$

from which we conclude $F(z) = UQ(z)G_0(z)$. Via the result (3.45) of Bulla et al. [25], it follows

$$\Sigma(z) = U \frac{Q(z)G_0(z)}{G(z)} = U^2 Q(z) \left(1 - \Sigma(z) G_0(z)\right) = \frac{U^2 Q(z)}{1 + U^2 Q(z) G_0(z)} \tag{3.50}$$

which is an expression for the self-energy that is dependent solely on the Q-function and the bare propagator. Inserting this into the Dyson equation (3.39) yields

$$G(z) = G_0(z) \left(1 + U^2 Q(z) G_0(z)\right) \tag{3.51}$$

which is a direct expression for the local propagator via the Q-function. The spectral density $\rho_Q(\omega) = -1/\pi \Im Q(\omega)$ of the Q-function obeys the sum rule [163, p.31]

$$\int_{-\infty}^{\infty} \rho_Q(\omega) \mathrm{d}\omega = n(1-n) \tag{3.52}$$

which implies a sum rule for the spectral density $\rho_\Sigma(\omega) = -1/\pi \Im \Sigma(\omega)$ of the self-energy that reads

$$\int_{-\infty}^{\infty} \rho_\Sigma(\omega) \mathrm{d}\omega = U^2 n(1-n). \tag{3.53}$$

For the non-interacting case $U = 0$, the spectral density $\rho_Q(\omega)$ of the Q-function can be calculated analytically [145, 163] with the help of the spectral densities $\rho_0(\omega) = -1/\pi \Im G_0(\omega)$ of the bare propagator $G_0(\omega)$ via the double integral

$$\rho_Q(\omega) = \int_0^{\omega} \mathrm{d}\omega_1 \rho_0(\omega_1 - \omega) \int_0^{\omega_1} \mathrm{d}\omega_2 \rho_0(\omega_2) \rho(\omega_1 - \omega_2). \tag{3.54}$$

The full Q-function can be calculated via Kramers-Kronig relations.

At last, we shall give the Q-operator $\mathscr{Q} = d^\dagger_\uparrow \left(n_{\mathrm{d},\downarrow} - n\right)$, whereby we can write the Q-function as

$$Q(z) = -\mathrm{i} \int_0^{\infty} \left\langle 0 \left| \{\mathscr{Q}^\dagger, \mathscr{Q}\} \right| 0 \right\rangle e^{\mathrm{i}zt} \mathrm{d}z, \tag{3.55}$$

in Jordan-Wigner transformed form. It reads

$$\mathscr{Q} = S_0^+ T_0^z + \left(\frac{1}{2} - n\right) S_0^+. \tag{3.56}$$

In the half-filled case, $n = 1/2$ so that the last term vanishes.

## 3.4 Impurity Solvers – an Overview

In this section, we briefly review common impurity solvers for DMFT. We restrict ourselves to impurity solvers for fermionic DMFT without extensions to incorporate spatial fluctuations or bosonic degrees of freedom. The review covers the methods

- Exact diagonalization (ED)
- Iterative Perturbation Theory (IPT)
- Quantum Monte-Carlo Methods (QMC)
- Non-crossing Approximation (NCA)
- Numerical Renormalization Group theory (NRG) and
- Dynamic Density-Matrix Renormalization Group theory (D-DMRG)

which all have their own subsections. It will turn out that D-DMRG (which is used in this thesis) yields Green functions at $T = 0$ with good resolution at low *and* high energies better than the other impurity solvers.

### 3.4.1 Exact Diagonalization

Since every quantum system whose energy spectrum is bounded from above and below is described by a Hamiltonian that is writable as a hermitian matrix, the method "exact diagonalization" is not a particular method for impurity solving but of quantum mechanics as such. The ubiquitous problem of this method is that the size of the matrix grows exponentially as a function of the system size. Hence, it is not clear from the beginning that the SIAM with a reasonable size of the bath can be treated that way.

In 1994, Caffarel and Krauth [34] introduced such an ED method. The main idea for their method was that the bath Green function $g_0$, which may be written as

$$g_0^{-1}(\mathrm{i}\omega_n) = \mathrm{i}\omega_n + \mu - \int_{-\infty}^{\infty} \mathrm{d}\omega' \frac{\Delta(\omega')}{\mathrm{i}\omega_n - \omega'} \tag{3.57}$$

with the hybridization function $\Delta(\omega)$ and with imaginary (Matsubara) frequencies, can be approximated by a discretized bath

$$\left(g_0^{n_\mathrm{s}}(\mathrm{i}\omega)\right)^{-1} = \mathrm{i}\omega_n + \mu - \sum_{p=2}^{n_\mathrm{s}} \frac{V_p^2}{\mathrm{i}\omega_n - \epsilon_p} \tag{3.58}$$

which has $n_\mathrm{s}$ orbitals (which determines $\{V_p, \epsilon_p\}$). Usually, $n_\mathrm{s}$ is between five and ten. The self-consistency cycle starts with an initial bath with which $g(\omega)$ is calculated. Then, a new $g_0$ is calculated which has to be approximated by a new $g_0^{n_\mathrm{s}}$. This approximation is carried out as a minimization of the distance $d$ between both baths

$$d := \frac{1}{n_\mathrm{max} + 1} \sum_{n=0}^{n_\mathrm{max}} \left| g_0(\mathrm{i}\omega_n)^{-1} - \left(g_0^{n_\mathrm{s}}(\mathrm{i}\omega_n)\right)^{-1} \right|^2 \tag{3.59}$$

in which $n_{\max}$ is a large upper cutoff. One should note that this minimization is taken at the imaginary and not the at real frequency axis. Hence, this method has a good resolution only for small frequencies. In addition, Matsubara frequencies are used that correspond to a certain temperature $T$. If $T = 0$ is calculated, this is a fictitious temperature that serves as a low-energy cutoff. Thus, this ED gives the low-energy physics with a certain finite resolution.

This drawback stems from the minimization procedure that is carried out at imaginary frequencies. In 1994, Si et al. [177] proposed another ED scheme that is carried out at the real axis. In their procedure, the bath is parametrized by the continued fraction coefficients of both parts[12] $\Delta^{>}(\omega)$ and $\Delta^{<}(\omega)$ of the hybridization function $\Delta(\omega) = \Delta^{<}(\omega)+\Delta^{>}(\omega)$. The depth $n_{\mathrm{c}}$ of both continued fractions is given by $n_{\mathrm{s}} = 2n_{\mathrm{c}} + 1$. This necessitates a very limited depth $n_{\mathrm{c}}$ so that this method gives accurate results only for the total energy and high-energy features. For this reason, it is mainly used for the insulating phase since it cannot resolve the Kondo resonance adequately.

Another variation of exact diagonalization was given in 2003 by Eastwood et al. [44]. Their main improvement for calculating the Hubbard bands of the insulator is to fix the energies $\epsilon_p$. In the prior mentioned method, the energies $\epsilon_p$ are placed freely. In contrast, the ED by Eastwood et al. fixes the energy range where the $\epsilon_p$ can be placed, hence the name "fixed energy ED" for this type of ED. Since no frequency can be positioned outside the bands, this method yields a better resolution of the bands if $n_{\mathrm{s}}$ is increased. Obviously, this method rests on the a priori guess of the finite frequency range which Eastwood et al. [44] deduce from a perturbation theoretical approach around the insulating phase. The ED introduced by Caffarel and Krauth [34] gives accurate results only for small energies and the fixed energy ED by Eastwood et al. [44] gives accurate results only for high energies. Recently in 2009, Hafermann et al. [78] proposed an ED method applied to perturbational approach around the atomic limit that seems to be able to capture also the intermediate range between weak and strong coupling.

One should note that the bath itself is not restricted to a one-band case. Koga et al. [107] in 2004, Liebsch [120] and Biermann et al. [20] in 2005 applied ED to two-band Hubbard models as well. But the number of bands seem to be limited due to the exponential growth of the dimension of the matrices involved. However, in 2007 Perroni et al. [153] showed that ED in the framework of DMFT can be used also for realistic multi-orbital materials. But Perroni et al. [153] were restricted to $T > 0$ to yield reasonable results.

One could conclude that ED is an impurity solver suited either for resolving low- *or* high-energy features but not both. Hence, it is best used for the insulating phase, i.e. the strong coupling limit. Since it involves exponentially growing computation efforts, it is not suited for complicated bands with a lot of features. But if no sharp features are present, ED yields accurate results.

### 3.4.2 Iterative Perturbation Theory

Iterative Perturbation Theory (IPT) uses a weak-coupling approximation for the local self-energy that is exact up to the second order of the coupling. It was introduced for the half-filled single-band Hubbard model in 1992 by Georges and Kotliar [67] and Jarrell [94]. For tracing back the ideas that led to IPT, see Ref. [68, p.50]. It can be used for all temperatures $T$ (including $T = 0$) and interaction strengths $U$. Although IPT starts as a perturbation theory, i.e. its origin stems from considering small perturbations around one analytic solution (the weak-coupling limit), it also correctly obtains the strong-coupling limit. However, between both limiting cases, IPT must be characterized as an

---

[12] See Eq. (4.19) on page 46 for the definition of the >- and <-part of a response function.

interpolation. In contrast to ED, IPT does not need to discretize the bath. It yields continuous functions from the beginning. For several years, IPT was restricted to the half-filling case because attempts to generalize it to arbitrary filling violated the Friedel sum rule (see Ref. [127, p.234]), i.e. charge conservation is violated, because IPT did not fulfill the Luttinger theorem [122].

This problem was solved 1996 by Kajueter and Kotliar [100]. They proposed an IPT for arbitrary filling which converges to the analytic results for the weak- and the strong-coupling regime and also for $\omega \to 0$ and $\omega \to \infty$ and which is in agreement with the Luttinger-theorem. This generalized IPT is in good agreement with ED results, although it is much faster than ED. However, IPT was still restricted to the one-band case. The generalization to the multi-orbital case was done in 2003 by Fujiwara et al. [57]. For a recent review on IPT including details of implementation, see Ref. [168].

In the review [168] of Radzimirski and Wojciechowski, the structure of IPT is clearly worked out. IPT correctly yields several limiting cases but between those limiting cases only an interpolation is carried out. This is clearly seen in the approximate formula for the self-energy reading

$$\Sigma(\omega) = Un + \frac{A\Sigma^{(2)}(\omega)}{1 - B(\omega)\Sigma^{(2)}(\omega)} \tag{3.60}$$

which is formula (7) in Ref. [168]. $\Sigma^{(2)}$ denotes the second order perturbation of the self-energy in the weak-coupling limit. The two parameters $A$ and $B(\omega)$ are determined such that the weak- and strong-coupling limit are correctly obtained in IPT. This implies that features obtained between those limits should be considered with greatest caution. In addition, the result of IPT near the Mott-transition strongly depends on the initial self-energy of the cycle. In particular, near the Mott-transition in the half-filled case IPT fails to give good results [92]. Hence, IPT is a fast technique to scan the parameter space for several interaction and hopping strengths and also for different temperatures. IPT is easily implemented and it is consistent with several limiting cases. But the rich physics in the intermediate regime and especially near the Mott-transition is not faithfully obtained.

### 3.4.3 Quantum Monte-Carlo Methods

The original Monte-Carlo method was invented in 1949 by Metropolis and Ulam [134] who worked in Los Alamos and needed a method to treat stochastic processes like the ones which occur in nuclear fission reactors. The main idea is to calculate expectation values of quantities that are given by a certain dynamic (say classical Hamilton equations or the Schrödinger equation) but without solving the dynamic equations. Instead, the phase or Hilbert space is sampled via a stochastic process. This works because of the *law of large numbers* which was first proven by J. Bernoulli[13] in 1713. The Monte-Carlo method was adapted to quantum systems by Hirsch and Fye [84] in 1986 (HF-QMC). For a review of QMC methods in many-body physics, see the review by von der Linden [121]. The main idea of Quantum Monte-Carlo (QMC) is that the imaginary time interval $\tau \in [0, \beta]$ (with $\beta$ being the inverse temperature) of the integral of the partition function is divided into several parts and that the Hilbert space of the corresponding slices are sampled individually. Slicing implies that the exponentials of the Hamiltonian are split. At this point the *Trotter decomposition* [197] is applied meaning that the approximation $\exp(\mathscr{A} + \mathscr{B}) \approx \exp \mathscr{A} \exp \mathscr{B}$ is used. For further details (including computer source code), the reader is referred to the DMFT-review of Georges et al. [68, p.34f.].

---

[13] Since the original work of Bernoulli is written in Latin, see the English translation by Oscar Sheynin at `http://www.sheynin.de/download/bernoulli.pdf`.

The above statements are enough to assess QMC as an impurity solver for DMFT. All Monte-Carlo methods lead to statistical errors of the calculated quantities, since the whole Hilbert space is not explored but only sampled via a (physically wrong) stochastic process. In addition, the Trotter decomposition leads to another source of systematic errors. A further drawback stems from the fact that the Green functions are calculated at imaginary frequencies but the Green function for real frequencies is needed for comparison with experiments. The latter is obtained by applying either least-square fits (see Schüttler and Scalapino [182, 183]) or maximum-entropy methods. For a general introduction to maximum-entropy methods, see Sec. 4.3 on page 68. For early applications of maximum-entropy methods for QMC to solve the Anderson model, see Silver et al. [187]. However, these works have shown that continuing Green functions from discrete imaginary frequencies to real frequencies is an ill-conditioned problem (see e.g. Gubernatis et al. [74]), although one can say as a rule of thumb that difficulties become the more severe the larger the real frequency is one wishes to obtain the spectral density from. Another disadvantage is that the HF-QMC is not able to calculate the Green function for temperature $T = 0$.

There are several attempts to overcome those drawbacks. The limit $T = 0$ is obtained via projection from small but finite temperatures to $T = 0$, i.e. by extrapolating the results to zero temperature. Early works on projective QMC (PQMC) to obtain Green functions at $T = 0$ are done by Assaad & Imada [14] in 1996. Assaad and Imada also refer to earlier works on PQMC that were numerically not so stable (see references in Ref. [14]). Feldbacher and Assaad [48] in 2001 published an improved version of PQMC whose computation is much quicker. In 2004, Feldbacher et al. [49] published an article about PQMC as an impurity solver for DMFT; see also Ref. [50].

The statistical errors can be decreased by longer sampling which needs more computer power. Since QMC is a highly parallelizeable method, statistical errors (in comparison to other errors) do not play a crucial role anymore. The problem that only Green functions of pure imaginary frequencies can be calculated cannot be avoided. The error stemming from the Trotter decomposition can be avoided and needs further comments.

The Trotter decomposition, i.e. the discretization of the imaginary time can be circumvented by so-called continuous time QMC (CT-QMC) methods. Rubtsov et al. [169] introduced a CT-QMC impurity solver for DMFT in 2005. Rubsov et al. combined QMC with a perturbation theory for the interaction $U$. One year later, Werner et al. [215] extended this approach by applying a perturbation theory also for the hybridization. Those works showed much better results than the prior HF-QMC of Hirsch and Fye. However, in the framework of DMFT the analysis of Blümer [21] showed that QMC in a limit of infinitesimal discretization yields a comparable resolution than CT-QMC algorithms.

QMC methods are very common in the field of correlated electrons and DMFT and they are flexible enough to extend them to more complicated situations. Sakai et al. [171] extended the standard QMC to multi-orbital systems. Haule [82] in 2007 extended CT-QMC to apply it for cluster DMFT. In 2008, Gull et al. [76] made further progress to apply CT-QMC to larger clusters in the framework of DMFT. Werner et al. [217] extended CT-QMC to apply it to the three-band Hubbard model in DMFT framework. In 2009, Werner et al. [216] combined QMC with diagrammatic techniques which made it possible to deal with non-equilibrium physics; see also Schiró and Fabrizio [172]. The recently much investigated iron pnictides were also investigated by CT-QMC in a LDA+U-DMFT-framework by Aichhorn et al. [1] in 2009.

We see that QMC and its extensions is a very flexible method with many applications in the framework of DMFT. Since it yields the Green functions at imaginary frequencies, it gives the best resolution for small frequencies. The $T = 0$-case can only be obtained via extrapolation. Since we need a method for small and high frequencies at $T = 0$, we have to use another method.

### 3.4.4 The Non-Crossing Approximations

There exist a lot of variations of so-called "non-crossing approximations" (NCA) and the nomenclature of them is not standardized so it involves some difficulties to review *the* non-crossing approximation. In contrast to such ambiguities of the further development, its origin is clear. The perturbational setup was invented by Keiter and Kimball [106] in 1971. They investigated the SIAM in the $U = \infty$-limit meaning that double occupancy at the impurity site does not occur. The small parameter in their perturbation theory is the hybridization $V$. This implies that the unperturbed part of the Hamiltonian comprises locally interacting electrons which in turn leads to the impossibility of using common tools like Wick's-theorem or Feynman diagrams. Instead, the so-called time-ordered Goldstone diagrams have to be used for a Brillouin-Wigner perturbation theory. This formulation made it possible to handle infrared divergencies via investigating infinite orders of the perturbation series which are very common in such systems (and in the Kondo system as well). Intensive studies of impurity systems utilizing this new perturbation theory done by Grewe [70, 71] in 1983, Kuramoto [114] in 1983 and Kojima et al. [108] in 1984 showed that only those diagrams need to be taken into account that have no crossing band-electron lines; hence the name non-crossing approximation.

The impossibility of applying Feynman diagrams in NCA was sometimes seen as a drawback of this approximation. However, the interacting part in the unperturbed part of the Hamiltonian prevented applying this common toolbox. One way to decouple the interacting electrons is to introduce bosonic excitations that bear the complex interaction between the electrons. This is the so-called slave boson approach (SBA) and this approach made it possible to apply Feynman diagrams to the problem. It was shown by Coleman [37] in 1983/84 that the SBA and NCA are equivalent. However, in the SBA there is another way of sorting the diagrams. The diagrams are sorted by orders of $1/\nu$ with $\nu$ being the spin degeneracy.

In the following years (until today), NCA was improved by taking into account several kinds of vertex corrections. Maybe the simplest extension to NCA is to allow double occupancy at the impurity site. This *simplest* extension of NCA, making it possible to apply it to finite $U$-ranges, is therefore called SNCA. Beyond this simple extension, there exists a whole bunch of generalizations of SNCA all having different names which are not consistently used in literature. But all of them can still be characterized as vertex corrections, i.e. more complex integral-equations are used to treat higher orders of perturbation in $V$ (hybridization) or $\nu$ (spin degeneracy). For example, Anders in his PhD-thesis [4] (see also the following articles [5]) introduced the post-NCA (PNCA) which takes into account all contributions up to the order of $1/\nu^2$ which also comprises crossing diagrams. Other extensions like the "enhanced NCA" take into account all contributions up to order $V^2$ and the so-called "full NCA" even up to order $V^4$ which has already been investigated by Pruschke and Grewe [158] in 1989. The last extension which comprises all diagrams with one crossing line was done by Grewe et al. [72] in 2008 in which they review all other extensions to NCA. An earlier review that also comprises the applications was given by Bickers [18] in 1987.

After having mentioned NCA and several extensions, we should briefly comment on the validity of those methods. The biggest advantage of NCA is that one directly calculates the propagators for real-valued frequencies and that no discretization of the bath occurs (i.e. NCA directly deals with the thermodynamic limit). Since more processes are taken into account, it yields better results than IPT. Apart from the mentioned early works of Grewe [70, 71], Kuramoto [114] and Kojima et al. [108], NCA was applied in a DMFT framework by Jarrell and Pruschke [95, 96] and Pruschke, Cox and Jarrell [159, 160] in 1993. In 2000/2001, NCA was successfully applied to a multi-band Hubbard model to describe cuprate planes; see the PhD-thesis of Zölfl [233] and the corresponding article [232]. In contrast to IPT, there exists for NCA a certain temperature $T_{\text{crit}}$ and for $T < T_{\text{crit}}$ NCA does not yield valid results. In particular, the height of the Kondo peak is not obtained correctly (but the correct low-energy Kondo-scale is obtained). NCA in general cannot reach the correct $T = 0$ Fermi-liquid behavior. Since for this thesis we are interested in the kinks (that are located in the vicinity of the Kondo peak) at $T = 0$, we have to use other techniques.

### 3.4.5 Numerical Renormalization Group Theory

The numerical renormalization group theory (NRG) approach was introduced in 1975 by Wilson [226] who solved the Kondo problem with it (see Sec. 3.3.1 on page 22). NRG starts with a logarithmic discretization of the hybridization function $\Delta(\omega)$ (see Eq. (3.24) on page 25). This discretized system is then mapped onto a semi-infinite chain which is iteratively solved. The latter term "iteratively" means that the chain is built up to a certain length and solved exactly. Then, a further site is added, the whole system is solved again and the Hamiltonian is truncated to the size before the site was added. This procedure is iterated until the desired length of the chain is reached which corresponds to a certain energy or temperature scale. The used truncation scheme of NRG is given by an energy criterion. The states with the lowest lying energy eigenvalues are kept for truncation. The flow of energy levels reveals certain fixed points whose stability is analyzed. Such an analysis for the symmetric and asymmetric SIAM was done by Krishna-murthy et al. in 1980 [110, 111]. The NRG works for all temperatures $T$ and frequencies $\omega$, but due to the logarithmic discretization a good energy resolution is only obtained for low frequencies. NRG has also been applied in a DMFT framework for $T = 0$ by Sakai and Kuramoto in 1994 [170] and Bulla [26] in 1999. However, both works showed that the energy resolution decreases for larger frequencies. In 2001, NRG was applied for $T > 0$ by Bulla et al. [27]. It is also possible to apply NRG to the multi-band case. It was applied to the two-band Hubbard model at $T = 0$ by Pruschke and Bulla in 2005 [162]. In the same year, Inaba et al. [89] published results for $T > 0$. Calculations with more than two bands are up to now not published since the numerical effort grows considerably with adding more bands. NRG is also applicable to non-equilibrium dynamics of quantum impurity systems in real-time which was shown by Anders and Schiller [6, 7] in 2005/2006. For a comprehensive review on NRG, covering its origin and the application in DMFT, see the review of Bulla et al. [28].

As a conclusion we state that NRG is a very flexible method for solving quantum impurity systems with a non-interacting bath. It is applicable for all temperatures, energies and even for non-equilibrium case. But due to the logarithmic discretization of the bath the energy resolution decreases for higher energies. This drawback can, to some extend, be improved by the so-called "z-averaging" introduced by Yoshida et al. [230] and Oliveira and Oliveira [150] and by using a longer chain which involves more numerical effort. A recent study on how z-averaging can yield a better energy resolution was done by Žitko and Pruschke [231] in 2009.

### 3.4.6 Dynamic Density-Matrix Renormalization Group Theory

Due to the great success in applying NRG to the Kondo problem, NRG was also applied to interacting electron systems like the one-dimensional Hubbard model where it gives rather poor results. White and Noack [218] showed that this is due to the truncation scheme. We address this problem in detail in Sec. 4.1.1 on page 40. To overcome this problem, a new truncation scheme is needed which was introduced by White in 1992/1993 [219, 220]. In contrast to NRG where the states with the lowest energy eigenvalues are kept, the new scheme keeps the states with the largest weight in the density-matrix; hence the name "density-matrix renormalization group" (DMRG). We explain the truncation in detail in Sec. 4.1.2 on page 41. Note that in dynamic DMRG (D-DMRG) no logarithmic but an equidistant discretization of the bath is done so that the energy resolution is the same for every energy range. In the beginning, DMRG was only used to obtain static quantities like the ground state energy. But since DMRG can also calculate excited states, one tried to obtain single particle excitations via a continued fraction approach. We explain in Sec. 4.1.4 on page 46 why this approach yields poor results and how it can be improved by the so-called correction-vector method introduced by Ramasesha [167], Kühner [112] and Kühner and White [113]. A variational formulation of the correction vector scheme was given by Jeckelmann [97] in 2002. With this improvement high-resolution Green functions at $T = 0$ (see Karski et al. [104, 103, 105]) and susceptibilities (see Raas and Uhrig [164]) of the Hubbard model in DMFT can be calculated.

DMRG is a powerful method not only in the framework of DMFT. It can treat fermions (and with some further difficulties bosons) in one dimension for $T \geq 0$. It is a non-perturbative approach meaning that in a DMFT framework it can handle the Mott-transition. In contrast to QMC (where the Green function is obtained at imaginary frequencies) it yields the Green function at complex frequencies implying that the whole frequency range can be calculated with good resolution. This is illustrated in Fig. 3.5. In addition, D-DMRG yields the Green functions at $T = 0$. But those advantages are gained for the sake of high computational effort. Since we are interested in well resoluted Green functions and susceptibilities at $T = 0$ for low and high energies, we use D-DMRG. For further details on DMRG, see the next chapter and in particular Sec. 4.1 starting on page 40, the review of Schollwöck [179] or (for a review of DMFT(D-DMRG)) the review of Hallberg [80]. Note that in the latter review, although it aims to review D-DMRG in a DMFT framework, only the first attempts to calculate the single-particle excitations, done by García et al. [62] from 2004, are present. The results of Karski et al. [104] with a much better resolution (allowing also better physical interpretation), published one year before this review, are missing.

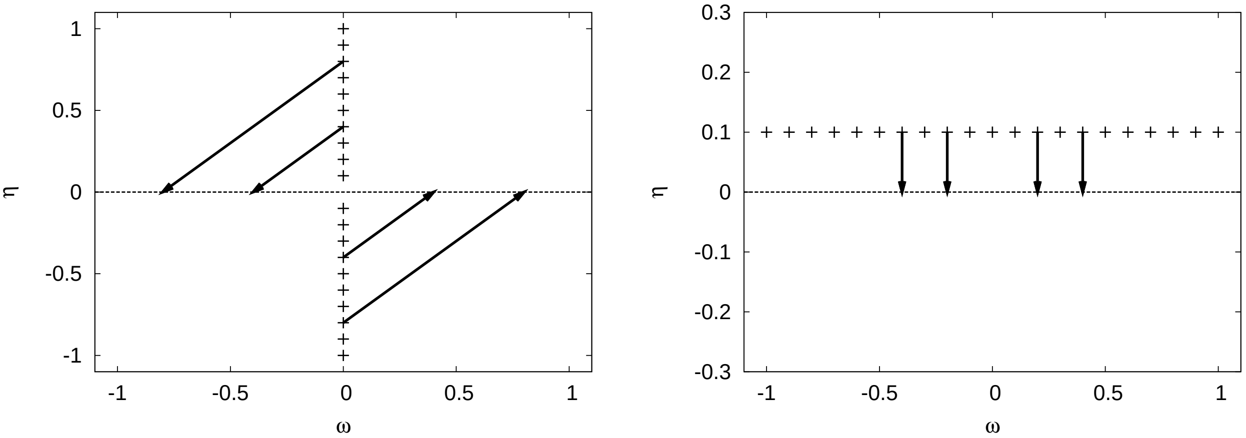

Figure 3.5: Complex plane of the frequencies $z = \omega + \mathrm{i}\eta$ with $\omega, \eta \in \mathbb{R}$ of the Green function $G(z)$. QMC (left) calculates $G$ for pure imaginary frequencies ($\omega = 0$), hence the extraction of $G$ for real frequencies ($\eta = 0$) is more difficult than for D-DMRG (right). D-DMRG calculates $G$ for complex frequencies $z = \omega + \mathrm{i}\eta$ which simplifies the extraction for $G$ for real frequencies. This illustrates why QMC has less accuracy for larger frequencies whereas D-DMRG has good accuracy for low *and* high frequencies.

# 4 Density-Matrix Renormalization Group in a DMFT Framework and its Implementation

## Contents

**4.1 Main Idea and Details of the DMRG . . . . . . . . . . . . . . . . . . . . . 40**
- 4.1.1 Density-Matrices and the Problems of Real-Space Block Renormalization – General Remarks . . . . . . . . . . . . . . . . . . . . . . . . . . . . . . . . 40
- 4.1.2 The DMRG Truncation . . . . . . . . . . . . . . . . . . . . . . . . . . . . . 41
- 4.1.3 Finite-System DMRG Algorithm . . . . . . . . . . . . . . . . . . . . . . . . 44
- 4.1.4 Local Dynamics and Dynamic DMRG . . . . . . . . . . . . . . . . . . . . . 46
- 4.1.5 Inhibition of Sticking to Local Minima – Adding Absent Fluctuations to the Density-Matrix . . . . . . . . . . . . . . . . . . . . . . . . . . . . . . . . 48
- 4.1.6 Aspects of DMRG Theory . . . . . . . . . . . . . . . . . . . . . . . . . . . 49
  - 4.1.6.1 Variational Rationale of the Finite-system DMRG . . . . . . . . . . . 49
  - 4.1.6.2 Why DMRG Works Most Efficiently in 1D . . . . . . . . . . . . . . . 50

**4.2 Implementation and Validation of the DMRG . . . . . . . . . . . . . . . . 52**
- 4.2.1 Details of the Parallelization . . . . . . . . . . . . . . . . . . . . . . . . . 52
- 4.2.2 Assessing the Choice of Parameters . . . . . . . . . . . . . . . . . . . . . . 53
  - 4.2.2.1 The Static Case . . . . . . . . . . . . . . . . . . . . . . . . . . . . 54
  - 4.2.2.2 The Dynamic Case . . . . . . . . . . . . . . . . . . . . . . . . . . . 60
- 4.2.3 Further Checks for the Asymmetric SIAM . . . . . . . . . . . . . . . . . . . 65

**4.3 Deconvoluting D-DMRG Raw Data . . . . . . . . . . . . . . . . . . . . . . 68**
- 4.3.1 Why Convoluted Data Appears . . . . . . . . . . . . . . . . . . . . . . . . . 68
- 4.3.2 The Least Bias Ansatz . . . . . . . . . . . . . . . . . . . . . . . . . . . . . 69
- 4.3.3 Checks for Deconvoluting Asymmetric Raw Data . . . . . . . . . . . . . . . . 70
- 4.3.4 Deconvoluting Self-Energies . . . . . . . . . . . . . . . . . . . . . . . . . . 71

**4.4 Closing the DMFT Cycle: Extraction of the Continued Fraction Coefficients . . . . . . . . . . . . . . . . . . . . . . . . . . . . . . . . . . . . . . 73**

In this chapter, the DMFT cycle is described. A complete DMFT cycle consists (see Fig. 3.1 on page 20) of the impurity solver, the application of the self-consistency conditions and, if those conditions are not met, the beginning of the next cycle. This procedure is reflected by the organization of this chapter which is as follows. In section 4.1, the impurity solver density-matrix renormalization is introduced and described. Afterwards in section 4.2, the details of the implementation are given, the choice of the internal parameters of the DMRG is motivated and the accuracy of the impurity solver is analyzed. The used D-DMRG produces raw-data so a deconvolution of the raw-data is necessary. Details of the deconvolution are therefore given in section 4.3. The self-consistency conditions can only be applied to the deconvoluted data. If they are not met, a new DMFT cycle begins, making it necessary to extract the coupling constants and local fields for the D-DMRG. This extraction scheme and an analysis of its accuracy is described in section 4.4.

## 4.1 Main Idea and Details of the DMRG

Historically, DMRG evolved from the numerical renormalization group (NRG) (see Sec. 3.4.5 on page 37 for details) which Wilson [226] developed for the Kondo problem. After this success, it was hoped that this real-space blocking scheme can also be applied to other one-dimensional quantum systems describing strongly correlated electrons like the 1D Hubbard or Heisenberg model. This was not the case. In Sec. 4.1.1, we give White's explanation for this finding which also led him to another truncation scheme that performs better in such systems. This new truncation scheme, the density-matrix renormalization, is explained in Sec. 4.1.2 on page 41. The specific DMRG algorithm used in this thesis, i.e., the finite-system algorithm and its main ingredient "sweeping" is explained in Sec. 4.1.3 on page 44. The details on how to calculate dynamic quantities via DMRG are given in Sec. 4.1.4 on page 46. Some DMRG calculations are flawed because the calculation sticks into a local energy minimum during the sweeps. Apart from mere numerical reasons for this sticking, there are physical reasons for it that are presented in Sec. 4.1.5 on page 48. Also a solution to this problem is given there. In the last subsection of this section, we present some aspects of DMRG theory (see Sec. 4.1.6 on page 49). We give a variational argument why the finite-system DMRG works (see Sec. 4.1.6.1 on page 49) and some general arguments why DMRG works most efficiently in one-dimensional systems (see Sec. 4.1.6.2 on page 50).

There exists plenty of literature introducing and reviewing DMRG. For a good introduction, the reader is referred to the proceedings on a workshop on DMRG in Dresden in 1998 [154]. For a general review on DMRG, see the article by Schollwöck [179]. For a review focussing on DMRG in a DMFT framework see the article by Hallberg [80]. The particular articles introducing the techniques presented in this section can be found in the respective subsections.

### 4.1.1 Density-Matrices and the Problems of Real-Space Block Renormalization – General Remarks

For pedagogical reasons, we start with some general remarks on density-matrices which we adopt from Ref. [54, p.39ff.] in order to make the problems of the Wilson real-space renormalization group (RG) [226] in application to quantum lattice systems (e.g. the 1D Hubbard chain) clearer. Let us consider a quantum mechanical system in an environment. If we denote the complete basis set of vectors for the system by $|s_i\rangle$ and the corresponding vectors for the environment by $|e_j\rangle$, then the most general wave function of this setup has the form

$$|\psi\rangle = \sum_{i,j} \psi_{ij} \, |s_i\rangle \, |e_j\rangle \, . \tag{4.1}$$

Let us now consider an operator $\mathscr{A}$ that acts only on the system (and not on the environment). If such an operator is applied to product states of system and environment, it is crucial to recognize that we have to take care of the inequality

$$\sum_{i,i',j} A_{ii'} \, |s_i\rangle \, |e_j\rangle \, \langle e_j| \, \langle s_{i'}| \neq \sum_{i,i'} A_{ii'} \, |s_i\rangle \, \langle s_{i'}| \tag{4.2}$$

where $A_{ii'}$ are the matrix elements of the operator $\mathscr{A}$. We now want to calculate the expectation value of such a system operator $\mathscr{A}$. By evaluating $\langle \mathscr{A} \rangle$, we find

$$\begin{aligned}\langle \mathscr{A} \rangle := \langle \psi | \mathscr{A} | \psi \rangle &= \sum_{i,j,i',j'} \psi^*_{ij} \psi_{i'j'} \left\langle e_j \left| \langle s_i | \mathscr{A} | s_{i'} \rangle \right| e_{j'} \right\rangle = \sum_{i,i'} \underbrace{\sum_j \psi^*_{ij} \psi_{i'j}}_{:=\rho_{ii'}} \langle s_i | \mathscr{A} | s_{i'} \rangle \\ &= \sum_{i,i'} A_{ii'} \rho_{ii'} = \mathrm{Tr}_S \; \widehat{\rho} \mathscr{A}\end{aligned} \tag{4.3}$$

where we defined the *density-matrix* $\rho_{ii'}$, the corresponding density operator $\widehat{\rho}$ (in particular, we introduced the density-matrix/operator of the whole system where the environment was traced out, i.e. $\widehat{\rho} = \mathrm{Tr}_E \, |\psi\rangle \, \langle\psi|$) and '$\mathrm{Tr}_S$' denotes the trace over the system states. From this consideration, we see that density-matrices $\rho_{ii'}$ naturally arise if quantum mechanical systems *with a connection to an environment* are treated. In view of this fact, the result of White and Noack [218] becomes rather obvious why the former real-space blocking RGs fail in such situations. Those RGs divide the system in two blocks (both represented by $m$ states), diagonalize the $2m$ dimensional superblock Hamiltonian and keep only $m$ states with the largest eigenvalues in an $m \times 2m$ dimensional transformation matrix $O$ which is then used to truncate the Hamiltonian $\mathscr{H}$ via $O\mathscr{H}O^\dagger$ (all other operators of interest are treated the same way). In Ref. [218], White and Noack showed that the ground state of a toy model obtained by such an RG is the ground state of two isolated blocks, i.e. the *connection* between the blocks was neglected by this real-space RG. Thus, a successful RG for systems connected with an environment needs to incorporate this connection adequately. Therefore, such an RG will make use of density-matrices [218, 223] and it is called *density-matrix renormalization group* (DMRG).

Before we proceed to elaborate the DMRG method further, some notes shall be added concerning the term *renormalization group* which some DMRG practitioners regard as a misnomer [179, p.262]. The DMRG and the NRG both systematically neglect unimportant degrees of freedom while constructing an effective Hamiltonian. This strategy to construct an effective Hamiltonian is part (but not the whole) of RG and in this sense DMRG is an RG. However, the core concept of the RG presented in the seminal paper by Wilson [226] comprise also the *cutoff* of energy-, time- or length-scales which become irrelevant in the vicinity of critical phenomena. The flow of renormalization transformations then exhibit fixed points whose stability is analyzed and which reveal the critical exponents of the transition. This is out of the scope of DMRG. Therefore, modern attempts to unify DMRG and NRG in one theoretical framework such as e.g. matrix product states (see e.g. Ref. [210]) capture only one aspect and not all of the concepts of the renormalization group.

### 4.1.2 The DMRG Truncation

After the general considerations of the last subsection, we describe the DMRG truncation in this subsection. First, we repeat the general blocking scheme which prevents the exponential growth of the Hilbert space while building up the system. Then, we show that the DMRG truncation is the result of three different optimization requirements. At last, we mention the adaption of the truncation scheme if several states are targeted.

Consider the Hamiltonian of a chain with $N_{\mathrm{tot}}$ sites where every site has $f$ degrees of freedom. Thus, the Hilbert space of the total system exhibits $f^{N_{\mathrm{tot}}}$ dimensions, i.e. the application of any operators implies dealing with $f^{N_{\mathrm{tot}}} \times f^{N_{\mathrm{tot}}}$ dimensional matrices. We are not able to deal with such exponentially growing Hilbert spaces. But this is not necessary for dealing with ground state properties and zero-temperature response functions because only a small partition of the Hilbert space is needed for these properties. Hence, we have to find a scheme that turns the exponentially growing effort into a linear one and which focusses on the most important part of the Hilbert space. One procedure to achieve this is the so-called blocking scheme. For NRG and DMRG, it consists of the following steps [179, p.263]:

1. Build the Hamiltonians $\mathscr{H}_S$ and $\mathscr{H}_E$ of the two blocks $S$ (system) and $E$ (environment) with $\ell_{\min} \leq \log_f m$ sites (i.e. both blocks can be represented with at most $m$ states).
2. Add one site $\bullet$ to each block and build the so-called superblock Hamiltonian $\mathscr{H}_{S\bullet-\bullet E}$ of the new system $S\bullet - \bullet E$. This new system is then represented by a $m^2 f^2 \times m^2 f^2$ dimensional matrix.
3. Find a basis transformation $O$ such that $\mathscr{H}_{\text{new}} = O^\dagger \mathscr{H}_{S\bullet-\bullet E} O$ is again represented by a $m^2 \times m^2$ dimensional matrix. Do so also for all operators of interest. Proceed until the whole system is built up.

The above scheme ensures that our effort grows only linearly (and not exponentially) with the system size, but it leaves the way how to build $O$ unspecified. This is the point where NRG and DMRG are different. Whereas NRG diagonalizes the Hamiltonian $\mathscr{H}_{S\bullet-\bullet E}$ and builds $O$ from the $m$ states with the lowest (energy) eigenvalues, the DMRG computes the density-matrix from the ground state (or a mixture of the ground state and other states) and keep the $m$ states of the $m$ largest eigenvalues of the density-matrix in order to project the respective $fm$-dimensional Hilbert space of the system $S$ and the environment $E$ down to $m$ states again. This obviously implies that the DMRG is appropriate only if the eigenvalues $w_\alpha$ decay fast so that the discarded weight $1 - \sum_\alpha^m w_\alpha$ of the density-matrix is sufficiently small. The latter mentioned DMRG truncation can be deduced via three different optimization requirements:

1. Find the best approximation of the wave function of the ground state [219, 220].
2. Find the best approximation for expectation values [223].
3. Find the wave function which contains the most entanglement in it [59, 60, 61, 151, 117].

Although all three requirements are *different*, they all lead to the *same* truncation scheme and truncation error.

If we require that the approximate superblock wave function $|\tilde{\psi}\rangle$ should be expressed by the $N_E$ states $|e_j\rangle$ of the environment and $m$ orthonormal states $|\alpha\rangle = \sum_i u_{\alpha i} |s_i\rangle$ of the system, i.e.

$$|\tilde{\psi}\rangle = \sum_{\alpha=1}^{m} \sum_{j=1}^{N_E} a_{\alpha j} |\alpha\rangle |s_j\rangle , \tag{4.4}$$

then the first requirement translates in minimizing the quadratic norm $\Big|\Big| |\psi\rangle - |\tilde{\psi}\rangle \Big|\Big|$. We follow the approach given in Ref. [179, p.264] and assume for simplicity real coefficients. Then, minimizing the above quadratic norm lead to the minimization of

$$1 - 2 \sum_{\alpha i j} \psi_{ij} a_{\alpha j} u_{\alpha i} + \sum_{\alpha j} a_{\alpha j}^2 \tag{4.5}$$

with respect to $a_{\alpha j}$ and $u_{\alpha i}$. For the stationary (with respect to $a_{\alpha j}$) solution, we must fulfill $a_{\alpha j} = \sum_i \psi_{ij} u_{\alpha i}$. Inserting this in (4.5), the requirement of (4.5) to be stationary translates in the minimization of

$$1 - \sum_{\alpha i i'} u_{\alpha i} \rho_{ii'} u_{\alpha i'} \tag{4.6}$$

where we again find the density-matrix $\rho_{ii'}$ of the whole system with the environment traced out. Thus it appears that $|\alpha\rangle$ have to be the eigenstates $|u_\alpha\rangle$ of the density-matrix $\rho_{ii'}$. The global minimum is reached by using the $m$ largest eigenvalues $w_\alpha$ of $\rho_{ii'}$ and we find that the minimal distance between the exact and approximative wave function squared is

$$\left|\left| |\psi\rangle - |\tilde{\psi}\rangle \right|\right|^2 = 1 - \sum_{\alpha=1}^{m} w_\alpha =: \epsilon_\rho \tag{4.7}$$

which is the truncated weight $\epsilon_\rho$ of the density-matrix.

The above derivation constitutes the DMRG as a variational principle for the wave function. It is somewhat technical. A more intuitive derivation is directly given via Eq. (4.3) where we found that the expectation value of some operator $\mathscr{A}$ acting only on the system is given by

$$\langle \mathscr{A} \rangle = \mathrm{Tr}_S \widehat{\rho} \mathscr{A} = \sum_{\alpha=1}^{M_S} w_\alpha \left\langle u_\alpha \left| \mathscr{A} \right| u_\alpha \right\rangle . \tag{4.8}$$

In the last step of Eq. (4.8), we used the eigenstates $|u_\alpha\rangle$ and the eigenvalues $w_\alpha$ of the density operator $\widehat{\rho}$. Obviously, this expectation value is approximated best with $m \leq M_S$ eigenstates of the density-matrix if we use the $m$ eigenstates with the largest eigenvalues $w_\alpha$. Consider $\mathscr{A}$ being a bounded operator, i.e. $||\mathscr{A}|| = \max_\phi \left| \left\langle \phi \left| \mathscr{A} \right| \phi \right\rangle / \left\langle \phi \right| \phi \rangle \right| \equiv c_{\mathscr{A}}$. Then the difference between the exact and the approximated expectation value is bounded by

$$\left| \langle \mathscr{A} \rangle_{\text{approx}} - \langle \mathscr{A} \rangle \right| \leq c_{\mathscr{A}} \left( 1 - \sum_{\alpha=1}^{m} w_\alpha \right) . \tag{4.9}$$

Thus, the relative error of the expectation value is bounded by the truncation error $\epsilon_\rho$ defined in (4.7). Both requirements, optimization of wave function and optimization of the expectation value, lead to the same truncation error. The third requirement shows that the DMRG truncation scheme in addition maximizes the von Neumann entropy, i.e. it is impossible to keep more entanglement with any other truncation scheme than with the DMRG. We come back to this property of the DMRG in section 4.1.6.2 on page 50.

So far, we assumed that the superblock is in a pure state and we showed that the DMRG uses an optimized truncation scheme to represent this pure state (here: the ground state). However, if we e.g. think of finite temperatures, the superblock is expected to be in a mixed state. If, in addition, we want to calculate another state than the ground state, we do not expect that the density-matrix, built up from the ground state only, is suitable for the calculation of those other states. Therefore, we need the truncation scheme for a superblock in a mixed state. This truncation scheme for multiple target states was given by Noack and White in Ref. [148].

They considered the following setup: The state of the superblock is given by the mixture of $K$ states $\left|\psi^k\right\rangle$ and their weights in the mixture are given by $W_k$ with $\sum_k^K W_k = 1$. The requirement for optimizing the wave function translates in minimizing

$$\sum_{k=1}^{K} W_k \sum_{ij} \left( \psi_{ij}^k - \sum_{\alpha} a_\alpha^k u_{i\alpha} v_{j\alpha}^k \right)^2 \tag{4.10}$$

where the superscript $k$ denotes an index and not the power (if a subscript were used, matrices and vectors may be mixed up with tensors and matrices). Note that we look for the unique system state $u_\alpha$, whereas the environment may choose a different state $v_\alpha^k$ for every $\psi_{ij}^k$. By minimizing over $a_\alpha^k, u_\alpha, v_\alpha^k$, we find

$$\begin{aligned} \widehat{\rho}\,|u_\alpha\rangle &= w_\alpha\,|u_\alpha\rangle && (4.11a)\\ \text{with}\ \ \rho_{ii'} &= \sum_k W_k \sum_k \psi_{ij}^k \psi_{i'j}^k && (4.11b)\\ \text{and}\ \ w_\alpha &= \sum_k W_k \left(a_\alpha^k\right)^2 . && (4.11c) \end{aligned}$$

Thus it appears that the same truncation scheme must be used for pure and for mixed states of the system. We just have to put the several desired states into the density-matrix and keep the $m$ eigenstates $|u_\alpha\rangle$ with the largest weight $w_\alpha$. Note that the particular values of the weights $W_k$ are not specified a priori. The particular choice of $W_k$ is a matter of experience; see Sec. 4.2.2 on page 53.

### 4.1.3 Finite-System DMRG Algorithm

The finite-system DMRG algorithm was described in detail several times (see e.g. Ref. [163, p.51] or Ref. [179, p.266]) so it is sufficient here to give a brief summary. Afterwards, we describe a method to speedup this algorithm and clarify why this algorithm works.

We assume that we have built up the system with $N_{\text{tot}}$ sites and kept $m$ states in the reduced density-matrix. If the system was grown from one side only, then this kind of DMRG is called "infinite-system DMRG". If the system was build up in the way Fig. 4.2 on page 53 illustrates, i.e. it consists of two blocks of equal size with one or two active sites in between connecting both blocks, then we have the starting configuration for the finite-system DMRG. The key ingredient of the finite-system algorithm is performing so-called "sweeps". One sweep consists of the iterative movement of the inner exact site(s) from the middle to one edge, then to the other edge and to the middle again. This is illustrated in Fig. 4.1. The DMRG truncation is carried out only for the respective growing block. Note that there are two different versions of this algorithm, depending on the number of exact sites between the blocks. They are called *one-site* or *two-site* DMRG respectively.

In every step, the density-matrix of the superblock has to be diagonalized for which e.g. a Lanczos or Davidson algorithm can be used. The initial guess for such an algorithm is not specified and experience shows that such an algorithm may need 100-200 steps to diagonalize the density-matrix for every step during one sweep. However, the respective wave function is not expected to differ very much from one step to another. This lead to the idea [221] that, once the wave function is found, one may be able to use this wave function as an initial guess for diagonalizing the density-matrix in the next step. Although the wave functions contain the same physics, both wave functions have a different basis. We therefore need a basis transformation which was first described by White [221] and which we

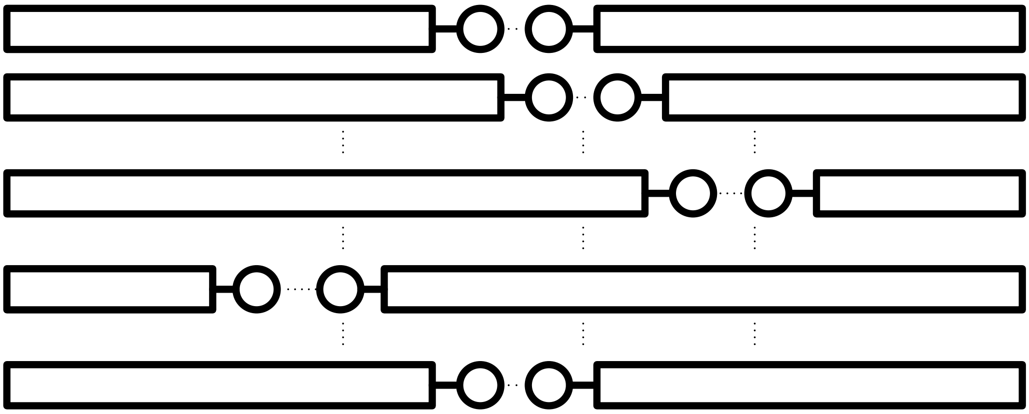

Figure 4.1: Illustration of the sweeping procedure of the two-site finite-system DMRG algorithm. In the one-site DMRG, there is only one active site present between both blocks. One sweep consists of the iterative movement of the active sites back and forth. We start with the active sites located in the middle (first row) and grow one block while the other one is shortened (second row). This is iterated until the one edge is reached (third row). Then the direction is reversed and the former growing block is reduced while the other block grows. This is iterated until the other edge is reached (fourth row). Then the directory is reversed again until we reach the symmetric configuration again (fifth row). The DMRG truncation is carried out only for the respective growing block.

briefly summarize here for the two-site DMRG. In the following, we explain the finite-system DMRG algorithm in combination with the wave function transformation.

Let $|\alpha_l\rangle$ be the states of the left block where $l$ denotes the rightmost site and let $|s_l\rangle$ be the states of the new site added to this block on the right[1]. The states of the new block $|\alpha_{l+1}\rangle$ are a linear combination of tensor products of the old block states and of states of the new site,

$$|\alpha_{l+1}\rangle = \sum_{s_l,\alpha_l} \langle \alpha_l s_l |\alpha_{l+1}\rangle \, |\alpha_l\rangle \otimes |s_l\rangle = \sum_{s_{l+1},\alpha_l} L^{l+1}\left[s_{l+1}\right]_{\alpha_{l+1}\alpha_l} |\alpha_l\rangle \otimes |s_l\rangle \, , \tag{4.12}$$

where we defined the left transformation matrix $L$ that consists of the matrix eigenvectors $u_{\alpha_{l+1}}$ of the reduced density-matrix, i.e. $L^{l+1}\left[s_{l+1}\right]_{\alpha_{l+1},\alpha_l} = u^{\alpha_{l+1}}_{s_{l+1}\alpha_l}$. The corresponding state of the right block is obtained similarly by

$$|\beta_{l+3}\rangle = \sum_{s_{l+3},\beta_{l+4}} R^{l+3}\left[s_{l+3}\right]_{\beta_{l+3}\beta_{l+4}} |s_{l+3}\rangle \otimes |\beta_{l+4}\rangle \, . \tag{4.13}$$

The superblock basis is the direct product of the used basis states and has the form

$$|\alpha_l s_{l+1} s_{l+2} \beta_{l+3}\rangle = |\alpha_l\rangle \otimes |s_{l+1}\rangle \otimes |s_{l+2}\rangle \otimes |\beta_{l+3}\rangle \, . \tag{4.14}$$

A superblock wave function $|\psi\rangle$ is a linear combination of those states

---

[1] We assume here that the sweep goes from left to right. For a reversed sweeping direction, this procedure works as well but with different matrices $L$ and $R$.

$$|\psi\rangle = \sum_{\alpha_l, s_{l+1}, s_{l+2}, \beta_{l+3}} \psi\left(\alpha_l, s_{l+1}, s_{l+2}, \beta_{l+3}\right) |\, \alpha_l s_{l+1} s_{l+2} \beta_{l+3}\rangle \,. \tag{4.15}$$

If no truncation occurred, this transformation would be exact. This is not the case since DMRG produces optimized (but in general not exact) wave functions (see first requirement in Sec. 4.1.2). For this reason, we can expect that the approximation

$$\sum_{\alpha_{l+1}} |\, \alpha_{l+1}\rangle \langle \alpha_{l+1}| \approx 1 \tag{4.16}$$

is still applicable. The quality of this approximation is not a major concern since this procedure is only meant to give a good initial guess and not the final result of the Lanczos algorithm. With this approximation, we obtain

$$\psi\left(\alpha_{l+1} s_{l+2} s_{l+3} \beta_{l+4}\right) \approx \sum_{\alpha_l s_{l+1} \beta_{l+3}} L^{l+1}\left[s_{l+1}\right]_{\alpha_{l+1}\alpha_l} \times \psi\left(\alpha_l s_{l+1} s_{l+2} \beta_{l+3}\right) \times R^{l+3}\left[s_{l+3}\right]_{\beta_{l+3}\beta_{l+4}} \tag{4.17}$$

as an approximation for the wave function in the next step. In addition to the DMRG without wave function transformation, we have to store the matrices $L$ and $R$ which costs additional memory. But we gain a lot of computation speedup: Experience shows that in the present program we only need $\approx 5$ Lanczos steps instead of $\approx 200$ by performing this wave function transformation. The respective transformation for one-site DMRG is analogous to the transformation described above.

### 4.1.4 Local Dynamics and Dynamic DMRG

The time-dependent fermionic retarded Green function for a time-independent Hamiltonian $\mathscr{H}$ at zero-temperature reads (see Ref. [149, p.118])

$$G^{\mathrm{ret}}\left(t - t'\right) := -\mathrm{i} \left\langle 0 \left| \left\{ \mathscr{A}(t), \mathscr{B}(t') \right\} \right| 0 \right\rangle \Theta\left(t - t'\right), \tag{4.18}$$

where $\{...\}$ denotes the anticommutator and $\mathscr{A}, \mathscr{B}$ are the operators which correspond to the response one wants to calculate. In the following, we restrict ourselves to single-particle response which implies that $\mathscr{B} = \mathscr{A}^\dagger$. Without loss of generality, we take $t' = 0$ and consider only $t > 0$. By Fourier transformation, we obtain

$$\begin{aligned} G^{\mathrm{ret}}\left(\omega + \mathrm{i}\eta\right) &= \mathrm{i} \int_0^\infty e^{\mathrm{i}(\omega+\mathrm{i}\eta)t} \left\langle 0 \left| \left\{ e^{\mathrm{i}\mathscr{H}t} \mathscr{A} e^{-\mathrm{i}\mathscr{H}t}, \mathscr{A}^\dagger \right\} \right| 0 \right\rangle \mathrm{d}t \\ &= \underbrace{\left\langle 0 \left| \mathscr{A} \frac{1}{\omega + \mathrm{i}\eta - (\mathscr{H} - E_0)} \mathscr{A}^\dagger \right| 0 \right\rangle}_{:=G^{>}(\omega+\mathrm{i}\eta)} + \underbrace{\left\langle 0 \left| \mathscr{A}^\dagger \frac{1}{\omega + \mathrm{i}\eta + (\mathscr{H} - E_0)} \mathscr{A} \right| 0 \right\rangle}_{:=G^{<}(\omega+\mathrm{i}\eta)}, \end{aligned} \tag{4.19}$$

where we defined the partial Green functions $G^{>}$ and $G^{<}$. Note that $\eta > 0$ is required to obtain a finite result of the Fourier transformation (4.19). The local operator $\mathscr{A}$ specifies what kind of Green function (4.19) is. If $\mathscr{A}$ is the creation operator, then (4.19) is the single particle Green function, if $\mathscr{A}$ is the Q-operator (see Sec. 3.3.4 on page 29) then (4.19) is the Q-function and so on. For the SIAM at particle-hole symmetry, $G^{>}(\omega + \mathrm{i}\eta) = G^{<}(-\omega + \mathrm{i}\eta)$ holds, hence only one of the partial Green functions has to be calculated. In general, both partial Green functions have to be calculated separately.

The first method to calculate such a Green function is known as the *continued-fraction method* which was first exploited by Gagliano and Balseiro [58] in 1987. They used the continued fraction representation of the partial Green function

$$G^{<}(z) = \cfrac{\langle 0 \,|\mathscr{A}^{\dagger}\mathscr{A}|\, 0\rangle}{z - a_0 - \cfrac{b_1^2}{z - a_1 - \cfrac{b_2^2}{z - \ldots}}} \tag{4.20}$$

(with $z = \omega + \mathrm{i}\eta$) and calculate the coefficients $a_i, b_i$ via Lanczos-method

$$\begin{aligned}
|f_0\rangle &= \mathscr{A}\,|0\rangle && (4.21a)\\
|f_{n+1}\rangle &= \mathscr{H}\,|f_n\rangle - a_n\,|f_n\rangle - b_n^2\,|f_{n-1}\rangle && (4.21b)\\
a_n &= \frac{\langle f_n \,|\mathscr{H}|\, f_n\rangle}{\langle f_n|\, f_n\rangle} && (4.21c)\\
b_n^2 &= \frac{\langle f_{n-1} \,|\mathscr{H}|\, f_n\rangle}{\langle f_{n-1}|\, f_{n-1}\rangle} = \frac{\langle f_n|\, f_n\rangle}{\langle f_{n-1}|\, f_{n-1}\rangle}. && (4.21d)
\end{aligned}$$

In principle, (4.21) can be calculated by DMRG and hence (4.20) can be calculated with DMRG (see Ref. [79]). To do so, one has to select many of the $|\, f_n\rangle$ as target states for the density-matrix. The more target states we choose, the less weight they have in the density-matrix. Therefore, as Raas has shown in Ref. [163, p.67-69], this method is not appropriate to resolve the spectrum adequately. Since it is not used in this thesis, we turn to an improved method for calculating Green functions with DMRG.

This is the so-called *correction vector method.* The main idea is to incorporate information about the spectral density at the correspondent frequency $\omega$ via a frequency dependent correction of the DMRG basis[2]. Such a correction was introduced by Ramasesha et al. [167] in 1997, Kühner [112] and Kühner and White [113] in 1999. The complex-valued correction vector $|\xi\rangle$ reads

$$\begin{aligned}
|\xi\rangle &= \frac{1}{\omega + \mathrm{i}\eta \pm \Delta\mathscr{H}} \underbrace{\mathscr{A}\,|0\rangle}_{:=|\mathscr{A}\rangle} = \underbrace{\frac{\omega \pm \Delta\mathscr{H}}{(\omega \pm \Delta\mathscr{H})^2 + \eta^2}\,|\mathscr{A}\rangle}_{:=\Re|\,\xi\rangle} + \mathrm{i}\underbrace{\frac{-\eta}{(\omega \pm \Delta\mathscr{H})^2 + \eta^2}\,|\mathscr{A}\rangle}_{:=\Im\,|\xi\rangle} \\
&= -\frac{\omega \pm \Delta\mathscr{H}}{\eta}\Im\,|\,\xi\rangle + \mathrm{i}\Im\,|\,\xi\rangle\,.
\end{aligned} \tag{4.22}$$

In (4.22), we used the abbreviation $\Delta\mathscr{H} := \mathscr{H} - E_0$. The positive sign in (4.22) is used for calculating $G^{<}$ and the negative sign is used for calculating $G^{>}$. During the calculation, linear equation solving

---

[2] Such an idea was proposed by Soos and Ramasesha [190] in 1989 before the advent of DMRG.

is needed only for the imaginary part $\Im\,|\xi\rangle$ of the correction vector. As Eq. (4.22) shows, the real part $\Re\,|\xi\rangle$ of the correction vector is obtained via multiplication of $\Im\,|\xi\rangle$ with $-1/\eta\,(\omega \pm \Delta\mathscr{H})$. The partial Green function $G^<(\omega + \mathrm{i}\eta)$ (or $G^>(\omega + \mathrm{i}\eta)$) is then obtained from

$$G^<(\omega + \mathrm{i}\eta) = \langle \mathscr{A}\,|\xi\rangle \tag{4.23}$$

(with the correct sign in (4.22) used). The above scheme yields the real and imaginary part of the Green function.

If we are interested only in the imaginary part, we may use a different correction vector scheme that was first proposed by Jeckelmann [97] in 2002. He reformulated the correction vector scheme in terms of a variational principle for the imaginary part $\Im\,|\xi\rangle$. The functional

$$W_{\mathscr{A},\eta}\,(\omega,\Psi) = \left\langle \Psi \left| (\omega \pm \Delta\mathscr{H})^2 + \eta^2 \right| \Psi \right\rangle + \eta\,\langle \mathscr{A}\,|\Psi\rangle + \eta\,\langle \Psi\,|\mathscr{A}\rangle \tag{4.24}$$

takes (see Ref. [97]) its minimum with respect to $|\Psi\rangle$ for $|\Psi_{\min}\rangle = \Im\,|\xi\rangle$. Hence, we find

$$\Im G^>(\omega + \mathrm{i}\eta) = \frac{1}{\eta} W_{\mathscr{A},\eta}\,(\omega, \Im\xi) \tag{4.25}$$

(with the correct sign in (4.24) used). Calculating the correction vector with this variational approach is equivalent with the scheme (4.22) if $\Im\,|\xi\rangle$ could be calculated exactly. Let us assume we have calculated an approximate solution $|\Psi\rangle = \Im\,|\xi\rangle + \epsilon\,|\Phi\rangle$ with $\langle\Phi\,|\Phi\rangle = 1$ and $\epsilon \ll 1$, i.e. the error of this approximation is of the order of $\epsilon$. Then the error of the solution in (4.22) is of the same order, whereas the error of the functional (4.24) is, due to general properties of the variation principle, of the order of $\epsilon^2$. In order to avoid the minimization of the functional (4.24), we calculate the imaginary part $\Im\,|\xi\rangle$ via (4.22) and calculate the imaginary part of the Green function by evaluating the functional (4.24) with the obtained solution, i.e. we use the obtained $\Im\,|\xi\rangle$ in Eq. (4.25).

With the schemes given above, we obtain Green functions at certain complex frequencies $\omega_j + \mathrm{i}\eta_j$. We are interested in the Green function at real and continuous frequencies $\omega$. To obtain $G(\omega)$, deconvolution is needed (see Sec. 4.3 on page 68). In order to obtain valid results for $G(\omega)$, we do not have to calculate a dense mesh of frequencies $\omega_j + \mathrm{i}\eta_j$. As Kühner at White [113] have shown $\omega_{j+1} - \omega_j \approx \eta_j$ is a good choice.

### 4.1.5 Inhibition of Sticking to Local Minima – Adding Absent Fluctuations to the Density-Matrix

For valid DMRG results, it is crucial to obtain the ground state during the calculation. This ground state is an approximation due to the DMRG truncation. The approximate ground state energy $E_{0,\mathrm{DMRG}}$ is larger or equal the exact ground state energy $E_0$. In many cases, increasing the number $m$ of kept states and/or more sweeps leads to $E_{0,\mathrm{DMRG}} \to E_0$. However, in some cases (see e.g. Ref. [222]) increasing $m$ or more sweeps does not improve $E_{0,\mathrm{DMRG}}$, i.e. the DMRG calculation does not find the best approximation of the exact ground state and get stuck to a local energy minimum. This problem can flaw the whole DMRG calculation. White addresses this problem in Ref. [224] and we mention here the most important points. White compares two-site with one-site DMRG. In the latter case, the calculation can have the problem that fluctuations which should be there are not because the environment block does not have the relevant states. In 1D systems with short range interactions, this problem can be solved by using two-site DMRG. But, as White points out, in systems with long range interactions or in wide ladder systems this may not help. The argument why this problem can occur and the answer how to solve this problem is the aim of this subsection.

White considers the power method for finding the ground state $\psi$, i.e. the iteration $\psi_{n+1} = (1-\epsilon\mathscr{H})\psi_n$. If $\psi_0$ is not orthogonal to the correct $\psi$ and for small enough $\epsilon$, this iteration converges to the correct ground state $\psi$. If the DMRG basis represents $\psi$ *and* $\mathscr{H}\psi$ exactly, this would lead to the exact ground state. But, and this is the crucial point, the DMRG basis lacks $\mathscr{H}\psi$ so we need to add the missing states to the basis. To this end, we need to add the absent fluctuations

$$\Delta\rho = \sum_{\alpha} a_\alpha \widehat{A}^\alpha \rho \widehat{A}^{\alpha\dagger}, \tag{4.26}$$

to the density-matrix. In Eq. (4.26), $a_\alpha$ is the weight of this correction, $\widehat{A}^\alpha$ are the operators in the system or environment that connect the system and the environment block and $\rho$ is the density-matrix obtained the usual way. For the SIAM under consideration, (4.26) takes the form

$$\Delta\rho = \widehat{S_z}\rho\widehat{S_z} + \widehat{S^+}\rho\widehat{S^-} + \widehat{S^-}\rho\widehat{S^+}. \tag{4.27}$$

White showed in Ref. [224] for a $S = 1$ Heisenberg chain that the accuracy of the two-site DMRG is reached if the one-site DMRG is improved by (4.26). This advancement proved to be very successful for the so-called ab initio DMRG in quantum chemistry (see Ref. [115] and references 9-12,17,18 and 30 therein), but in every case it has to be shown that the results improve with this density-matrix correction (see the comprehensive analysis in Ref. [115]). Analyzing the literature citing Ref. [224], one obtains that this was not always documented or done. For the SIAM used here, this is done in Sec. 4.2.2 on page 53. Such an analysis should not be omitted because although this correction may be useful [115] or negligible, it can also lead to a loss of accuracy. This is the result of our analysis in Sec. 4.2.2.

### 4.1.6 Aspects of DMRG Theory

There are many studies elucidating the theoretical basis of DMRG. A review is found in Ref. [179, p.273f.]. In this subsection, we want to mention two aspects of DMRG theory. In particular, we want to understand why the finite-system algorithm (see Sec. 4.1.3) works and why DMRG often fails for two- or more-dimensional systems.

#### 4.1.6.1 Variational Rationale of the Finite-system DMRG

It was shown that the DMRG truncation optimizes the wave function (and the expectation values) because this scheme is variational. Furthermore, it turns out that the finite-system algorithm described in Sec. 4.1.3 on page 44 leads to very accurate results (see e.g. Refs. [178, 179] and Ref. [163, p.55]). We want to clarify here why the finite-system algorithm works. A first step in answering this question is the empirical finding that the eigenvalues of the density-matrix decrease fast and that hence the discarded information about the system is small. This, however, does not clarify *why* moving the inner site(s) lead to improved results compared to the infinite DMRG algorithm without sweeps.

The quantum information theory (QIT) provides an elegant framework for answering the question why the finite-system DMRG works. A comprehensive introduction and overview about QIT is found in the textbook of Nielsen and Chuang [147]. A QIT analysis of the finite-system DMRG was done by Verstraete et al. [207] in 2004. They reformulate the DMRG in terms of matrix-product states and show that sweeping, i.e. moving the inner site(s) back and forth, constitutes a variational setup for the ground state energy as a function of the sweeping step number. To show this, we make use of the procedure introduced in Sec. 4.1.3. Here, we follow the formulation of Ref. [180]. In order to write down the states in terms of matrix-product states, we start with the expressions

$$\begin{aligned} |\psi\rangle &= \sum_{\sigma_1,\dots\sigma_L} A^1[\sigma_1]\dots A^\ell[\sigma_\ell] \times \Psi[\sigma_{l+1}] \times \tilde{A}^{\ell+2}[\sigma_{\ell+2}]\dots\tilde{A}^L[\sigma_L]\,|\sigma_1\dots\sigma_L\rangle && \text{(4.28a)} \\ |\psi\rangle &= \sum_{\sigma_1,\dots\sigma_L} A^1[\sigma_1]\dots A^\ell[\sigma_\ell] \times \Psi[\sigma_{l+1}\sigma_{\ell+2}] \times \tilde{A}^{\ell+3}[\sigma_{\ell+3}]\dots\tilde{A}^L[\sigma_L]\,|\sigma_1\dots\sigma_L\rangle\,. && \text{(4.28b)} \end{aligned}$$

Eq. (4.28a) is an ansatz for one-site DMRG and Eq. (4.28b) is an ansatz for two-site DMRG. All matrices without tilde correspond to the block on the left side of the active site(s) and all matrices with tilde correspond to the block on the right side of the active site(s). Verstraete et al. in Ref. [207] introduce auxiliary Hilbert spaces of dimension $M$: $a_\ell$ denotes the auxiliary Hilbert space to the left and $b_\ell$ denotes the auxiliary Hilbert space to the right of the site $\ell$. These auxiliary Hilbert spaces correspond to the matrix-product state above. Without loss of generality, we omit the tilde above the matrices $A$. In order to apply the variational Ritz method, we require that $\langle\psi\,|\mathscr{H}|\,\psi\rangle$ takes its minimum as a function of the matrices $A$. As noted in Ref. [180], this yields a very complex, non-linear expression that is "numerically close on useless". But there is a way to turn this requirement into a linear problem. To this end, we start with some (educated) guess for the matrices $A$ and consider $\langle\psi\,|\mathscr{H}|\,\psi\rangle$ as a function of $\Psi$. Then we shift the position of the active site(s) which changes the corresponding matrix $A$ where the active site(s) was/were before. For every shift of the active site(s), solving $\langle\psi\,|\mathscr{H}|\,\psi\rangle$ as a function of $\Psi$ is a linear problem. The question arises how to obtain this new matrix $A$ if we require to keep as much information as possible. It turns out that this requirement leads to the finite-system DMRG algorithm. Thus it appears that the sweeping in the finite-system algorithm is equivalent to a variational optimization of a matrix-product state. It is variational because of the Ritz principle stated above. By comparing both expressions (4.28a) and (4.28b), we see that $\Psi$ in the two-site ansatz has a different dimension then the $A$ matrices at all other sites. Thus, the two-site DMRG is not strictly variational within one class of states, whereas the one-site DMRG is strictly variational within one class of states. If not stated otherwise, we therefore use one-site DMRG for all calculations in this thesis.

#### 4.1.6.2 Why DMRG Works Most Efficiently in 1D

Now, we turn to the question why the quality of DMRG results depends on the dimensionality of the system under consideration. In view of the fact that DMRG incorporates the connection of a quantum system with its environment in an optimal way (see Sec. 4.1.1 on page 40 and Sec. 4.1.2 on page 41) and given the great success of applying DMRG in many 1D systems, it remains unclear why DMRG in general fails for two- or more-dimensional systems. One hint to the answer is given by the eigenvalue spectrum of the density-matrix. DMRG rests on a fast decaying eigenvalue spectrum and in two-dimensional systems (and in one-dimensional systems at criticality) this is in general not the case. But this is just the empirical finding. The explanation why DMRG in general fails in one-dimensional systems at criticality or in two- or more dimensional systems was given in the context of quantum information theory (QIT) in which the main focus is set on entanglement.

In general, a quantum state $|\psi\rangle$ of a many-body system with $N$ particles with single-particle states $|\psi_i\rangle$ is said to be *entangled* if $|\psi\rangle$ cannot be written as the tensor product $|\psi_1\rangle \otimes |\psi_2\rangle \otimes \ldots \otimes |\psi_N\rangle$. As Latorre et al. [117] emphasize, it is difficult to define a quantitative measure for entanglement in a general quantum mechanical many-body system. For our purpose, it is sufficient to focus on one-dimensional chains of $N$ spins. Latorre et al. [117] showed that the von Neumann entropy

$$S_L = -\mathrm{Tr}\left(\rho_L \log_2 \rho_L\right), \tag{4.29}$$

with reduced density-matrix $\rho_L = \mathrm{Tr}_{N-L} |\psi_0\rangle \langle\psi_0|$ of $L$ contiguous spins ($|\psi_0\rangle$ is the ground state of the chain of $N$ spins), is an appropriate measure for entanglement. Analyzing $S_L$ of a 1D system at criticality reveals that $S_L \to \infty$ whereas $S_L$ stays finite for non-critically 1D systems (see Ref. [117]). The entanglement kept during DMRG – its truncation scheme is known to keep the maximum possible entanglement; see Sec. 4.1.2 – is finite and hence it will fail describing 1D systems at criticality. For higher dimensional systems, one can define the *geometric entropy* (see Callan and Wilczek [35]). For criticality, entanglement can be linked to the geometric entropy [117, 60]. This gives rise to analyze the geometric entropy for general $d$-dimensional systems and use the geometric entropy as a quantitative measure for entanglement. We therefore speak of *entanglement entropy*. A bipartition of a $d$-dimensional space share a $(d-1)$-dimensional hypersurface as the border between both parts. The two parts represent the system and its environment. It is argued in Ref. [59] that the entanglement entropy resides at this hypersurface (and by Schmidt decomposition we conclude that the entanglement entropy is the same for system and environment). This entanglement entropy $S_L$ of a $d$-dimensional system of size $L$ obeys the scaling law

$$S_L \propto L^{d-1}. \tag{4.30}$$

Given the number $m$ of kept states during DMRG truncation, the kept entanglement entropy by DMRG is bounded by this number via

$$S_L \leq \log_2 m. \tag{4.31}$$

This gives (see Ref. [180]) the scaling law for the number $m$ of states to be kept during the calculation. It takes the form

$$m(L) \propto 2^{L^{d-1}}. \tag{4.32}$$

For one-dimensional systems, relation (4.32) gives a constant and we have to keep this certain number of states to describe the system adequately[3]. For two- or more-dimensional systems, the number $m(L)$ of states to be kept for a system of size $L$ diverges exponentially. Since DMRG cannot incorporate more entanglement, it has to fail for such systems. But since DMRG can be embedded in the field of matrix-product-states (MPS), one may suspect that more general product states are able to keep more entanglement and thus may define a generalized DMRG. Such a generalization to DMRG was proposed by Verstraete et al. [208] in 2005. Later, Verstraete and Cirac [209] showed that those generalized states have the appropriate scaling for the entanglement entropy. See Ref. [210] for a recent review on this topic.

---

[3] For 1D systems at criticality, Eq. (4.30) will have further logarithmic corrections, see Refs. [180, 15].

## 4.2 Implementation and Validation of the DMRG

In this section, we give details about the implementation of DMRG. In Sec. 4.2.1, we briefly mention strategies for parallelizing the code. In Sec. 4.2.2, we assess the choice of internal parameters of DMRG (i.e. number $m$ of kept states in the density-matrix, number of sweeps and the weight of the different target states) and see what accuracy can be reached. This section only deals with the symmetric case of the SIAM at half-filling. In Sec. 4.2.3, further checks for the asymmetric case are done.

### 4.2.1 Details of the Parallelization

Since the computation of one DMFT cycle takes, for a reasonable choice of the chain size, number of frequencies and size of the reduced DMRG basis, quite some time[4], it is worthwhile to think about how to parallelize the code. Therefore, one has to search for independent steps in the algorithm and one has to choose one strategy of parallelization. There are essentially two such strategies. The first one makes use of the several cores of one computer: One master-thread forks the task into several slave-threads. All threads share the same memory. One common free application programing interface is OpenMP[5]. Although it is possible to fork into more threads than available cores, this is obviously not reasonable if all threads take the same time[6]. In addition, if the program needs a lot of RAM, the number of threads is limited because all threads use the same RAM. If there is $N$ GB RAM at the computer with $T$ cores and one thread needs $m$ GB, the number of usable threads is limited by $Tm < N$. The strategy to overcome this limitation is to use several computers for parallelization. This requires the implementation of an interface for communication between the different computers so that the calculation can be organized and the results shared. One common open source one is the Open Message Passing Interface OpenMPI[7]. The program used here makes only use of OpenMP.

There are several starting points for parallelization of the DMRG[8]. Let us mention a few:

- The SIAM has conserved quantum numbers so that matrix multiplication (e.g. application of the Hamiltonian) can be split into the multiplication of the corresponding blocks of the matrices.
- The calculation of the Green function for different frequencies $z_i$ and $z_j$ are independent of each other.
- If different states $|\mathscr{B}_j\rangle$ are obtained by applying different operators $\mathscr{B}_j$ on the ground state $|0\rangle$, this can also be parallelized.

The program used here employs the second of the above mentioned starting points. For different frequencies, the values of the spectral density $\rho(z_i)$ and $\rho(z_j)$ differ but the ground state $|0\rangle$ and the corresponding energy $E_0$ do not. Thus it appears that it is not reasonable to build up the chain and to calculate the ground state separately in every frequency thread. Therefore, the program splits into two parts, a *preparation* and an *operation* one.

---

[4] On a standard PC in 2009, the computation of a spectral density for a chain with 160 fermions, $\Delta\omega = 0.1$ and size of the reduced basis $m = 128$ takes approximately one day.

[5] See `http://www.openmp.org` for details.

[6] If the different threads take different amounts of time, it may be more advantageous to use more threads than cores available in order to prevent empty threads.

[7] See `http://www.open-mpi.org` for details.

[8] A whole DMFT cycle consists of the DMRG, the deconvolution and the calculation of the new coupling constants. But since the DMRG nearly takes over 99% of the time for the whole cycle, only the parallelization of the DMRG is considered here.

During the preparation part, the system (the SIAM chain and all operators) is built up. This is illustrated by Fig. 4.2 where the `C++` module names are also given. The buildup consists of the routines `EBuildLeft` and `EBuildRght` which build exact chain blocks with a certain number of sites. The number of sites depends on the number of kept states in the reduced density-matrix. Then, the routines `JoinLeft` and `JoinRght` are applied which add one site on the left or right side of the blocks respectively. After this, the superblock Hamiltonian is constructed and its ground state is calculated. Then all other states of interest are calculated. In the next step, the density-matrix is calculated, diagonalized and the $m$ eigenvectors of the $m$ largest eigenvalues of the density-matrix are used to project the blocks+sites down to $m$ states. This is also done for all operators of interest. This adding and projecting is iterated until the desired size of the chain is reached.

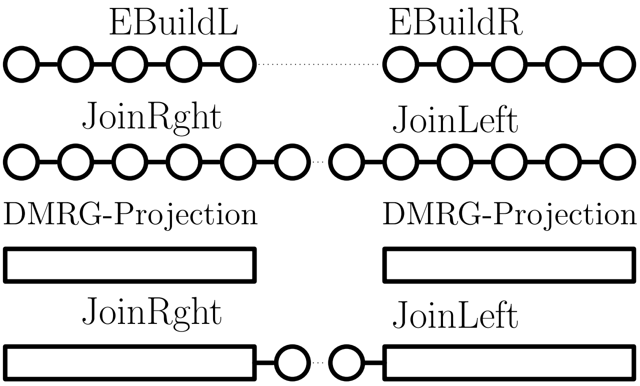

Figure 4.2: Illustration of the buildup procedure. First, the routines `EBuildLeft` and `EBuildRght` build up exact chain blocks. The `JoinLeft` and `JoinRght` routines add sites at the corresponding sides of the block. The superblock is build (dotted lines). Next, the density-matrix projection is applied to obtain the projected blocks. Then, `JoinLeft` and `JoinRght` are applied again. Projecting and joining is iterated until the desired chain size is reached.

For calculations of Green functions, we use a correction vector with $\omega_{\text{buildup}} = 0.0$ in the middle of the spectrum with a large broadening $\eta_{\text{buildup}} \in [1;3]$ so that we also have some information in the density-matrix about the spectrum for the other frequencies away from $\omega = 0.0$. The time for this part of the calculation can be shortened by using the first of the above mentioned starting points of parallelization. After preparing the system in this way, the calculation for the needed frequencies is started; every frequency in a single thread. This is the *operation* part of the calculation. The spectral density is (if not stated otherwise) calculated with a broadening of $\eta = 0.1 = \Delta\omega$ throughout this thesis. After $2-3$ sweeps, the ground state energy, the filling and the spectral density reached their optimal value for the given frequency. After this is done for all frequencies, the deconvolution is carried out.

### 4.2.2 Assessing the Choice of Parameters

Apart from physical parameters of the problem such as the repulsion $U$, the chemical potential $\mu$ and the choice of the bath $G_0$, there is a set of internal parameters that influence the quality and the accuracy of the results. Those are the number of kept states $m$ in the truncated DMRG basis, the number of sweeps and the distribution of weight of the different target states in the density-matrix. Obviously, the number of sweeps has to be chosen such that no reasonable improvement of accuracy is gained for choosing a higher number of sweeps. Also the influence of $m$ is rather clear – the more states are kept the higher accuracy is reached. In contrast, the question which weight distribution of which target states for the density-matrix to choose is a more complex task. The aim of this section is twofold,

1. to motivate the choice (or exclusion) of the target states in the density-matrix and
2. to assess the accuracy of the results for the most reasonable choice of parameters.

The second issue depends on the particular aim of the calculation. If we are just interested in static quantities such as the ground state energy $E_0$ and filling $n$, we will choose another set of target states than if we are interested in dynamic quantities like the Green function or a susceptibility. Therefore, we assess two different cases separately, the *static* (see Sec. 4.2.2.1 below) and the *dynamic* one (see Sec. 4.2.2.2 on page 60). For both cases, we analyze the SIAM on a Bethe-lattice (i.e. $\Im G_0$ is semielliptic) with 160 fermions for $U = D$ and $U = 2D$. If not stated otherwise, we use symmetric measurement, i.e. the quantities are taken for the superblock configuration with the exact site located in the middle of the chain.

#### 4.2.2.1 The Static Case

In a static calculation, we can only obtain the ground state energy (GSE) $E_0$ and the filling $n$. The filling for the particle-hole symmetric case reads $n = 0.5$ and the GSE obeys a variational principle. Therefore, the task is to find a set of parameters such that $n$ does not deviate much from its exact value and $E_0$ takes the lowest value. The reasonable different target states for the density-matrix are the ground state $|\psi_0\rangle$, the filling $|n\rangle := \widehat{S_0^+}\,|\psi_0\rangle$ (note that $n = \langle n|\,n\rangle$) and the density-matrix correction (DMC) $\Delta\rho = \widehat{S_z}\rho\widehat{S_z} + \widehat{S^+}\rho\widehat{S^-} + \widehat{S^-}\rho\widehat{S^+}$ described in Sec. 4.1.5 on page 48. The first observation made during this analysis is that $E_0$ reaches its lowest value if the ground state is targeted alone. In the following, we compare the results for $E_0$ with the reference quantities obtained via one-site DMRG with $m = 800$ shown in Tab. 4.1.

| $U/D$ | $E_0$ |
|---|---|
| 1.0 | -101.5382081242884 |
| 2.0 | -101.6510394823815 |

Table 4.1: Reference quantities for the ground state energy $E_0$ used in this section.

First, we compare the reference quantities with calculations having less states kept in the reduced basis. In Fig. 4.3, the relative error in comparison to the reference quantities in Tab. 4.1 are shown. We see that there is no improvement of the results if two-site DMRG is used and that no noticeable change of the results is seen if more than one sweep is made.

We now want to analyze the effect of adding absent fluctuations (see Sec. 4.1.5) to the density-matrix. In view of the fact that DMC was introduced for one-site DMRG calculations to yield the same accuracy as in two-site DMRG, we do not expect any improvement here. As shown in Fig. 4.3, one- and two-site calculations reach the same accuracy. To analyze the effect of DMC anyway, we lowered the weight for the ground state and set three different values for the extra weight $a_\alpha$ in Eq. (4.26). We calculate the relative error of $E_0$ for $a_\alpha = 0.0001, 0.001$ and $a_\alpha = 0.01$. The results are shown in Fig. 4.4. All $E_0$ obtained via the “corrected” density-matrix were higher than the reference quantities in Tab. 4.1. Inspecting Fig. 4.4, we see that adding absent fluctuations always worsens the results. In

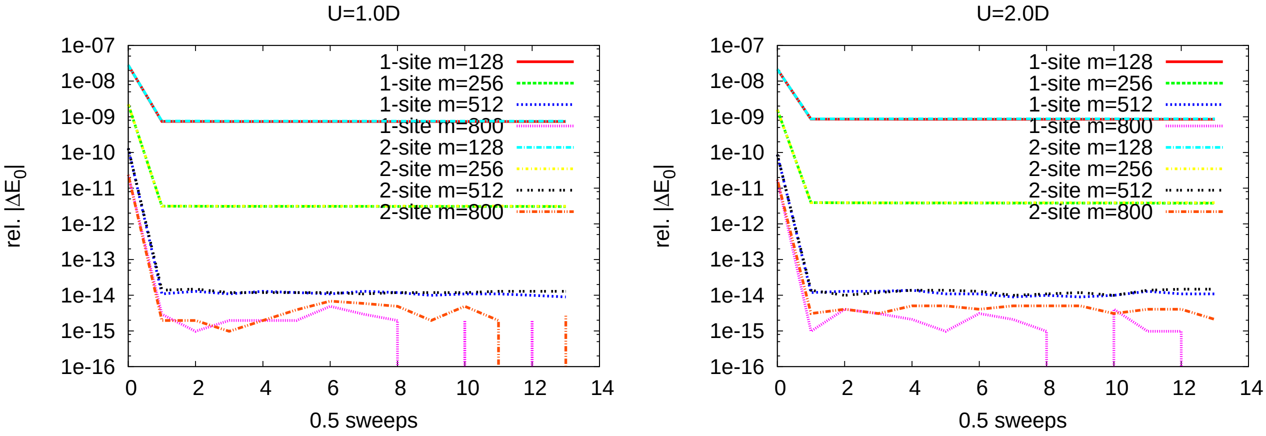

Figure 4.3: Relative difference of the symmetric measurement of the GSE for a chain with 160 fermions for $U = 1.0D$ (left) and $U = 2.0D$ (right) with the density-matrix consisting only of the ground state. We see that one- and two-site DMRG yield the same accuracy.

particular, we lose up to one order of magnitude of accuracy by using DMC. For a static calculation of the SIAM, we can exclude the suspicion that the calculation got stuck in a local minimum. But the crucial question here is, whether this worsening stems from the lowered weight for the ground state in the DMRG basis or if this worsening is due to the state for which the remaining weight is used for. To address this question, we calculated $E_0$ with another distribution of weight in the truncated basis where 1% of the weight was used for targeting the filling[9] $|n\rangle$ instead of using it for DMC. It turns out (not shown) that the accuracy of $E_0$ does *not* change in comparison to the calculation where all the weight is used for the ground state. This implies that using DMC leads to a situation we wanted to avoid, i.e. sticking of the calculation in a local energy minimum. This sticking is clearly seen in Fig. 4.5 where the relative difference from the reference quantities of $E_0$ (shown in Tab. 4.1) for $U = D$ is plotted as a function of the position of the exact site in the superblock. In the upper panel, $a_\alpha$ is set to 0.0001 whereas in the lower panel $a_\alpha = 0$ is set. DMRG is known to be a variational method for $E_0$ and that it reaches the ground state better if more sweeps are calculated. Such a behavior is seen in the lower panel of Fig. 4.5 where the error decreases with more and more sweeps. In contrast to this, an oscillatory behavior is seen in the upper panel of Fig. 4.5. There, more sweeps do not improve the result; actually more sweeps worsen the results. This is a clear evidence that the calculation got stuck in a local minimum.

Now, we turn to the analysis for the filling. We calculated the filling with a density-matrix consisting only of the ground state. This is shown in Fig. 4.6. We see that no further improvement is obtained if more than 256 states are kept in the reduced basis. For using DMC, we again obtain a worsening of accuracy. The results for the filling $n$ if DMC is used are shown in Fig. 4.7. In contrast to $E_0$, we see that the worsening of the accuracy can be obviated by increasing the number of kept states $m$. Also in contrast to the results of $E_0$, the worsening of the accuracy is of the same order of magnitude if we do not use DMC but target at the filling instead (not shown). For including the filling to the density-matrix, we rather obtain the same results as for using DMC.

---

[9] This means, we add $|n\rangle\langle n|$ to the density-matrix $\rho$.

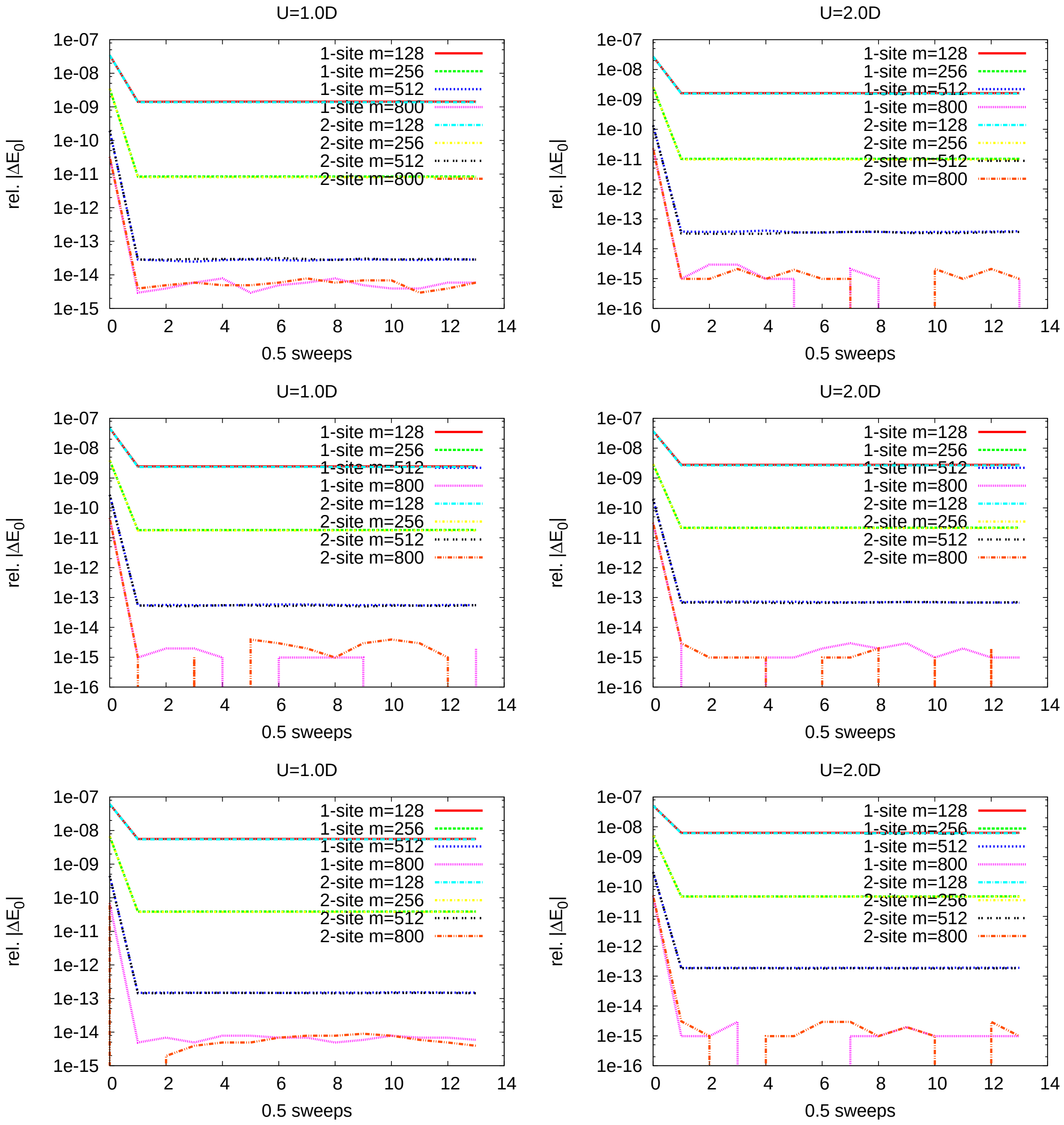

Figure 4.4: Relative difference of the symmetric measurement of the GSE for a chain with 160 fermions for $U = 1.0D$ (left) and $U = 2.0D$ (right) for several values of weight for the correction of the density-matrix. Upper: Weight = 0.0001; middle: weight = 0.001; lower: weight = 0.01.

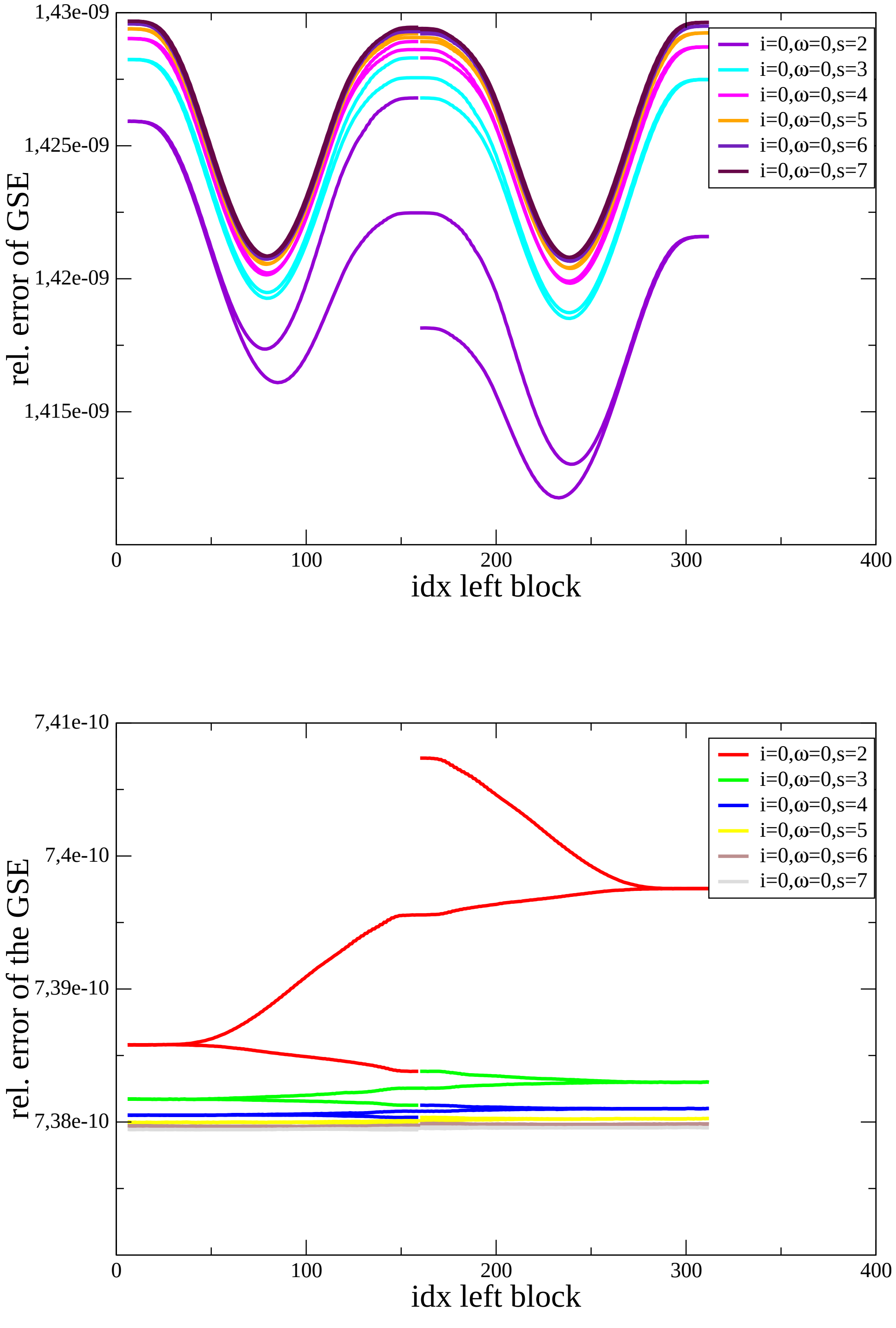

Figure 4.5: Relative difference of the GSE as a function of the position of the exact site (for $s$ sweeps) for one-site DMRG, $U = 1.0D$ and 128 kept states in the reduced basis if 0.0001 (top) weight is used for DMC or not (bottom). The wavy behavior in the upper panel is a hint that the calculation got stuck in a local minimum. It appears that DMC, which is used to avoid such sticking, can lead to such sticking. In contrast to this, we see in the lower panel the expected behavior for $E_0$ obeying a variational principle.

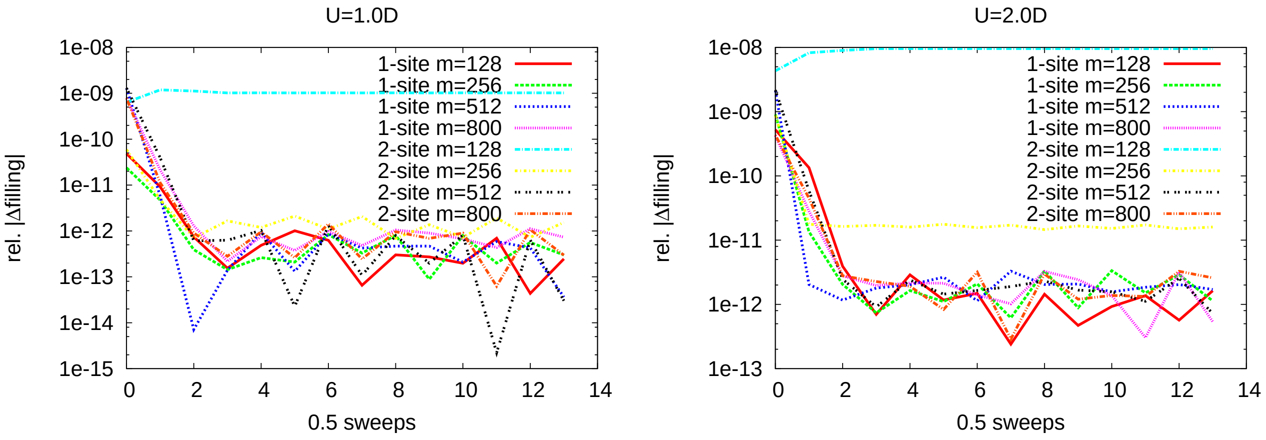

Figure 4.6: Relative difference of the symmetric measurement of the filling of the symmetric SIAM for full weight for the GS for $U = 1.0D$ (left) and $U = 2.0D$ (right).

In summary, we obtain that the best choice for static calculations is using all the weight in the density-matrix for the ground state. Targeting at other states of interest, like the filling, does not lead to better results; the accuracy is even worsened. Surprisingly, it turned out that the correction of the density-matrix (DMC) introduced by White [224] to avoid sticking to local minima (see. Sec. 4.1.5) for the SIAM considered here leads to sticking to local minima. This is even true for very small values of weight used for DMC. To our knowledge, such a result was not found before.

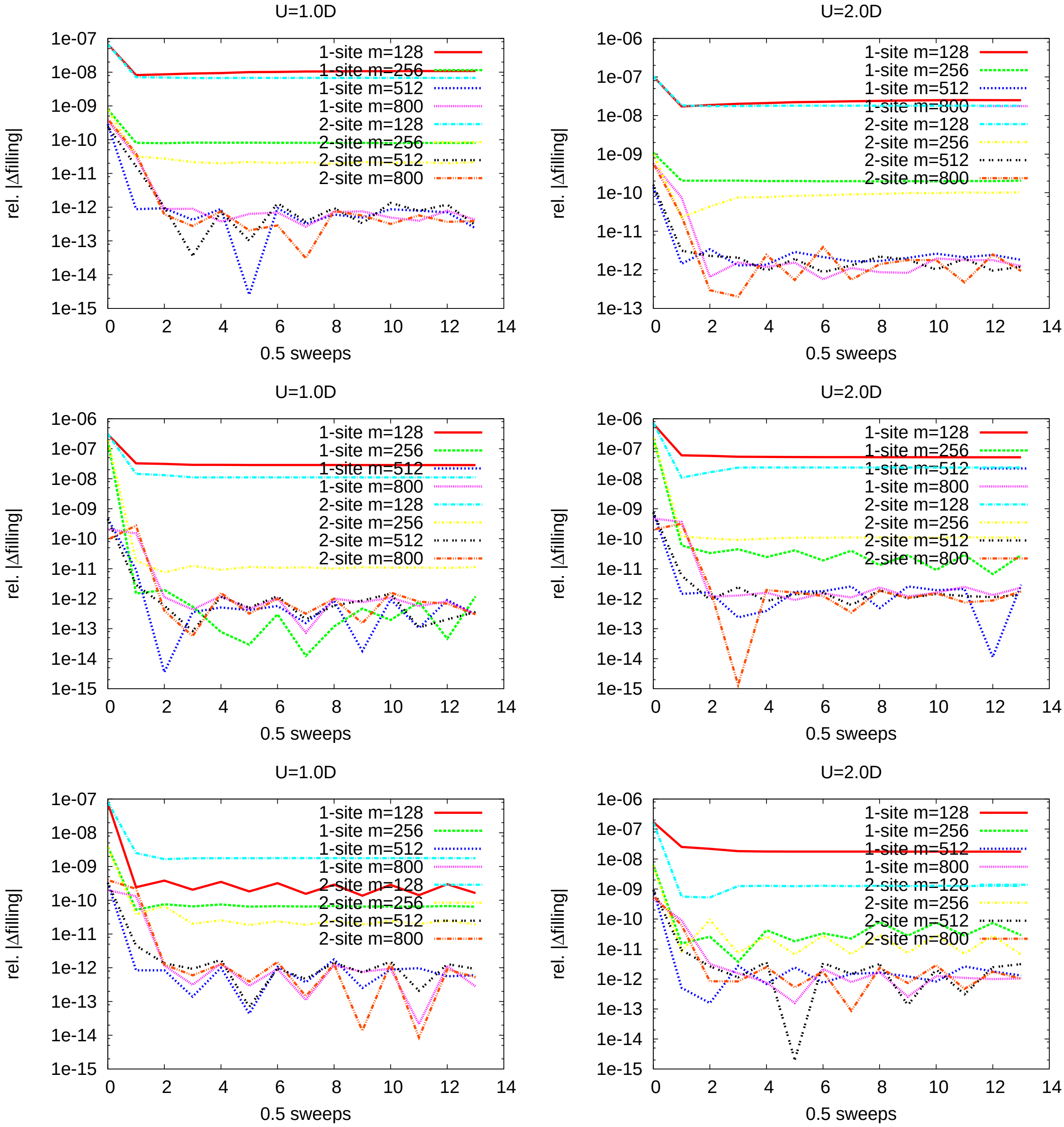

Figure 4.7: Relative difference of the symmetric measurement of the filling for a chain with 160 fermions for $U = 1.0D$ (left) and $U = 2.0D$ (right) for several values of weight used for adding DMC into the density-matrix. Upper: weight $= 0.0001$; middle: weight $= 0.001$; lower: weight $= 0.01$.

#### 4.2.2.2 The Dynamic Case

Assessing the choice of parameters for a dynamic calculation is a more complex task than for a pure static calculation. This is not merely due to the need to target at other states than the ground state. In contrast to $E_0$ or $n$, we cannot calculate a "reference quantity" for a Green function. For the calculation of a Green function we need (see Eq. (4.19) on page 46) the complex-valued correction vector (CV) $|\xi\rangle = \Re|\xi\rangle + i\Im|\xi\rangle$ (see Eq. (4.22) on page 47) which depends on $E_0$ and the first excited state which itself depends on the ground state.

Despite the problems in validating the quality of the spectral density, we can analyze the quality of $E_0$ and $n$ if less weight is used for targeting the ground state in the density-matrix. We can analyze the effect of targeting at the filling vector $|n\rangle$ or using density-matrix correction (DMC) described in Sec. 4.1.5 on page 48. We calculate the relative error of $E_0$ in comparison to the quantities shown in Tab. 4.1 on page 54 and set the weight for the ground state to 30%, 40% and 39%. In the last case, we use 1% for DMC. The results are shown in Fig. 4.8. In comparison to the pure static case, we lose approximately $1 - 1.5$ orders of magnitude of accuracy. We see no difference between the 30%-ground state- and 40%-ground state-configuration. The worsening of the results by DMC, which we obtained for the static calculation, is seen here as well, although it is not as drastic as for the static case.

The results for the filling $n$ are shown in Fig. 4.9. Comparing Fig. 4.9 and Fig. 4.6 (relative error of the filling $n$ for the static calculation), we obtain a loss of 2-4 orders of magnitude of accuracy. This is twice as much as for $E_0$ which is plausible since for the filling the ground state enters twice. By comparing the middle and the lower row of Fig. 4.9, we observe an increased accuracy of one order of magnitude by using DMC.

As stated above, we cannot calculate a reference quantity for a Green function. But we can study how many sweeps are reasonable for dynamic calculations, i.e., after how many sweeps the spectral density does not change anymore. We analyze the following weight distributions (WD):

1. GS 0.30, first excited state 0.2, CV 0.5 (equally distributed over real and imaginary part).
2. GS 0.40, first excited state 0.3, CV 0.3 (equally distributed over real and imaginary part).
3. GS 0.40, first excited state 0.2, CV 0.4 (equally distributed over real and imaginary part).
4. GS 0.39 (plus 0.01 weight for DMC), first excited state 0.2, CV 0.4 (equally distributed over real and imaginary part).

We calculated the spectral densities for $U = D$ and $U = 2D$ for the frequencies $\omega + i\eta = 0.0 + i$ (buildup frequency), $\omega + i\eta = 1.0 + 0.1i$, $\omega + i\eta = 2.0 + 0.1i$ and $\omega + i\eta = 3.0 + 0.1i$ for all distributions mentioned above. We chose one- and two-site DMRG and different choices for the number of kept states $m$ in the truncated basis. First, we set $m = 400$. It appears that for all weight distributions above, almost the same value for the spectral density for a certain frequency is obtained. To make quantitative statements about this finding, we count the number of constant valid digits for a certain frequency. This is shown in Tab. 4.2 on page 63. Comparing left and right part of this table (i.e. $U = 1.0D \rightarrow 2.0D$), we see that for higher Coulomb repulsion the four weight distributions differ more since less valid constant digits are found. The same statement has to be made for comparing lower and higher frequencies. Both results are reasonable and intuitively expected findings.

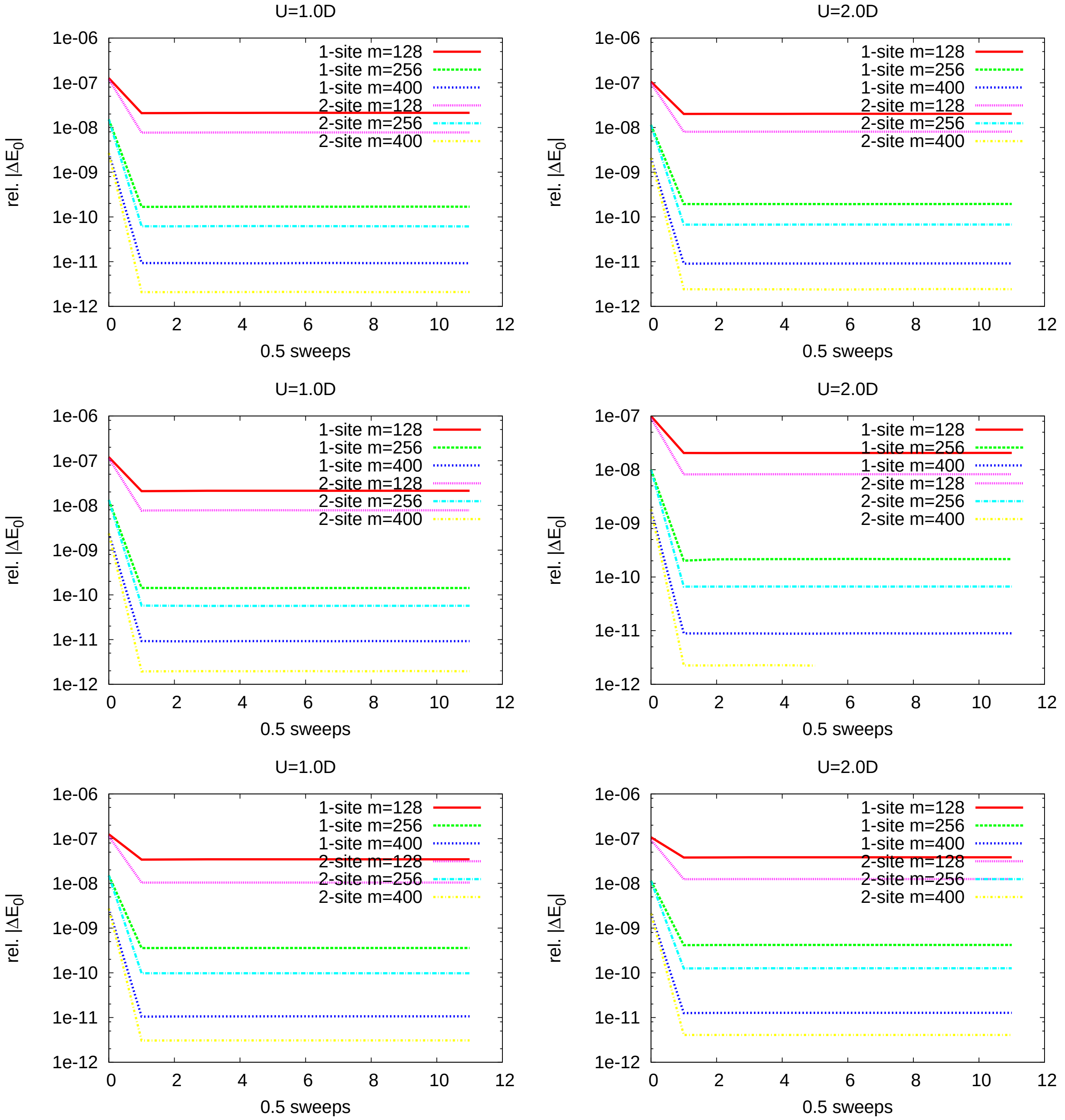

Figure 4.8: Relative difference of the symmetric measurement of the GSE for $U = 1.0D$ (left) and $U = 2.0D$ (right). Weight for the GS is set to 0.30 (upper), 0.40 (middle) an 0.39 (lower), while in the last case 0.01 weight was used for adding DMC into the density-matrix.

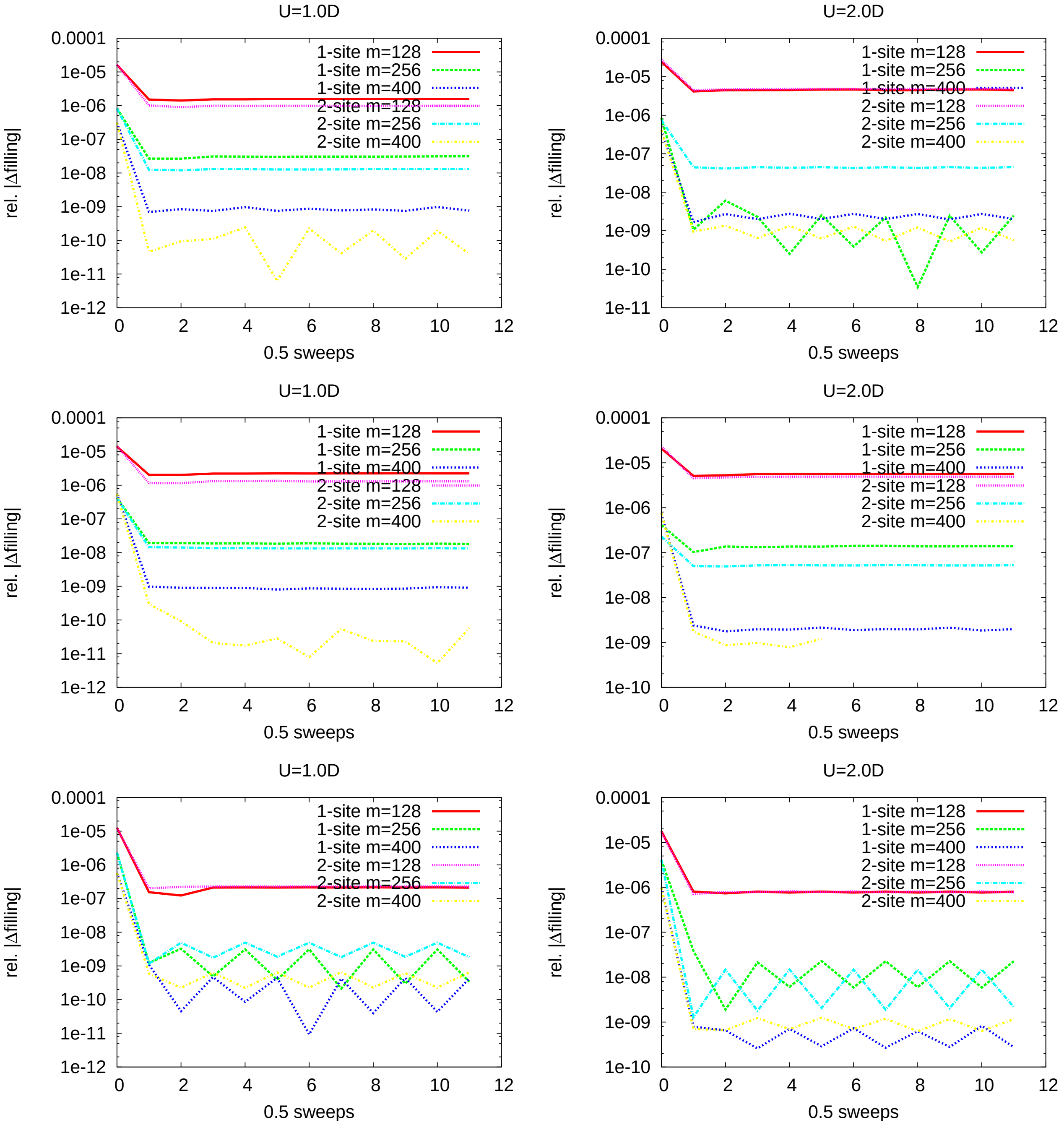

Figure 4.9: Relative difference of the symmetric measurement of the filling for $U = 1.0D$ (left) and $U = 2.0D$ (right). Weight for the GS is set to 0.30 (upper), 0.40 (middle) an 0.39 (lower), while in the last case 0.01 weight was used to add DMC to the density-matrix.

| Sites | WD | $\omega/D$ | $\eta/D$ | functional $W \cdot D$ |
|---|---|---|---|---|
| 1 | 1 | 0.0 | 1.0 | -4.893817963675083e-02 |
| 1 | 2 | 0.0 | 1.0 | -4.893817962055123e-02 |
| 1 | 3 | 0.0 | 1.0 | -4.893817963278776e-02 |
| 1 | 4 | 0.0 | 1.0 | -4.893817967838975e-02 |
| 2 | 1 | 0.0 | 1.0 | -4.893817970865996e-02 |
| 2 | 2 | 0.0 | 1.0 | -4.893817970346651e-02 |
| 2 | 3 | 0.0 | 1.0 | -4.893817970838647e-02 |
| 2 | 4 | 0.0 | 1.0 | -4.893817974206625e-02 |
| number of constant valid digits: **8** | | | | |
| 1 | 1 | 1.0 | 0.1 | -1.845175541797971e-01 |
| 1 | 2 | 1.0 | 0.1 | -1.845174925921831e-01 |
| 1 | 3 | 1.0 | 0.1 | -1.845175147735539e-01 |
| 1 | 4 | 1.0 | 0.1 | -1.845175013704822e-01 |
| 2 | 1 | 1.0 | 0.1 | -1.845176298973693e-01 |
| 2 | 2 | 1.0 | 0.1 | -1.845175480053235e-01 |
| 2 | 3 | 1.0 | 0.1 | -1.845175707782817e-01 |
| 2 | 4 | 1.0 | 0.1 | -1.845175337351473e-01 |
| number of constant valid digits: **6** | | | | |
| 1 | 1 | 2.0 | 0.1 | -1.188430783183688e-01 |
| 1 | 2 | 2.0 | 0.1 | -1.188421870137998e-01 |
| 1 | 3 | 2.0 | 0.1 | -1.188422738826481e-01 |
| 1 | 4 | 2.0 | 0.1 | -1.188421959820155e-01 |
| 2 | 1 | 2.0 | 0.1 | -1.188432948583218e-01 |
| 2 | 2 | 2.0 | 0.1 | -1.188419870095896e-01 |
| 2 | 3 | 2.0 | 0.1 | -1.188424392431158e-01 |
| 2 | 4 | 2.0 | 0.1 | -1.188423543821709e-01 |
| number of constant valid digits: **5** | | | | |
| 1 | 1 | 3.0 | 0.1 | -6.701351340275195e-03 |
| 1 | 2 | 3.0 | 0.1 | -6.701342657125207e-03 |
| 1 | 3 | 3.0 | 0.1 | -6.701330271272220e-03 |
| 1 | 4 | 3.0 | 0.1 | -6.701421867051389e-03 |
| 2 | 1 | 3.0 | 0.1 | -6.701713377647868e-03 |
| 2 | 2 | 3.0 | 0.1 | -6.701593750383292e-03 |
| 2 | 3 | 3.0 | 0.1 | -6.701648250575363e-03 |
| 2 | 4 | 3.0 | 0.1 | -6.701678818016796e-03 |
| number of constant valid digits: **4** | | | | |

| Sites | WD | $\omega/D$ | $\eta/D$ | functional $W \cdot D$ |
|---|---|---|---|---|
| 1 | 1 | 0.0 | 1.0 | -4.016667783457693e-02 |
| 1 | 2 | 0.0 | 1.0 | -4.016667783397115e-02 |
| 1 | 3 | 0.0 | 1.0 | -4.016667784532034e-02 |
| 1 | 4 | 0.0 | 1.0 | -4.016667788607233e-02 |
| 2 | 1 | 0.0 | 1.0 | -4.016667793145309e-02 |
| 2 | 2 | 0.0 | 1.0 | -4.016667791639907e-02 |
| 2 | 3 | 0.0 | 1.0 | -4.016667791468105e-02 |
| 2 | 4 | 0.0 | 1.0 | -4.016667801250247e-02 |
| number of constant valid digits: **7** | | | | |
| 1 | 1 | 1.0 | 0.1 | -6.578881983870681e-02 |
| 1 | 2 | 1.0 | 0.1 | -6.578875854878476e-02 |
| 1 | 3 | 1.0 | 0.1 | -6.578878422727176e-02 |
| 1 | 4 | 1.0 | 0.1 | -6.578875642632180e-02 |
| 2 | 1 | 1.0 | 0.1 | -6.578887934290756e-02 |
| 2 | 2 | 1.0 | 0.1 | -6.578878622352699e-02 |
| 2 | 3 | 1.0 | 0.1 | -6.578883422343802e-02 |
| 2 | 4 | 1.0 | 0.1 | -6.578877057642080e-02 |
| number of constant valid digits: **5** | | | | |
| 1 | 1 | 2.0 | 0.1 | -1.610126173532761e-01 |
| 1 | 2 | 2.0 | 0.1 | -1.610108890574770e-01 |
| 1 | 3 | 2.0 | 0.1 | -1.610115673157419e-01 |
| 1 | 4 | 2.0 | 0.1 | -1.610099841846489e-01 |
| 2 | 1 | 2.0 | 0.1 | -1.610118334967933e-01 |
| 2 | 2 | 2.0 | 0.1 | -1.610090262318971e-01 |
| 2 | 3 | 2.0 | 0.1 | -1.610118172277819e-01 |
| 2 | 4 | 2.0 | 0.1 | -1.610110224979300e-01 |
| number of constant valid digits: **4** | | | | |
| 1 | 1 | 3.0 | 0.1 | -1.115489336954664e-02 |
| 1 | 2 | 3.0 | 0.1 | -1.115455110465731e-02 |
| 1 | 3 | 3.0 | 0.1 | -1.115451080713885e-02 |
| 1 | 4 | 3.0 | 0.1 | -1.115610285120414e-02 |
| 2 | 1 | 3.0 | 0.1 | -1.115595458596825e-02 |
| 2 | 2 | 3.0 | 0.1 | -1.115576312029320e-02 |
| 2 | 3 | 3.0 | 0.1 | -1.115583040728069e-02 |
| 2 | 4 | 3.0 | 0.1 | -1.115727536644691e-02 |
| number of constant valid digits: **4** | | | | |

Table 4.2: Results (see fifth column) for the functional $W$ (see Eq. (4.24) on page 48) for $U = 1.0D$ (left table) and $U = 2.0D$ (right table) both with $m = 400$ kept states in the reduced basis obtained by one- or two-site DMRG (see first column) with the above described weight distribution WD (see second column) for given frequencies $\omega$ and broadenings $\eta$ (see third and fourth column).

Since all weight distributions lead to almost the same results, we can compare the results of the spectral density for less states $m$ with one of the values for a certain frequency with $m = 400$. This shows which weight distribution reaches the corresponding reference best. To make a long story short, this analysis does not lead to conclusive results. As an example, we show the results for $U = 1.0D$, $\omega = 2.0D$ and $\eta = 0.1D$ in Fig. 4.10. From this figure, we see that using DMC (lower right) requires two sweeps to get a constant value for the spectral density. All other weight distributions only need one sweep. But with respect to accuracy (in the sense of reaching the corresponding value in Tab. 4.2), we do not obtain conclusive results which weight distribution one should favor. We obtain the same non-conclusive result also for the other frequencies (not shown).

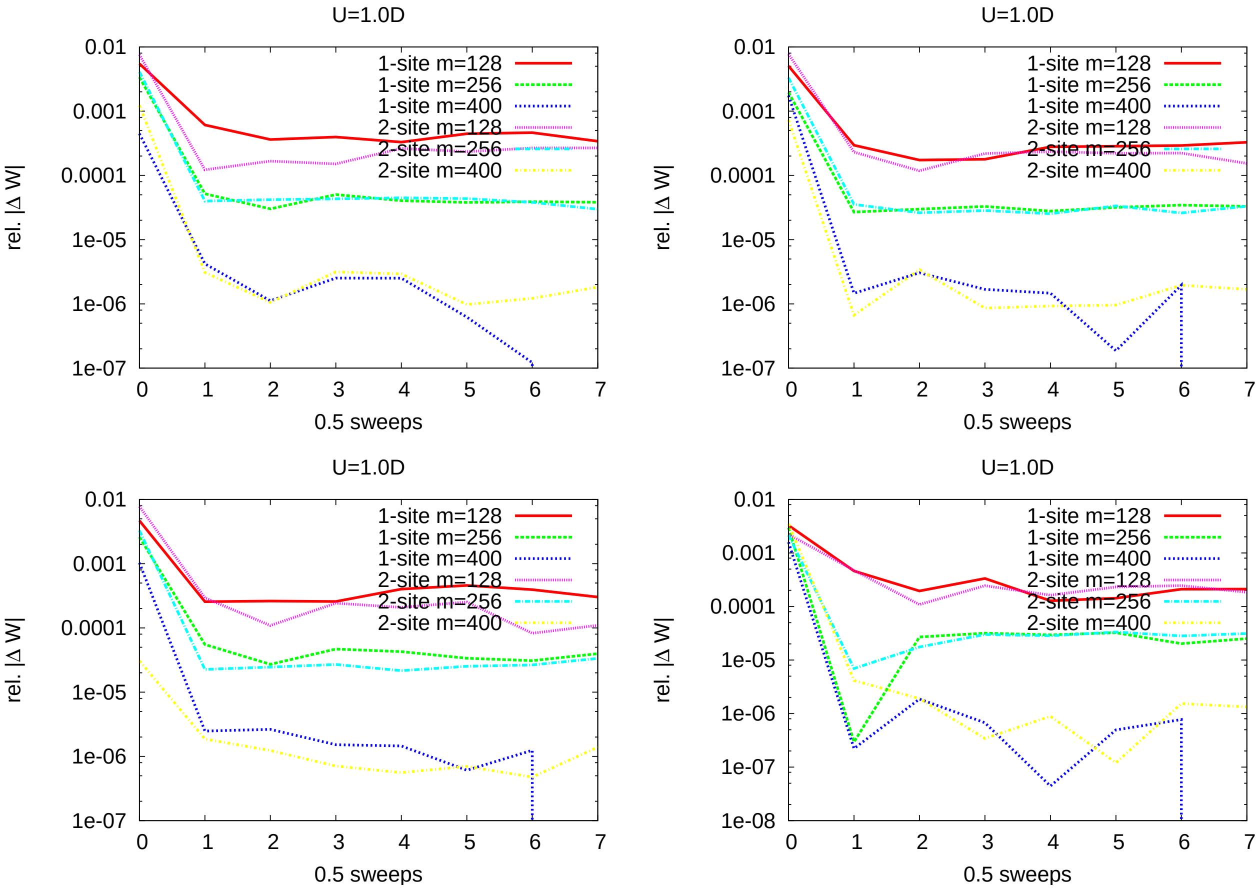

Figure 4.10: Relative difference of the functional $W$ for $U = 1.0D$, $\omega = 2.0D$ and $\eta = 0.1D$. The upper row displays the results for the first (left) and the second (right) weight distribution and the lower row displays the results for the third (left) and fourth (right) weight distribution.

In all situations above, an equal distribution for targeting the real and imaginary part of the correction vector (CV) was chosen. Both parts of the CV depend on each other, i.e. the real part is directly obtained from the imaginary part (see Eq. (4.22) on page 47). Therefore, one may suspect that the results improve for an asymmetric targeting at the CV where more weight is used for the imaginary part. To check this hypothesis, we chose

1. 0.4 weight for the GS, 0.2 weight for the first excited state (like in the third weight distribution), 0.3 for the imaginary part of the CV and 0.1 for the real part of the CV.

2. 0.3 weight for the GS, 0.2 weight for the first excited state (like in the first weight distribution), 0.4 for the imaginary part of the CV and 0.1 for the real part of the CV.

The accuracy of the static quantities ($E_0$ and filling) for both weight distributions stay the same as in the corresponding weight distribution for symmetric targeting. This is reasonable since we used the same percentage of weight for the GS. But in contrast to our expectation for the dynamic quantities, we do not achieve any clear improvement for the spectral density. The results are the same as for the first or third weight distribution respectively (not shown).

One residual way of assessing which weight distribution to use utilizes the deconvolution (see Sec. 4.3 on page 68). For all weight distributions, we calculated the spectral densities and analyze them in a more qualitative manner. Although all weight distributions lead to slightly different spectral densities (not shown), none of them is obviously the best neither in the sense that it exhibits the least number of wiggles nor in the sense that it resolves sharp features best. Also the check of the pinning criterion[10] and the check of the norm criterion[11] does not signalize which weight distribution is the best.

Against the background of these findings, it is difficult to come to a decisive conclusion for all parameters. The only two conclusive results obtained here are that

1. the density-matrix correction should not be used and
2. one should not use weight to target the filling $n$.

Apart from this, the choice of parameters is a matter of experience. This result has also positive implications: It turns out that the results for a dynamic calculation are not very sensitive to the particular choice of weight distribution. If not stated otherwise, we use the third weight distribution (i.e. 40% ground state, 20% for the first excited state and 40% for the correction vector with equal distribution over real and imaginary part) throughout this thesis. If not stated otherwise, we use for DMFT calculations one-site DMRG with $m = 128$ states in the reduced basis until convergence of the self-consistency cycle and at least two cycles with $m = 256$ states afterwards. For susceptibilities, we use $m = 256$ states in the reduced basis.

### 4.2.3 Further Checks for the Asymmetric SIAM

The preceding checks only analyzed the symmetric SIAM after JW transformation (i.e. $\epsilon_\text{d} = -{}^U\!/2$ & $\epsilon_i = 0$). In order to calculate static quantities and spectral densities for the asymmetric SIAM, local $\widehat{S_z}$-fields are added to the Hamiltonian of the symmetric SIAM. First, we have to check if they are implemented correctly. Second, we have to check to which accuracy the new program reproduces the spectral densities for no local $\widehat{S_z}$-fields. Then, we check static quantities and spectral densities for the SIAM with $U = 0$ and $\mu \neq 0$ by comparing them with the exact results. Afterwards, we analyze the results for $U \neq 0$ and check to which accuracy certain symmetries are fulfilled.

For the check whether the local $\widehat{S_z}$-fields are implemented correctly, calculations of the Hamiltonian

$$\mathscr{H} = \mu \sum_{i=0}^{N_s} \widehat{S_z^i} \tag{4.33}$$

---

[10] The spectral density $\rho_G(\omega = 0)$ is for all $U$ pinned to the value of the non-interacting spectral density $\rho_0(\omega = 0)$.

[11] The spectral density $\rho_G$ obeys for all $U$ the sum rule $\int_{-\infty}^{\infty} \rho_G(\omega)\mathrm{d}\omega = 1$.

are done. This is the Hamiltonian of the SIAM with no hopping or Coulomb repulsion, i.e. a Hamiltonian consisting only of the new implemented terms. In this special case, the SIAM consists of $N_s$ non-interacting Jordan Wigner spins with a local field strength $\mu$. Obviously, the state with the lowest lying ground state energy $E_0$ is the fully polarized state with all spins down (up) if $\mu$ is positive (negative). The corresponding ground state energy reads $E_0 = -|\mu| N_s$. Both, the particular value of $E_0$ and its independence of the sign of $\mu$ was checked for several values of $N_s$ with a density-matrix consisting only of the ground state. In all cases, the exact $E_0$ was reached with machine precision. Hence, we conclude that the local magnetic fields are implemented correctly.

Next, we reproduce the results for the spectral densities for $\mu = 0$ and check their quality. At first sight, the spectral densities look the same (not shown). For the symmetric SIAM, we only need to calculate one part of the Green function $G = G^> + G^<$ since the other part is obtained via $G^<(\omega) = G^>(-\omega)$. We want to check the symmetry of $G$ for $\mu = 0$. To this end, we analyze to which accuracy the symmetry condition $\Im G^>(\omega) = \Im G^<(-\omega)$ is fulfilled in a realistic calculation (160 fermions, $m = 128$) for $U = D$ and $U = 2D$. The error of $\Im G^<$ in comparison to $\Im G^>$ is shown in Fig. 4.11. We see a worsening of the accuracy for higher frequencies. In order to check whether this behavior is due to a bug in the program or due to the increasing difficulty of the DMRG to calculate $\Im G^>$ for increasing frequencies, we compare the accuracy of $E_0$ and $n$ as a function of $\omega$. Of course, $E_0$ and $n$ are static quantities and hence do not depend on $\omega$. However, depending on $\omega$, the DMRG basis is not always equally suited to calculate $E_0$ and $n$. Hence, we calculate $E_0(\omega)$ & $n(\omega)$ and the results are shown in Fig. 4.12. We see that for calculations of $\Im G^>$ ($\Im G^<$) the accuracy worsens for positive (negative) frequencies which is the expected behavior. The asymmetry in the accuracy seen in Fig. 4.11 stems from our choice to compare $\Im G^>(\omega)$ with $\Im G^<(-\omega)$ (and not $\Im G^<(\omega)$ with $\Im G^>(-\omega)$).

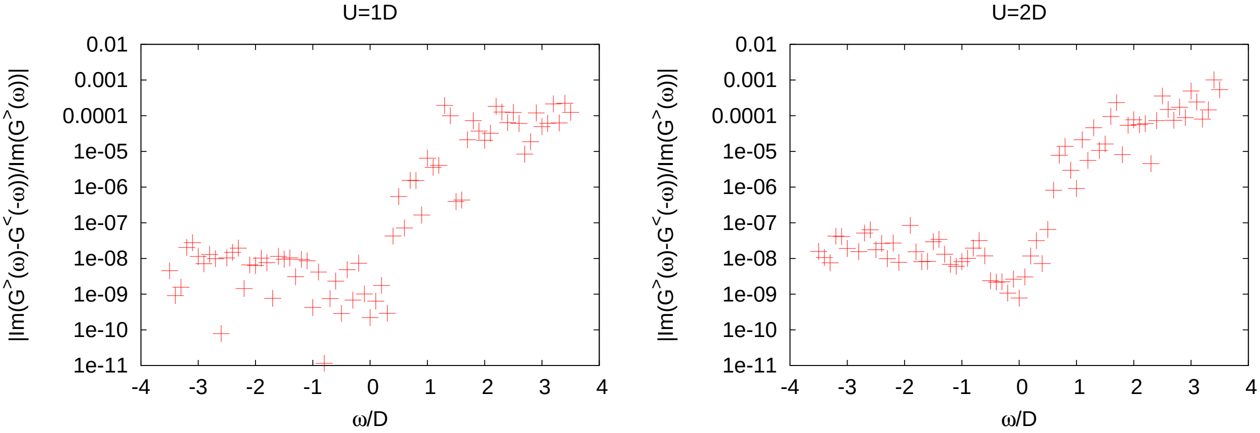

Figure 4.11: Symmetry test I: Relative difference of $\Im G^<(\omega)$ and $\Im G^>(-\omega)$ for $U = D$ (left) and $U = 2D$ (right). For positive frequencies, the symmetry condition holds less accurately. The asymmetry in the accuracy stems from our choice to compare $\Im G^>(\omega)$ with $\Im G^<(-\omega)$ (and not $\Im G^<(\omega)$ with $\Im G^>(-\omega)$).

Next, we check the filling for $\mu \neq 0$ ($E_0$ was checked via (4.33)) for $U = 0$ for a chain of 160 fermions and $m = 128$. For $U = 0$, switching on $\mu$ leads to a semielliptic spectral density $\rho_G(\omega, \mu) = {}^2/_\pi \sqrt{D^2 - (\omega + \mu)^2}$ whose maximum is shifted by $\mu$. In general, the filling $n$ is given by

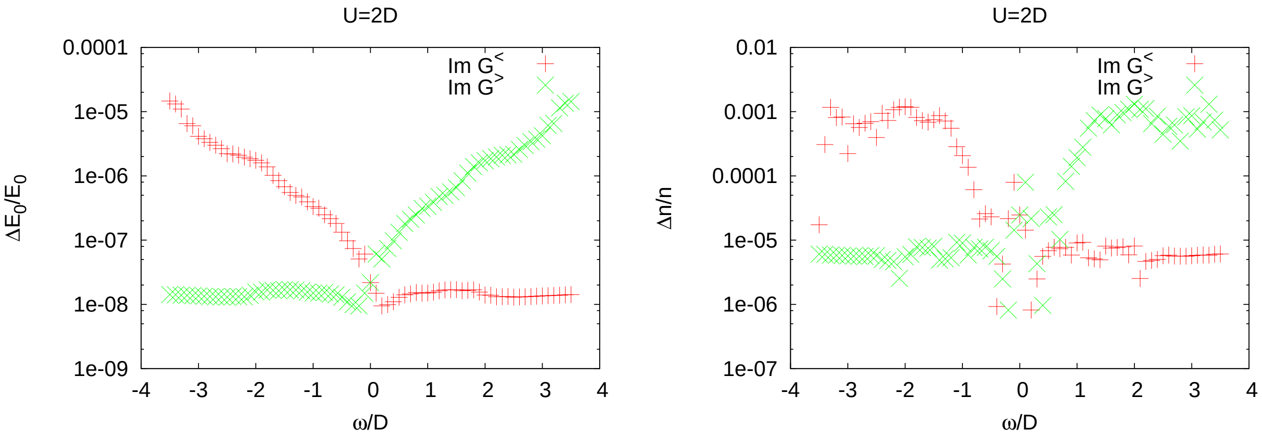

Figure 4.12: Symmetry test II: Relative difference of $E_0$ (left) in comparison to the quantity in Tab. 4.1 for $U = 2D$ and relative error of the filling $n$. Both are calculated as a function of $\omega$ during a dynamic calculation. If $\Im G^{>}$ ($\Im G^{<}$) is calculated, the error rises for positive (negative) frequencies.

$$n(\mu) = \int_{-\infty}^{0} \rho_G(\omega, \mu) \mathrm{d}\omega. \tag{4.34}$$

In Fig. 4.13, we show the continuous $n(\mu)$ obtained via (4.34) and the filling for certain $\mu$ obtained by DMRG. Both are in very good agreement; in particular the relative error ranges from 0 to $10^{-3}$ (not shown).

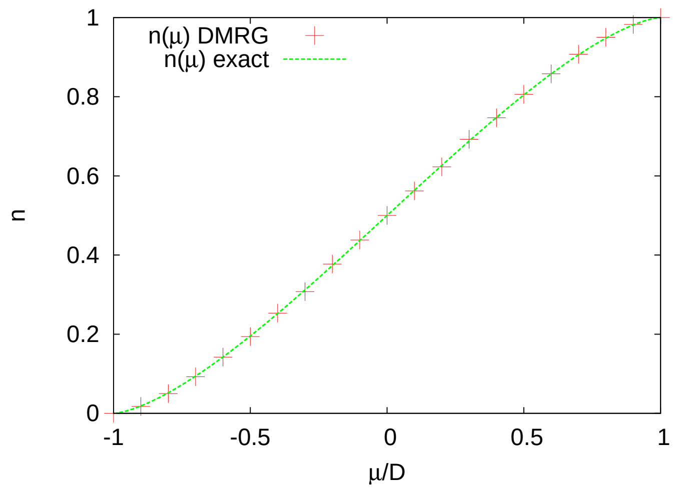

Figure 4.13:
The filling $n$ for $U = 0$ with $m = 128$ states in the reduced basis compared to the exact value obtained via (4.34). The relative error is below $10^{-3}$.

After having checked the static quantities for $\mu \neq 0$ and the symmetry of $G$ for $\mu = 0$, we now validate $\Im G$ for $\mu \neq 0$. We restrict the analysis to convoluted data with $\eta = 0.1D$. For $U = 0$, $\Im G$ is known exactly for all $\mu$, i.e. $\Im G$ is a semiellipse whose maximum is shifted by $\mu/D$. This expectation is confirmed (not shown). For $U \neq 0$, the exact Green function is not known, but certain symmetry conditions also apply here. In particular, $\Im G^{>}(\omega, \mu) = \Im G^{<}(-\omega, -\mu)$ must be fulfilled. To check this, we calculate spectral densities for $\mu = 0.25D$ and $\mu = -0.25D$ for $U = 1D$ and $U = 2D$ ($m = 128$) and compare $\Im G^{>}(\omega, \mu)$ with $\Im G^{<}(-\omega, -\mu)$. The results are shown in Fig. 4.14. As for $\mu = 0$ (see. Fig. 4.11), the asymmetry in the accuracy stems from our choice to compare $\Im G^{>}(\omega, \mu)$ with $\Im G^{<}(-\omega, -\mu)$ (and not $\Im G^{<}(\omega, \mu)$ with $\Im G^{>}(-\omega, -\mu)$). The accuracy is of the same order as in the prior program.

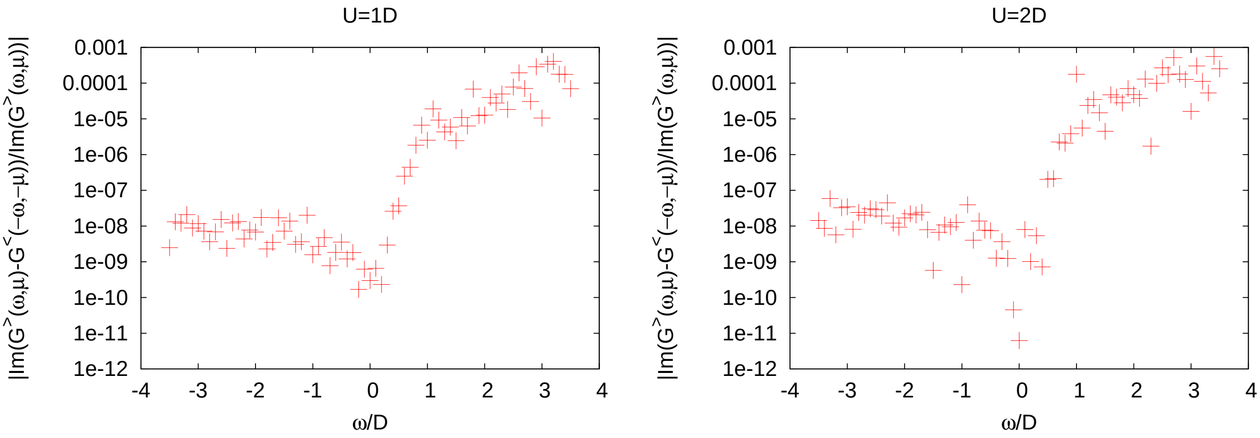

Figure 4.14: Test to what accuracy the symmetry condition $\Im G^{>}(\omega, \mu) = \Im G^{<}(-\omega, -\mu)$ is fulfilled for $\mu = 0.25D$, $U = 1D$ (left) and $U = 2D$ (right). Shown are the relative error with respect to $\Im G^{>}(\omega, \mu)$.

In this section, we accomplished several checks of the program for $\mu \neq 0$. First, we checked that the local magnetic fields are implemented correctly. Dealing with the SIAM for $\mu \neq 0$ also implies that both parts of the Green function $G = G^{>} + G^{<}$ have to be calculated separately. The accuracy of static quantities $E_0$ and $n$ is expected to worsen for positive (negative) frequencies if $G^{>}$ ($G^{<}$) is calculated. Analyzing whether this is the case was the second check of the new program. Afterwards, we tested the new program by comparing the filling and the spectral densities with the exact quantities for $U = 0$. At last, we checked the symmetry of the spectral densities for $U \neq 0$ by comparing $\Im G^{>}(\omega, \mu)$ with $\Im G^{<}(-\omega, -\mu)$. The program passed all those tests and showed the same accuracy of the particular quantities as the prior program did. Thus it seems that everything was implemented correctly.

## 4.3 Deconvoluting D-DMRG Raw Data

### 4.3.1 Why Convoluted Data Appears

As described in Sec. 4.1.4 on page 46, dynamic DMRG gives the retarded response function

$$G^{\text{ret}}(\omega_j + \mathrm{i}\eta_j) = \left\langle 0 \middle| \mathscr{A} \frac{1}{\omega_j + \mathrm{i}\eta_j - (\mathscr{H} - E_0)} \mathscr{A}^{\dagger} \middle| 0 \right\rangle + \left\langle 0 \middle| \mathscr{A}^{\dagger} \frac{1}{\omega_j + \mathrm{i}\eta_j + (\mathscr{H} - E_0)} \mathscr{A} \middle| 0 \right\rangle \tag{4.35}$$

of some operator $\mathscr{A}$ at discrete complex frequencies $z_j := \omega_j + \mathrm{i}\eta_j$. This response function becomes the Green function if $\mathscr{A}$ is the creation operator or it becomes the Q-function if $\mathscr{A}$ is the Q-operator (see Sec. 3.3.4 on page 29). For comparison with experiment, one is interested in the spectral density

$$\rho(\omega) := -\frac{1}{\pi}\Im G^{\mathrm{ret}}(\omega) \tag{4.36}$$

where the limit $\eta \to 0^+$ is carried out. Since the response function is *causal* and exhibits a finite norm, the response function $G^{\mathrm{ret}}(z)$ and the spectral density $\rho(\omega)$ are connected by the Hilbert transform (see Ref. [29, p. 267-272])

$$G^{\mathrm{ret}}(z) = \frac{1}{\pi}\int\limits_{-\infty}^{\infty} \frac{\rho(\omega')}{z-\omega'}\mathrm{d}\omega' \qquad \text{with } z = \omega + \mathrm{i}\eta \quad \text{and} \quad \omega, \omega', \eta \in \mathbb{R}. \tag{4.37}$$

For $\eta = 0$, the integrand of (4.37) exhibits a singularity for $\omega' = \omega$. In this case, the Cauchy principal value of the integral has to be considered. The imaginary part of the integral in (4.37) reads

$$\Im(G^{\mathrm{ret}}(\omega + \mathrm{i}\eta)) = -\frac{1}{\pi}\int\limits_{-\infty}^{\infty} \frac{\rho(\omega')\eta}{(\omega-\omega')^2+\eta^2}\mathrm{d}\omega'. \tag{4.38}$$

Thus it appears that the imaginary part of D-DMRG raw data $\Im(G^{\mathrm{ret}}(\omega + \mathrm{i}\eta))$ is the convolution of the spectral density $\rho(\omega)$ and a Lorentzian $L_\eta(\omega - \omega')$ with broadening $\eta$ and the maximum at $\omega = \omega'$. In order to extract $\rho(\omega)$ from $\Im(G^{\mathrm{ret}}(\omega + \mathrm{i}\eta))$, a deconvolution algorithm is needed.

### 4.3.2 The Least Bias Ansatz

In order to calculate the continued fraction coefficients via integration (see Sec. 4.4 on page 73), we need to close the self-consistency cycle for which non-negative and continuous spectral densities $\rho(\omega)$ without broadening are necessary. As analyzed by Raas [163], the standard tools like Fourier transform or matrix inversion do not always work properly. In Ref. [163], the *least bias*-method (LB-method) was introduced. It belongs to the maximum entropy methods[12] which assures that the extracted spectral density contains no other information than the information contained in the raw data. We therefore have to minimize the negative entropy of the spectral density given by

$$-S = \int\limits_{-\infty}^{\infty} \rho(\omega)\ln(\rho(\omega)) \tag{4.39}$$

under the constraints given by Eq. (4.38). We add every constraint (i.e. raw data) $g_i = -{}^1\!/\!_\pi \Im(G^{\mathrm{ret}}(\omega_i + \mathrm{i}\eta_i))$ with a Lagrange multiplier $\lambda_i$, calculate $\delta S = 0$ and obtain

$$\rho(\omega) \propto \exp\left[\sum_{i=0}^{p} \lambda_i L_{\eta_i}(\omega - \omega')\right] \tag{4.40}$$

---

[12] Indeed, maximum entropy methods are known for a long time. E.T. Jaynes [93] in 1957 showed the fundamental connection between information theory and statistical mechanics. This was the basis for the work of Gull and Daniell [75] in 1978 who employed this method for data analysis for the first time. However, the question what can reasonably be concluded if we have insufficient knowledge is much older and traces back to J. Bernoulli (1713) and to the seminal works of Bayes (1763) and Laplace (1812). See Ref. [188] for a review and the references therein.

as the LB-ansatz for the spectral density. This non-linear equation for $\lambda_i$ can be solved by any standard algorithm. We use the Newton method to make the deviations

$$\Delta g_i := g_i - \frac{1}{\pi} \int_{-\infty}^{\infty} \frac{\rho(\omega')}{z_i - \omega'} \mathrm{d}\omega' \tag{4.41}$$

zero (or as small as possible). Unfortunately, the solution of Eq. (4.40) is very sensitive to small errors in the raw data (see Ref. [163, p.98f.] for more details). In order to make the ansatz (4.40) robust against small errors, an improved functional of the spectral density was proposed in Ref. [163], namely

$$F\left[\rho(\omega)\right] := \int_{-\infty}^{\infty} \rho(\omega) \ln\left(\rho(\omega)\right) + A \sum_i \left(\Delta g_i\right)^2 . \tag{4.42}$$

The minimization of this functional is straight forward. The only difference between (4.40) and the corresponding ansatz deduced from (4.42) lies in the Lagrange multipliers which are now given by $\lambda_i = 2A\Delta g_i$. The set of these non-linear equations determine in this improved ansatz the Lagrange multiplier $\lambda_i$ in (4.40). This improved ansatz contains a further parameter $A$ which is a measure for the tolerance with respect to small errors. In the limit $A \to \infty$ the original spectral density is retrieved. A good choice of $A$ is a matter of experience. One has to calculate deconvolutions for many choices of $A$. Typically, there is some parameter range for $A$ where the spectral density does not change very much and does not show significant oscillations. If this range is only found for high values of $A$ (typically $A \approx 10^5$), no tolerance is needed. If the spectral density oscillates very much at low[13] ($A \approx 1 - 10$) and high ($A \approx 10^5$) values for $A$, then some moderate value for $A$ should be chosen. In the latter case, the variance of the spectral densities as a function of $A$ gives an estimate of the error introduced by the tolerance.

### 4.3.3 Checks for Deconvoluting Asymmetric Raw Data

As shown in Sec. 4.2.3, the program for the asymmetric SIAM cannot produce perfect symmetric data even if $\mu = 0$ is set and that the symmetry of the raw data for $\mu \neq 0$ is not perfect either. Since the LB-deconvolution is known to be sensitive to minor errors in the raw data, we have to assess the effect of the imperfect symmetry of the raw data. The study of this sensitivity is performed in this subsection.

To check this sensitivity, we compare $\Im G(\omega, \mu = 0)$ with $\Im G(-\omega, \mu = 0)$ and $\Im G(\omega, \mu = 0.25D)$ with $\Im G(-\omega, \mu = -0.25D)$ for $U = 1D$ and $U = 2D$. The results are shown in Fig. 4.15. In comparison to Fig. 4.11 (for $\mu = 0$) and Fig. 4.14 (for $\mu = 0.25D$) where we checked the symmetry in the raw data, we see in Fig. 4.15 that the accuracy of the deconvoluted data deteriorate by an order of magnitude (except at the band edges where only little weight is located and the LB-deconvolution is prone to produce artifacts). In comparison to the results for spoiling the symmetric raw data done in Ref. [163, p.98f.] which made it necessary to alter the ansatz of the deconvolution, the effect of asymmetry in the raw data to the deconvolution is much less drastic. Since we only lose one additional order of magnitude of accuracy, we do not make any additional change of the deconvolution scheme for asymmetric raw data.

---

[13] One may wonder why low values of $A$ leads to oscillating spectral densities since low values of $A$ imply much tolerance. Experience shows that too low values of $A$ (i.e. too much tolerance) hamper the solver to yield accurate results.

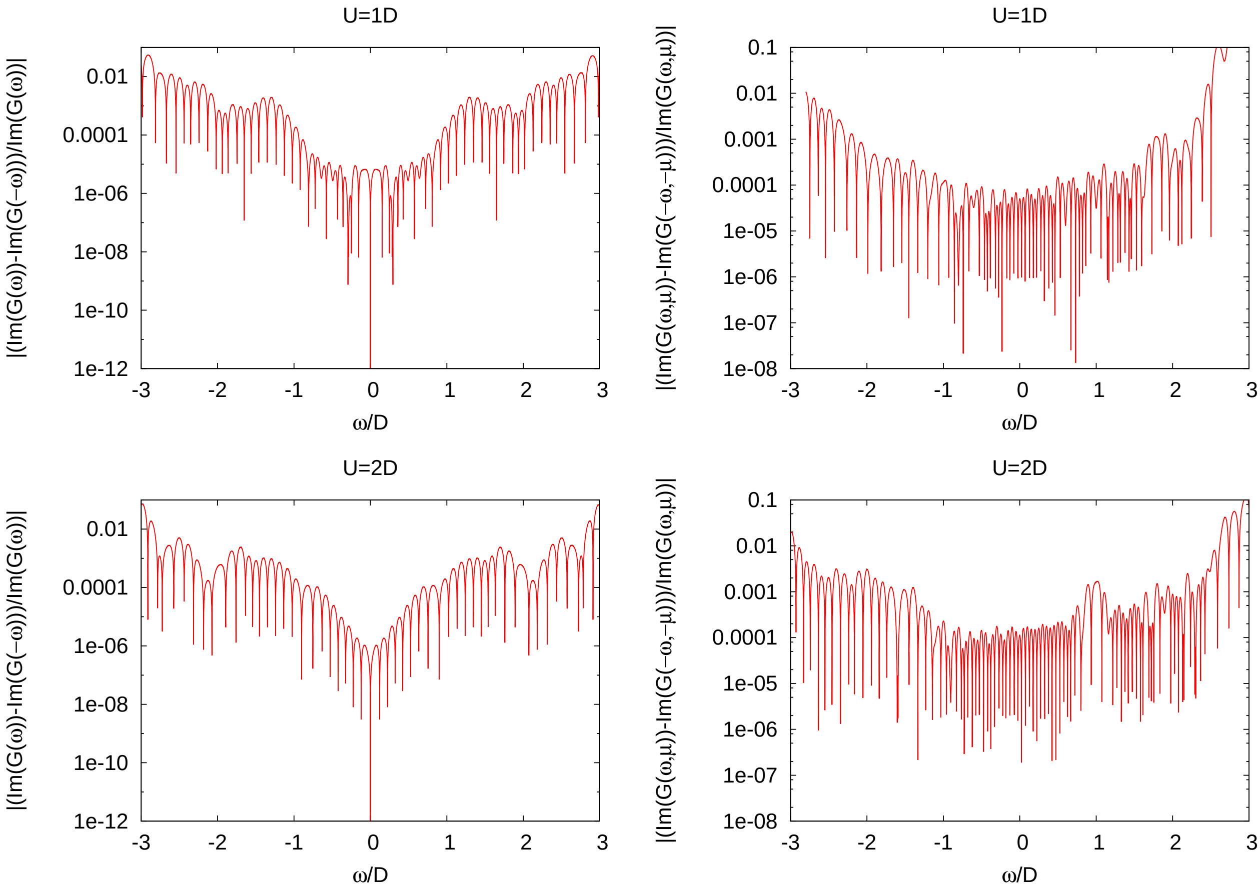

Figure 4.15: Test of the symmetry of deconvoluted data $\Im G$ for $U = 1D$ (top) and $U = 2D$ (bottom) and $\mu = 0$ (left) and $|\mu| = 0.25$ (right). Except for the band edges (where only little weight is located and the LB-deconvolution is prone to produce artifacts) the accuracy of the deconvoluted data in comparison to the raw data deteriorates by one order of magnitude.

### 4.3.4 Deconvoluting Self-Energies

The preceding discussion of the LB-Ansatz (except the analysis of asymmetric data done in Sec 4.3.3) summarized the analysis in Ref. [163]. The task in Ref. [163] was to deconvolute one-particle Green functions. In this thesis, we also want to deconvolute self-energies. Self-energies are also response functions and we calculate their raw-data with the same dynamic DMRG so that we can use the same functional (4.40) or (4.42) for deconvolution respectively. Despite those mathematical statements, there are differences between both kinds of response functions causing practical problems which we shall address here.

The Fermi-liquid property of the one-particle Green function of the Hubbard model causes the pinning of the one-particle Green function and the quadratic vanishing of the spectral density of the self-energy at $\omega = 0$. In addition, in contrast to $\rho_G$, $\rho_\Sigma$ exhibits two maxima whose heights increase significantly with increasing repulsion $U$. Note that in contrast to the one-particle Green function, which reaches zero only at the edges of the spectrum, the self-energy does so also at $\omega = 0$. By inspecting ansatz

(4.40), we see that both differences may cause numerical problems. If the spectrum becomes zero, the Lorentzians nearby must have a very large negative Lagrange multiplier. Whatever the particular value of this Lagrange multiplier is, the corresponding spectral density does not strictly vanish there. Due to this property, self-energies deconvoluted with the LB-ansatz can not strictly obey the Fermi-liquid behavior. The other numerical problem for deconvoluting self-energies is that the spikes in the spectral density of the self-energies correspond to large positive Lagrange multiplier at that position but smaller ones for the Lorentzians nearby. This can cause wiggles nearby the spikes.

In order to solve the problem of deconvoluted non-Fermi-liquid self-energies, we multiply formula (4.40) with the frequency-dependent factor

$$b(\omega) = \frac{\omega^2}{E^2 + \omega^2}. \tag{4.43}$$

The factor $b(\omega)$ is nearly constant if $|\omega| > E$ but it vanishes quadratically for $|\omega| \to 0$. This improvement leads to minor changes of the spectral density but it ensures the correct Fermi-liquid behavior for $|\omega| \to 0$. It turns out that the particular choice of $E$ does not affect the result very much. We use $E = 0.05D$ throughout this thesis. A comparison between a spectral density with and without $b(\omega)$ is shown in Fig. 4.16. It turns out that this factor $b(\omega)$ is a real improvement in a strict information-theoretic sense, i.e. it leads to a lower entropy of the spectral density. In the example shown in Fig. 4.16, this bias reduce the entropy by 0.2%. This finding suggests that the problem of non-Fermi-liquid behavior lies in the numerics of solving non-linear equations and not necessarily in the data itself.

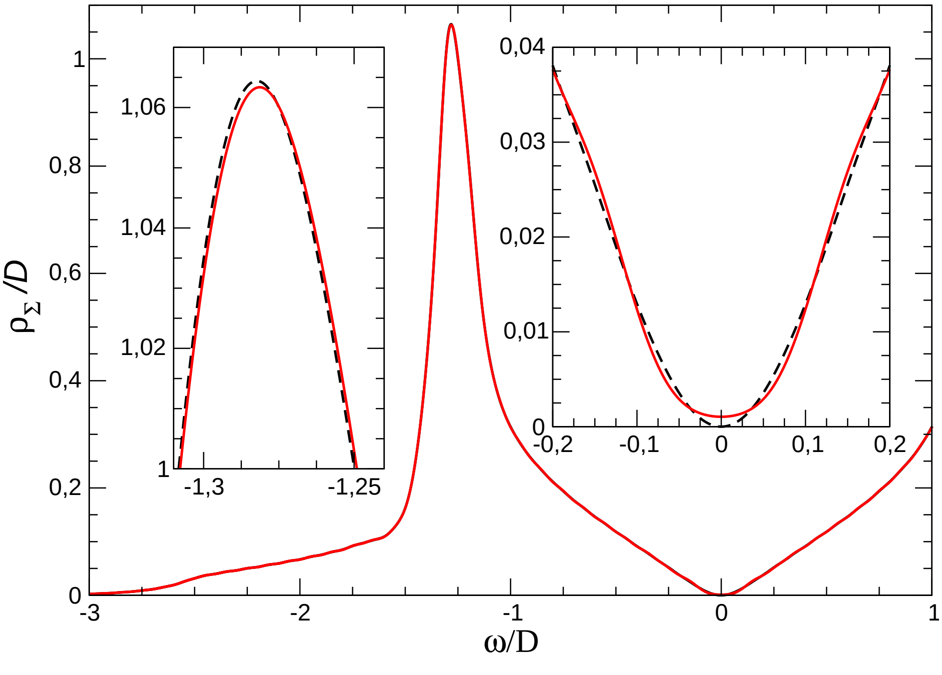

Figure 4.16: Comparison of the spectral density of the self-energy for $U = 2.0D$, 160 fermions and with $m = 128$ states in the reduced DMRG basis at a Bethe lattice. The dashed curve is the result of the improved ansatz. The insets show details of the two curves. The improved curve has the correct Fermi-liquid behavior and 0.2% lower entropy.

In contrast, no solution for the problem of deconvoluting self-energies near the metal-to-insulator transition was found. Near this transition, the height of the maxima (see Fig. 4.16 at $\omega \approx 1.25D$)

increase significantly. This impede an adequate deconvolution of the self-energy. Hence, whenever the Coulomb repulsion $U$ is too large to deconvolute the self-energy directly, we deconvolute the Green function instead of the self-energy.

## 4.4 Closing the DMFT Cycle: Extraction of the Continued Fraction Coefficients

The last step in every DMFT cycle is the extraction of the new continued fraction coefficients (CFC)[14]. The Green function and the corresponding CFCs $a_n$ and $b_n$, given in the equation

$$G(\omega) = \cfrac{b_0^2}{\omega - a_0 - \cfrac{b_1^2}{\omega - a_1 - \cfrac{b_2^2}{\omega - a_2 - \ldots}}}, \tag{4.44}$$

constitute a bijective mapping $\{a_n, b_n\} \Leftrightarrow G(\omega)$. The issue in this section is to analyze how errors on one side influence the other side of this mapping. Note that the frequencies $\omega$ used in this section are real valued. Although all formulas given in this section also work for complex valued frequencies $z = \omega + i\eta$, it turns out that the numerical extraction of the CFC for complex valued frequencies does not work. Thus, the (sometimes numerically difficult) deconvolution cannot be omitted by extracting the CFCs for complex valued frequencies[15]. By inspection of Eq. (4.44), we see that $G(\omega)$ would exhibit a finite number of poles if the number of CFCs were finite. In order to obtain a smooth $G(\omega)$, the number of CFCs must be infinite. If $G(\omega)$ has a finite support[16] $[-B + \mu, B + \mu]$, it follows (see Refs. [73, 155, 212]) that the asymptotic CFCs read

$$\begin{aligned} a_\infty &= \mu & (4.45a) \\ b_\infty &= 0.5B. & (4.45b) \end{aligned}$$

At a certain depth $m$ of the continued fraction, the coefficients have approximately the values (4.45), so that for $n > m$ the continued fraction (4.44) has a self-similar structure

$$s(\omega) = \frac{b_\infty^2}{\omega - a_\infty - s(\omega)}. \tag{4.46}$$

The solution of (4.46) reads

---

[14] In mathematics, continued fractions (CF) are an old and very rich topic since they appear in very distinctive fields of mathematics. Physicists are interested in their application, e.g. the recursion method which is used here and may find Pettifor [155] or Viswanath [212] useful for further reading. To be able to understand the mathematical literature on CFs, both books will not be sufficient. For mathematical details and theory on CFs, the reader is referred to the review of Grosso and Parravicini [73].

[15] In contrast, the other direction *is* possible: If the CFCs are known, they can be used in Eq. (4.44) by setting $\omega \to \omega + i\eta$ to obtain the Green function for any complex valued frequency $z = \omega + i\eta$ with $\omega, \eta \in \mathbb{R}$; no (numerically demanding) convolution of $\rho_G(\omega)$ is necessary.

[16] Strictly speaking, the support of a Green function in an interacting electron system is expected to be infinitely large so that in a strict sense the procedure in this section cannot be applied. However, the subset of the support where most of the spectral weight lies is finite. This has also been observed in other calculations, see e.g. Refs. [44, 105].

$$s(\omega) = \frac{1}{2}\left(\omega - a_\infty \pm \sqrt{(\omega - a_\infty)^2 - 4b_\infty^2}\right). \tag{4.47}$$

Expression (4.47) is called "square-root terminator". The correct sign is determined by the requirement that $\Im s(\omega)$ should be causal (i.e. no sign changes in $\Im s(\omega)$ occur) for all $\omega$.

The above cited convergence behavior of the CFCs is the justification for the presumption that the thermodynamic limit of the system can be described by calculating a finite system. We now turn to the extraction of the CFCs.

If (4.44) is given on a dense mesh for real frequencies $\omega$, one can extract the CFCs $a_n$ and $b_n$ with the following iteration (see Ref. [105]). We define recursive Green functions $p_i(\omega)$ by

$$p_0(\omega) := G(\omega) \tag{4.48a}$$

$$p_{n+1}(\omega) = \omega - a_n - \frac{b_n^2}{p_n(\omega)} \tag{4.48b}$$

in which the coefficients $a_n$ and $b_n$ are given by

$$b_n^2 = -\frac{1}{\pi}\int_{-\infty}^{\infty} \mathrm{d}\omega \Im p_n(\omega) \tag{4.49a}$$

$$a_n = -\frac{1}{\pi b_n^2}\int_{-\infty}^{\infty} \mathrm{d}\omega \omega \Im p_n(\omega). \tag{4.49b}$$

From (4.48) and (4.49), we see that for extracting CFCs only the basic arithmetic operations and integration are needed. With this simple observation in mind, it is generally believed that only minor numerical problems occur. To analyze this hypothesis we take the function

$$f(\omega) = -\sqrt{9 - (\omega - 0.5)^2} \tag{4.50}$$

as a test function. All CFCs of $f(\omega)$ are known analytically (see Eqs. (4.45)), i.e $a_n = 0.5\ \forall n \in [0, \infty]$ and $b_n = 1.5\ \forall n \in [1, \infty]$ ($b_0 = 4.5\pi$). We extract the CFCs via (4.48) and (4.49) (the integration is done via trapezoidal rule, the real part is obtained by Kramers-Kronig relation) and compare them with the exact results. This is shown in Fig. 4.17. We see that the accuracy of the $a_n$ is much higher than of the $b_n$, and that there is a systematic shift in the error of the $b_n$ to larger values for higher $n$. But the effect of those errors on the re-calculated test function is very small. This is shown in the upper left part of Fig. 4.20 on page 77. The relative error is of the order of $10^{-8}$ (except at the band edges of the imaginary part and $\omega = 0$ in the real part where the test function has zeros which is difficult to reproduce exactly).

The least-bias deconvolution is prone to produce wiggles. Therefore, it is useful to know the effect of wiggles on the CFCs and how well such wiggly functions can be approximated by continued fractions. To analyze this, we add $-|0.05 \sin 30\omega|$ to (4.50) within the support. Outside the support $f(\omega)$ remains unchanged. This neither changes the width $B$ nor the shift $\mu$. It is therefore reasonable to compare the CFCs with the exact CFCs of the pure test function mentioned above. The results are shown in Fig. 4.18.

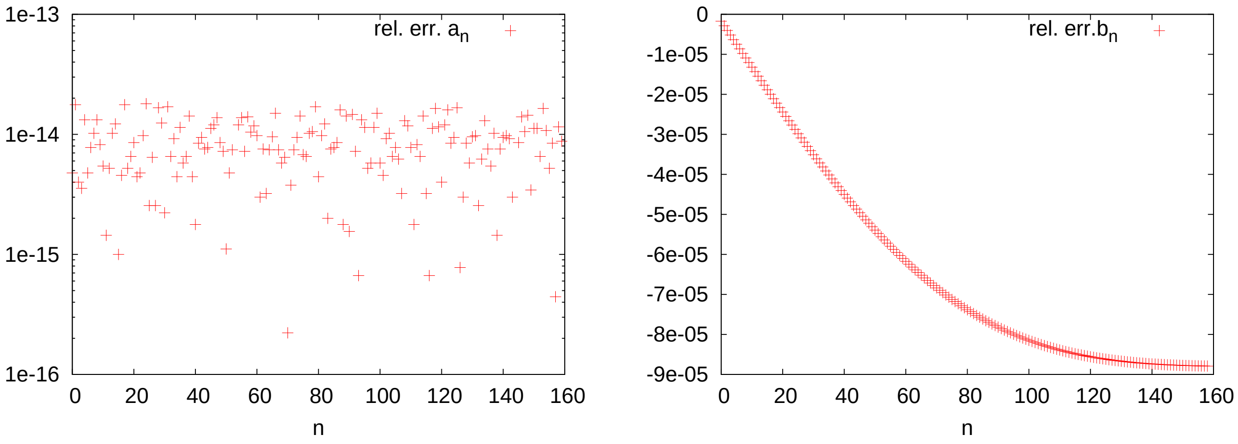

Figure 4.17: Relative error of the continued fraction coefficients $a_n$ (left) and $b_n$ (right) obtained from the pure test function (4.50). The apparent systematic error in the $b_n$ is due to the finite frequency increment $\Delta\omega = 10^{-4}$ used for the integration.

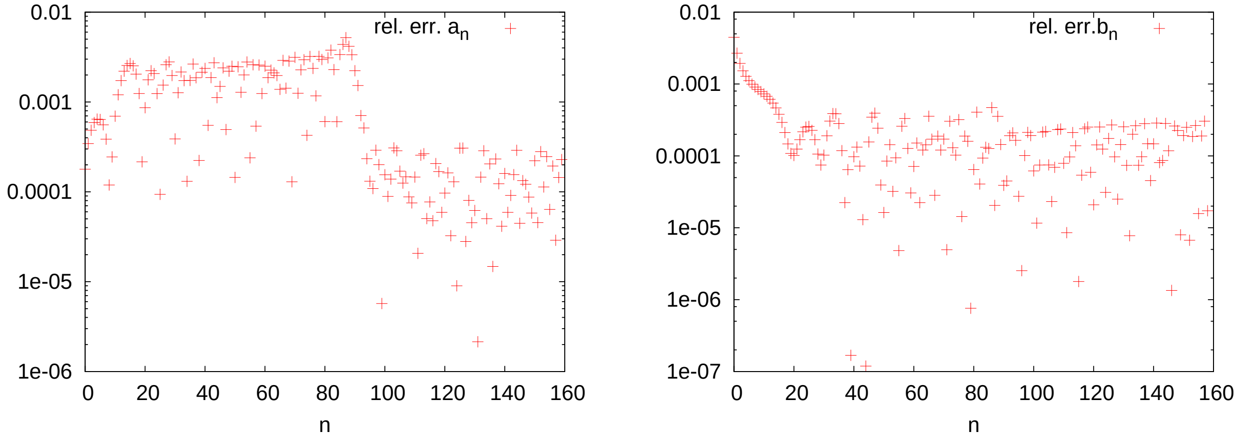

Figure 4.18: Relative error of the continued fraction coefficients $a_n$ (left) and $b_n$ (right) obtained from the test function (4.50) with wiggles $-|0.05 \sin 30\omega|$ added (only within the support). In comparison to the results shown in Fig. 4.17 it appears that the accuracy of the $a_n$ deteriorates drastically by nine order of magnitude, whereas the accuracy of the $b_n$ only deteriorates by one order of magnitude.

Those small wiggles deteriorate the accuracy of the $a_n$ in comparison to the pure test function very drastically (over nine orders of magnitude), whereas the accuracy of the $b_n$ deteriorates only by one order of magnitude. The effect of those errors on the re-calculated test function, however, is small which is shown in the upper right part of Fig. 4.20 on page 77. In comparison with the pure test function (see upper left part of Fig. 4.20), the accuracy deteriorates by one order of magnitude.

By inspection of the LB-ansatz, we see that the least-bias deconvolution is incapable to produce functions with a finite support, i.e. for high frequencies the spectral density becomes very small but not strictly zero. To mimic this here, we add $-\exp\left(-0.5(\omega-0.5)^2\right)$ to the test function (4.50) outside its original support. This changes the support but not the symmetry of the test function. Although by first inspection the pure and changed test function do not differ very much (not shown), the change in the CFCs, shown in Fig. 4.19, is drastic. Despite this drastic change, the accuracy of the re-calculated test function plus exponential outside of the support of the test function is of the same order as the re-calculated test function with a sine added. This can be seen by comparing the lower left with the upper right part of Fig. 4.20 on page 77.

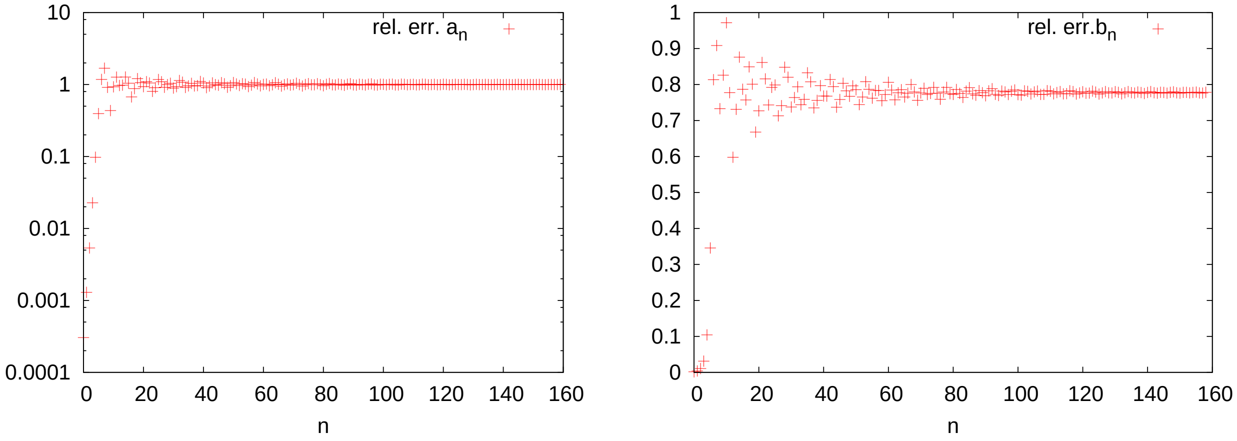

Figure 4.19: Relative error of the continued fraction coefficients $a_n$ (left) and $b_n$ (right) obtained from the test function (4.50) with an exponential $-\exp\left(-0.5(\omega-0.5)^2\right)$ added (only outside the support). This minor change has large influence on the final coefficients. They now read $a_\infty = 0$ and $b_\infty = 2$. Note that $b_\infty = 2$ is due to the chosen integration interval whose edges are determined by $|\omega| = 4$. Any other choice of the integration interval would lead to another value of $b_\infty$.

If we add the sine and the exponential to the test function, the same result for the relative error of the CFCs as the exponential alone is found (not shown). Comparing the lower left and the lower right part of Fig. 4.20, we see that the relative error of the re-calculated test function remains of the same order of magnitude.

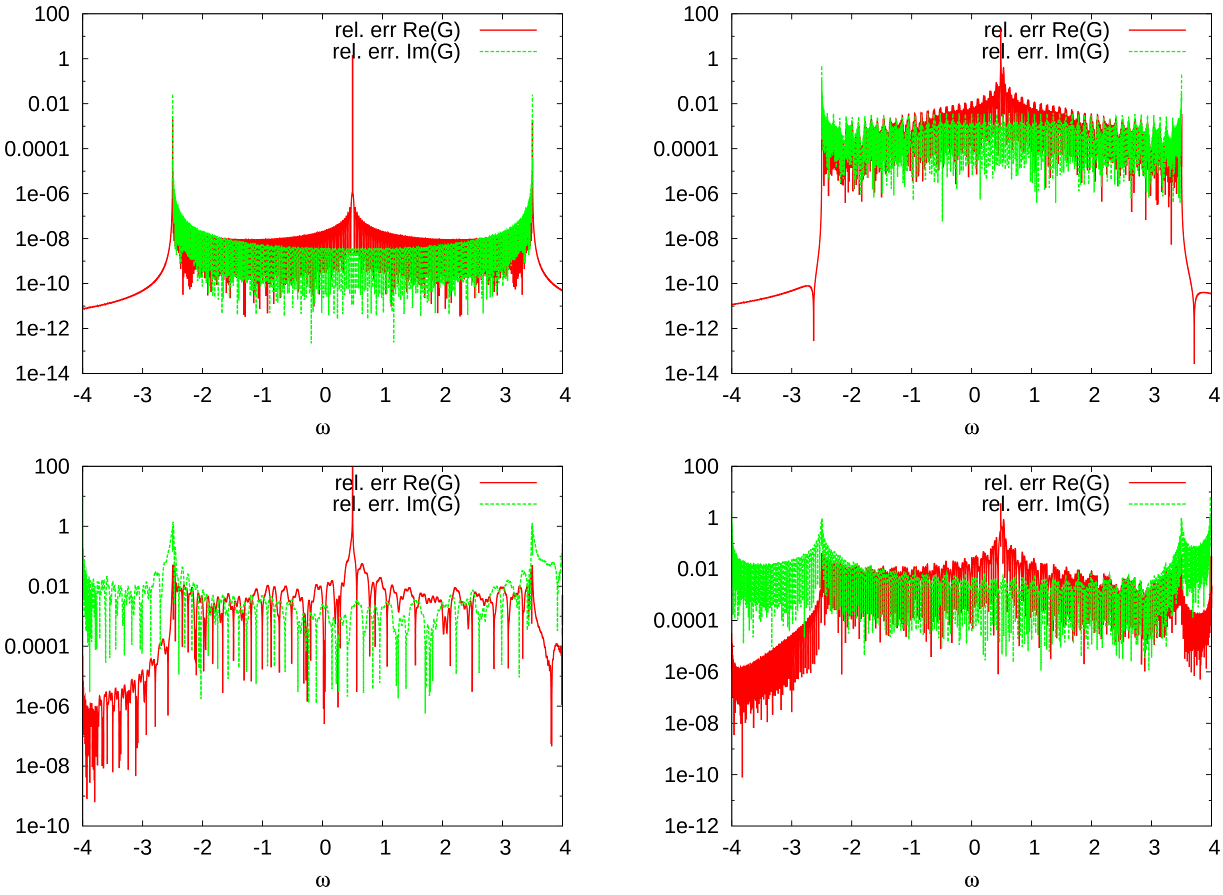

Figure 4.20: Error of the test functions obtained from the continued fraction coefficients (CFCs) relative to the corresponding test functions itself. The error shown here is gives an estimate of the sensitivity of the numerical procedure to extract the CFCs to certain imperfections. Upper left: Pure test function. Upper right: Test function with sine added. Lower left: Test function with exponential added. Lower right: Test function with exponential and sine added. For details of the additional terms see text.

The convergence of the $b_n$ is taken as a hint that the chain is large enough to mimic an infinite bath (see e.g. Ref. [105]). We therefore analyze the effects of the above mentioned disturbance sources for the test function on the $b_n$. To this end, we plot the $b_n$ as a function of the continued fraction depth $n$ which is shown in Fig. 4.21. We see that the sine induces an oscillation of the $b_n$ with an amplitude of $\approx 0.0005$, the exponential alone induces an oscillation of the $b_n$ with an amplitude of $\approx 0.005$ and the combination of both induces an oscillation with an amplitude of $\approx 0.02$. Those oscillations do *not* vanish for a higher continued fraction depth. In a realistic calculation, we would conclude from this finding that we need a larger chain because the CFCs do not seem to be converged. However, a larger chain does not necessarily lead to better spectral densities (see e.g Ref. [105]). The analysis here suggests that we have to accept such oscillations and should not automatically conclude the need for larger chains from them.

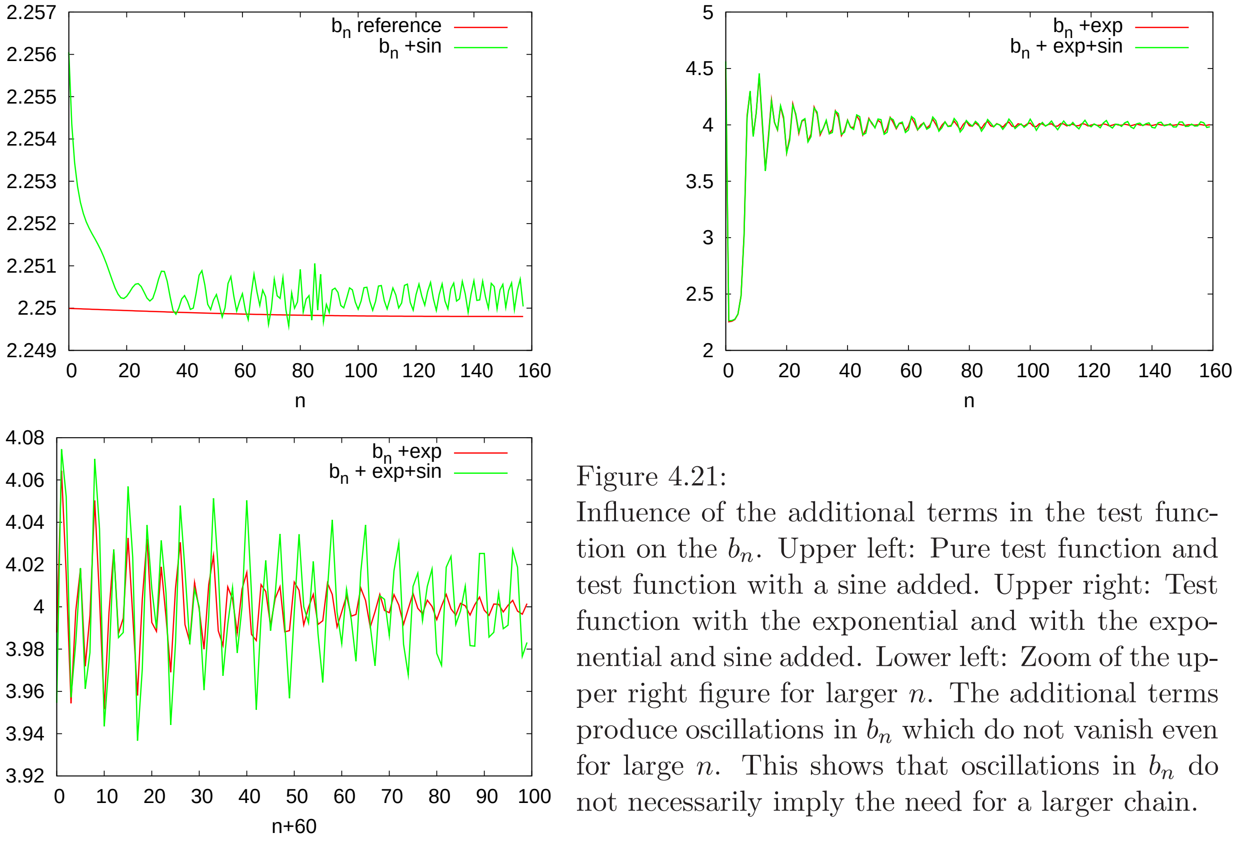

Figure 4.21:
Influence of the additional terms in the test function on the $b_n$. Upper left: Pure test function and test function with a sine added. Upper right: Test function with the exponential and with the exponential and sine added. Lower left: Zoom of the upper right figure for larger $n$. The additional terms produce oscillations in $b_n$ which do not vanish even for large $n$. This shows that oscillations in $b_n$ do not necessarily imply the need for a larger chain.

In this section, we showed how to extract the continued fraction coefficients (CFCs) from the spectral densities and analyzed the influence of small errors in the spectral density on the CFCs. The kind of errors investigated here were inspired by the deconvolution artifacts, i.e. wiggles and non-vanishing spectral densities. It was found that every minor change in the support of the spectral density changes the CFCs drastically, although the spectral density could easily be re-calculated from the CFCs. The integration interval is always symmetric around $\omega = 0$ since the DMRG raw data is, in all results presented in this thesis, symmetrically positioned around $\omega = 0$. This automatically leads to $a_\infty = 0$. The $a_n$ correspond to the magnetic field at every JW spin in the chain which is set as an external parameter. In order to keep the right $a_\infty$, we use a shifted integration interval so that the correct value for $a_\infty$ is obtained. In addition, it was found that certain minor imperfections, which appear in data deconvoluted by the LB-scheme, induce oscillations in the $b_n$ which hitherto were interpreted as a sign for a too short chain. Our finding suggests that this induction is not compelling.

# 5 Results

Contents

**5.1 Preliminaries: Spectral Densities for the Asymmetric SIAM on a Bethe Lattice . . . 80**
**5.2 Q-function for the Asymmetric SIAM on a Bethe Lattice . . . 83**
**5.3 Kinks in the Self-Energy in the DMFT Approach . . . 87**
**5.4 Dynamic Mean-Field Results for the Half-Filled Case . . . 92**
5.4.1 Results for the Semielliptic DOS . . . 92
5.4.2 Results for the Rectangular DOS . . . 97
5.4.2.1 Single Particle Green Functions for the Rectangular DOS . . . 98
5.4.2.2 Local Self-Energy for the Rectangular DOS . . . 102
5.4.2.3 Local Susceptibilities for the Rectangular DOS . . . 104
5.4.2.4 Kinks and Local Bosonic Excitations for the Rectangular DOS . . . 107
5.4.3 Results for the Triangular DOS . . . 108
5.4.3.1 Single Particle Green Functions for the triangular DOS . . . 108
5.4.3.2 Local Self-Energy for the Triangular DOS . . . 110
5.4.3.3 Local Susceptibilities for the Triangular DOS . . . 111
5.4.3.4 Kinks and Local Bosonic Excitations for the Triangular DOS . . . 113
**5.5 Dynamic Mean-Field Results away from Half-Filling . . . 114**
5.5.1 Introduction . . . 114
5.5.2 Local Spectral Densities for the Doped Metal . . . 115
5.5.3 Local Self-Energies for the Doped Metal . . . 120
5.5.4 Local Susceptibilities for the Doped Metal . . . 127
5.5.5 Kinks and Local Bosonic Excitations away from Half-Filling . . . 136

After having set up the context in the field of strongly correlated electrons in solid state physics in chapter 2 for treating especially the correlation driven metal-insulator transition via DMFT (see chapter 3) and after having described the used impurity solver D-DMRG (see chapter 4), we turn in this chapter to our results for the single-band Hubbard model. We start in Sec. 5.1 by presenting results for the SIAM embedded in a Bethe lattice (which means a semielliptic DOS) and we compare our D-DMRG results with ENCA results. In Sec. 5.2, we analyze if the Q-function (see Sec. 3.3.4 on page 29) can be applied for the SIAM away from half-filling. After these preliminary sections, we turn to the results of DMFT calculations. In Sec. 5.3, we present some general remarks on kinks in the real part of self-energies in DMFT. In Sec. 5.4, we show DMFT results for a half-filled band for the semielliptic DOS (see Sec. 5.4.1), for the rectangular DOS (see Sec. 5.4.2) and for the triangular DOS (see Sec. 5.4.3). In Sec. 5.5, we present DMFT results for the semielliptic DOS away from half-filling. For all cases, we calculated the kink positions in $\Re\Sigma$ of the self-energy $\Sigma$ and the local susceptibilities and analyze if the kinks can be linked to local internal bosonic excitations.

## 5.1 Preliminaries: Spectral Densities for the Asymmetric SIAM on a Bethe Lattice

The main focus of this thesis is the calculation of spectral densities and self-energies of metallic solutions of the Hubbard model in infinite dimensions. To this end, a self-consistency cycle (see Fig. 3.1 on page 20) with an impurity solver was implemented whose components were assessed exhaustively (see Sec. 4.2 on page 52). Before we proceed presenting results for the DMFT of the Hubbard model away from half-filling, we show results for the asymmetric SIAM for the semielliptic DOS (i.e. on a Bethe lattice). We have calculated them with a chain of 160 fermions, $m = 128$ states in the reduced basis and with a frequency increment $\Delta\omega = \eta = 0.1D$. We compare them with results obtained by ENCA (see Sec. 3.4.4 on page 36 for more details on NCA) done by Schmitt[1] [176]. Note that ENCA cannot calculate spectral densities $\rho_g$ for $T = 0$ and that ENCA calculations fail for too low temperatures. Hence, we compare our D-DMRG calculations for $T = 0$ with ENCA calculations for low temperatures. Due to the different temperatures, we do not expect exact congruence. This is shown in Fig. 5.1. For all parameters, both methods agree remarkably well.

The agreement between both methods is most remarkable for low repulsions $U = 1D$ & $U = 1.5D$ (first two rows of Fig. 5.1). For the parameters shown in the first two rows, the SIAM exhibits intermediate valency and shows large valence fluctuations which cause difficulties for ENCA calculations. Therefore, the observed differences between both methods seen in the first two rows is larger than for higher repulsions. But a qualitative agreement, e.g. position of the bands, is still achieved.

For larger repulsion $U$ (remaining rows in Fig. 5.1), the SIAM enters the strong coupling regime. ENCA was originally introduced for this regime. Hence, compared to lower repulsions we expect a better agreement between both methods. This expectation is fulfilled. However, the degree of agreement (for $\omega < 0$ we see nearly exact congruence) has not been expected to be found.

There are two other consistency checks of the D-DMRG data for the SIAM:

- The filling. Static DMRG calculation should yield the same result as formula (4.34) on page 67 where the filling $n$ is obtained by integration of $\rho_g$ over the negative real $\omega-$axis. In addition, the filling $n$ can be obtained from the sum rule of the self-energy (3.53) shown on page 31. The filling obtained from those three methods should yield the same numerical value.
- The pinning criterion.

The latter requirement needs further comments which we cite from Uhrig [205]:

Let us remember the Dyson Eq. (3.5) for the SIAM

$$\frac{1}{g} = \frac{1}{g_0} - \sigma \tag{5.1}$$

with the single-particle Green function $g$, the bath Green function $g_0$ and the self-energy $\sigma$. In addition, we need the equation for the bath Green function

$$\frac{1}{g_0} = \omega + \mathrm{i}\eta + \mu - \Gamma(z) \tag{5.2}$$

with $z := \omega + \mathrm{i}\eta$ and the hybridization function $\Gamma(z)$ which reads

---

[1] S. Schmitt implemented ENCA for his PhD-thesis [174].

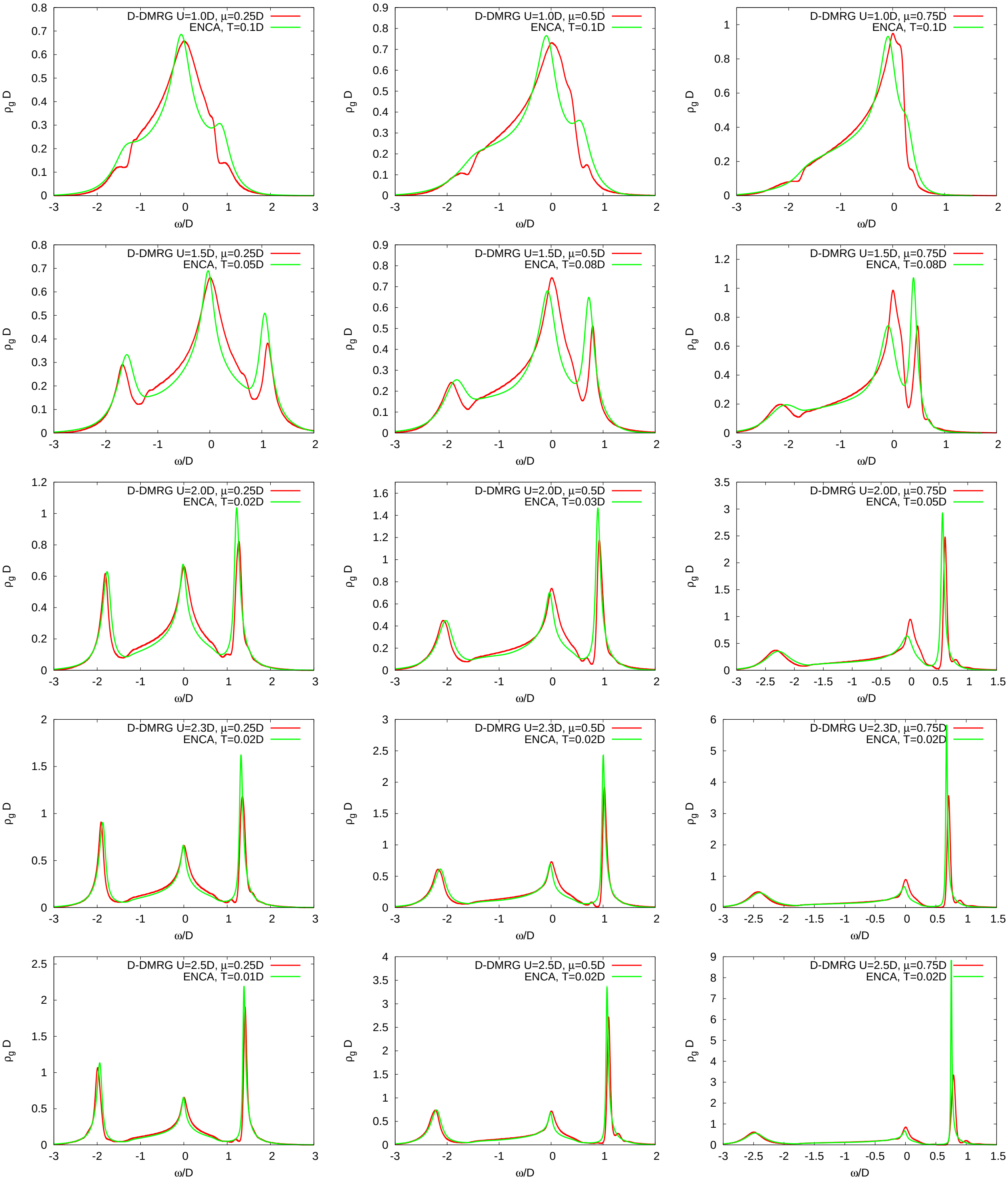

Figure 5.1: Comparison of $\rho_g$ for the semielliptic DOS obtained via D-DMRG (red) and ENCA (green) done by Schmitt [176] for $U = 1D$ (first row), $U = 1.5D$ (second row), $U = 2.0D$ (third row), $U = 2.3D$ (fourth row) and $U = 2.5D$ (fifth row) and $\mu = 0.25D$ (first column), $\mu = 0.5D$ (second column) and $\mu = 0.75D$ (third column). Note that ENCA does not work for $T = 0$. Both methods show remarkably good agreement. For further discussion, see text.

$$\Gamma(z) = \frac{D^2}{4} g(z) \tag{5.3}$$

for a semielliptic DOS (see Eq. (3.13) on page 21). This implies that the inverse Green function reads

$$\frac{1}{g} = \omega + \mathrm{i}\eta + \mu - \Gamma(z) - \sigma(z). \tag{5.4}$$

For further calculation, we expand the Green function

$$g = \frac{1}{g^{-1}} = \frac{\left(g^{-1}\right)^*}{g^{-1}\left(g^{-1}\right)^*} = \frac{1}{|g^{-1}|^2}\left(\Re\left(g^{-1}\right) - \mathrm{i}\Im\left(g^{-1}\right)\right). \tag{5.5}$$

For $\eta = 0$, it follows from Eq. (5.4) that

$$\Im\left(g^{-1}\right) = -\Im\left(\Gamma + \sigma\right) \tag{5.6}$$

and with formula (5.5) we can write the imaginary part of $g$ as

$$\Im g = -\frac{\Im\left(g^{-1}\right)}{|g^{-1}|^2} = \underbrace{\left|\frac{\Im\left(g^{-1}\right)}{|g^{-1}|}\right|^2}_{\leq 1} \frac{1}{-\Im\left(g^{-1}\right)} = \left|\frac{\Im\left(g^{-1}\right)}{|g^{-1}|}\right|^2 \frac{1}{-\Im\left(\Gamma + \sigma\right)}. \tag{5.7}$$

Since the prefactor is less or equal to unity[2], we can derive the following upper bound

$$|\Im g| \leq \frac{1}{|\Im\left(\Gamma + \sigma\right)|} \leq \frac{1}{|\Im\Gamma|} \overset{(5.3)}{=} \frac{4}{D^2}\frac{1}{|\Im g_0|}. \tag{5.8}$$

For $\omega = 0$, $\Im\sigma$ vanishes due to the Fermi-liquid property. Then, the equality holds in (5.8) and it serves as the pinning criterion for $\Im g(\omega = 0)$. The results for the filling and the pinning criterion for the asymmetric SIAM are shown in table 5.1.

In this section, we have compared the results of $\rho_g$ for the asymmetric SIAM obtained via D-DMRG and ENCA. Both methods are in remarkable good agreement. In addition, we compared the filling obtained via static DMRG and via $\rho_g$ and $\rho_\sigma$. For lower Coulomb repulsion, $n_\sigma$ yields a better agreement with $n_{\text{static}}$ than $n_g$. But for larger Coulomb repulsion and $\mu = 0.75D$, $n_g$ yields a better agreement with $n_{\text{static}}$. We further checked the pinning criterion which we derived in this section for the asymmetric SIAM. For $U \leq 1.5D$, the difference between exact and the calculated value is below 2%. For larger values of $U$, the error rises up to a maximum of 14% (for $U = 2.5D$ and $\mu = 0.75D$).

As a conclusion we state that the program works well and yields reasonable results for $\rho_g$ and $\rho_\sigma$ if $g$ is the excitation operator of D-DMRG. Hence, we can use the program for the Hubbard model in infinite dimensions away from half-filling.

---

[2] For every complex number $c = a + \mathrm{i}b$ with $a, b \in \mathbb{R}$, the inequality $|\Im c| = |b| \leq \sqrt{a^2 + b^2} = |c|$ holds.

| $U = 1D$ | | | | | |
|---|---|---|---|---|---|
| $\mu/D$ | $n_{\text{static}}$ | $n_g$ | $n_\sigma$ | $\text{pin}_g$ | $\text{pin}_{\text{ex}}$ |
| 0.25 | 0.572 | 0.571 | 0.571 | 2.064 | 2.066 |
| 0.50 | 0.650 | 0.647 | 0.650 | 2.295 | 2.309 |
| 0.75 | 0.743 | 0.747 | 0.742 | 2.978 | 3.024 |

| $U = 1.5D$ | | | | | |
|---|---|---|---|---|---|
| $\mu/D$ | $n_{\text{static}}$ | $n_g$ | $n_\sigma$ | $\text{pin}_g$ | $\text{pin}_{\text{ex}}$ |
| 0.25 | 0.549 | 0.548 | 0.548 | 2.074 | 2.066 |
| 0.50 | 0.601 | 0.597 | 0.600 | 2.323 | 2.309 |
| 0.75 | 0.658 | 0.661 | 0.655 | 3.087 | 3.024 |

| $U = 2D$ | | | | | |
|---|---|---|---|---|---|
| $\mu/D$ | $n_{\text{static}}$ | $n_g$ | $n_\sigma$ | $\text{pin}_g$ | $\text{pin}_{\text{ex}}$ |
| 0.25 | 0.534 | 0.533 | 0.534 | 2.078 | 2.066 |
| 0.50 | 0.570 | 0.566 | 0.568 | 2.312 | 2.309 |
| 0.75 | 0.604 | 0.608 | 0.598 | 2.971 | 3.024 |

| $U = 2.3D$ | | | | | |
|---|---|---|---|---|---|
| $\mu/D$ | $n_{\text{static}}$ | $n_g$ | $n_\sigma$ | $\text{pin}_g$ | $\text{pin}_{\text{ex}}$ |
| 0.25 | 0.528 | 0.527 | 0.528 | 2.070 | 2.066 |
| 0.50 | 0.556 | 0.553 | 0.554 | 2.282 | 2.309 |
| 0.75 | 0.582 | 0.587 | 0.575 | 2.805 | 3.024 |

| $U = 2.5D$ | | | | | |
|---|---|---|---|---|---|
| $\mu/D$ | $n_{\text{static}}$ | $n_g$ | $n_\sigma$ | $\text{pin}_g$ | $\text{pin}_{\text{ex}}$ |
| 0.25 | 0.525 | 0.524 | 0.526 | 2.056 | 2.066 |
| 0.50 | 0.549 | 0.546 | 0.547 | 2.244 | 2.309 |
| 0.75 | 0.571 | 0.576 | 0.561 | 2.660 | 3.024 |

Table 5.1: Comparison of the filling $n$ for the corresponding Coulomb repulsion $U$ and chemical potential $\mu$ obtained by static DMRG, via $\rho_g$ ($n_g = \int_{-\infty}^{0} \rho_g(\omega)\mathrm{d}\omega$) and via $\rho_\sigma$ ($U^2 n_\sigma (1 - n_\sigma) = \int_{-\infty}^{\infty} \rho_\sigma(\omega)\mathrm{d}\omega$). The fifth column shows the value of $\text{pin}_g := \Im g(\omega = 0)$. The last column ($\text{pin}_{\text{ex}}$) shows the exact value $\text{pin}_g$ should have according to (5.8) in which the equality holds for $\omega = 0$.

## 5.2 Q-function for the Asymmetric SIAM on a Bethe Lattice

In Sec. 3.3.4 on page 29, we introduced the Q-function by which it is possible to calculate the self-energy directly. Faßbender in his diploma thesis [47] already applied the Q-function for the symmetric SIAM. Several routes from Q-function raw data to deconvoluted spectral densities were mentioned there, i.e.

$$Q(z) \xrightarrow{\text{dec}} Q(\omega) \longrightarrow \sigma(\omega) \longrightarrow g(\omega) \tag{5.9a}$$

$$Q(z) \longrightarrow \sigma(z) \xrightarrow{\text{dec}} \sigma(\omega) \longrightarrow g(\omega) \tag{5.9b}$$

$$Q(z) \longrightarrow g(z) \xrightarrow{\text{dec}} g(\omega) \longrightarrow \sigma(\omega) \tag{5.9c}$$

("dec" names the step where the deconvolution takes place, see Sec. 4.3 on page 68), and it turns out that route (5.9b) is the best one. In the present thesis, we employ the Q-function with several routes in a whole DMFT cycle for the Hubbard model at half-filling. It turns out that route (5.9a) is the most unstable one and route (5.9b) the most stable one which is consistent with the results of Faßbender. However, as was already mentioned in Sec. 4.3.4 on page 71, the shape of the self-energy (i.e. their peaks that tend to infinity in the proximity of the Mott-transition) makes it impossible to employ the Q-function in a DMFT framework for such high Coulomb repulsions. Already the analysis of Faßbender [47] revealed that using the Q-function leads only to minor improvements for larger repulsions $U$ compared to the direct calculation of $\rho_g$ so it is not a major drawback if we cannot use the Q-function for higher Coulomb repulsion.

In this section, we use the Q-function for the asymmetric SIAM and assess whether or not it can be used for calculating self-energies. We use a chain with 160 fermions, $m = 128$ states in the reduced basis, a frequency increment $\Delta\omega = \eta = 0.1D$ and the deconvolution without tolerance. We begin the analysis by calculating the Q-function for $U = 0$ where we can compare the results with the exact solution (see Eq. (3.54) on page 31) given in Ref. [145]. This is shown in Fig. 5.2 where a good agreement between the exact and the DMRG results is seen. With those spectral densities, we can use the sum rule (3.52) given on page 31 to compare the filling $n$ with the exact filling. This is shown in table 5.2 where we see a good agreement. In addition, we can check the symmetry of the Q-function. Inspecting Eq. (3.54), it appears that $\rho_Q(\omega, \mu) = \rho_Q(-\omega, -\mu)$. A comparison between both (for $\mu = 0.5D$), including the relative difference between them, is shown in Fig. 5.3. In comparison with the symmetry test for $g$ (not shown), the accuracy is approximately the same.

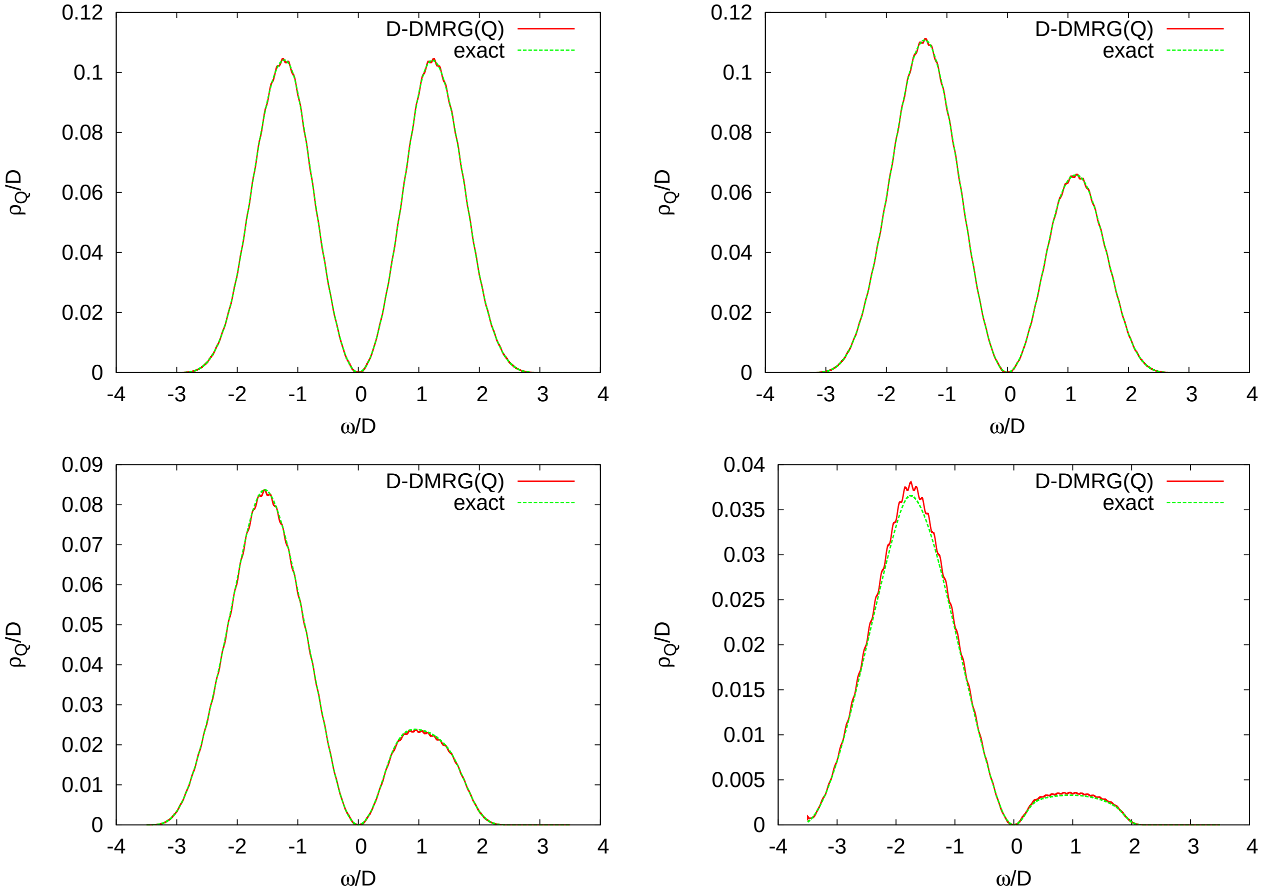

Figure 5.2: Spectral densities of the Q-function $\rho_Q(\omega)$ for $U = 0$ and $\mu = 0$ (upper left), $\mu = 0.25D$ (upper right), $\mu = 0.5D$ (lower left) and $\mu = 0.75D$ (lower right) obtained via D-DMRG and by Eq. (3.54) on page 31. Exact and D-DMRG results show good agreement.

For $U \neq 0$, we do not have exact solutions to which we can compare our results. However, the results of Sec. 5.1 on page 80 prompt us to assume that the D-DMRG program produces reliable spectral densities $\rho_g$. Hence, we can compare the self-energies obtained from the Green functions and Dyson equation with the self-energies obtained from the Q-functions, i.e we compare the routes

$$\text{D-DMRG(G)} \longrightarrow g(z) \longrightarrow \sigma(z) \xrightarrow{\text{dec}} \sigma(\omega) \longrightarrow g(\omega) \tag{5.10a}$$

$$\text{D-DMRG(Q)} \longrightarrow Q(z) \longrightarrow \sigma(z) \xrightarrow{\text{dec}} \sigma(\omega) \longrightarrow g(\omega) \tag{5.10b}$$

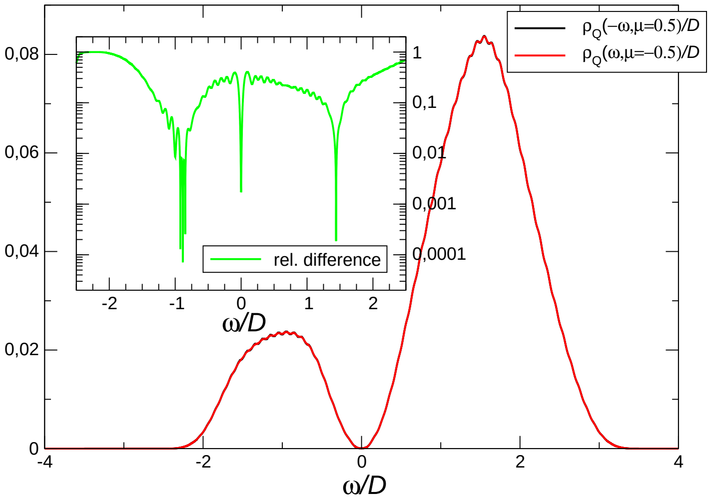

Figure 5.3:
Comparison between $\rho_Q(\omega, \mu = 0.5D)$ and $\rho_Q(-\omega, \mu = -0.5D)$. The inset shows the relative difference between them. The accuracy of the symmetry is approximately the same as for the Green function $g$ (not shown).

Table 5.2:
Comparison of the filling $n$ for $U = 0$ obtained via the exact Q-function (see Eq. (3.54) for $\rho_Q$ and (3.52) for $n$, both on page 31) and the Q-function calculated via D-DMRG with 160 fermions and $m = 128$ states in the reduced density-matrix for the shift $\mu$ of the semiellipse. The absolute relative error shows a good agreement.

| $U = 0$ | $n_{\text{exact}}$ | $n_{\text{D-DMRG(Q)}}$ | $\lvert\Delta n\rvert / n_{\text{exact}}$ |
|---|---|---|---|
| $\mu = 0.00$ | 0.5 | 0.5 | 0 |
| $\mu = 0.25D$ | 0.6575 | 0.6581 | 0.001 |
| $\mu = 0.50D$ | 0.8045 | 0.8061 | 0.002 |
| $\mu = 0.75D$ | 0.9279 | 0.9254 | 0.003 |

with each other. With the notation “D-DMRG(X)”, we mean that a D-DMRG calculation is done with the excitation operator X. We trust $\rho_g$ obtained by (5.10a) because we already compared the results of this route with another method (see Sec. 5.1). In the following, we therefore use (5.10a) as the reference for comparing D-DMRG(Q) with D-DMRG(G). From this comparison, we can assess the quality of the self-energies that we obtain from the Q-function. First, we check if $\mu = 0$ lead to the results Faßbender [47] obtained already. This is the case (not shown) for all values of $U$ under consideration. In contrast to this good agreement for $\mu = 0$, the results for $\mu \neq 0$ show differences. In particular, for $U \geq 1D$ and finite $\mu$ the spectral densities of the self-energy $\rho_\sigma(\omega)$ obtained via the different routes (5.10a) and (5.10b) show considerable differences. This is shown in Fig. 5.4 where we also show the corresponding spectral densities $\rho_g$ of the Green function. In Tab. 5.2, we compared the filling $n$ for $U = 0$ obtained exactly via Eq. (3.54) with the results from the Q-function calculated by D-DMRG. For $U \neq 0$, we do not have exact solutions to check our results but we can compare the filling obtained by static DMRG with the filling obtained by the sum rule for $\sigma$ (see Eq. 3.53 on page 31) and with the filling obtained via the Green function $g$ (see Eq. (4.34) on page 67). This is shown in table 5.3 for $\mu = 0.5D$ and $U = 1.0D, 1.5D$ and $2.0D$.

From the results of Tab. 5.3 and Fig. 5.4, one may suggest that there is a bug in the program. Although checked very carefully, such a bug was not found. If it is a bug, it is a very subtle one because several consistency conditions are met. The raw data of the Q-function is causal and obeys the symmetry $\Im Q(\omega{+}\mathrm{i}\eta, \mu) = \Im Q(-\omega{+}\mathrm{i}\eta, -\mu)$ (not shown) and it leads for $\mu = 0$ to deconvoluted results that are consistent with Faßbender [47] (not shown). As mentioned above, the program yields the correct results for $U = 0$ which is quite remarkable if there is a bug in the program. In addition, and this is even more remarkable, $\rho_\sigma$ for $U \neq 0$ obeys its sum rule (see Eq. (3.53) on page 31) for both routes (5.10) although $\rho_\sigma$ (see Fig. 5.4) differs considerably for the different routes of calculation. The

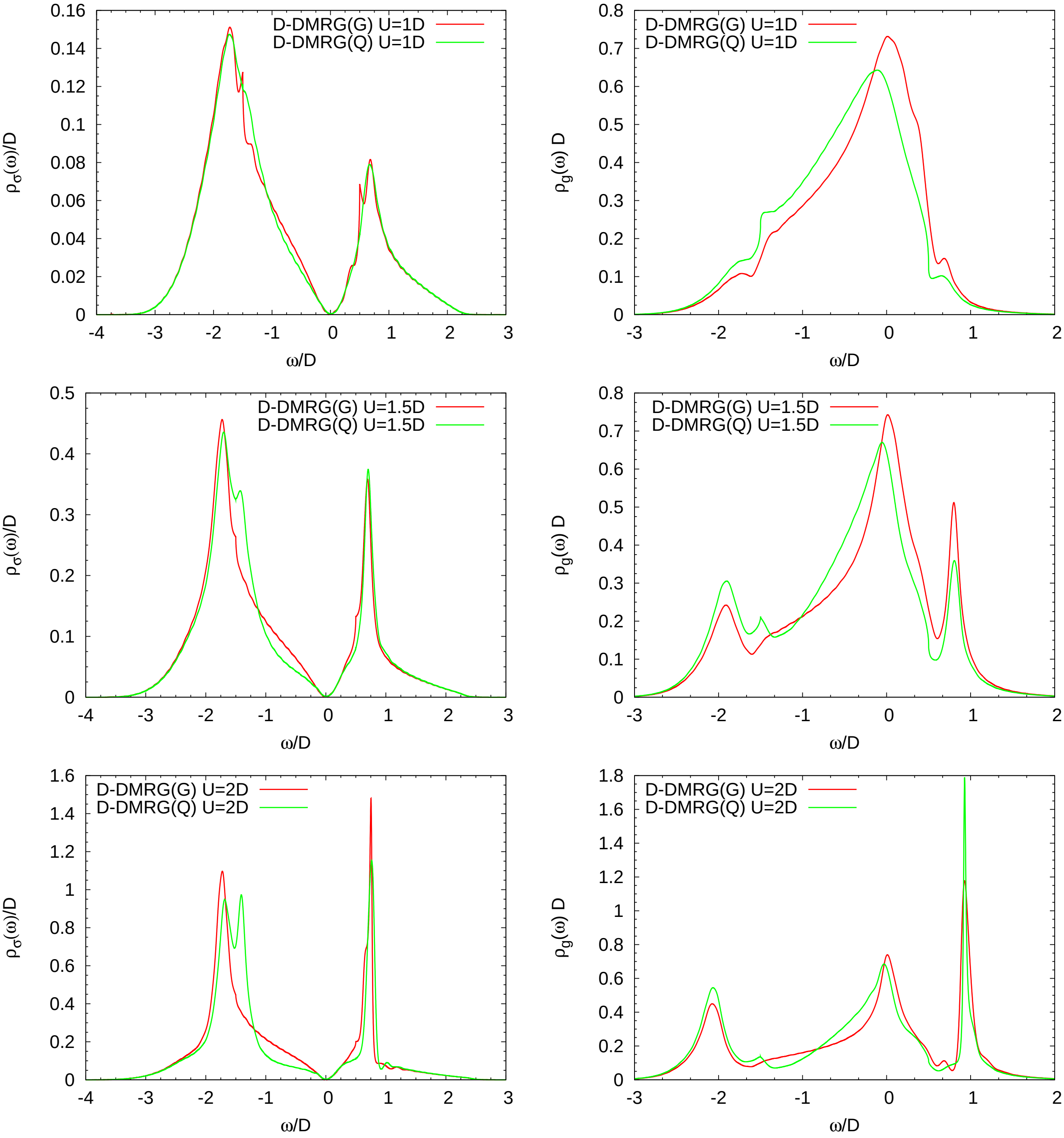

Figure 5.4: Comparison of spectral densities obtained via D-DMRG(G) (red curves) and D-DMRG(Q) (green curves) of $\rho_\sigma$ (left column) and of $\rho_g$ (right column) for $\mu = 0.5D$ and $U = 1D$ (upper row), $U = 1.5D$ (middle row) and $U = 2.0D$ (lower row). For discussion see text.

| $U = D$ | | | |
|---|---|---|---|
| | D-DMRG(G) | D-DMRG(Q) | static |
| $\sigma$ | 0.650 | 0.650 | 0.651 |
| $g$ | 0.647 | 0.753 | |
| $U = 1.5D$ | | | |
| | D-DMRG(G) | D-DMRG(Q) | static |
| $\sigma$ | 0.601 | 0.601 | 0.601 |
| $g$ | 0.597 | 0.700 | |
| $U = 2D$ | | | |
| | D-DMRG(G) | D-DMRG(Q) | static |
| $\sigma$ | 0.569 | 0.569 | 0.570 |
| $g$ | 0.566 | 0.648 | |

Table 5.3:
Comparison of the filling $n$ obtained via D-DMRG(G) and D-DMRG(Q) (see Eqs. (5.10)) calculated from $\sigma$ or $g$ or from static DMRG for $\mu = 0.5D$ and $U = 1D$ (upper table), $U = 1.5D$ (middle table) and $U = 2.0D$ (lower table). For all values of $U$, the sum rule for $\Sigma$ obtained by D-DMRG(Q) and D-DMRG(G) yields approximately the result of the static DMRG (although $\rho_\sigma$ itself differs for the corresponding calculations; see left part of Fig. 5.4). The sum rule for $g$ yields approximately the result of the static DMRG calculation only for D-DMRG(G) whereas significant differences occur for D-DMRG(Q).

differences for $\rho_g$ are also very distinct. The different weight of the upper and lower band and the different shape and weight of the Kondo resonance can clearly be seen in Fig. 5.4. The filling obtained from $\rho_g$ differs considerably from the static DMRG calculation if D-DMRG(Q) is used but the filling $n$ obtained from $\rho_g$ is consistent with the static calculation if D-DMRG(G) is used.

The results of this section imply that the Q-function cannot be used for the asymmetric SIAM and hence not for DMFT calculations away from half-filling although the reason for this finding remains unclear.

## 5.3 Kinks in the Self-Energy in the DMFT Approach

In this section, we first summarize the findings by Byczuk et al. [31] in 2007 who analyzed kinks in the self-energy in the DMFT approach. Afterwards, we present our complementary ideas about kinks in the self-energy in the DMFT approach. We close with a discussion.

The analysis in Ref. [31] starts with the equation of the DMFT approach

$$\Sigma(\omega) = \omega + \mu - \frac{1}{G(\omega)} - \Gamma(\omega) \tag{5.11}$$

where $\Sigma(\omega)$ represents the self-energy at the real frequency $\omega$, $\mu$ the chemical potential, $G$ the full one particle Green function and $\Gamma$ the hybridization function. In the following, the most important assumption is that the spectral density $\rho_G := -{}^{1}\!/_{\pi}\Im G(\omega)$ exhibits a three-peak-structure with minima at $\omega = \Omega_\pm$, the Kondo peak at $\omega = 0$ and Hubbard bands for $\omega > \Omega_+ > 0$ and $\omega < \Omega_- < 0$. For the symmetric case ($\mu = 0$), the equation $|\Omega_+| = |\Omega_-|$ holds. This setup is the basis for the following argument. Byczuk et al. [31] consider the first part of the right-hand side of Eq. (5.11), i.e. the complex function $\omega - 1/G(\omega)$ (the constant shift $\mu$ is omitted). If there are minima and maxima in $\Im G$, then there are maxima and minima in $-\Im G$. The maxima at $\Omega_\pm$ of the latter term imply (by Kramers-Kronig) zeros in $\omega - \Re(1/G)$ near $\Omega_\pm$. Since $\omega - \Re(1/G)$ is not constant within this interval, we conclude that there exist a minimum and a maximum inside of $[-\Omega_-, \Omega_+]$. Since no other minima/maxima exist within this interval, we infer that $\omega - \Re(1/G)$ is monotonous there and approximate it by a linear function. Now, we turn back to $\Re\Gamma$ (the remaining term in Eq. (5.11)) and see that it is also linear, but within a smaller range than $\omega - \Re(1/G)$. Thus it appears that $\Re\Sigma$ has kinks in $[-\Omega_-, \Omega_+]$. The smart thing in this deduction is that it uses only mathematical arguments; no further physical ingredient is needed.

Byczuk et al. [31] calculated the position of the kinks by using the linearity of $1/G$ up to the first order, i.e. $1/G = z_0 + z_1\omega + O(\omega^2)$. By setting $z_0 := (-\omega_0 + i\gamma)/Z_{\text{CP}}$ and $z_1 := (1 + i\gamma')/Z_{\text{CP}}$ they write the Green function as

$$G(\omega) = \frac{Z_{\text{CP}}}{\omega - \omega_0 + \mathrm{i}(\gamma + \gamma'\omega)} \tag{5.12}$$

with $Z_{\text{CP}}$ being the weight of the central peak of $\Im G$. For a symmetric $\Im G$, $\omega_0 = \gamma' = 0$ holds. From a technically deduction (omitted here) it follows that the kinks can be found at the points of maximum curvature of $\Re G$, i.e. by solving $\partial^3 \Re G/(\partial\omega)^3 = 0$. This leads to a fourth-order polynomial whose solutions are given by

$$\omega_{\text{kink 1}} = \omega_0 - \frac{\gamma + \gamma'\omega_0}{\sqrt{1+\gamma'^2}} \left(1 + \sqrt{2}\sqrt{1 - \frac{\gamma'}{\sqrt{1+\gamma'^2}}}\right) \tag{5.13a}$$

$$\omega_{\text{kink 2}} = \omega_0 - \frac{\gamma + \gamma'\omega_0}{\sqrt{1+\gamma'^2}} \left(1 - \sqrt{2}\sqrt{1 - \frac{\gamma'}{\sqrt{1+\gamma'^2}}}\right) \tag{5.13b}$$

$$\omega_{\text{kink 3}} = \omega_0 + \frac{\gamma + \gamma'\omega_0}{\sqrt{1+\gamma'^2}} \left(1 - \sqrt{2}\sqrt{1 + \frac{\gamma'}{\sqrt{1+\gamma'^2}}}\right) \tag{5.13c}$$

$$\omega_{\text{kink 4}} = \omega_0 + \frac{\gamma + \gamma'\omega_0}{\sqrt{1+\gamma'^2}} \left(1 + \sqrt{2}\sqrt{1 + \frac{\gamma'}{\sqrt{1+\gamma'^2}}}\right). \tag{5.13d}$$

Only solutions[3] (5.13b) and (5.13c) correspond to maxima of the curvature of $\Re G$. For the symmetric case, the relevant solutions (5.13b) and (5.13c) reduce to[4]

$$\omega_{\text{kink}} = \pm(\sqrt{2} - 1) Z_{\text{QP}} D \tag{5.14}$$

if we identify (see supplement of Ref. [31] for details) $Z_{\text{QP}} D := \gamma$ ($Z_{\text{QP}}$ is the quasi-particle weight and $D$ is the bandwidth).

The authors of Ref. [31] intended to establish a new mechanism for the appearance of kinks in the real part of the self-energy. We discussed in Sec. 2.1.3 on page 11 that kinks in $\Re\Sigma$, i.e. abrupt changes of the energy shift of the quasi-particle, may indicate the presence of an excitation coupled with the quasi-particle. The physical origin of this presumed excitation is not revealed by the discovery of a kink. By the above presented deduction, Byczuk et al. [31] wish to show that the kinks in $\Re\Sigma$ are a generic feature for strongly correlated electron systems but that the kinks “are not related to any coupling of excitations” (see abstract of Ref. [31]). This statement is imprecise. Of course, the fermionic Hubbard model (3.1) does not comprise any explicit bosonic mode and Byczuk et al. [31] showed that

---

[3] Note that the solutions (5.13) differ from the solutions in the supplement of Ref. [31] by some sign permutations. The solutions (5.13) were checked very carefully and are the correct ones.

[4] The erroneous solution of $\partial^3 \Re G/(\partial\omega)^3 = 0$ presented in the supplement of Ref. [31] reduce to the same solution in the symmetric case.

we do not have to add an *external* bosonic mode to the Hubbard model. However, the presence of *internal* bosonic modes (e.g. spin-, charge- or Cooper-pair excitations) of the electrons themselves is not excluded by the deduction of Byczuk et al. In particular, the basis of the above derivation is the assumption of the three-peak-structured spectral density which of course has a physical basis which may or may not comprise internal bosonic excitations. One main aim of this thesis is to analyze what kind (if any) of collective modes are present and whether or not they can be related to the occurrence of kinks in the real part of the self-energy.

The reasoning behind the hypothesis that internal bosonic modes may be present is the following [165]: A linear behavior of the real part of the self-energy around $\omega = 0$ leads, due to Kramers-Kronig relations, to a quadratic behavior of the imaginary part of the self-energy around $\omega = 0$. In addition, the imaginary part of the self-energy vanishes quadratically at $|\omega| \to 0$ due to the Fermi-liquid property. The imaginary part of the self-energy (see Sec. 2.1.3 on page 11) determines the life time of the quasi-particle. Both parts of the self-energy depend on each other. Hence, it is worthwhile to investigate what effect a kink in the real part of the self-energy in the proximity of $\omega = 0$ has on the imaginary part of the self-energy. To this end, we analyze the test-function

$$f(\omega) = \frac{(a|\omega - c| - b|\omega + c|) - g\omega}{\left(e^{h(\omega - r)} + 1\right)\left(e^{-h(\omega + r)} + 1\right)}. \tag{5.15}$$

$f(\omega)$ exhibits a single zero at $\omega = \omega_0$. We consider $f(\overline{\omega}) := f(\omega - \omega_0)$ so that the zero of $f(\overline{\omega})$ is fixed at $\overline{\omega} = 0$. The test-function $f(\overline{\omega})$ serves as a toy real part of a self-energy. By inspection (see Fig. 5.5), we see that $f(\overline{\omega})$ is linear for $\overline{\omega} \in [-c - \omega_0, c - \omega_0]$ and exhibits kinks for $\overline{\omega}_- = -c - \omega_0$ and $\overline{\omega}_+ = c - \omega_0$. Outside this interval, $f(\overline{\omega})$ is linear with another slope determined by the parameter $g$. The denominator assures that $f(\overline{\omega})$ vanishes for $|\overline{\omega}| \to \infty$ (this property is needed for the Kramers-Kronig relations) without changing the kinks very much. To assure the latter, the parameter $r$ has to be chosen such that $r \gg c$. The parameter $h$ controls how fast $f(\overline{\omega})$ decays to zero. For $a = b$, we obtain an anti-symmetric function with $\omega_0 = 0$ by which we can mimic the half-filled case. For other choices, an asymmetric function occurs by which we mimic the case away from half-filling. For simplicity, we set for the symmetric case $a = b = c = 0.5g = 0.2r = 0.1h = 1$ and for the asymmetric case we only change $b = 0.25$ (which leads to $\omega_0 \approx 0.223$). With this choice, we set the physically relevant energy scale of this toy real part. In particular, the former Kondo-regime $[\Omega_-, \Omega_+]$ is located inside the interval $[-r - \omega_0, r - \omega_0]$. This is shown in Fig. 5.6. The Kramers-Kronig relations ensure a quadratic behavior in the vicinity of $\overline{\omega} = 0$ but the minimum is not located at $y = 0$ so we shifted the imaginary part (the shift is $\beta \approx 9.6878$ for the symmetric case and $\beta \approx 8.47437$ for the asymmetric case). From Fig. 5.6, we clearly see that the kinks in the real part lead to a trough-like feature of the imaginary part. If we fit a parabola to the minimum (the parameters are $0.91841\overline{\omega}^2$ for the symmetric case and $0.6445\overline{\omega}^2$ in the asymmetric case), we see that the imaginary part is larger in the vicinity of the kinks. The difference is marked with colored shading. We see that the shaded area is the larger the more pronounced the corresponding kink is.

Of course, one can call into question if the Fermi-liquid parabola is valid for such large energy $\omega$ and if hence a comparison is reasonable. This is ensured by the parameter $r$, i.e. the range where the Kondo resonance is located and $1/G$ can be approximated by a line (see. Eq. (5.12)). As Byczuk et al. [31] showed, the Kondo resonance introduces a new relevant energy scale $[\Omega_-, \Omega_+]$ where the real part of the self-energy is well approximated by a linear function. For the Kondo resonance, the quasi-particle weight is a relevant physical quantity which is given by the slope of $\Re\Sigma(\omega = 0)$. As shown, such a linear behavior leads (due to Kramers-Kronig relations) to a parabolic behavior of $\Im\Sigma(|\omega| \approx 0)$. Hence, if $[\Omega_-, \Omega_+]$ is said to be the relevant energy scale for the Kondo resonance which is mainly

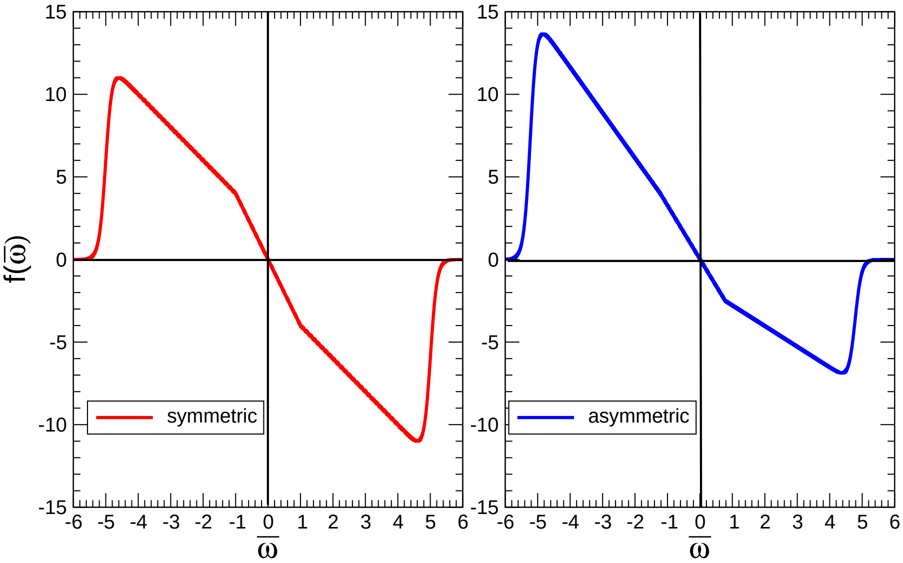

Figure 5.5:
Examples of the test-function $f(\overline{\omega})$ for the symmetric case (left) and the asymmetric case (right). For the symmetric case, we chose $a = b = c = 0.5g = 0.2r = 0.1h = 1$ (which leads to $\omega_0 = 0$). For the asymmetric case, only parameter $b$ was altered and set to $b = 0.25$ (which leads to $\omega_0 \approx 0.223$).

determined by the quasi-particle weight and if it is reasonable to connect the kinks in the real part of the self-energy at $\omega_\pm$ to the quasi-particle at $\omega = 0$, it is also reasonable to compare the Fermi-liquid parabola with the imaginary part of the self-energy within the same energy range. As the shaded area in Fig. 5.6 shows, there is a difference between the parabola and the self-energy. Physically this difference implies that the decay rate of the quasi-particle is enhanced. This reduction may be due to a new decay channel. Fluctuations are the typical suspects for this channel and the only relevant fluctuations in a local approach are *spin-*, *charge-* and *Cooper-pair-fluctuations*. For concrete results on that issue, see Sec 5.4 on page 92 for the half-filled case and Sec. 5.5 on page 114 for away from half-filling.

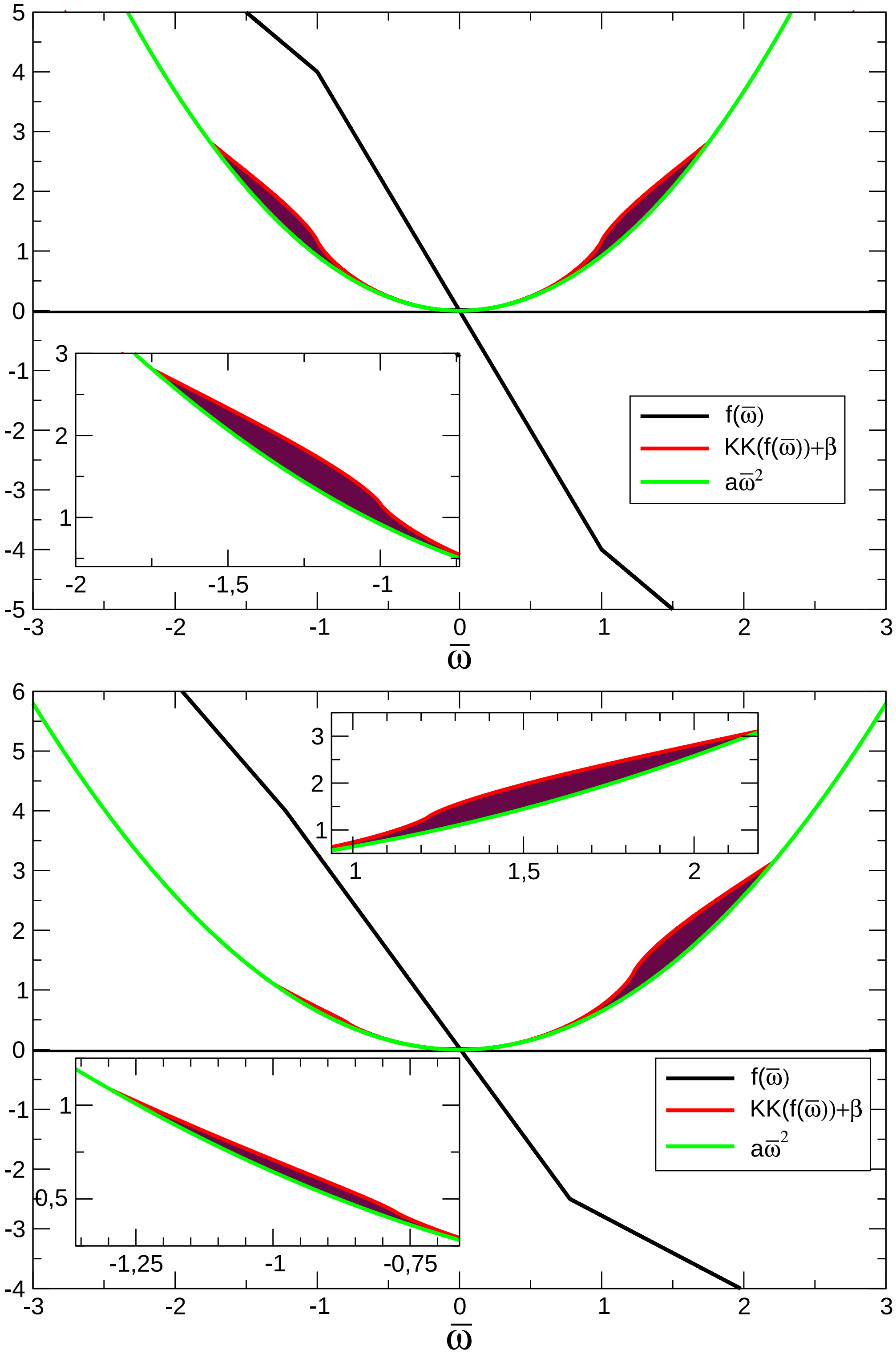

Figure 5.6: Imaginary part if $f(\overline{\omega})$ is set as the real part (for parameters see text). Kinks in the real part correspond to troughs in the imaginary part. Physically, the change of the imaginary part (compared to the Fermi-liquid parabola) leads to change of the quasi-particle life time which hints to a new decay channel of the quasi-particle. For the asymmetric case, the more pronounced kink at positive $\overline{\omega}$ causes the more pronounced change for positive $\overline{\omega}$ indicated by the shaded area (the other shaded area for negative $\overline{\omega}$ is only visible in the zoomed inset).

## 5.4 Dynamic Mean-Field Results for the Half-Filled Case

In this section, we present dynamic quantities such as the spectral density $\rho_G$ of the local single-particle Green function $G$, the local self-energy $\Sigma$, the local spin susceptibility $\chi_{\text{spin}}$ and charge susceptibility $\chi_{\text{charge}}$ which are obtained for a single-band Hubbard model in infinite dimensions. We use three different DOSs, namely the semielliptic (see Sec. 5.4.1), the rectangular (see Sec. 5.4.2 on page 97) and the triangular (see Sec. 5.4.3 on page 108) one.

### 5.4.1 Results for the Semielliptic DOS

In this section, we present DMFT results of local dynamic quantities of the Hubbard model with the semielliptic DOS at half-filling. We omit the analysis of $\rho_G$ and the susceptibilities because they were obtained with the same program and are already published and exhaustively discussed in Refs. [103, 104, 105, 163, 164]. Therefore, we restrict our analysis here to the self-energy for the correlated metal. First, we focus on applying the Q-function (see Sec. 3.3.4 on page 29) to directly calculate the self-energy in DMFT. Second, we present an analysis of the kinks in the real part of the self-energy and show how they are connected to internal bosonic excitations (see Sec. 5.3 on page 87).

In his diploma thesis, Faßbender [47] describes several routes from Q-function raw data to spectral densities $\rho_G$ (see. Eqs. (5.9) on page 83) and found that route (5.9b) is the best one. We apply this route for DMFT and compare the corresponding $\Sigma$ and $G$ with the ones obtained by D-DMRG(G) (see route (5.10a)). For this purpose, we use a chain of 160 fermions, $m = 128$ states in the reduced basis and a frequency increment of $\Delta\omega = \eta = 0.1D$. Generic examples are shown in Fig. 5.7.

In Fig. 5.7, we see that the Green functions do not differ very much; only minor differences can be seen in the insets. In the left column of Fig. 5.7, we see that using the Q-function assures causal self-energies, i.e. the imaginary part of the self-energies is negative or vanishes. In contrast, route (5.10a) yields sign changes or other numerical artifacts at $\omega \approx 0$. The property $\Im\Sigma(\omega \to 0) \to 0$ for route (5.10b) is ensured by the modified deconvolution[5] described in Sec. 4.3.4 on page 71. The kinks in the real part are a little bit more pronounced if D-DMRG(Q) is used although the slope at $\omega = 0$ (which determines the quasi-particle weight) is approximately the same. However, for Coulomb repulsion $U \geq 2.0D$ the self-energies cannot be extracted with good quality as has already been mentioned in Sec. 4.3.4 on page 71. As an example for the generic problems, we show a comparison between DMFT(D-DMRG(Q)) and DMFT(D-DMRG(G)) for $U = 2.2D$ in Fig. 5.8. We see that for increasing repulsion $U$ the wiggles in the FL-regime become more pronounced. This leads to wiggles in the Kondo peak as well. In addition, the sharp feature at the inner side of the Hubbard bands change in size and weight and it is followed by spurious wiggles (which are already visible for $U = 2D$ in Fig. 5.7). All those features change from one self-consistency cycle to the next. Hence, we interpret them as numerical artifacts. In addition, we do not obtain a stable solution of the self-consistency cycle. Thus, for $U \geq 2.0D$ we have to use route (5.10a) to extract the self-energy.

Now, we turn to the analysis of the kinks (troughs) of the real (imaginary) part of self-energy near $\omega = 0$. In Fig. 5.9, some self-energies with insets zoomed on the kinks/troughs are depicted.

In Fig. 5.9, we can clearly see the correspondence between troughs in the imaginary part of the self-energy and the kinks in the real part which we explained in Sec. 5.3 on page 87 for a test-function. In order to extract the kink positions systematically, we use

---

[5] Note that the modified deconvolution described in Sec. 4.3.4 on page 71 only ensures that $\Sigma(\omega \to 0) \to 0$. Even without modified deconvolution, the causality of $\Im\Sigma$ is always fulfilled for route (5.10b). In contrast, route (5.10a) could lead to sign changes in $\Im\Sigma$ (see insets in the left parts of Figs. 5.7 and 5.8).

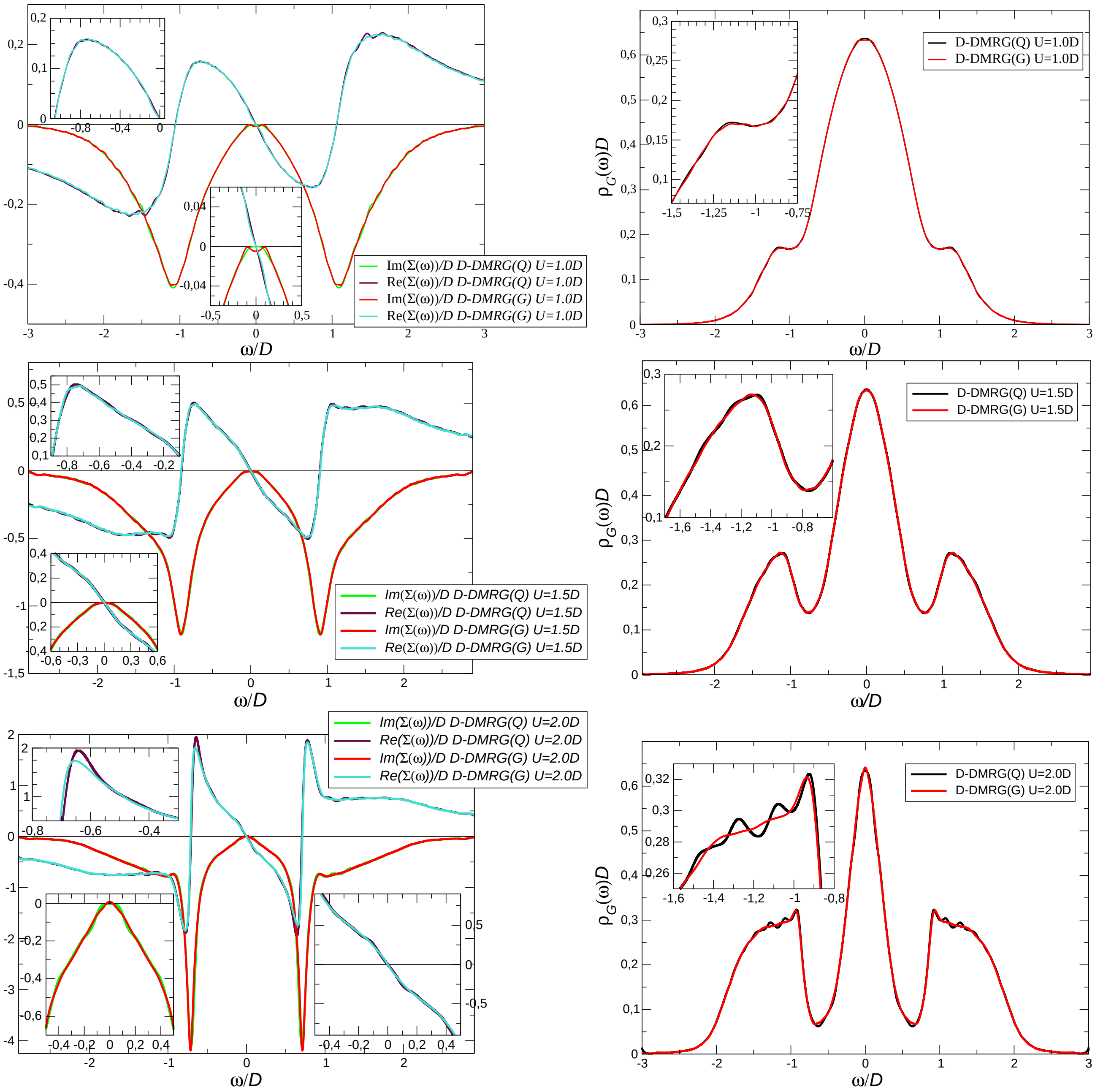

Figure 5.7: Comparison of D-DMRG(G) with D-DMRG(Q) for $U = 1D$ (upper row), $U = 1.5D$ (middle row) and $U = 2D$ (lower row). The complex self-energies $\Sigma$ are shown in the left part and the spectral densities $\rho_G$ are shown in the right part of the figure. For low $U$ (two upper rows), only minor differences between both methods can be seen but the kinks in $\Re\Sigma$ are more pronounced. In addition, $\Im\Sigma$ is always causal if D-DMRG(Q) is used. For $U = 2D$, spurious wiggles occur near the sharp feature at the inner side of the Hubbard bands but we still obtain a stable solution in the self-consistency cycles to extract the kinks in $\Re\Sigma$. In addition, the weight of this feature does not change whether D-DMRG(Q) or D-DMRG(G) is used.

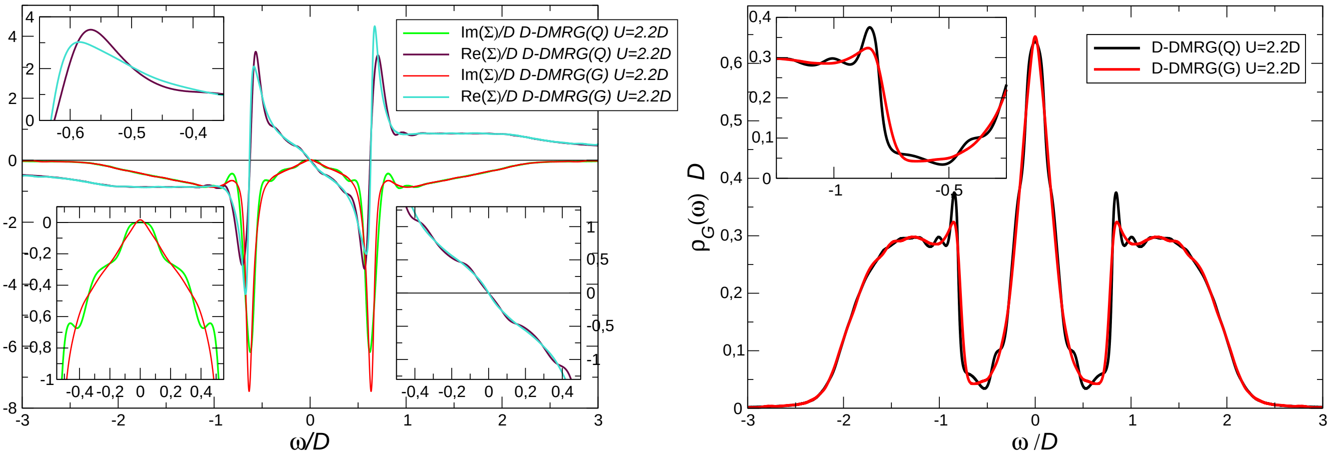

Figure 5.8: Left: Comparison of the self-energy $\Sigma$ (real and imaginary part) obtained by D-DMRG(Q) (maroon is the real part and green is the imaginary part) and D-DMRG(G) (turquoise is the real part and red is the imaginary part). Right: Comparison of the spectral density $\rho_G$ for $U = 2.2D$ obtained by D-DMRG(Q) (black) and D-DMRG(G) (red). Both methods yield considerable differences: The sharp features at the inner side of the Hubbard bands differ in size. If D-DMRG(Q) is used, the imaginary part of the self-energy shows spurious wiggles for $\omega \in [-0.5D, 0.5D]$. Those wiggles in the imaginary part also lead, due to Kramers-Kronig relations, to wiggles in the real part of the self-energy there.

$$f(\omega) = \frac{1}{2}a\left(|\omega - b| - |\omega + b|\right) - c\omega \tag{5.16}$$

for a non-linear least-square fit of the real part of the self-energy for the corresponding frequency range. In the right inset of the upper panel of Fig. 5.9, we show such a fit for $U = 2.0D$. The calculated fit parameters read $a = 1.13366$, $b = 0.104753D$ and $c = 1.44054$. In Sec. 5.3, we argued that the trough should be compared with the FL parabola in order to interpret the trough as a change of the quasi-particle life time. We illustrate this hypothesis with Fig. 5.10 where we show the trough for $U = 2D$. In addition, we show two different fits. The first fit is for the trough only and the second fit is for a wider range. A priori, both the fit for the narrower and for the wider frequency range are consistent with FL theory. We see that the trough cannot be fitted by a $\propto \omega^2$-term alone. We need a large $\propto \omega^4$-term for an adequate fit. Within a FL framework, we have problems to argue for such a huge quartic term. Instead, we assume that FL theory can be applied to a larger range. With this view, we can intuitively understand the troughs as the hint to a new decay channel. Note that in the latter view and the corresponding fit, the quartic term is much smaller and can hence be seen as a plausible higher order term in the FL theory.

Within a DMFT framework, only local spin-, charge- and Cooper-pair-fluctuations are relevant. For the model under consideration, they have been calculated by D-DMRG by Raas and Uhrig [164]. Among them, spin-fluctuations $\chi_{\text{spin}}$ are the only ones with considerable peaks in the corresponding energy range. Some of them, taken from Ref. [164], are shown in Fig. 5.11. Note that in Fig. 5.11 we only show $\chi^{>}_{\text{spin}}$ and not $\chi_{\text{spin}} = \chi^{>}_{\text{spin}} + \chi^{<}_{\text{spin}}$. It turns out here, that adding the other part of $\chi_{\text{spin}}$ does not change the position of the maxima very much. Note that the full susceptibility $\chi_{\text{spin}}$ exactly obeys $\chi_{\text{spin}}(\omega = 0) = 0$. In addition $\chi^{>}_{\text{spin}}(\omega = 0) = \chi^{<}_{\text{spin}}(\omega = 0) = 0$ holds either. The fulfillment of those conditions gives an estimate of the quality of the data. If we showed the full $\chi_{\text{spin}}$, we would

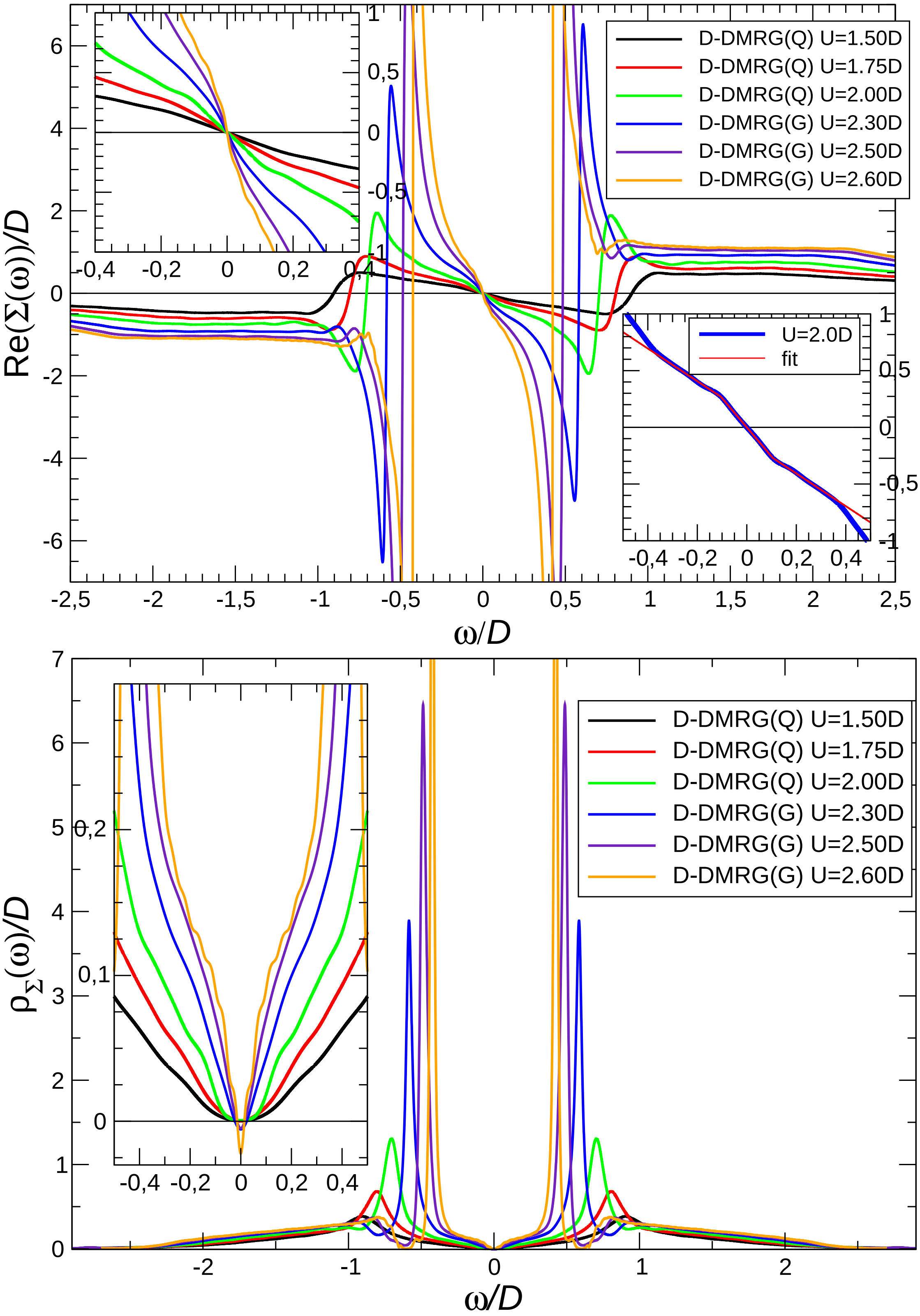

Figure 5.9: Real (upper panel) and imaginary (lower panel) part of the self-energy $\Sigma$ obtained by D-DMRG(Q) or D-DMRG(G) (see legends). In the left insets, the kinks (troughs) in the real (imaginary) parts are depicted. The right inset in the upper panel shows a fit with function (5.16) to obtain the kink positions. The corresponding fit parameters read $a = 1.13366$, $b = 0.104753D$ and $c = 1.44054$.

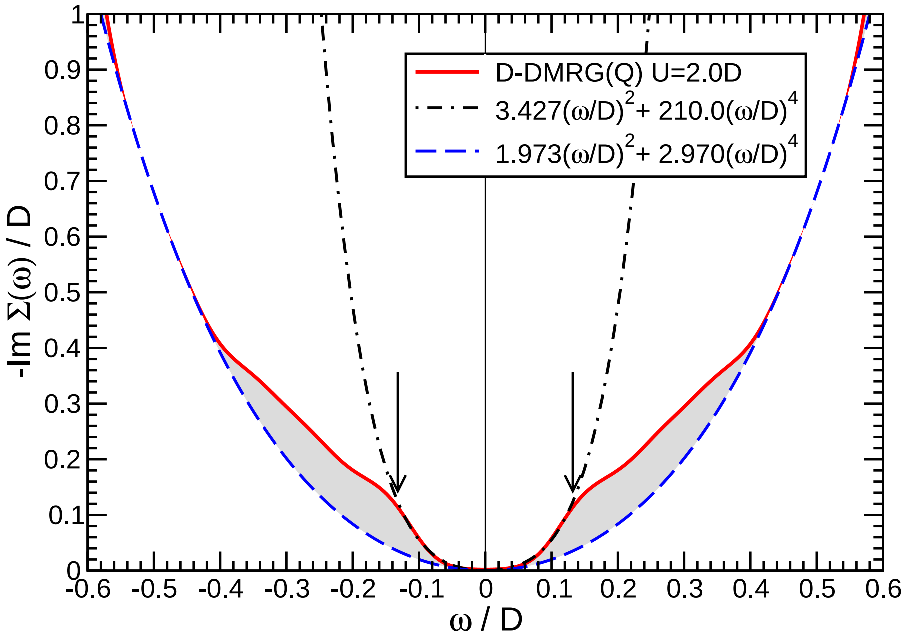

Figure 5.10: Imaginary part of the self-energy $\Sigma$ for $U = 2D$ obtained by D-DMRG(Q) (red) and two fits. The dashed blue curve is a parabolic fit with a moderate quartic term for the wider $\omega$-range $[-0.5D, 0.5D]$ and the dashed-dotted line is a fit for a narrower $\omega$-range. In contrast to the wider $\omega$-range fit, it is not possible to fit a pure quadratic (FL) parabola to $\Im\Sigma$ in the narrower $\omega$-range $[-0.1D, 0.1D]$ (note the huge quartic term in that fit). If we apply FL theory to the larger $\omega$-range, we can interpret the trough feature in the imaginary part, which directly corresponds to the kinks in the real part, as a change of the life time of the quasi-particle (see shaded area) which we connect to spin-fluctuations as internal bosonic modes (see Fig. 5.12).

always fulfill $\chi_{\text{spin}}(\omega = 0) = 0$ because of the anti-symmetry of $\chi^{>}_{\text{spin}}$ and $\chi^{<}_{\text{spin}}$. This would pretend a quality of the data, the method is unable to give. We see that $\chi^{>}_{\text{spin}}(\omega = 0) \neq 0$ and its deviation from zero gives an estimate of the quality of the data.

We extract the position of the peaks in $\chi^{>}_{\text{spin}}$ and show them in Fig. 5.12 together with the position of the kinks (extracted via fitting with (5.16)) as a function of the repulsion $U$. In addition, we use formula (5.14) to calculate the position of the kinks from the quasi-particle weight $Z$ which we also show in Fig. 5.12. Note that this formula relies on the validity of the assumption that the inverse Green function is approximately a linear function (see Eq. (5.12) on page 88) within the range of the Kondo peak [31] by which a new relevant energy scale is introduced.

As we have already explained at the end of Sec. 5.3, the linear behavior in this energy range is another argument for comparing the imaginary part of the self-energy with a parabola in that wider range (in contrast to the narrower range which we show as the dashed-dotted line in Fig. 5.10). In Fig. 5.12, we see that the spin excitation maxima and the kink positions coincide within the error bars. Hence, we deduce that the additional decay channel seen in Fig. 5.10 results from the excitation of the spin resonance by the propagating single fermion quasi-particle. The additional decay channel seen as the trough in $\Im\Sigma(\omega \approx 0)$ leads, due to Kramers-Kronig relations, to kinks in $\Re\Sigma$. The coincidence of the kink and spin excitation maxima positions seen in Fig. 5.12 strongly supports our claim that the

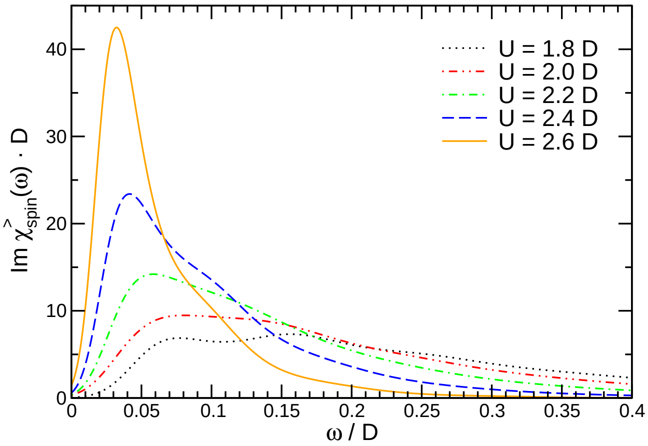

Figure 5.11:
Some generic spin-susceptibilities for several Coulomb repulsions $U$ taken from Ref. [164] published by Raas and Uhrig. We see an increasing excitation maximum which we compare with the position of the kinks in the real part of $\Sigma$, see Fig. 5.12.

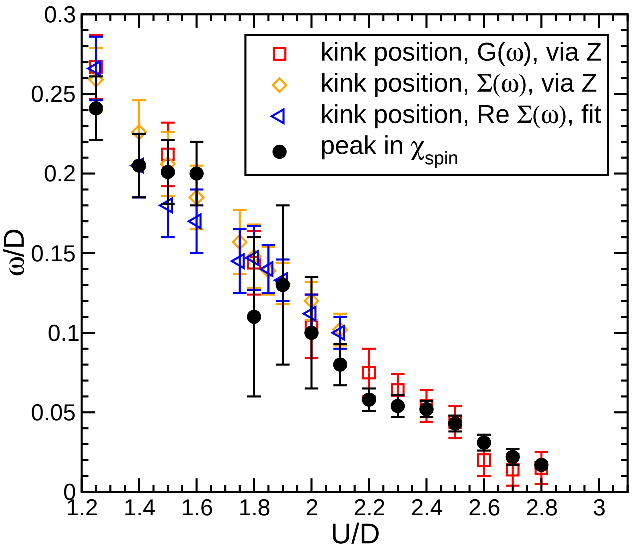

Figure 5.12:
Comparison of the kink positions obtained via the quasi-particle weight $Z$ and formula (5.14). The quasi-particle weight $Z$ is obtained from the first derivative of the Green function (red squares), i.e. by $Z^{-1} = D^2/2\partial G(0)/\partial\omega$ [104, 105], and the slope of $\Re\Sigma(\omega = 0)$ (orange diamonds), i.e. by $Z^{-1} = 1 - \partial/\partial\omega\Re\Sigma(0)$. The blue triangles show the kink positions obtained from a fit of $\Re\Sigma$ to the function (5.16). Within the error bars the kink position and the position of the maxima of the spin-fluctuation coincide. This is a clear hint that spin-fluctuations are the internal bosonic modes that cause a reduced quasi-particle life time which is seen in the trough feature of $\Im\Sigma$ and in the kinks in $\Re\Sigma$.

kinks are in fact due to *emergent* internal modes. Here these modes are the spin fluctuations.

### 5.4.2 Results for the Rectangular DOS

In this section, we present DMFT results for the rectangular DOS. In particular, the free DOS reads

$$\rho_G(\omega) = \begin{cases} 0.5D & \text{for } \omega \in [-D, D] \\ 0.0 & \text{else} \end{cases} \tag{5.17}$$

with bandwidth $W = 2D$. The above definition assures that the sum rule $\int \rho_G \mathrm{d}\omega = 1$ is fulfilled. For every non-semielliptic DOS, we have to use the more complex self-consistency cycle shown in Fig. 3.1 on page 20. We start our calculation with $U = 0$, set the repulsion $U$ to its desired value and iterate the self-consistency cycle until convergence. In order to handle the finite depth of the continued fraction of $G$, we use the square-root terminator (4.47) on page 74 in which we substitute $\omega \to \omega - \Sigma(\omega)$. The correct sign of the terminator is determined by the requirement of the correct causality of $G$.

In order to assure causality of $G$, we have to deconvolute $\Im\sigma$ *and* $\Im g$. If we deconvoluted $\Im g$ only, then (due to numerical problems) $\Im\sigma$ from the Dyson equation could violate causality which would then lead to problems with the choice of the right sign in the square-root terminator. The problem of violated causality (i.e. sign changes of $\Im\sigma$) occurs in the vicinity of $\omega = 0$. The violation is in general not very large; see the lower left insets in the left part of Fig. 5.7 for $U = 2D$ and in the left part of Fig. 5.8 for $U = 2.2D$. Hence, we could artificially set $\Im\sigma = 0$ in the vicinity of $\omega = 0$. But due to Kramers-Kronig relations, this would significantly affect the slope of the real part of the self-energy at $\omega = 0$. The latter determines the quasi-particle weight. In addition, this would lead to a further kink in $\Re\sigma$. Since we are especially interested in the slope of $\Re\sigma(\omega = 0)$ and in the kinks of $\Re\sigma$ in the vicinity of $\omega = 0$, we cannot use this way of correcting the causality violation of $\Im\sigma$. Hence, we have to deconvolute $\Im\sigma$ and $\Im g$. Note that the deconvolution of both $\Im\sigma$ and $\Im g$ implies that we cannot circumvent the problem of deconvoluting self-energies (see Sec. 4.3.4 on page 71) for Coulomb repulsions in the proximity of the metal-insulator transition.

For the D-DMRG, we use a chain with 160 fermions and a frequency increment $\Delta\omega = \eta = 0.1D$. For $\rho_G$ and $\rho_\Sigma$, we use $m = 128$ states in the reduced DMRG basis and for the susceptibilities we use $m = 256$ states in the reduced basis.

#### 5.4.2.1 Single Particle Green Functions for the Rectangular DOS

The free DOS exhibits a plateau for $\omega \in [-D, D]$. For finite $U$, the edges of the rectangular are expected to be rounded due to life time effects. From those rounded edges, the Hubbard bands should split for increasing repulsion $U$. This regime of low repulsion is shown in Fig. 5.13. We see that for $U \geq 1.0D$ the Hubbard bands emerge, i.e. we enter the strong-coupling regime, but most of the spectral weight is still located at the quasi-particle peak.

For larger $U$, we enter the strong-coupling regime in which the Hubbard bands are clearly separated from the quasi-particle peak. This is shown in Fig. 5.14.

For larger Coulomb repulsions ($U \geq 2.2D$), the Hubbard bands are split even more clearly from the central peak and the sharp features at the inner side of the Hubbard bands become more pronounced. They gain more weight from the Hubbard bands and are less sharp than for the other DOSs. Unfortunately, the calculations become less stable for larger repulsions. This is shown in Fig. 5.15. One hint for numerical problems is the rising amplitude of wiggles on the Hubbard bands. Even the Kondo resonance show spurious wiggles near $\omega = 0$. Such spurious features do neither vanish if more states are kept in the density-matrix (not shown) nor are they due to a too small chain. The latter can be seen from the hopping constants $\gamma_n$ as a function of the site position in the chain of 160 fermions. This is shown for several values of $U$ in Fig. 5.16 where we see that the hopping constants converge long before the end of the chain. This finding implies that a longer chain does not improve the results.

We were able to calculate spectral densities up to $U = 2.8D$. For larger $U$, the above mentioned numerical problems obviate stable results. Because of the spurious wiggles at the Kondo resonance, we are not able to calculate the quasi-particle weight $Z$ via the first derivative of the Green function at $\omega = 0$ (see Ref. [105, p.15]). We will see in the next subsection that in contrast to $G$ the self-energy $\Sigma$ is smooth for values of $U$ up to $U = 2.8D$. We will therefore postpone the analysis of the quasi-particle weight to the next subsection.

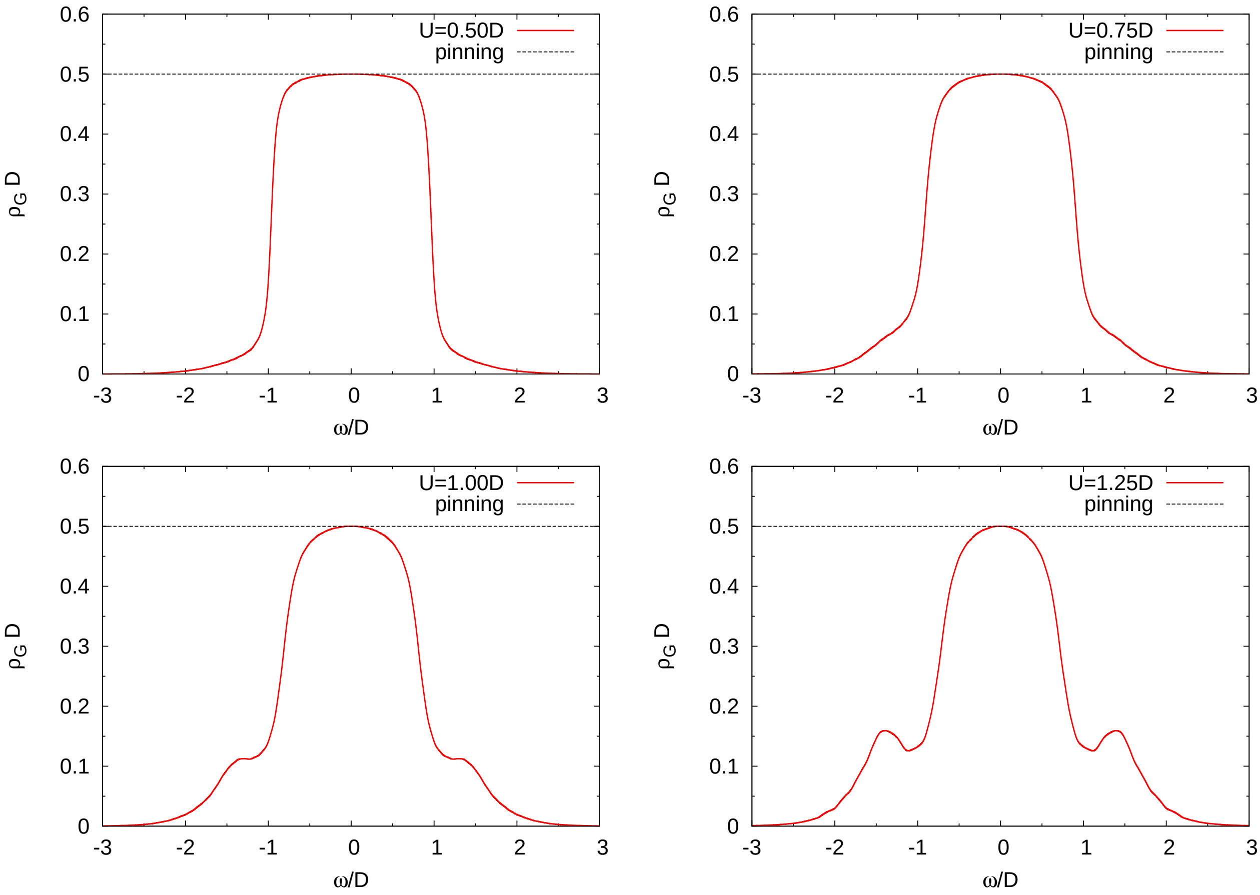

Figure 5.13: Spectral densities $\rho_G$ for the rectangular DOS for $U = 0.5D$ (upper left), $U = 0.75D$ (upper right), $U = 1.0D$ (lower left) and $U = 1.25D$ (lower right) obtained by D-DMRG(Q) (with a chain of 160 fermions and $m = 128$ states in the reduced basis) in the DMFT approach. The dashed line shows the pinning criterion $\rho_G(\omega = 0) = 0.5D$.

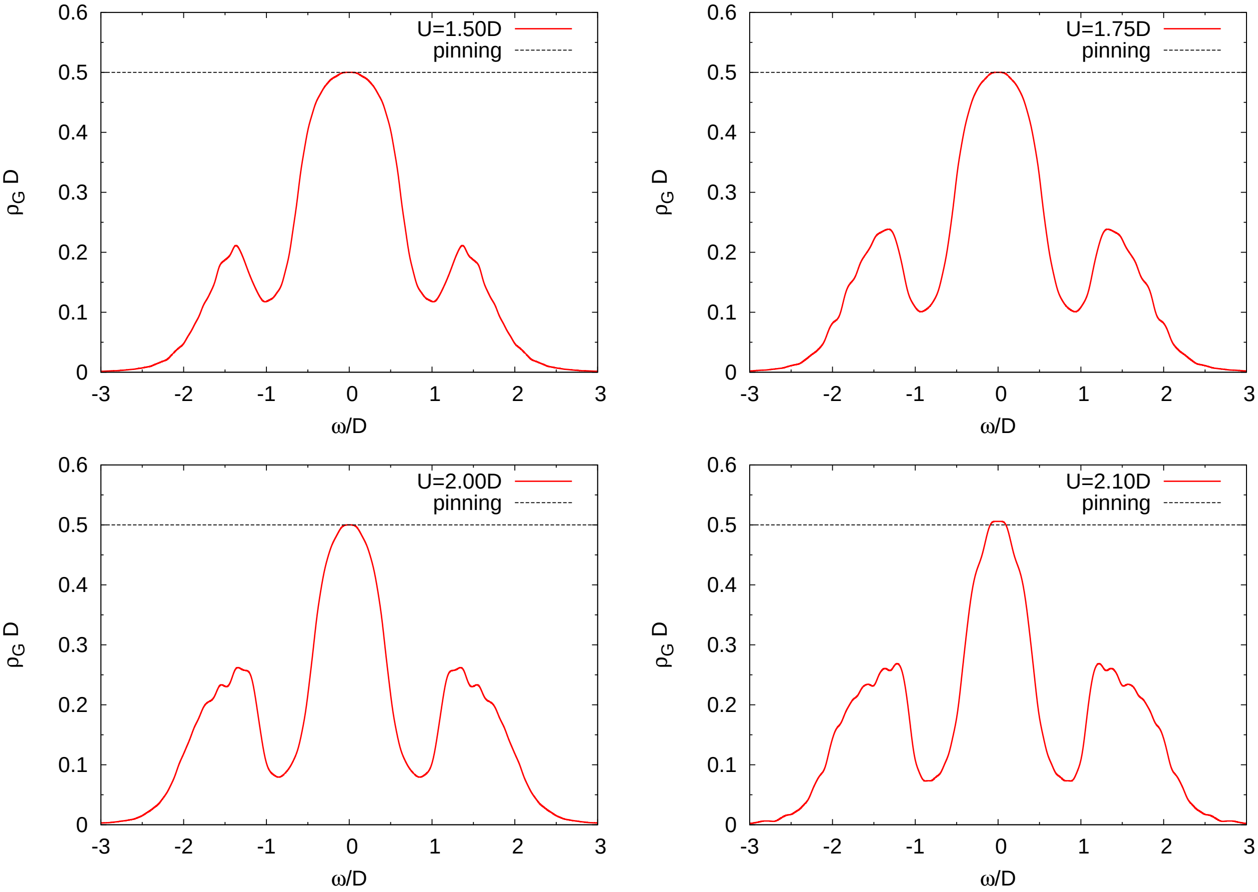

Figure 5.14: Spectral densities $\rho_G$ for the rectangular DOS for $U = 1.5D$ (upper left), $U = 1.75D$ (upper right), $U = 2.0D$ (lower left) and $U = 2.10D$ (lower right) obtained by D-DMRG(Q) for $U \leq 2.0D$ and D-DMRG(G) for $U = 2.1D$ (with a chain of 160 fermions and $m = 128$ states in the reduced basis) in the DMFT approach. The dashed line shows the pinning criterion $\rho_G(\omega = 0) = 0.5D$.

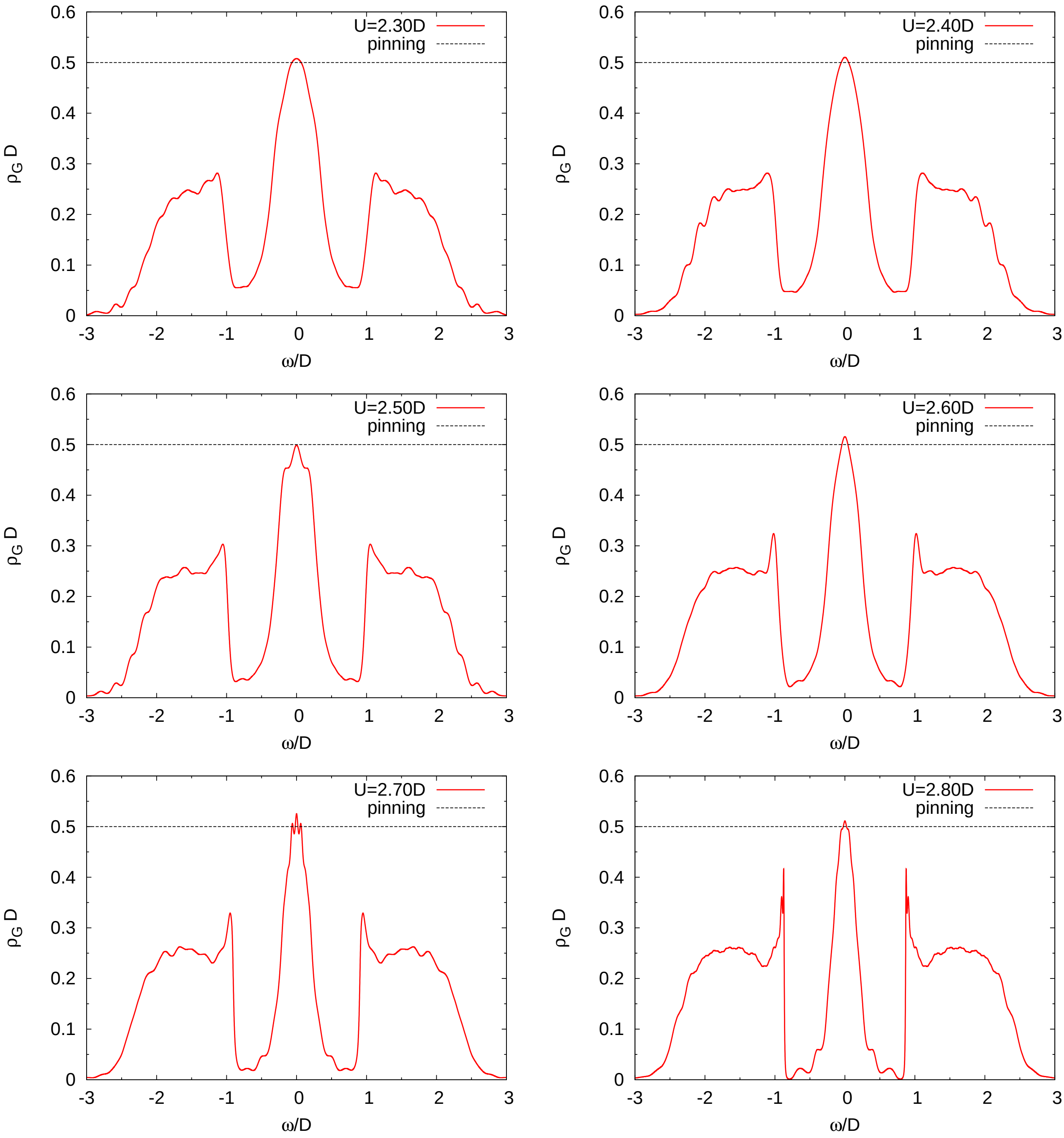

Figure 5.15: Spectral densities $\rho_G$ for the rectangular DOS for $U = 2.3D$ (upper left), $U = 2.4D$ (upper right), $U = 2.5D$ (middle left), $U = 2.60D$ (middle right), $U = 2.7D$ (lower left) and $U = 2.8D$ (lower right) obtained by D-DMRG(G) (with a chain of 160 fermions and $m = 128$ states in the reduced basis) in the DMFT approach. The dashed line shows the pinning criterion $\rho_G(\omega = 0) = 0.5D$.

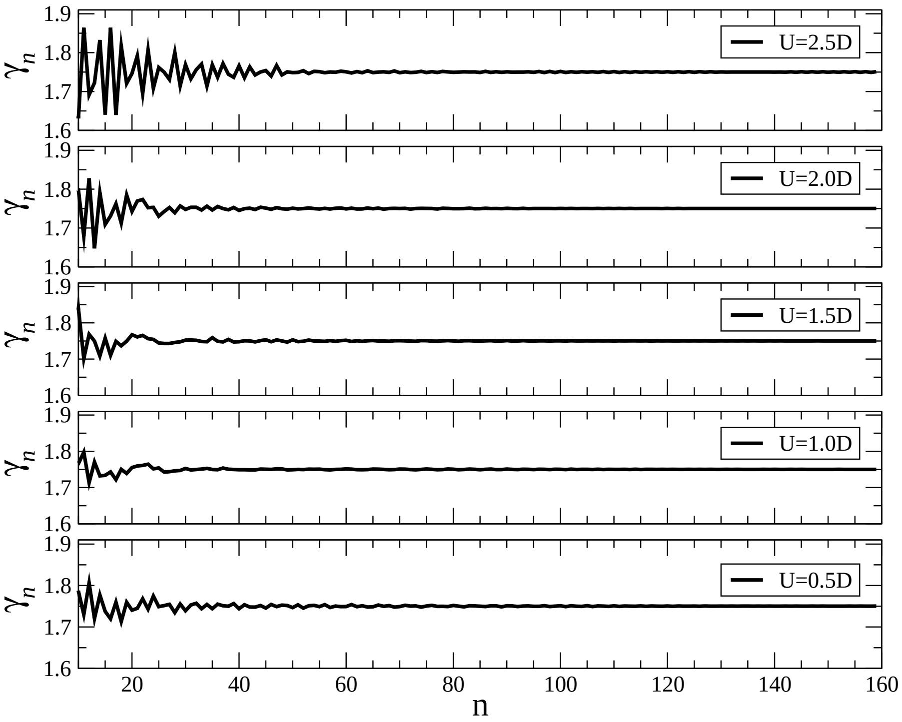

Figure 5.16: Hopping constants $\gamma_n$ as a function of the continued fraction depth $n$ (i.e. position of the site in the chain, see Fig. 3.3 and Eq. (3.29)) for several values of Coulomb repulsion $U$. For all $U$, the coefficients $\gamma_n$ converge to $\gamma_\infty = 1.75D$ long before the chain ends. From this finding, we conclude that the bath of the impurity is large enough.

#### 5.4.2.2 Local Self-Energy for the Rectangular DOS

As for every non semielliptical DOS, we have to deconvolute the self-energy directly. In contrast to the deconvolution of the Green function $G(\omega)$, the deconvolution of the self-energy $\Sigma(\omega)$ turns out to be more stable. In Fig. 5.17, we show the self-energy for low and high Coulomb repulsions.

We see from Fig. 5.17 that for low repulsions ($U \leq 1.00D$), where the Hubbard bands in $\rho_G$ are not yet separated from the central peak, that the real part of the self-energy is linear over the whole range of the Kondo resonance and that the corresponding imaginary part is quadratic without any trough-like structure. This is true until $U = 1.25D$ where the three-peak-structure becomes discernible around $\omega = 0$. For larger repulsions, kinks in the real part of the self-energy and troughs in the imaginary part emerge (lower part of Fig. 5.17).

In contrast to the Green functions $G$ for $\omega \approx 0$, the self-energies $\Sigma$ are smooth there for all accessible Coulomb repulsions. Hence, we can calculate the quasi-particle weight from the slope of the real part of the self-energy at $\omega \approx 0$ (see Eq. (2.5) on page 12) in order to determine the critical repulsion $U_{c2}$ where the metal-insulator transition occurs. The quasi-particle weight $Z$ as a function of $U$ is shown in Fig. 5.18. By linear extrapolation, we obtain $U_{c2}/D = 3.3$ which we compare with Tab. 1 in Ref. [157] where Potthoff shows the result from a private communication of Bulla. Bulla obtains $U_c = 6.32W$ for a bandwidth of $W = 2\sqrt{3}$. Here our bandwidth equals $W = 2D$ After rescalation, Bulla's result reads $U_{c2}/D = 3.65$ which is approximately 10% above the value we obtain. Unfortunately, we do not have stable results for larger repulsion. Results for repulsions $U \geq 2.8D$ could improve our calculation of $U_{c2}$. Against this background, together with the fact that Bulla used another method, both results agree[6].

---

[6] Since no details are given in Ref. [157] how Bulla's result for $U_{c2}$ is obtained, a further discussion of the agreement between his and our result cannot be given.

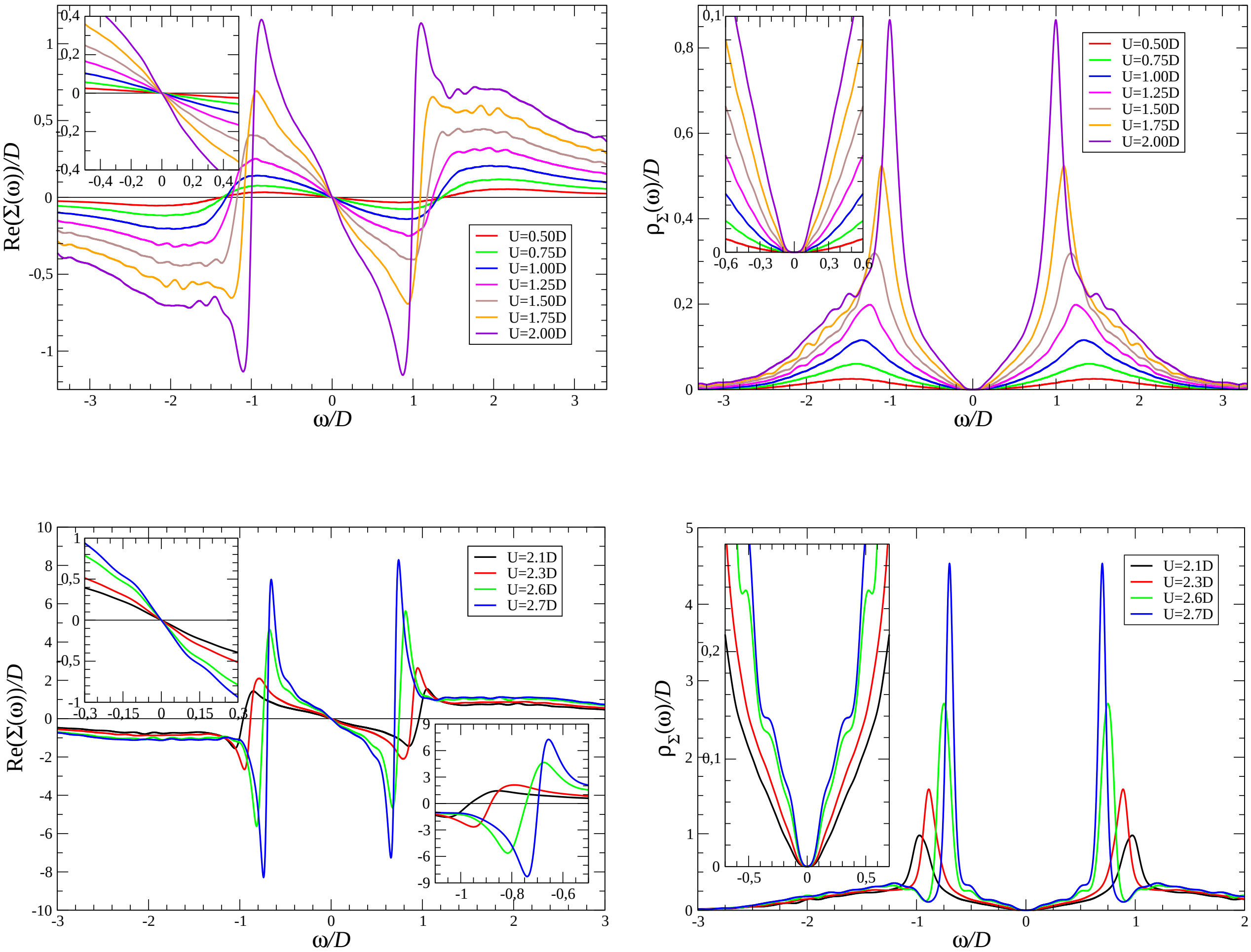

Figure 5.17: Real part (left) and imaginary part (right) of the self-energy of the rectangular DOS for $U \in [0.5D; 2.0D]$ (up) and $U \in [2.1D; 2.7D]$ (down) with zoomed insets for the kinks (troughs) in the real (imaginary) part.

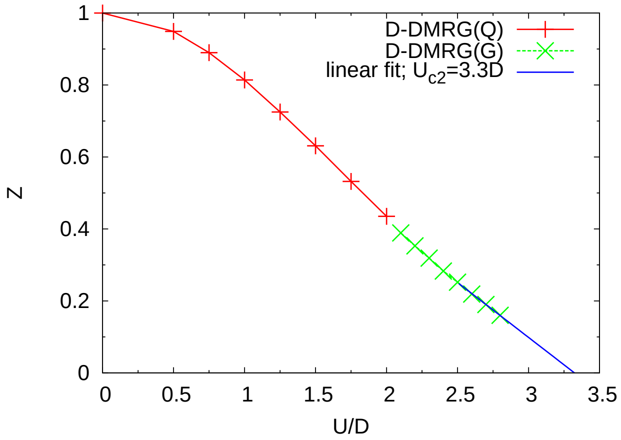

Figure 5.18:
Quasi-particle weight $Z$ as a function of the Coulomb repulsion $U/D$. For $U/D \in [0, 2.0]$ D-DMRG(Q) was used. For $U/D \in [2.1, 2.8]$ D-DMRG(G) was used. The critical interaction $U_{c2}/D$ where the Mott-transition occurs was extracted via a linear fit for $U/D \in [2.5, 2.8]$ and it reads $U_{c2}/D = 3.3$.

#### 5.4.2.3 Local Susceptibilities for the Rectangular DOS

Local susceptibilities can be calculated in the DMFT framework if the excitation operator $\mathscr{A}$ (see Eq. (4.19) in Sec. 4.1.4 on page 46) is changed into the corresponding operator for the susceptibility under consideration. Such a D-DMRG calculation uses the bath obtained by the converged solution of $\rho_G$ of the last DMFT cycle. The operators read (see Ref. [164])

$$\mathscr{A} = \begin{cases} d^\dagger_\uparrow d^\dagger_\downarrow + d_\downarrow d_\uparrow & = S_0^+ T_0^+ + T_0^- S_0^- \qquad \text{Cooper-pair susceptibility} \\ d^\dagger_\uparrow d_\uparrow + d^\dagger_\downarrow d_\downarrow - 1 & = S_0^z + T_0^z \qquad \text{charge susceptibility} \\ d^\dagger_\uparrow d_\uparrow - d^\dagger_\downarrow d_\downarrow & = S_0^z - T_0^z \qquad \text{spin susceptibility} \end{cases} \tag{5.18}$$

for the corresponding susceptibilities in the fermionic and in the Jordan-Wigner language. The pair susceptibility measures the effect of a Cooper pair being created and annihilated at the impurity site. For the Hubbard model, it is expected to be strongly suppressed due to Coulomb repulsion. However, at higher energies we may see certain effects of pair dynamics. The charge susceptibility measures charge fluctuations around half-filling. The latter is indicated by the $1 = \langle n_\uparrow \rangle + \langle n_\downarrow \rangle$ in the definition of (5.18). Hence, this operator must be altered for the Hubbard model away from half-filling. Note that both susceptibilities are identical for half-filling on a bipartite lattice which has already been observed by Raas and Uhrig [164]. This identity is due to a SO(5) symmetry which is reviewed by Demler et al. [40]. Thus, for the Hubbard model at half-filling, we only discuss the charge susceptibility. The spin susceptibility measures the spin fluctuations around zero magnetization.

We begin the discussion with the charge susceptibility. Note that we only show $\chi^>$ and not $\chi = \chi^> + \chi^<$ for the same reasons we mentioned on page 94. Generic results are shown in Fig. 5.19. The $\chi^>$ is calculated with a frequency increment in the raw data of $\Delta\omega = 0.1D$ and with $m = 256$ states in the reduced basis. The raw data has a broadening $\eta = 0.1D$ and the tolerance $A$ of the deconvolution (see Eq. (4.42) on page 70) is between 10 and 100.

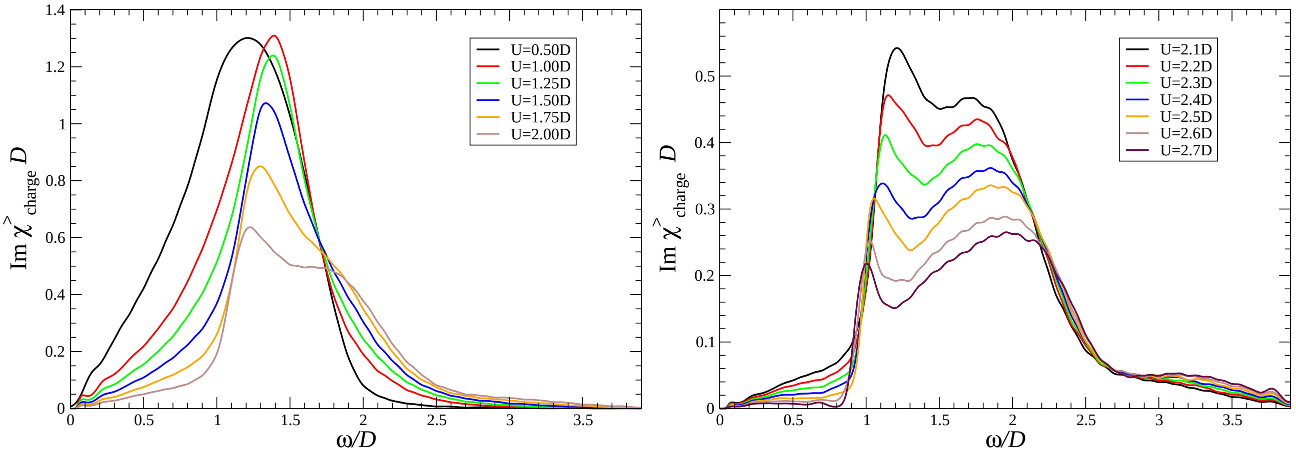

Figure 5.19: Charge susceptibilities for low (left) and high (right) Coulomb repulsions for the rectangular DOS.

Qualitatively, we see the same behavior as for the semielliptic DOS (see Ref. [164]). The charge fluctuations are suppressed for increasing on-site repulsion $U$ and for larger repulsion we roughly see three different ranges. The quantitative differences between the rectangular and the semielliptic

DOS are due to the different quasi-particle weight and the weight of the Hubbard bands for the corresponding repulsion $U$. Hence, the analysis is fully parallel to the discussion of Raas and Uhrig [164] which we briefly summarize.

For low repulsion $U$ (below $U = D$), the susceptibility is linear for $\omega \approx 0$ which is the expected behavior for a Fermi liquid (see e.g. Ref. [156]). For larger repulsion, we can discern three different energy ranges. The first one is the low energy range for $\omega \in [0, 1D]$ which is heavily suppressed for $U \rightarrow U_{c2}$, the second one for $\omega \in [1D, 2.5D]$ where most of the weight is located and the remaining range $\omega \geq 2.5D$ where we see just a hump without any further structure. In a first attempt, we try to understand this finding from the single-particle dynamics alone. This means to consider a convolution of the spectral density $\rho_G$ with itself[7]. As an illustrative example, we compare $\rho_G * \rho_G$ with $\Im \chi^{>}_{\text{charge}}$ for $U = 2.0D$ in Fig. 5.20. The spectral density $\rho_G$ consists of a quasi-particle peak and Hubbard bands so we expect structures stemming from a convolution of the quasi-particle peak with itself, the quasi-particle peak with one Hubbard band and a convolution of the Hubbard band with itself. Hence, this approach gives an explanation for the three different energy ranges mentioned above.

However, the particular spectral weight of the certain ranges are not given by this approximation. We see in Fig. 5.20 that the charge susceptibility is heavily suppressed for $\omega \in [0, 1D]$ whereas a convolution of the quasi-particle peak with itself yield a lot of spectral weight. Most of the weight is located in the second range and we see a pronounced peak in analogy to the sharp feature at the inner site of the Hubbard bands in the spectral densities $\rho_G$ in Fig. 5.15. The sharp feature is more pronounced than for the semielliptic DOS.

In Ref. [164], Raas and Uhrig pose the question if the feature in the charge susceptibility is the cause of the sharp feature in $\rho_G$ or if the sharp feature in $\rho_G$ is the cause for the sharp feature in $\chi_{\text{charge}}$. To assess this question, they determined the weight $W$ of this feature as a function of the quasi-particle weight $Z$. To this end, they calculated a polynomial fit of the charge susceptibility and determined the different weight of the fit and the susceptibility by numerical integration. Such a procedure is repeated here for the rectangular DOS and the result is shown in Fig. 5.21. Unfortunately, we are not able to calculate Green functions and susceptibilities for the high repulsions $U$ where the quasi-particle weight $Z$ is below 0.15. Hence, we cannot answer conclusively whether we obtain a quadratic or a linear behavior. Both fits are shown in Fig. 5.21. However, it is likely (since semielliptical and rectangular DOS do not differ very much which is reflected by all other findings in this section) that it is the same behavior as for the semielliptical DOS. This leads us to assume that the sharp feature in the charge susceptibility is the effect of the sharp feature in the single-particle propagator which is the cause for this feature in the charge susceptibility.

---

[7] A diagrammatic perturbation calculation for a free electron Hamiltonian with small interactions between the electrons starts (see e.g. Ref. [65]) in first order with a term that consists of a convolution of $\rho_G$ with itself.

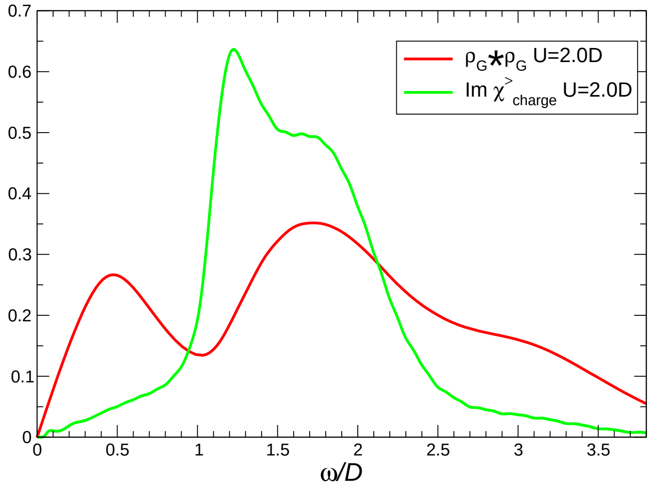

Figure 5.20:
Comparison of the convolution $\rho_G * \rho_G$ with the charge susceptibility $\chi^>_{\text{charge}}$. We see that the three different energy ranges can be explained by this first approximation but $\chi^>_{\text{charge}}$ yields considerable differences to $\rho_G * \rho_G$. The response for $\omega \in [0, 1D]$ and for $\omega \geq 2.5D$ is more suppressed than $\rho_G * \rho_G$ prompt us to expect. On the contrary, more weight is located in $\omega \in [1D, 2.5D]$ for $\Im\chi^>_{\text{charge}}$.

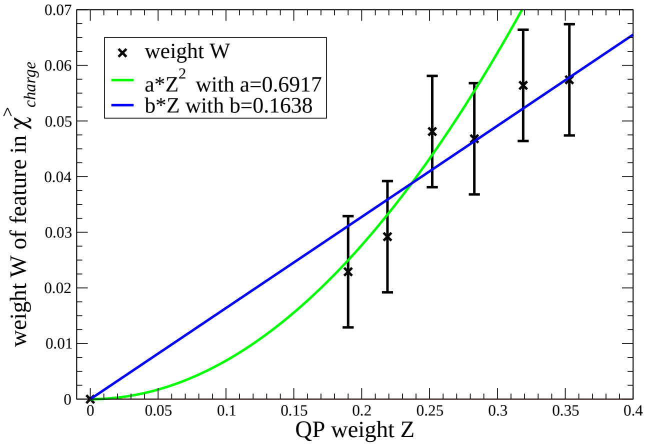

Figure 5.21:
Weight $W$ of the feature in the charge susceptibility as a function of the quasi-particle weight $Z$. We obtain no conclusive result whether this is a linear or a quadratic dependence since we are not able to calculate Green functions and susceptibilities with quasi-particle weights $Z < 0.18$. However, it is unlikely that we obtain a different result than for the semielliptic DOS since all other findings are analogous to the results for the semielliptic DOS.

Next, we discuss the spin susceptibility. Generic spin susceptibilities are shown in Fig. 5.22. They are calculated with a frequency increment in the raw data of $\Delta\omega = 0.1D$ and $m = 256$ states in the reduced basis. The raw data is computed with a broadening $\eta = 0.1D$ and the tolerance $A$ of the deconvolution (see Eq. (4.42) on page 70) is between 10 and 100.

The spin susceptibility is dominated by a maximum that becomes sharper on increasing repulsion $U$. Its maximum moves to $\omega = 0$ for $U \to U_{c2}$, i.e. we obtain the same behavior as for the semielliptical DOS. For a discussion of the connection of this spin excitation to the kinks in the self-energy, see subsection 5.4.2.4 below.

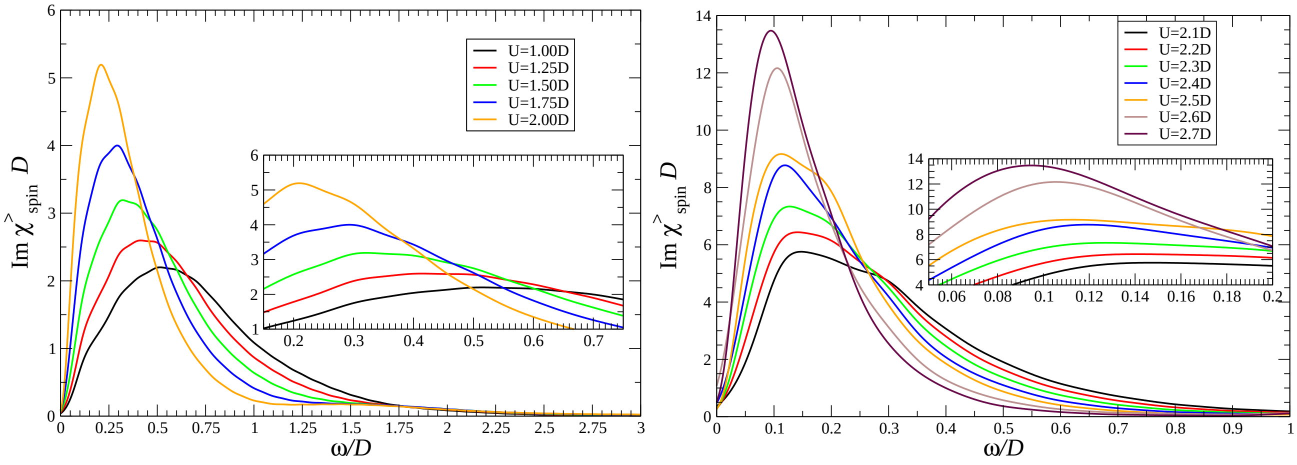

Figure 5.22: Spin susceptibilities for low (left panel) and higher (right panel) values of $U$ for the rectangular DOS. The insets show the position of the maxima of the susceptibility.

#### 5.4.2.4 Kinks and Local Bosonic Excitations for the Rectangular DOS

In view of the results of subsection 5.4.2.3, it appears that only spin-fluctuations show peaks in the same energy range where the kinks occur. A quantitative comparison is shown in Fig. 5.23. As in Sec. 5.4.1 on page 92, we extracted the kink position by a fit with formula (5.16). Furthermore, we also show the kink position from the formula (5.14) on page 88 for which we used the quasi-particle weight obtained from the self-energy (see Fig. 5.18) and we show the corresponding maximum of the spin susceptibility. In Fig. 5.23, we see that the kink positions and the spin susceptibility maxima coincide within the numerical accuracy. Note that we do not show data for $U \leq D$ because for such low repulsion there is no three-peak structure in the local Green functions (see Sec. 5.4.2.1) and no kink in the self-energies (see Sec. 5.4.2.2). As a conclusion we state that for the rectangular DOS spin-fluctuations of the propagating quasi-particle are the internal bosonic excitations that provide the additional decay of the quasi-particle seen as the trough feature in $\Im\Sigma$. Due to Kramers-Kronig relations, those troughs lead to the kinks in the real part of the self-energy.

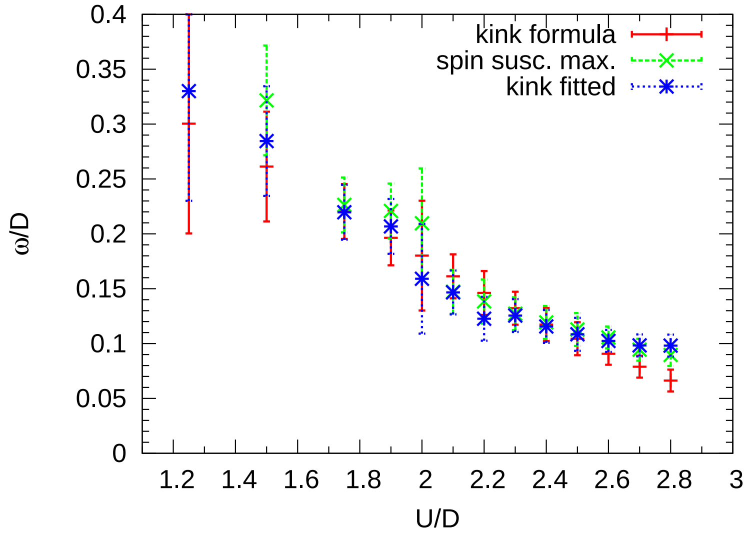

Figure 5.23:
Kink positions obtained via the quasi-particle weight $Z$ and formula (5.14), maxima of the spin susceptibility (see Fig. 5.22) and kink positions obtained from the real part of the self-energy (see Fig. 5.17) as a function of the Coulomb repulsion $U$. All positions agree within the error bars. From this, we conclude that for the rectangular DOS spin-fluctuations are the internal bosonic excitation that are responsible for the kinks in the real part of the self-energy.

### 5.4.3 Results for the Triangular DOS

In this section, we present DMFT results for the triangular DOS. In particular, the free DOS reads

$$\rho_G(\omega) = \begin{cases} \frac{1}{D} - \left|\frac{\omega}{D^2}\right| & \text{if } \omega \in [-D, D] \\ 0.0 & \text{else} \end{cases} \tag{5.19}$$

which is a symmetric triangle with bandwidth $W = 2D$ and area equal one. The procedure to obtain the dynamic quantities is completely the same as for the rectangular DOS (see Sec. 5.4.2 on page 97). We also use the same parameters for the impurity solver, i.e. a chain with 160 fermions, $m = 128$ states in the reduced DMRG basis and a frequency increment $\Delta\omega = \eta = 0.1D$.

#### 5.4.3.1 Single Particle Green Functions for the triangular DOS

The free DOS is a triangle whose cusp is located at $\omega = 0$. For increasing repulsion $U$, we expect that the legs of the triangle become curved and that for larger $U$ the Hubbard bands separate from them. This is the case for $0 \le U \le D$ and it is shown in Fig. 5.24.

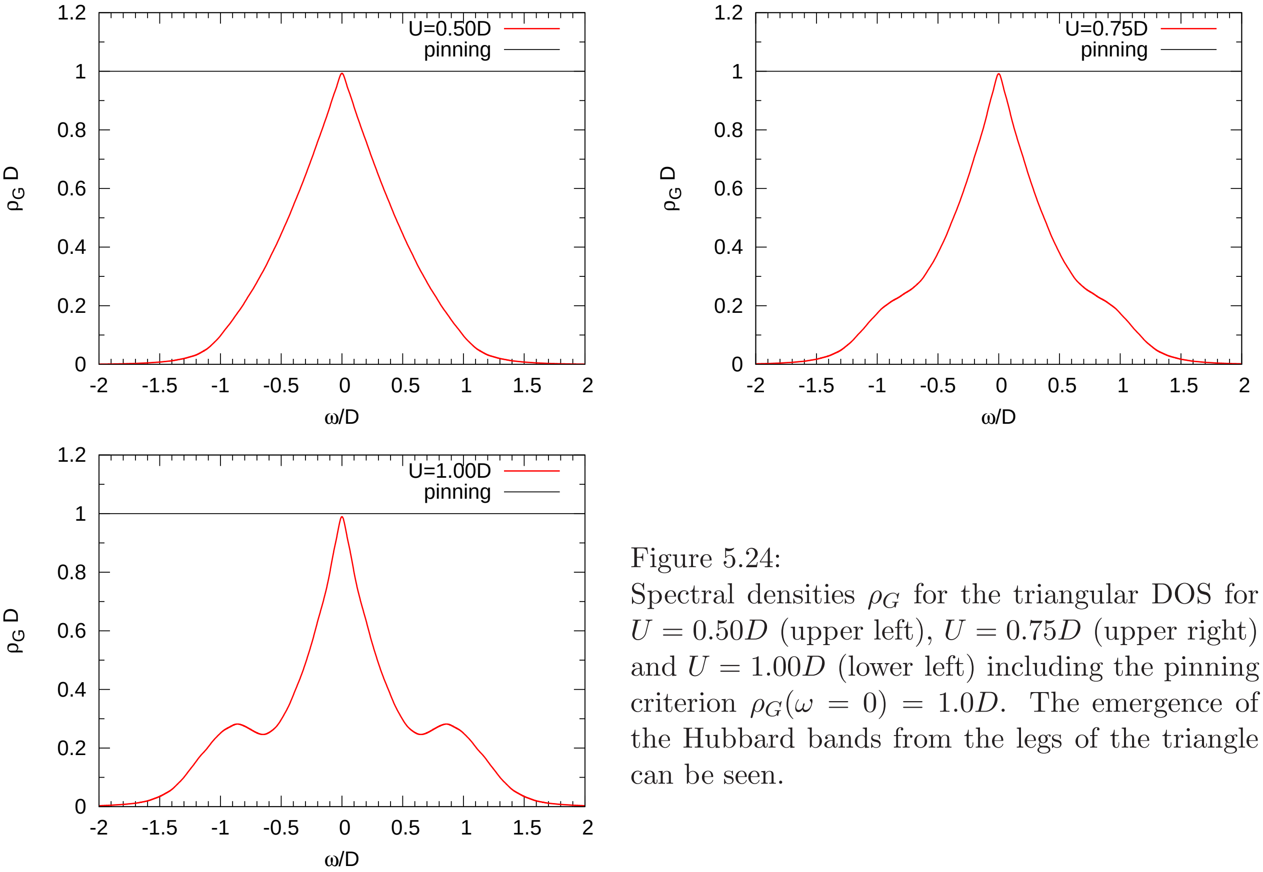

Figure 5.24:
Spectral densities $\rho_G$ for the triangular DOS for $U = 0.50D$ (upper left), $U = 0.75D$ (upper right) and $U = 1.00D$ (lower left) including the pinning criterion $\rho_G(\omega = 0) = 1.0D$. The emergence of the Hubbard bands from the legs of the triangle can be seen.

For $U \ge 1.25D$, we enter the strong-coupling regime where Hubbard bands separate from the quasi-particle peak. From $U = 1.75D$ on, a sharp feature at the inner side of the Hubbard bands shows up which we already obtained for the semielliptic and for the rectangular DOS. Spectral densities for $1.25D \le U \le 2.1D$ are shown in Fig. 5.25. For $U \ge 2.1D$, no reliable solutions can be obtained. A longer chain or more kept states $m$ in the reduced basis do not improve this finding (not shown).

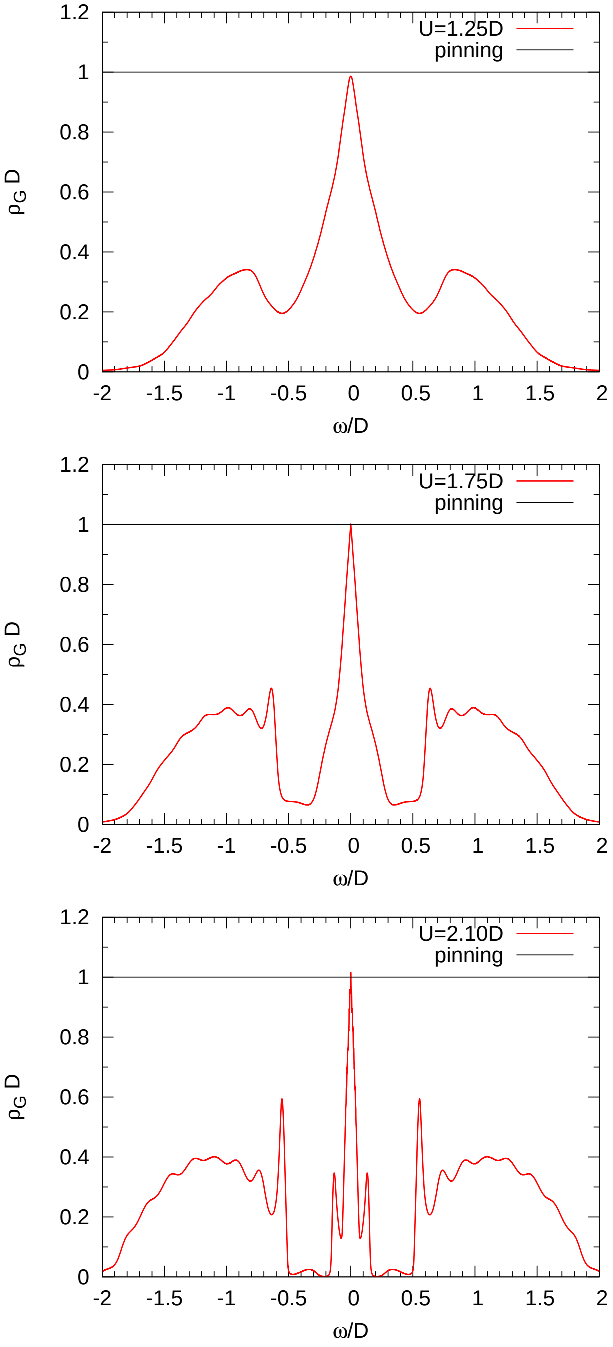

Figure 5.25:
Spectral densities $\rho_G$ for the triangular DOS for $U = 1.25D$ (upper left), $U = 1.50D$ (upper right), $U = 1.75D$ (middle left), $U = 2.00D$ (middle right). We see the emergence of the Hubbard bands which exhibit a sharp feature at the inner side. For $U \geq 2.1D$ (lower left), no reliable solutions can be obtained since spurious side features in the immediate proximity ($\omega \approx \pm 0.1D$) of the Kondo peak appear.

#### 5.4.3.2 Local Self-Energy for the Triangular DOS

As for the rectangular DOS, we have to deconvolute the self-energy directly. Results are shown in Fig. 5.26 where we show self-energies up to $U = 2D$ since for larger repulsion no reliable solutions could be obtained. For $U = 2D$, we see a gapped structure, i.e. $\Im\Sigma$ at $\omega = \pm 0.5D$ touches the $\omega$-axis, which likely is the reason that we could not obtain results for larger repulsions. For repulsions $U \geq 1.00D$, kinks in the real part of the self-energy are discernible which coincides with the repulsion where $\rho_G(\omega)$ exhibit a three-peak structure. For $U = 0.75D$, beginnings of kinks are visible but their positions could not be faithfully obtained.

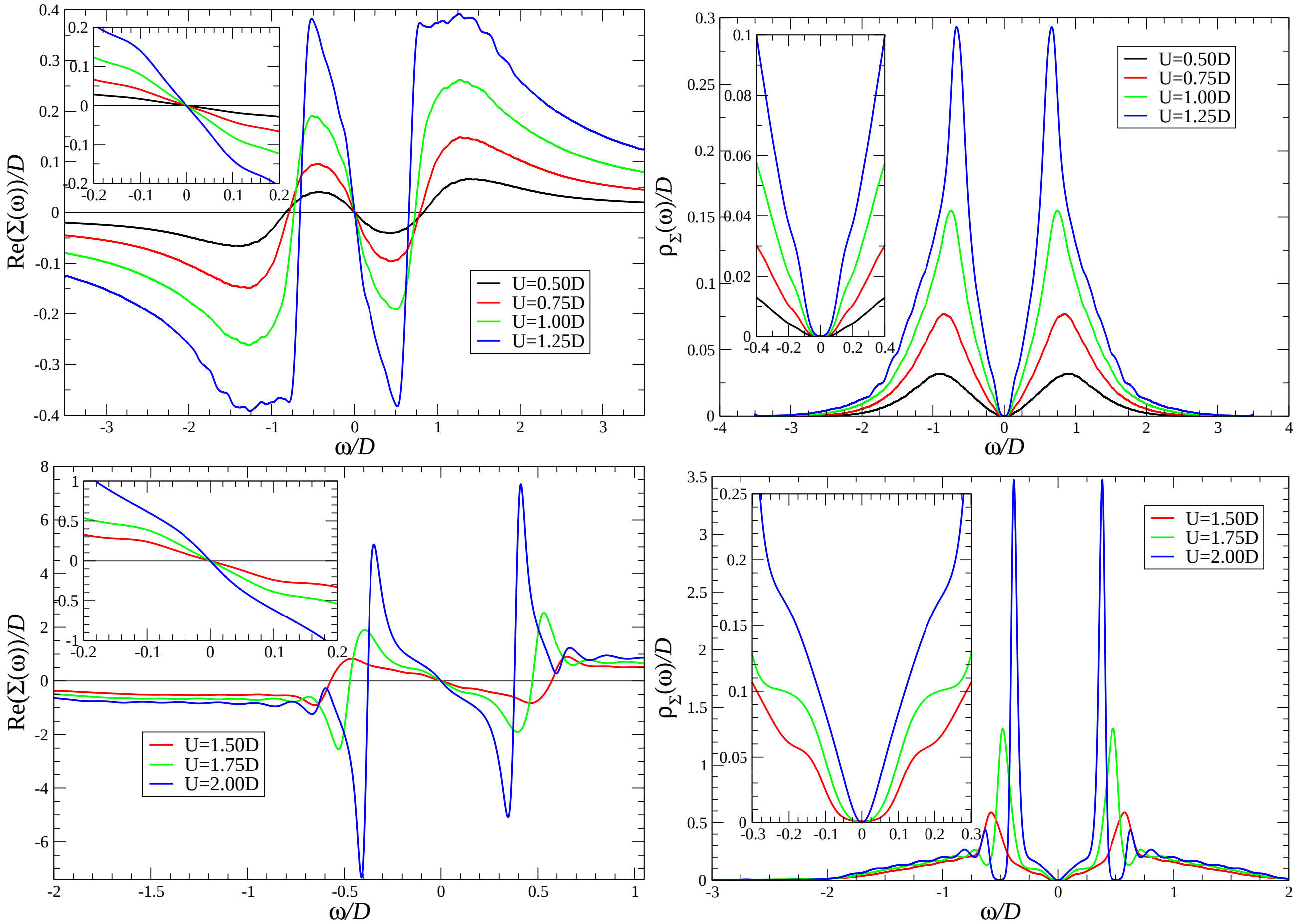

Figure 5.26: Real part (left) and spectral density $\rho_\Sigma = -1/\pi \Im\Sigma$ (right) of the self-energy $\Sigma(\omega)$ for the triangular DOS for low values (up) and high values (down) of the Coulomb repulsion $U$. For $U \geq 1.00D$ kinks (troughs) appear in the real (imaginary) part of the self-energy $\Sigma$.

Next, we calculate the quasi-particle weight $Z$ by Eq. (2.5) on page 12 from the slope of the real part of the self-energy at $\omega = 0$. From the spectral densities shown in Fig. 5.25, it appears that for the largest repulsion $U$ for which stable solutions can be obtained, the quasi-particle weight is quite large so that an extrapolation to $Z = 0$ would not yield a faithful result. In order to obtain at least a rough approximation, we use results for larger repulsion $U$. Although they are not reliable for the whole frequency range, the quasi-particle peak itself behaves in the expected way. The quasi-particle peak becomes narrower and narrower for larger repulsion $U$ and also the real part of the self-energy is linear with an increasing slope in the frequency range of the quasi-particle peak. Hence, we may use the results for the self-energy within this range[8]. With those words of caution in mind, we obtain the result for the quasi-particle weight $Z$ shown in Fig. 5.27. We obtain $U_{c2} = 2.9D$. Although Potthoff [157] also mentions the triangular DOS in his paper, he does not present a DMFT result of $U_{c2}$ for this DOS. Instead, we compare it with the result of the linearized DMFT from Potthoff [157] which reads $U_{c2}^{\text{L-DMFT}}/W = 3$ which is only 2.6 % above our result.

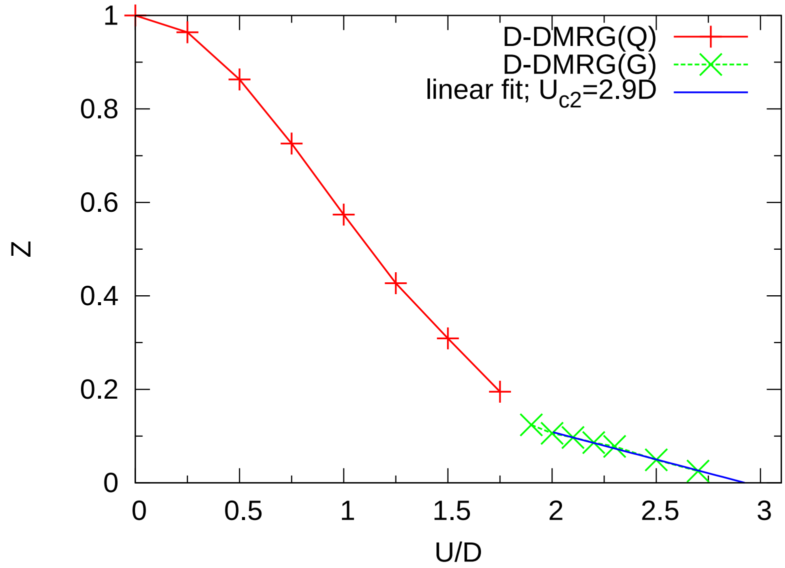

Figure 5.27:
Quasi-particle weight $Z$ as a function of $U/D$ for the triangular DOS obtained by D-DMRG(Q) (red crosses) for $U \leq 1.75D$ and by D-DMRG(G) (green ×) for larger repulsions. Note that for $U \geq 2.1D$ no reliable spectral densities could be obtained. For such large repulsions, only the Kondo resonance itself and the slope of the self-energy are stable features so the results for such large repulsions must be treated/interpret with greatest caution. We obtain a critical repulsion $U_{c2} = 2.9D$.

#### 5.4.3.3 Local Susceptibilities for the Triangular DOS

We begin the discussion with the charge susceptibility which is shown in Fig. 5.28. Qualitatively, we obtain the same results as for the rectangular DOS (see Sec. 5.4.2.3) or the semielliptical DOS (see Ref. [164]). For low repulsion $U$, i.e. for repulsions where no Hubbard bands in $\rho_G$ are present, the charge susceptibility is linear for $\omega \to 0$ and exhibits a single maximum at $\omega \approx 0.85D$ without any further structure. For larger repulsions, more or less three ranges are discernible: The first range for $\omega \in [0.0; 0.6D]$, the second range for $\omega \in [0.6D; 2.0D]$ and the third range for $\omega > 2.0D$. The existence of three ranges for the rectangular DOS was explained by the single-particle dynamics in the last section. This argument also applies here. The only qualitative difference of the charge susceptibility for the triangular DOS (compared to the rectangular DOS) is that the sharp feature at $\omega \approx 0.6D$ has much less weight. Whereas it is a pronounced feature for the rectangular DOS – even if this feature did not emerged in $\rho_G$ (e.g. for $U = 2.1D$) – it occurs here only as a small peak for $U \geq 1.9D$.

Next, we discuss the spin susceptibility. It is calculated with a frequency increment $\Delta\omega = 0.1D = \eta$, with $m = 256$ states in the reduced basis. For low repulsion (upper left panel of Fig. 5.29), we set the tolerance value of the deconvolution to $A = 200$ and for all other repulsions we used no tolerance ($A = \infty$). Results are shown in Fig. 5.29. The spin susceptibility consists of one main peak with decreasing frequency and increasing height on increasing repulsion $U$. In addition, there is a small hump approximately located at $\omega = 0.2D$ that forms a shoulder to the main peak for repulsions $U$ where the main peak is nearby. This is shown in the upper left and upper right part of Fig. 5.29. The

---

[8] For the rectangular DOS (see Fig. 5.18), this was not possible because the quasi-particle peak for $U > 2.8D$ did not converge to a stable form.

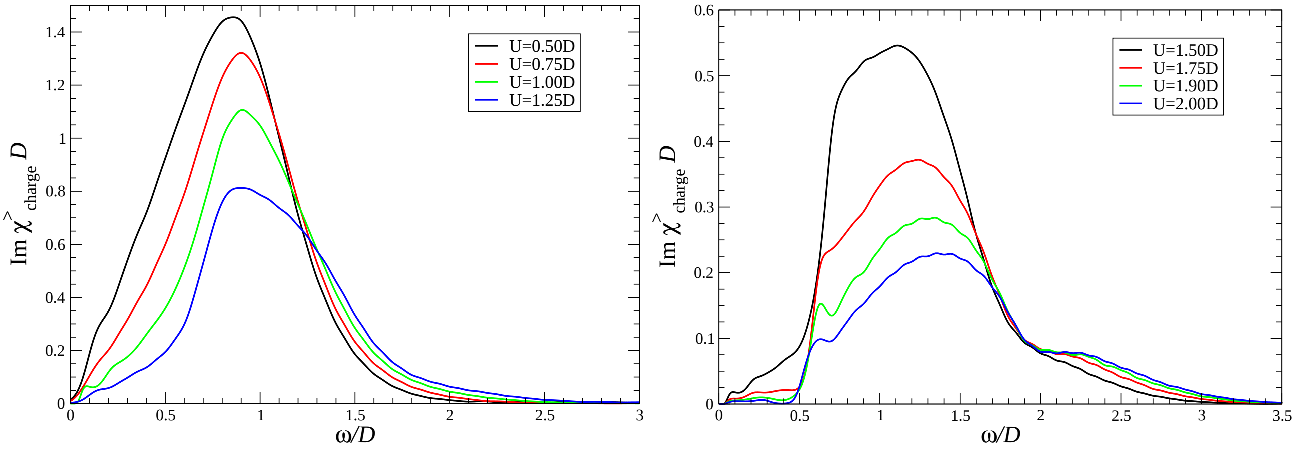

Figure 5.28: Charge susceptibilities for the triangular DOS for low (left) and high (right) Coulomb repulsion.

spectral functions $\rho_G$ for $U \geq 2.1D$ are unreliable only at higher frequencies. However, for $U \geq 2.1D$ the quasi-particle peak prevail as a stable feature in $\rho_G$ and we assume that the quasi-particle peak itself is more or less correctly calculated. Hence, we also calculated the spin susceptibility for repulsions $U \geq 2.1D$. They show the same behavior as the other spin susceptibilities (see lower left part of Fig. 5.29), i.e. an increasing maximum which position moves to $\omega = 0$ and a second one at $\omega \approx 0.2D$. Compared to the first very sharp maximum, the second maximum is a small hump. Since all features of the spin susceptibility are located within the range of the quasi-particle peak, we think that our results are reliable in this range. But certainly, they are less reliable than for $U \leq 2.0D$.

A maximum in the local spin susceptibility corresponds to the energy of the spin singlet-triplet excitation. From this point of view, the meaning of a second maximum in a local spin susceptibility is difficult to give. Maybe it is a spurious artifact. However, it is a very stable artifact but its origin could not be clarified in this thesis.

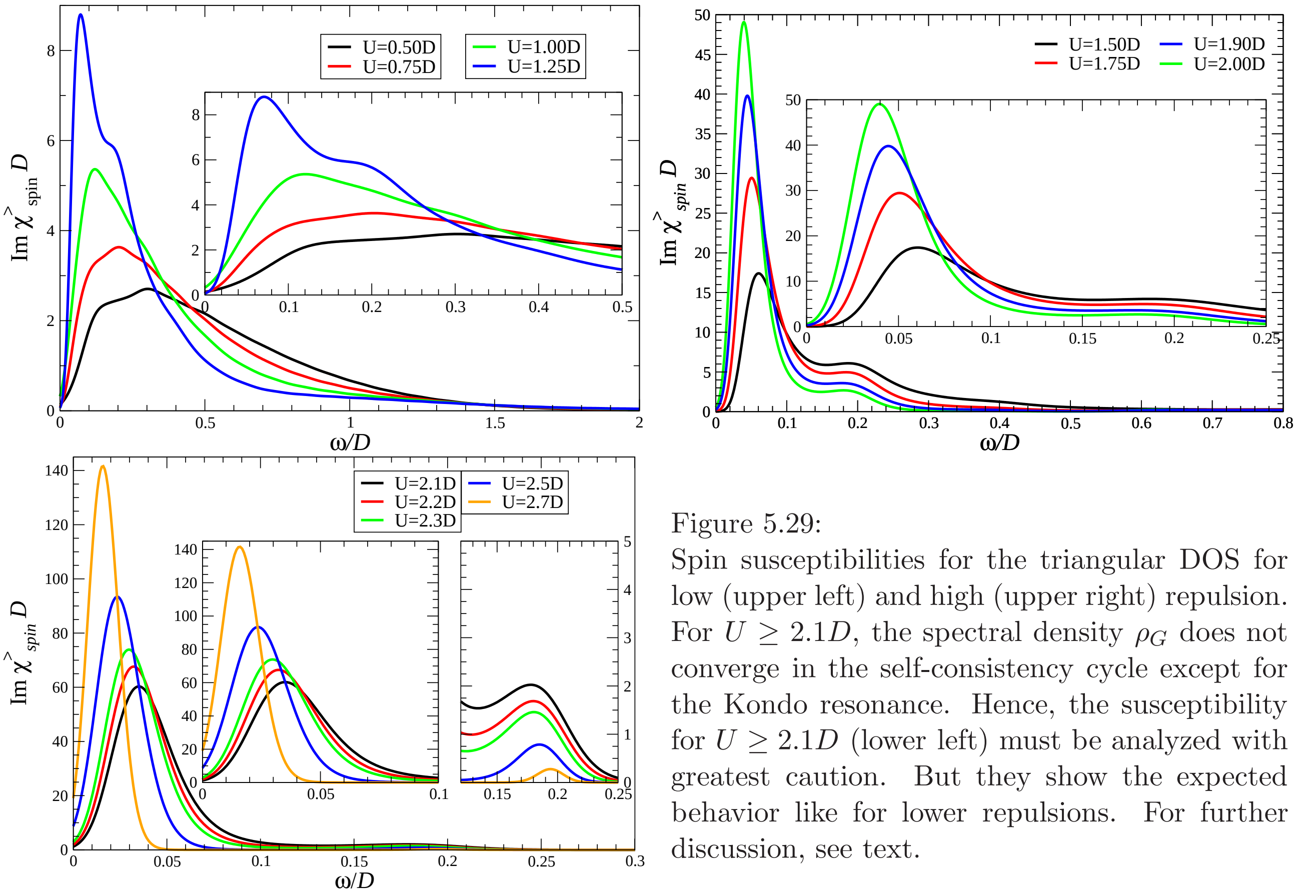

Figure 5.29:
Spin susceptibilities for the triangular DOS for low (upper left) and high (upper right) repulsion. For $U \geq 2.1D$, the spectral density $\rho_G$ does not converge in the self-consistency cycle except for the Kondo resonance. Hence, the susceptibility for $U \geq 2.1D$ (lower left) must be analyzed with greatest caution. But they show the expected behavior like for lower repulsions. For further discussion, see text.

#### 5.4.3.4 Kinks and Local Bosonic Excitations for the Triangular DOS

In this section, we compare the position of the kinks in $\Re\Sigma$ with the corresponding position of the peaks in the spin susceptibility since the charge susceptibility does not show any peaks in the particular range. As shown in Sec. 5.4.3.3, the spin susceptibility exhibits two maxima which have comparable weight and amplitude for repulsion $U \leq 1.75D$. For those repulsions, we calculated the mean value of both maxima. For repulsions $U \geq 2.0D$, both maxima are clearly separated and the first one has most of the spectral weight. For those repulsions, we took the position of the maximum with the lowest frequency. This is shown in Fig. 5.30. Note that for $U \geq 2.1D$ the spectral density $\rho_G$ did not fully converged except for the range where the quasi-particle peak is located. But the spin susceptibility exhibits most of its weight in the energy range where the quasi-particle peak is located so we are confident that the calculation of $\chi_{\text{spin}}$ is reasonable.

In Fig. 5.30, we see that the spin maxima and the kink positions coincide within the error bars. This statement holds, even if the less reliable data points for $U \geq 2.1D$ are excluded. We conclude that for the triangular DOS spin fluctuations provide the decay channel for the quasi-particle and are hence the internal bosonic excitations that cause the kinks in the real part of the self-energy.

We showed (see Ref. [165] and Secs. 5.4.1 and 5.4.2.4) that the spin excitation of the propagating quasi-particle provide the additional decay for the quasi-particle which is seen as the trough in $\Im\Sigma$ and as the kinks in $\Re\Sigma$. The spin excitations set in at the same frequency where the kinks are located. It is plausible to assume that this finding does not change for similar DOSs. The results for the rectangular DOS (see Sec. 5.4.2.4) and for the triangular DOS strongly supports this hypothesis.

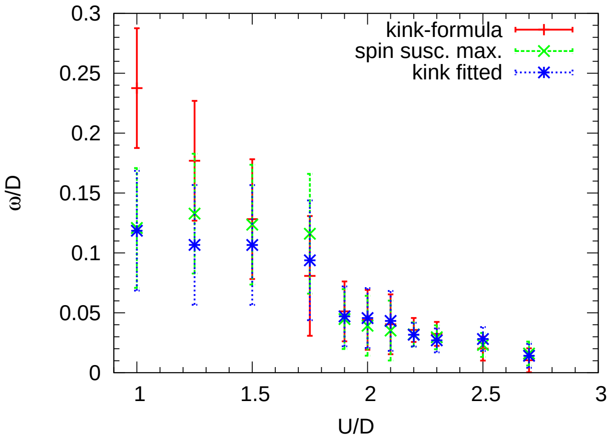

Figure 5.30:
Position of the kinks in $\Re\Sigma$ as a function of the repulsion $U$, position of the kinks calculated from the quasi-particle weight $Z$ by formula (5.14), position of the mean value of both maxima in the spin-susceptibility (for $U \leq 1.75D$) and position of the first maxima for higher repulsions. Within the error bars, the quantities coincide. Note that for $U \geq 2.1D$, only the quasi-particle peak could be obtained in the DMFT calculations. Hence, the results for $U \geq 2.1D$ should not be fully trusted although it seems that they capture the correct physics. However, the result that kink positions and spin susceptibility maxima coincide holds even if the data for $U \geq 2.1D$ is excluded.

## 5.5 Dynamic Mean-Field Results away from Half-Filling

### 5.5.1 Introduction

In this section, we present DMFT results of the single-band Hubbard model away from half-filling for the semielliptic DOS. To this end, we use the chemical potential $\mu$ whereby we shift the local fields $\epsilon_{\mathrm{d}}$ and all other $\epsilon_i$ in Hamiltonian (3.33). For $U = 0$, this leads to a semielliptic spectral density $\rho_G$ of the Green function $G$ whose maximum is shifted by $\mu$. Throughout this section, we use positive $\mu$, i.e. we dope electrons. But since we consider a single-band model on a bipartite lattice, results for hole-doping can be obtained by reflecting $\omega \to -\omega$. For all calculations presented here, we use a chain of 160 fermions and a frequency increment $\Delta\omega = \eta = 0.1$ for the D-DMRG. We started all self-consistency cycles with the non-interacting Green function (i.e. $\rho_G$ being the shifted semiellipse) and used $m = 128$ states in the reduced basis. After convergence, we carried out at least three further self-consistency cycles with 256 states in the reduced basis. This bath is used to calculate any susceptibility for which we also used $m = 256$ states in the reduced basis.

Although the infinite-dimensional single-band Hubbard model away from half-filling is, after the half-filled case, the easiest case concerning theoretical and computational effort and although there exists a couple of different impurity solvers (see Sec. 3.4 on page 32), there exist only a small number of articles where spectral densities away from half-filling are presented.

An early DMFT result away from half-filling was obtained by iterated perturbation theory (IPT) [100] (for a review about IPT see Ref. [168]). IPT is a fast method but it just interpolates between known limit cases so the work of Kajueter et al. [100] gives only a first overview. Shortly after this work, Kajueter et al. [101] published results for the doped insulator where they combined exact diagonalization (ED) with IPT. In 2002, Tong [203] published ED results for the doped insulator which he compared with the Gutzwiller approximation. There are two articles presenting numerical renormalization (NRG) DMFT results for the single band away from half-filling. The first is the work of Krug von Nidda et al. [146] where they also calculated spin susceptibilities and the second is the work of Freericks et al. [56] (both from 2003) where data for inelastic scattering was calculated for which single-particle Green functions are needed. The enhanced non-crossing approximation can calculate spectral functions for $T \neq 0$ which leads to a good agreement with D-DMRG data (see Sec. 5.1 on page

80) and Schmitt et al. [175] recently published dynamic susceptibilities for the SIAM calculated with ENCA. Early works using ENCA for the Hubbard model in a DMFT framework are done by Jarrell and Pruschke [96]. A detailed ENCA study including the doped case was done by Pruschke et al. [161] in 1995. At last, we mention the recent DMFT results for the single-band Hubbard model away from half-filling at $T = 0$ obtained by D-DMRG published by Garcia et al. [63, 64] in 2007 and Miranda et al. [137] in 2008. Although they did the calculations via D-DMRG, they used the continued-fraction method which is prone (see Raas [163, p.67-69]) to produce spiky spectral densities. The reason for this is that many higher excited states have to be added to the density-matrix with the lower weight the more higher excited states are added. With those higher excited states, the continued-fraction coefficients at the corresponding depth of the continued-fraction are calculated. The accuracy of the continued-fraction coefficients obtained by this method is not high enough to yield continuous spectral densities without spikes. In this thesis, we use the correction-vector method (see Sec. 4.1.4 on page 46) to obtain spectral densities.

Setting a certain chemical potential $\mu$ leads to an asymmetric spectral density $\rho_G$ and hence to a filling $n \neq 0.5$. However, a certain shift $\mu$ does not specify the filling alone; the filling $n(\mu, U)$ is a function of the chemical potential $\mu$ and the repulsion $U$. For $U = 0$, the function $n(\mu, 0)$ is given in Fig. 4.13 on page 67. For increasing repulsion $U$ and positive $\mu$, the filling $n(\mu, U)$ is below the corresponding value for $U = 0$ because the repulsion impede the occupation of the impurity site. This implies that the spectral densities $\rho_G$ as a function of $U$ for fixed $\mu$ correspond to different fillings. Hence it is more difficult to analyze e.g. the shift of spectral weight as a function of $U$. Therefore, we not only present local dynamical quantities $\mathscr{G}(\omega, U, \mu)$ as a function of the shift $\mu$. In addition, we also use those results to obtain $n(\mu, U)$ and calculate $\mathscr{G}(\omega, U, n)$ for $n = 0.55$ and $n = 0.65$.

### 5.5.2 Local Spectral Densities for the Doped Metal

We start the presentation of spectral densities by showing $\rho_G$ as a function of the chemical potential $\mu$. For $U = 1D, U = 1.25D, U = 1.5D$ and $U = 1.75D$, Fig. 5.31 shows the results.

In Fig. 5.31, we see that doping with electrons leads to a shift of spectral weight towards the Kondo resonance. This is plausible since doping with electrons makes the system more metallic which increases the quasi-particle weight. At the same time, the upper Hubbard band moves towards lower energies and becomes a shoulder of the Kondo resonance for large $\mu$. But the height of the maximum of the upper Hubbard band stays more or less the same. On the other hand, for $U = 1D$ and $U = 1.25D$, the height of the maximum of the lower Hubbard band decreases considerably. This decreasing of the height of the maximum becomes less for increasing repulsion $U$. As already mentioned, for larger repulsion $U$ the system deviates less from half-filling, see Tab. 5.4 for the particular values. Whereas the filling for $U = 1D$ reads $n = 0.75$ for $\mu = 0.75D$, the filling for $U = 1.75D$ and $\mu = 0.75D$ only reads $n = 0.66$. Hence, the general trend for doping with electrons is – apart from the expected larger quasi-particle weight – that the height of the maximum of the lower Hubbard band diminishes whereas the height of the maximum of the upper Hubbard band stays more or less constant. The position of the maximum of the lower Hubbard band moves faster towards negative energies than the position of the maximum of the upper Hubbard band.

Physically, the upper Hubbard band corresponds to the excitation from the single to double occupied states, the quasi-particle peak is a many-body effect of single occupied states and the lower Hubbard band corresponds to excitations from single occupied states to the empty state. Shifting the chemical potential $\mu$ implies that the energies of the double occupied and single states change. As long as both Hubbard bands are separated from the quasi-particle peak, a considerable change of the quasi-particle

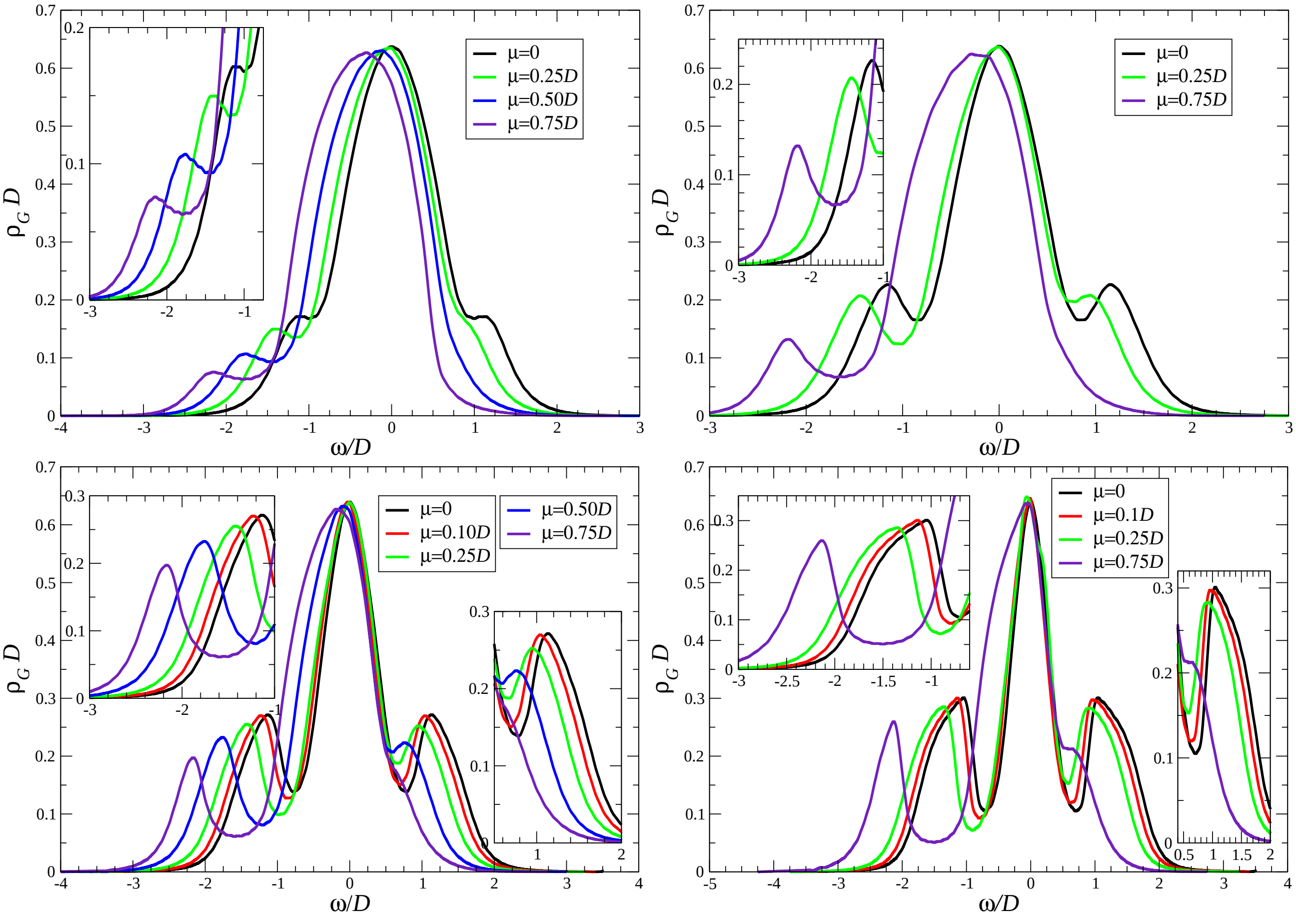

Figure 5.31: Spectral densities for $U = 1D$ (upper left), $U = 1.25D$ (upper right), $U = 1.5D$ (lower left) and $U = 1.75D$ (lower right). The insets show the Hubbard bands.

peak is not expected. This statement does not apply for $\mu$ being so large that the energy of the double occupied states reaches the energy of the single occupied states which happens when the upper Hubbard band becomes a shoulder of the quasi-particle peak or merges with. Then, the quasi-particle weight increases considerably. This is illustrated by the spectral densities for $U = 1.5D$ or $U = 1.75D$. Changing $\mu$ from $0 \rightarrow 0.25D$ yields shifted Hubbard bands but the shape of the quasi-particle peak stays constant. But for $\mu = 0.75D$, the upper Hubbard band has merged with the quasi-particle peak and the quasi-particle peak becomes much broader.

Spectral densities for larger repulsions are shown in Fig. 5.32. Due to the larger Coulomb repulsion, the deviation from half-filling decreases (see Tab. 5.4 for the particular values). In contrast to lower Coulomb repulsion (see Fig. 5.31), the heights of the maxima of the Hubbard bands for larger Coulomb repulsions stay constant. As for lower Coulomb repulsions, $\mu$ shifts the upper Hubbard band towards the quasi-particle peak and the lower Hubbard band towards lower energies.

The Hubbard bands for $U \geq 2.0D$ show the sharp feature at the inner side which was already found for the half-filled case. The spectral densities in Fig. 5.32 exhibit this sharp feature at the inner side of the Hubbard bands also for the doped case. For increasing $\mu$, the feature persists at the lower Hubbard band but it diminishes considerably at the upper Hubbard band. Since the physical origin of this feature is still not fully understood, no physical reason can be given for this finding. The cases

| | $\mu = 0.1D$ | | | | | $\mu = 0.25D$ | | | | |
|---|---|---|---|---|---|---|---|---|---|---|
| $U/D$ | $n_G$ | $n_\Sigma$ | st. DMRG | $\Delta n_G$ | $\Delta n_\Sigma$ | $n_G$ | $n_\Sigma$ | st. DMRG | $\Delta n_G$ | $\Delta n_\Sigma$ |
| 1.00 | 0.542 | 0.524 | 0.522 | 0.038 | 0.003 | 0.577 | 0.589 | 0.588 | -0.019 | 0.001 |
| 1.25 | — | — | — | — | — | 0.562 | 0.576 | 0.574 | -0.021 | 0.002 |
| 1.50 | 0.535 | 0.525 | 0.515 | 0.038 | 0.019 | 0.548 | 0.565 | 0.561 | -0.024 | 0.006 |
| 1.75 | 0.531 | 0.528 | 0.512 | 0.038 | 0.031 | 0.537 | 0.556 | 0.550 | -0.025 | 0.012 |
| 2.00 | 0.528 | 0.532 | 0.509 | 0.037 | 0.045 | 0.524 | 0.550 | 0.539 | -0.028 | 0.020 |
| 2.30 | 0.524 | 0.536 | 0.506 | 0.036 | 0.058 | 0.511 | 0.545 | 0.527 | -0.031 | 0.034 |
| 2.50 | 0.522 | 0.537 | 0.504 | 0.034 | 0.064 | 0.503 | 0.543 | 0.520 | -0.033 | 0.043 |
| 2.70 | — | — | — | — | — | 0.517 | 0.529 | 0.511 | 0.011 | 0.035 |
| 2.80 | — | — | — | — | — | 0.519 | 0.528 | 0.507 | 0.024 | 0.042 |

| | $\mu = 0.50D$ | | | | | $\mu = 0.75D$ | | | | |
|---|---|---|---|---|---|---|---|---|---|---|
| $U/D$ | $n_G$ | $n_\Sigma$ | st. DMRG | $\Delta n_G$ | $\Delta n_\Sigma$ | $n_G$ | $n_\Sigma$ | st. DMRG | $\Delta n_G$ | $\Delta n_\Sigma$ |
| 1.00 | 0.662 | 0.680 | 0.681 | -0.027 | 0.000 | 0.768 | 0.751 | 0.752 | 0.021 | -0.002 |
| 1.25 | — | — | — | — | — | 0.733 | 0.718 | 0.720 | 0.019 | -0.003 |
| 1.50 | 0.631 | 0.613 | 0.613 | 0.030 | 0.001 | 0.702 | 0.687 | 0.690 | 0.017 | -0.004 |
| 1.75 | — | — | — | — | — | 0.672 | 0.659 | 0.662 | 0.015 | -0.005 |
| 2.00 | 0.592 | 0.580 | 0.575 | 0.028 | 0.009 | 0.645 | 0.633 | 0.636 | 0.013 | -0.005 |
| 2.30 | 0.570 | 0.566 | 0.556 | 0.025 | 0.017 | 0.614 | 0.605 | 0.608 | 0.010 | -0.005 |
| 2.50 | 0.557 | 0.557 | 0.544 | 0.023 | 0.024 | 0.595 | 0.587 | 0.590 | 0.009 | -0.006 |
| 2.70 | 0.549 | 0.543 | 0.533 | 0.031 | 0.020 | 0.578 | 0.571 | 0.574 | 0.008 | -0.005 |
| 2.80 | 0.543 | 0.541 | 0.528 | 0.030 | 0.025 | 0.555 | 0.575 | 0.571 | -0.029 | 0.007 |

Table 5.4: Filling $n$ as a function of repulsion $U$ and chemical potential $\mu$. The filling $n_G$ is obtained from the Green function $G$ by the formula $n = \int_{-\infty}^{0} \rho_G \mathrm{d}\omega$. The filling $n_\Sigma$ is obtained from the self-energy $\Sigma$ by the sum rule $\int_{-\infty}^{\infty} \rho_\Sigma \mathrm{d}\omega = U^2 n_\Sigma (1 - n_\Sigma)$. The columns named with "st. DMRG" show the filling obtained by static DMRG. The columns named with $\Delta n_X$ shows the relative error of the filling $n$ obtained via the dynamic quantity $X$ with the static DMRG result as a reference. For the missing values, the DMFT cycle unfortunately did not converged.

for $U = 2.3D$ and $U = 2.5D$ (for $\mu = 0.75$) show that the persistence of this sharp feature at the lower Hubbard band is stronger than for the upper Hubbard band.

Now, we turn to spectral densities for fixed filling. We restrict ourselves to Coulomb repulsions $U \geq 2.0D$. Results for $n = 0.55$ and $n = 0.65$ are shown in Fig. 5.33. We see that the right edge of the upper Hubbard band is fixed for one value of $n$. For increasing Coulomb repulsion, the minimum between the upper Hubbard band and the quasi-particle peak deepens only slightly whereas the analogous minimum for negative frequencies deepens and broadens considerably. For increasing $U$ and $n = 0.55$, the lower Hubbard band gains considerable spectral weight. The sharp feature at the inner side of the Hubbard bands for $n = 0.55$ decreases at the upper Hubbard band but persists at the lower Hubbard band. For $n = 0.65$, the upper Hubbard band becomes a shoulder of the quasi-particle peak. The lower Hubbard band changed its form and resembles a triangle. Inspecting the inner side of the lower Hubbard band, we cannot distinguish between the sharp feature and the band anymore. In contrast to the spectral density for $n = 0.55$, the height of the maximum of the lower Hubbard band increases for increasing $U$. An increasing height as a function of $U$ is a known property of the sharp feature at the inner side of the Hubbard bands, see Refs. [103, 104, 105]. But an increasing height of the Hubbard bands on increasing $U$ has not been found before. In order to understand the

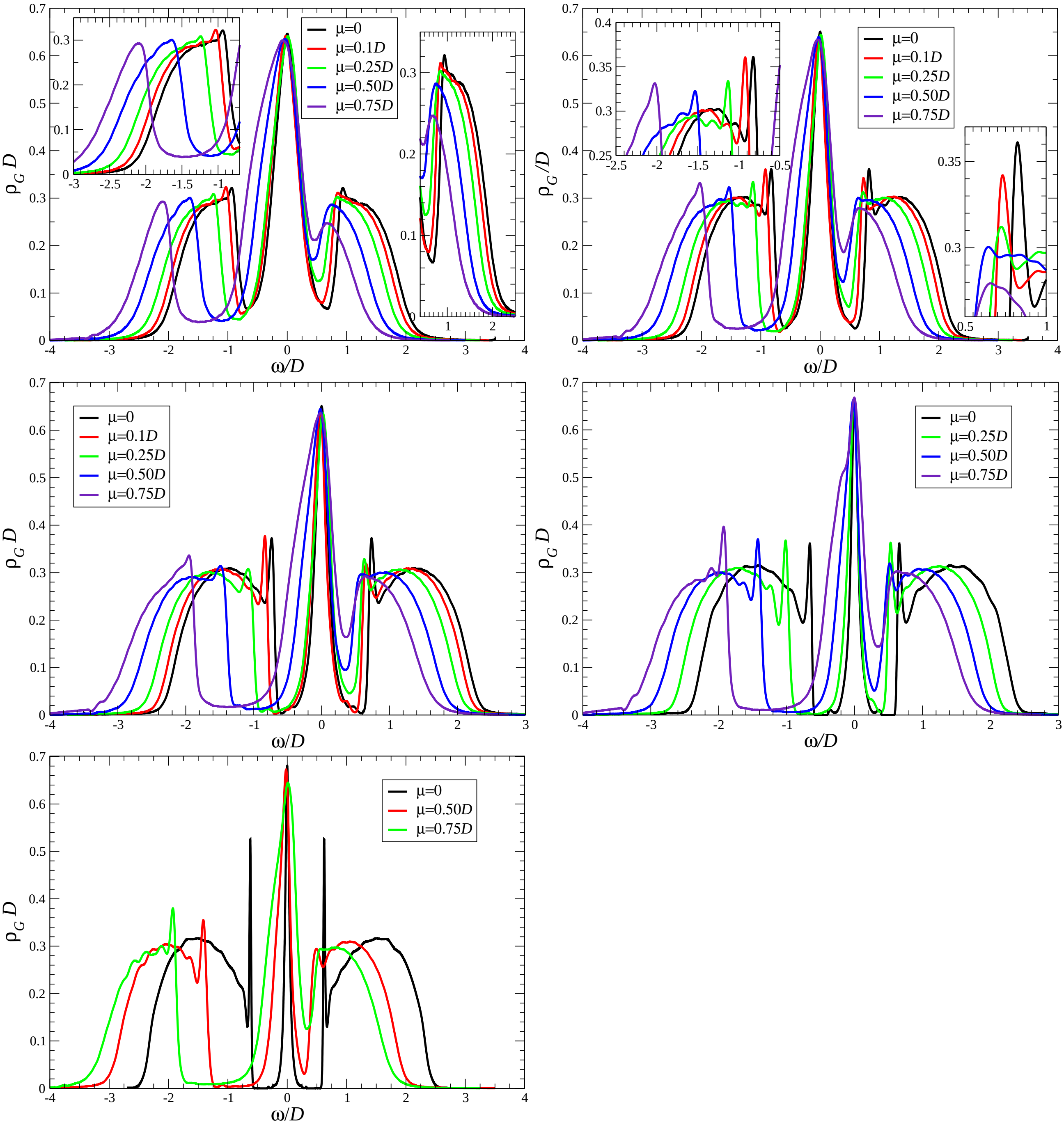

Figure 5.32: Spectral densities $\rho_G$ for $U = 2D$ (upper left), $U = 2.3D$ (upper right), $U = 2.5D$ (middle left), $U = 2.7D$ (middle right) and $U = 2.8D$ (lower left) for several values of $\mu$ (see legends).

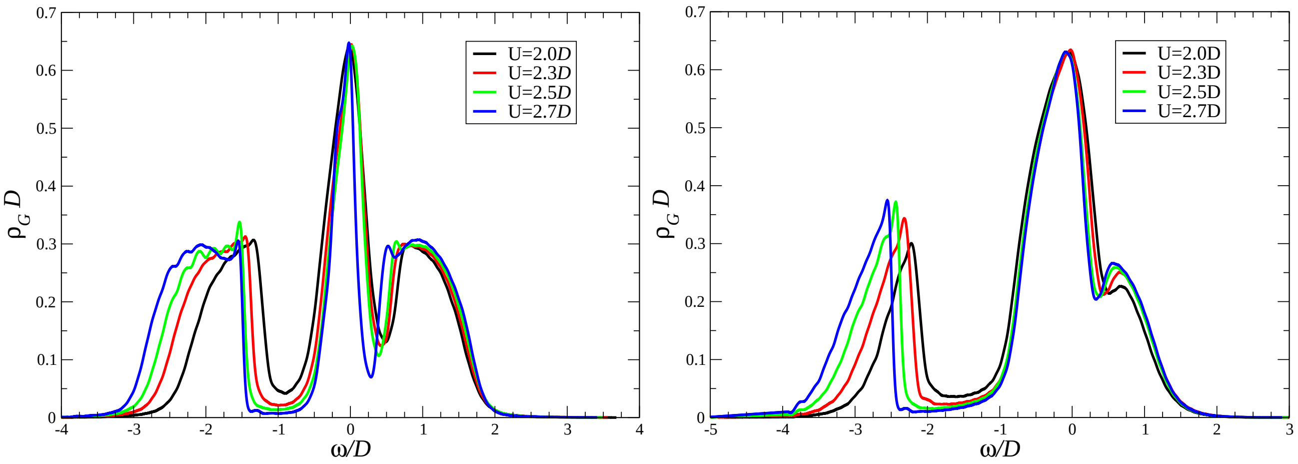

Figure 5.33: Spectral densities $\rho_G$ for fixed filling $n = 0.55$ (left) and $n = 0.65$ (right) for several Coulomb repulsions $U$ (see legends).

increasing height of the Hubbard bands on increasing $U$ seen in the right panel of Fig. 5.33, we may speculate that the sharp feature and the band merged.

As for the half-filled case in Sec. 5.4, we postpone the analysis of the quasi-particle weight to Sec. 5.5.3 where the self-energy is analyzed.

In Sec. 5.1 on page 80, we compared spectral densities of the SIAM for the semielliptic DOS obtained by D-DMRG and ENCA. We saw from Fig. 5.1 that both methods yield comparable results. Therefore, it is reasonable to compare both methods in a DMFT calculation. This is shown in Fig. 5.34 where D-DMRG and ENCA results (the latter from Ref. [176]) for two values of $U$ and $\mu$ are depicted. Note that ENCA does not work for $T = 0$. We see that the lower edge of the lower Hubbard band and the upper edge of the upper Hubbard band for both methods coincide. The spectral weight of the quasi-particle peak is much lower for ENCA than for D-DMRG. Since a higher temperature leads to a less high Kondo resonance, the different height of the Kondo resonance can to some extend be explained by the different temperatures D-DMRG and ENCA use. On the other hand, it is a known fact that the ENCA underestimates the width of the Kondo resonance for the SIAM, see Grewe [71] or the PhD-thesis of Schmitt [174] and the references therein. If we keep in mind that both densities exhibit equal norm and that the upper edge of the upper Hubbard band and the lower edge of the lower Hubbard band coincide for both methods, it is clear that ENCA has to shift the spectral weight that it has not located at the Kondo resonance towards the minima between the quasi-particle peak and the Hubbard bands. Hence, the upper Hubbard band in the ENCA curves becomes a shoulder to the quasi-particle peak and the right edge of the lower Hubbard band moves towards the quasi-particle peak. In contrast to the upper Hubbard band, the lower Hubbard band and the quasi-particle peak in the ENCA curves can clearly be distinguished. The sharp feature at the inner side of the Hubbard bands seen in the D-DMRG data for $U = 2.7D$ is absent in the ENCA data.

In view of the good agreement between both methods seen in Fig. 5.1, one may be surprised about the larger difference between both methods in a DMFT framework seen in Fig. 5.34. One rough explanation is the experience that differences between both methods in general amplify during the self-consistency cycles. However, a conclusive answer about the reason for the larger difference was not found in this thesis. We may explain the difference by the fact that distinct methods of calculating spectral densities unavoidably yield to different results. In contrast to the dynamic quantities, the

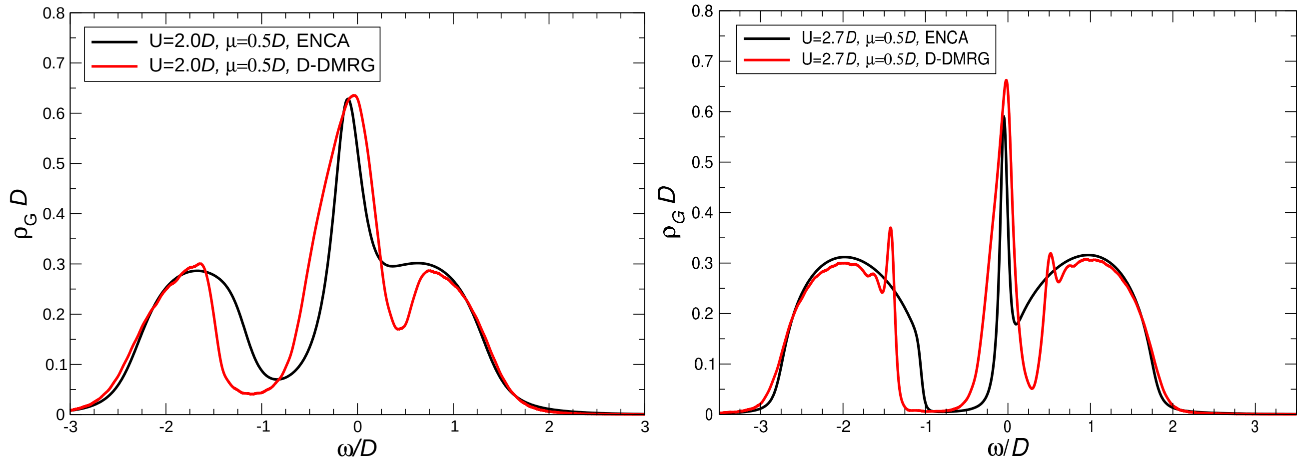

Figure 5.34: Comparison of the spectral density $\rho_G$ for $U = 2.0D$ & $\mu = 0.5D$ (left) and $U = 2.7D$ & $\mu = 0.5D$ (right) between ENCA (black curves) and D-DMRG (red curves). The temperature $T$ is $0.1D$ (left) and $0.03D$ (right). The ENCA data are taken from Ref. [176]. For discussion see text.

static quantities like the filling deviates much less. The filling for $U = 2D$ is $n = 0.575$ for D-DMRG and $n = 0.566$ for ENCA and for $U = 2.7D$ the filling is $n = 0.533$ for D-DMRG and $n = 0.520$ for ENCA, i.e. ENCA yields only by 1.6% (for $U = 2D$) or by 2.4% (for $U = 2.7D$) lower filling than D-DMRG which is a remarkably good agreement.

### 5.5.3 Local Self-Energies for the Doped Metal

In this section, we present local self-energies away from half-filling. Since we found in Sec. 5.2 that the Q-function cannot be used for the doped case and that hence self-energies could not be calculated directly, all self-energies for the doped case are calculated from $G$ and $G_0$ via the Dyson equation (3.5). We begin with results for small Coulomb repulsion. The imaginary part of the self-energies are shown in Fig. 5.35. The corresponding real part of the self-energies are shown in Fig. 5.36. They belong to the spectral densities $\rho_G$ shown in Fig. 5.31.

The spectral density $\rho_\Sigma$ consists of two maxima and vanishes quadratically for $\omega \to 0$ between both maxima in accordance to Fermi-liquid theory. The height of the maxima for positive frequencies decreases upon electron doping whereas the height of the maxima for negative frequencies is less affected by different dopings. The position of the maxima for negative frequencies moves to the left (larger negative frequencies) upon doping whereas the position of the maxima for positive frequencies is less affected by different dopings. Those shifts of the heights and positions of the maxima correspond to the result for the doping dependence of the Hubbard bands seen in Fig. 5.31. For increasing $\mu$, the lower Hubbard band moves to larger negative frequencies whereas the upper Hubbard band moves slower towards the quasi-particle peak and eventually merges with it.

The real part $\Re\Sigma$ of the self-energies exhibits a maximum for negative frequencies and a minimum for positive frequencies which correspond to the minimum between the quasi-particle peak and the Hubbard bands. Within the energy range where the quasi-particle peak is located, the real part of the self-energy is well approximated by a linear function. For increasing $\mu$, the depth of the minimum for

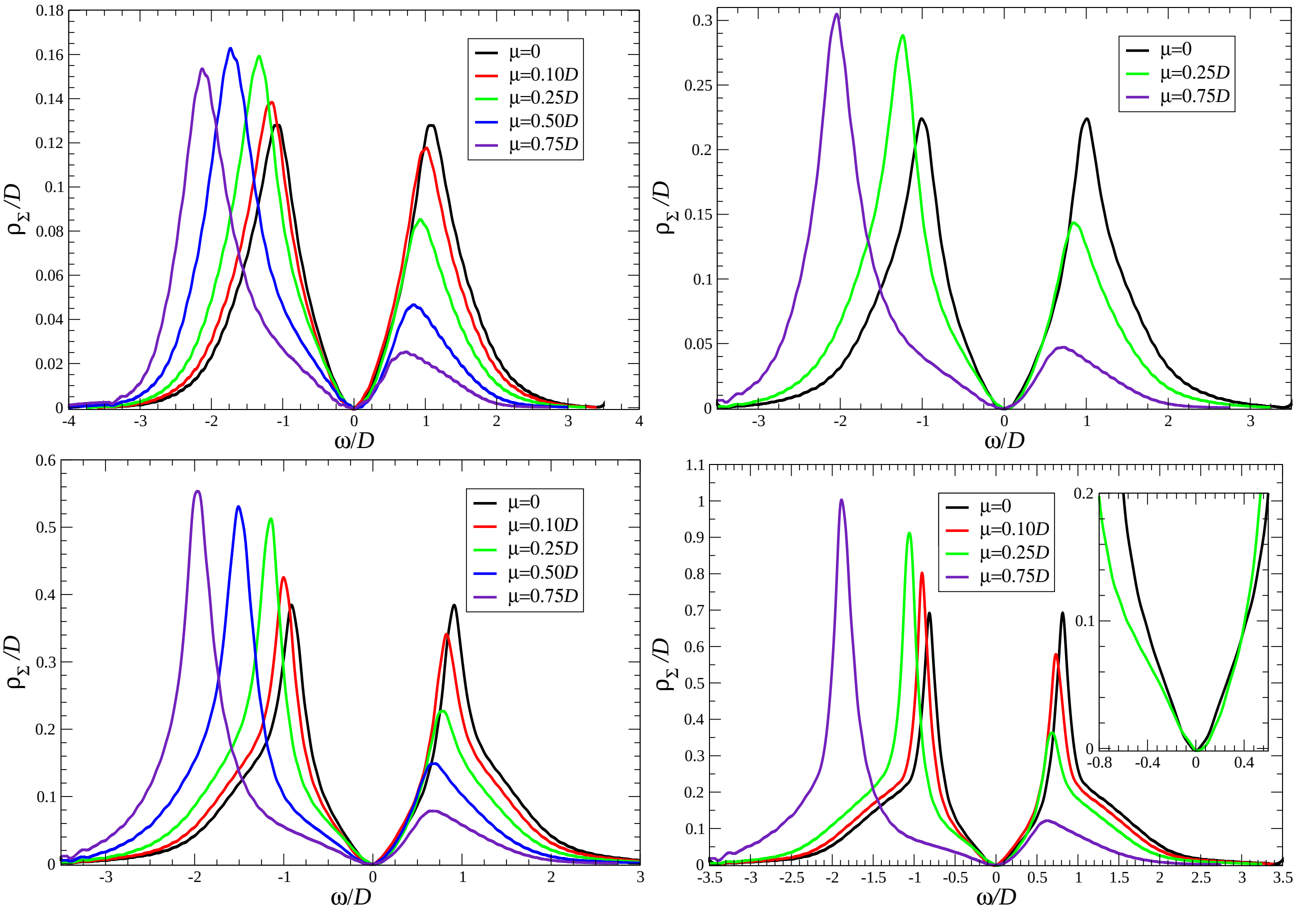

Figure 5.35: Spectral densities $\rho_\Sigma$ of the self-energy $\Sigma$ for $U = 1D$ (upper left), $U = 1.25D$ (upper right), $U = 1.5D$ (lower left) and $U = 1.75D$ (lower right) for several values of $\mu$ (see legends). The corresponding real part of the self-energies are shown in Fig. 5.36 and the corresponding Green functions are shown in Fig. 5.31.

positive frequencies decreases and the kink for positive frequencies becomes less pronounced or even vanishes (see e.g. for $U = 1.5D$ and $\mu = 0.5D$). In contrast, the kink for negative frequencies becomes more pronounced.

Spectral densities $\rho_\Sigma$ for larger Coulomb repulsions $U$ are shown in Fig. 5.37 and the corresponding real parts of the self-energy are shown in Fig. 5.38. They belong to the spectral densities $\rho_G$ shown in Fig. 5.32.

For larger Coulomb repulsion, the three-peak structure in $\rho_G$ has developed more clearly. Also the trough-like feature of $\rho_\Sigma$ in the vicinity of $\omega = 0$ can clearly be seen. For the doped metal, the trough is asymmetric. In particular, for positive frequencies the trough-like feature becomes less pronounced. As the case for $U = 2.5D$ and $\mu = 0.5D$ shows exemplarily, the trough-like feature can even vanish for positive frequencies. In contrast to the result for positive frequencies, we obtain for negative frequencies that the trough-like feature persists. The $\mu$-dependence of the maxima in $\rho_\Sigma$, which was already discussed for lower Coulomb repulsions, is also found here.

For larger Coulomb repulsions, the $\mu$-dependence of the real part $\Re\Sigma$ of the self-energy is analogous

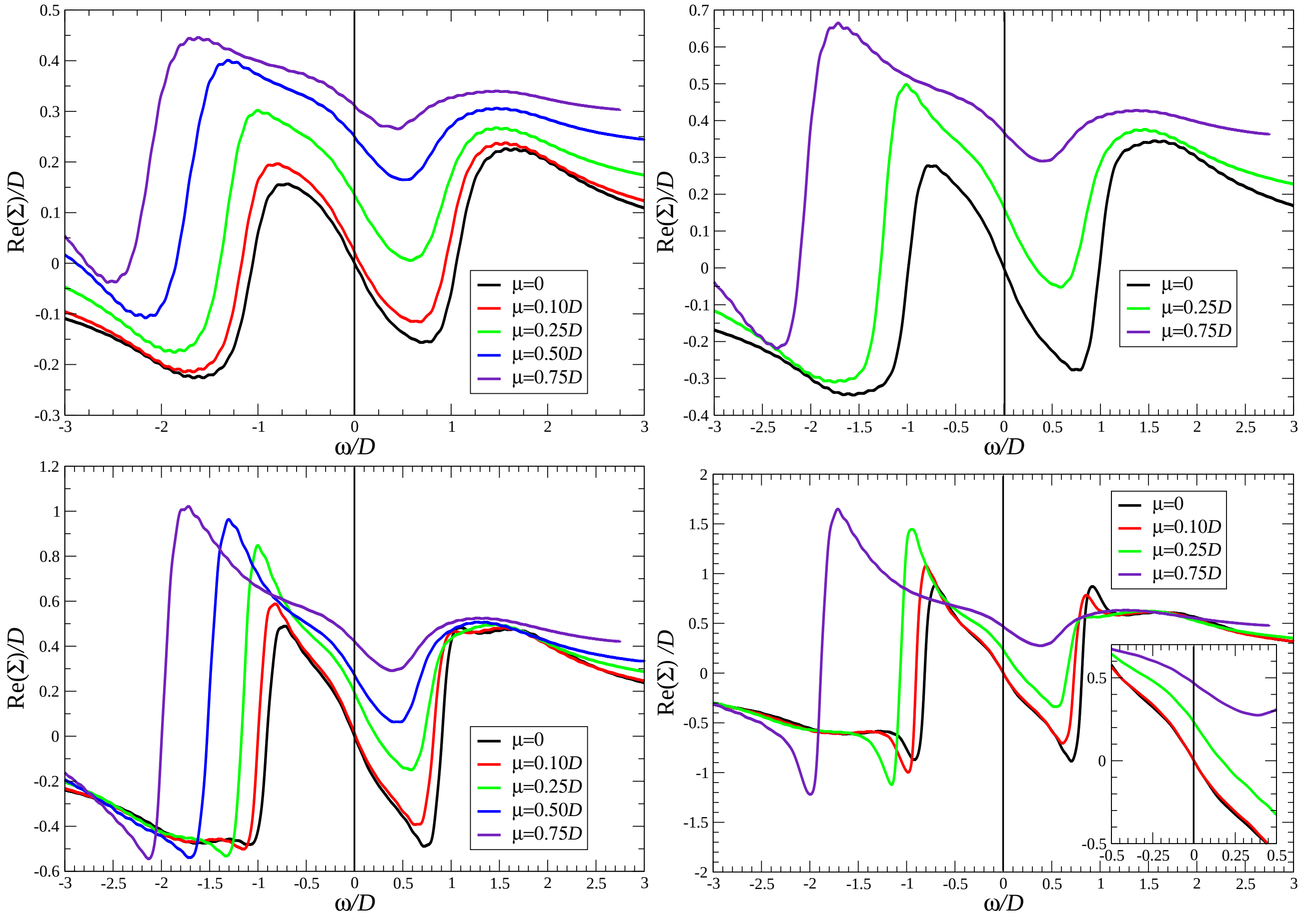

Figure 5.36: Real parts of the self-energy $\Sigma$ for $U = 1D$ (upper left), $U = 1.25D$ (upper right), $U = 1.5D$ (lower left) and $U = 1.75D$ (lower right) for several values of $\mu$ (see legends). The corresponding imaginary part of the self-energies are shown in Fig. 5.35 and the corresponding Green functions are shown in Fig. 5.31.

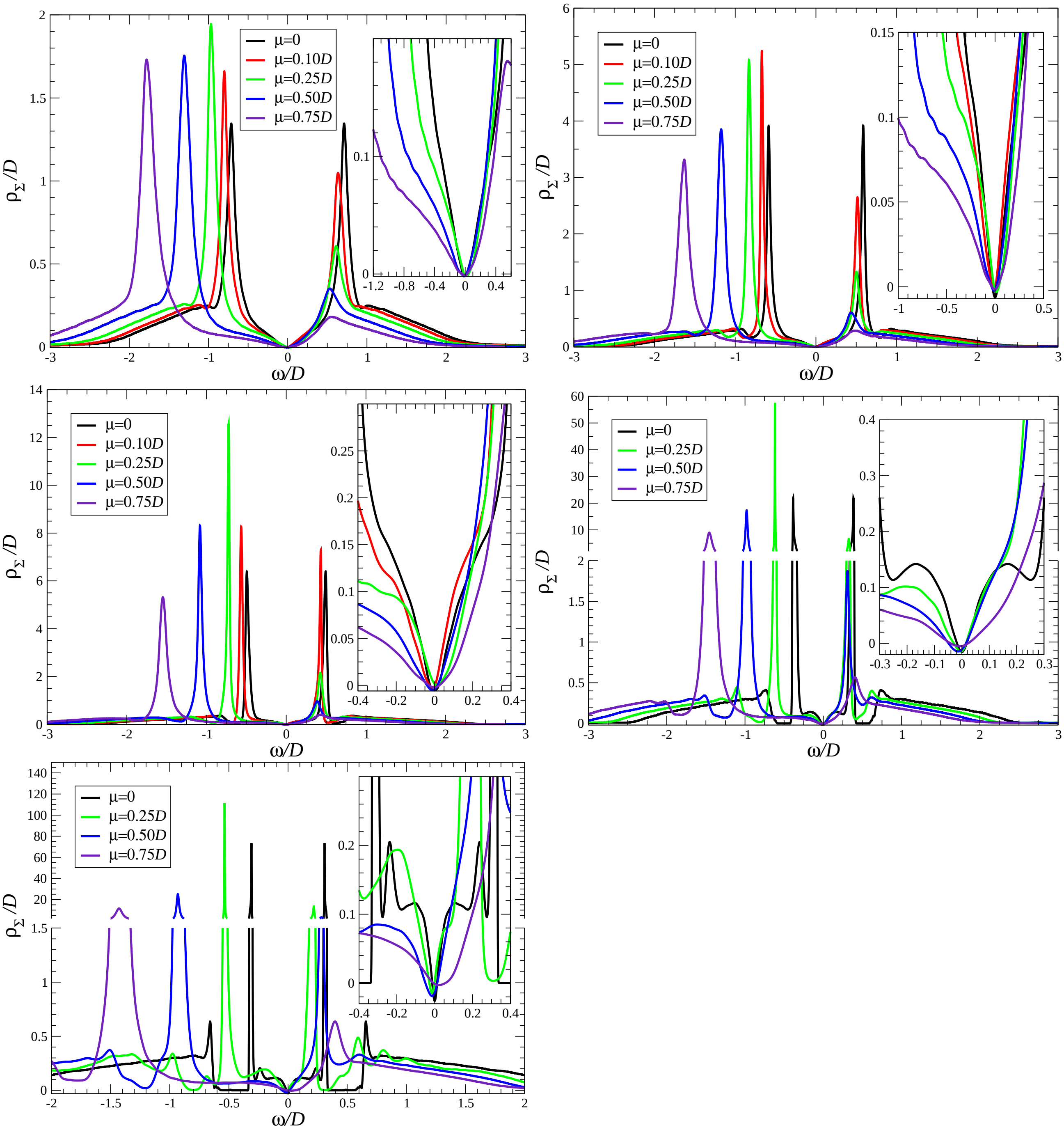

Figure 5.37: Spectral densities $\rho_\Sigma$ for $U = 2D$ (upper left), $U = 2.3D$ (upper right), $U = 2.5D$ (middle left), $U = 2.7D$ (middle right) and $U = 2.8D$ (lower left) for several values of $\mu$ (see legends). The insets show the trough-like feature.

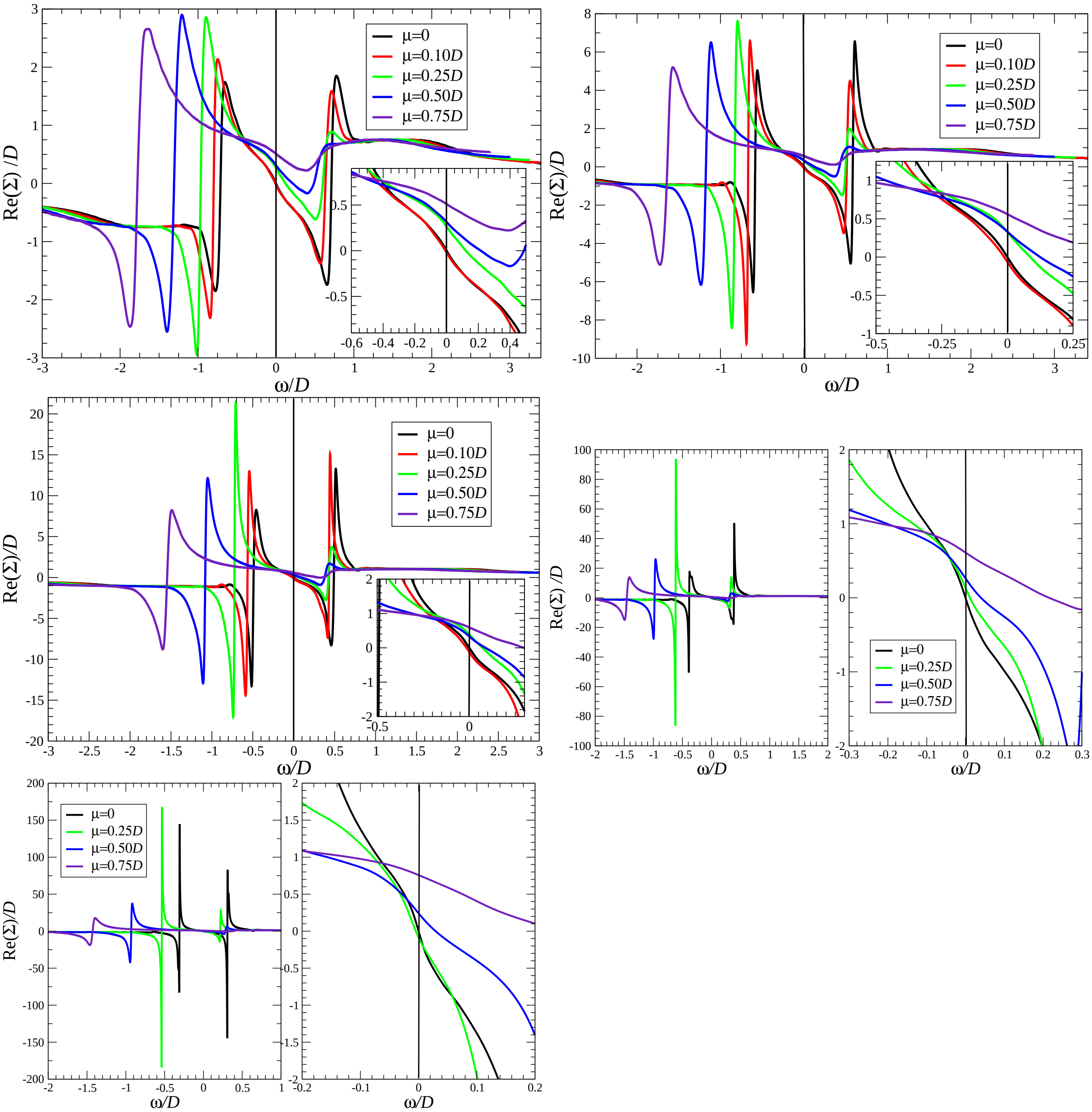

Figure 5.38: Real parts $\Re\Sigma$ of the self-energy for $U = 2D$ (upper left), $U = 2.3D$ (upper right), $U = 2.5D$ (middle left), $U = 2.7D$ (middle right) and $U = 2.8D$ (lower left) for several values of $\mu$ (see legends). The insets show the kinks.

to the result for lower Coulomb repulsion, i.e. for increasing $\mu$ the height of the maxima for negative frequencies rises and the depth of the minima for positive frequencies diminishes. In some cases, the depth of this minimum diminishes so much that the nearby kink for positive frequencies vanishes (e.g. for $U = 2.3D$ and $\mu = 0.75D$). This result is analogous to the finding that the trough-like feature in $\rho_\Sigma$ is more pronounced for negative frequencies than for positive frequencies. This also corresponds to the finding for $\rho_G$ that the upper Hubbard band begins to merge with the quasi-particle peak.

Next, we discuss the self-energies for fixed filling. The self-energies for $n = 0.55$ and for $n = 0.65$ are shown in Fig. 5.39. The findings do not differ from the analysis of the $\mu$-dependence of the Green functions. For increasing $U$, the Hubbard bands separate more clearly from the quasi-particle peak and the corresponding maxima in $\rho_\Sigma$ rise. The left Hubbard band is better separated from the quasi-particle peak than the right Hubbard band so the left maximum is more pronounced than the right maximum. The trough is asymmetric, i.e. it is more pronounced for negative frequencies than for positive frequencies. Analogous to this finding is that the kinks are more pronounced for negative frequencies than for positive frequencies.

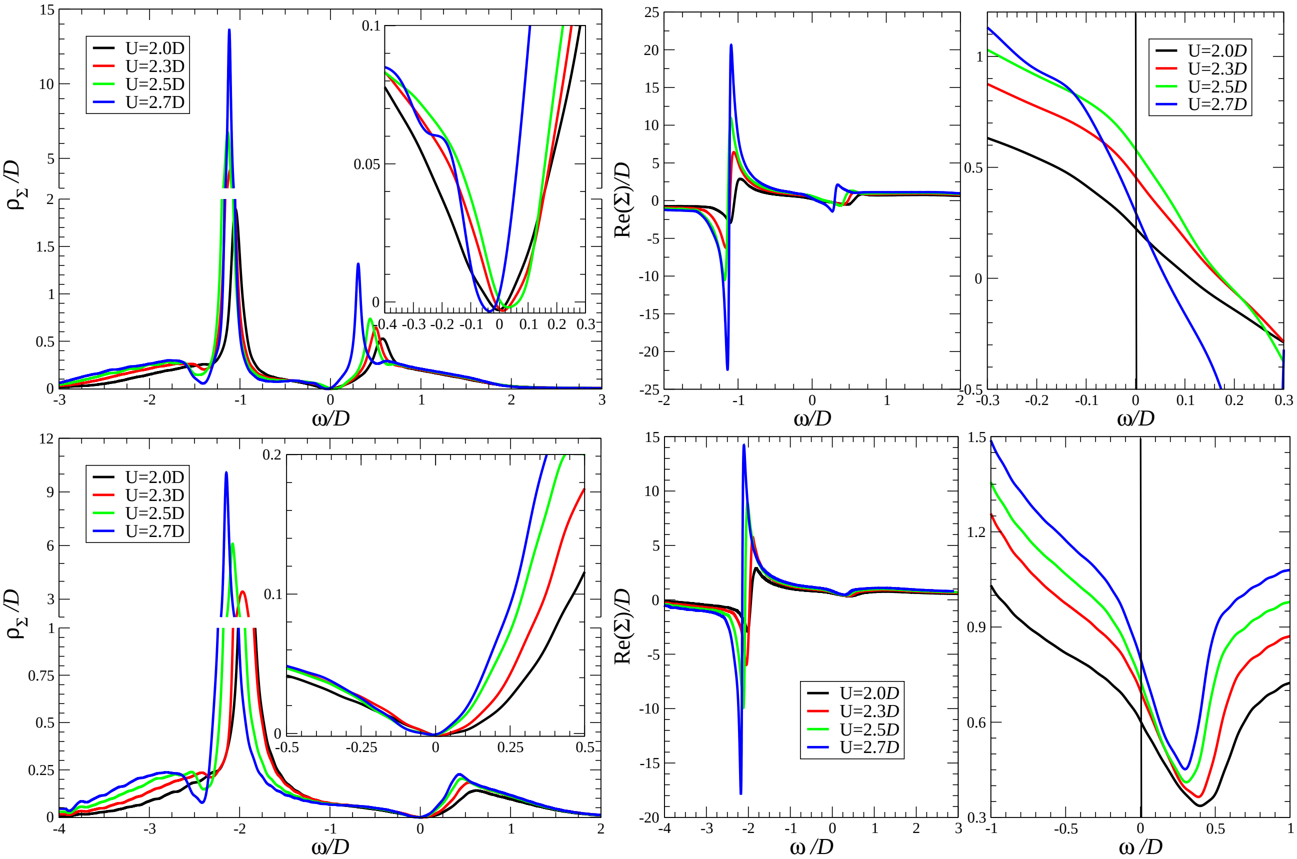

Figure 5.39: $\rho_\Sigma$ (left) and real part $\Re\Sigma$ (right) of the selfenergy $\Sigma$ for filling $n = 0.55$ (upper row) and $n = 0.65$ (lower row).

From the slope $s$ of the real part of the self-energy at $\omega = 0$, one can calculate the quasi-particle weight $Z$ via $Z = 1/(1-s)$. Those values $Z$ are shown in Fig. 5.40 as a function of the repulsion $U$ for the particular values of $\mu$.

For the particular values of $\mu$, one can extrapolate $Z(U)$ to find the critical value $U_{c2}$ when the

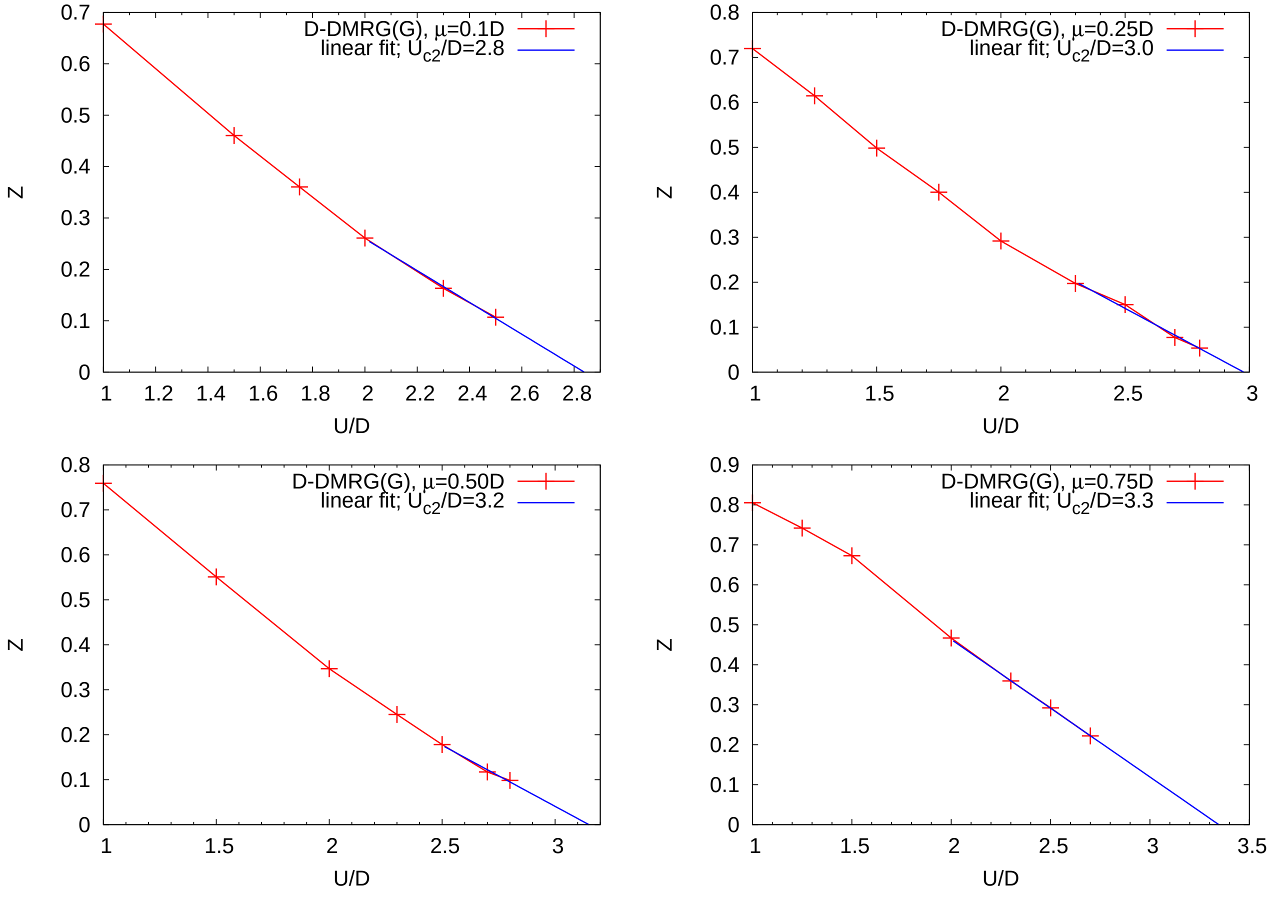

Figure 5.40: Quasi-particle weight $Z$ as a function of repulsion $U$ for $\mu = 0.1D$ (upper left), $\mu = 0.25D$ (upper right), $\mu = 0.5D$ (lower left) and $\mu = 0.75D$ (lower right). The linear fits are calculated with the last three (left column) or four (right column) data points. For the critical repulsion $U_{c2}$ where the metal-insulator transition occurs, see legends.

| $\mu/D$ | $U_{c2}/D$ (our results) | $U_{c2}/D$ (from Miranda et al.) |
|---|---|---|
| 0.10 | 2.8 | $\approx 2.9$ |
| 0.25 | 3.0 | $\approx 3.1$ |
| 0.50 | 3.2 | $\approx 3.3$ |
| 0.75 | 3.3 | — |

Table 5.5: Critical Coulomb repulsion $U_{c2}$ where the metal-insulator transition occurs for the particular values of $\mu$. In the third column, we show the results of Miranda et al. [137]. With "$\approx$", we indicate that we extracted those values from a figure. Especially for $\mu = 0.25D$, we had to interpolate between two data points.

quasi-particle weight vanishes. For the half-filled case, this vanishing implies that the metal-insulator transition occurs. Here, we consider the doped case away from half-filling. Note that in a strict sense there is no metal-to-insulator transition away from half-filling. But increasing $U$ drives the system even for $\mu \neq 0$ back towards half-filling which re-enables the possibility of a metal-insulator transition. The function $Z(U)$ and the linear extrapolation to $Z = 0$ is shown in Fig. 5.40. The particular values of $U_{c2}$ are shown in Tab. 5.5 where we also show the results of Miranda et al. [137]. The differences are between two and five percent and they are likely due to the different methods for obtaining dynamical quantities and to the extrapolation.

### 5.5.4 Local Susceptibilities for the Doped Metal

In this section, we present the results for local susceptibilities for the doped case, i.e. away from half-filling. Away from half-filling, charge and Cooper-pair susceptibility are not the same anymore since the mentioned SO(5) symmetry (see Sec. 5.4.1 on page 92) does not hold. We again show only the imaginary part of $\chi^>$ for the same reason we mentioned at the end of Sec. 5.4.1.

We begin the discussion with the local spin susceptibility. For all values of $U$ and $\mu$, $\Im\chi^>$ consists of one peak which height increases and width decreases on increasing $U$. For increasing $\mu$, the height of the maximum decreases and the peak becomes broader. For low values of $U$, $\Im\chi^>$ are shown in Fig. 5.42 and for larger values of $U$ $\Im\chi^>$ are shown in Fig. 5.43. For fixed filling, $\Im\chi^>$ are shown in Fig. 5.41. In the latter Fig. 5.41 for fixed filling, the $U$ dependence is shown. We see there that the position of the maximum of the peak moves towards smaller frequencies. This behavior was also found for the half-filled case, see Secs. 5.4.1, 5.4.2.3, 5.4.3.3 and Ref. [164].

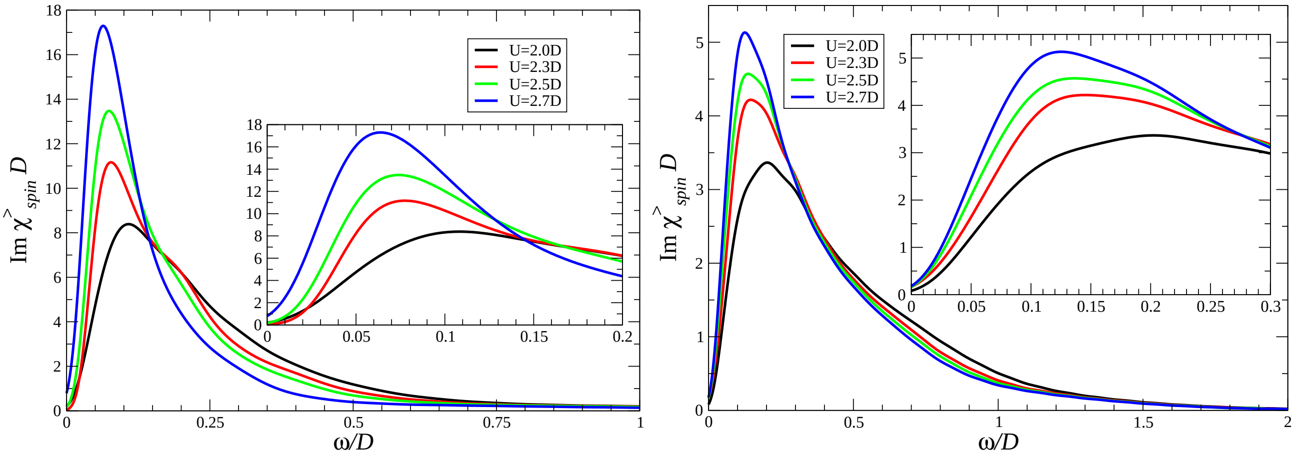

Figure 5.41: Imaginary part of the spin susceptibility $\chi^>$ for filling $n = 0.55$ (left) and $n = 0.65$ (right) for several values of $U$ (see legends).

The physical interpretation of the found $\mu, U$-dependence in the spin susceptibility is that for increasing $\mu$ the number of single occupied sites decreases which suppresses the magnetic response. For increasing $U$, the system is driven towards half-filling again implying more single occupied sites and hence an enlarged magnetic response.

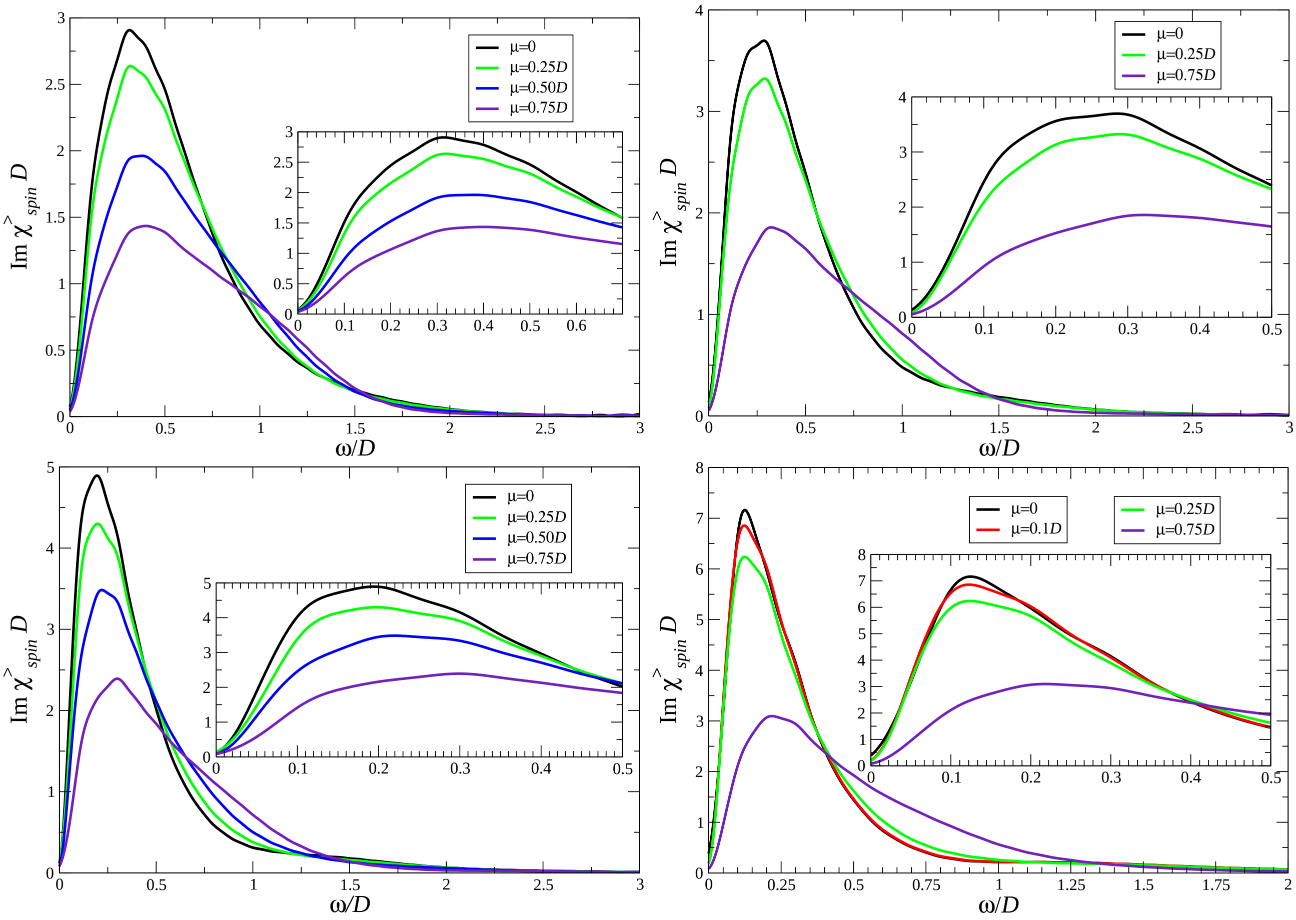

Figure 5.42: Imaginary part of the spin susceptibility $\chi^>$ for $U = D$ (upper left), $U = 1.25D$ (upper right), $U = 1.5D$ (lower left) and $U = 1.75D$ (lower right) for several values of $\mu$ (see legends). The height of the peak increases on increasing $U$ and decreases on increasing $\mu$.

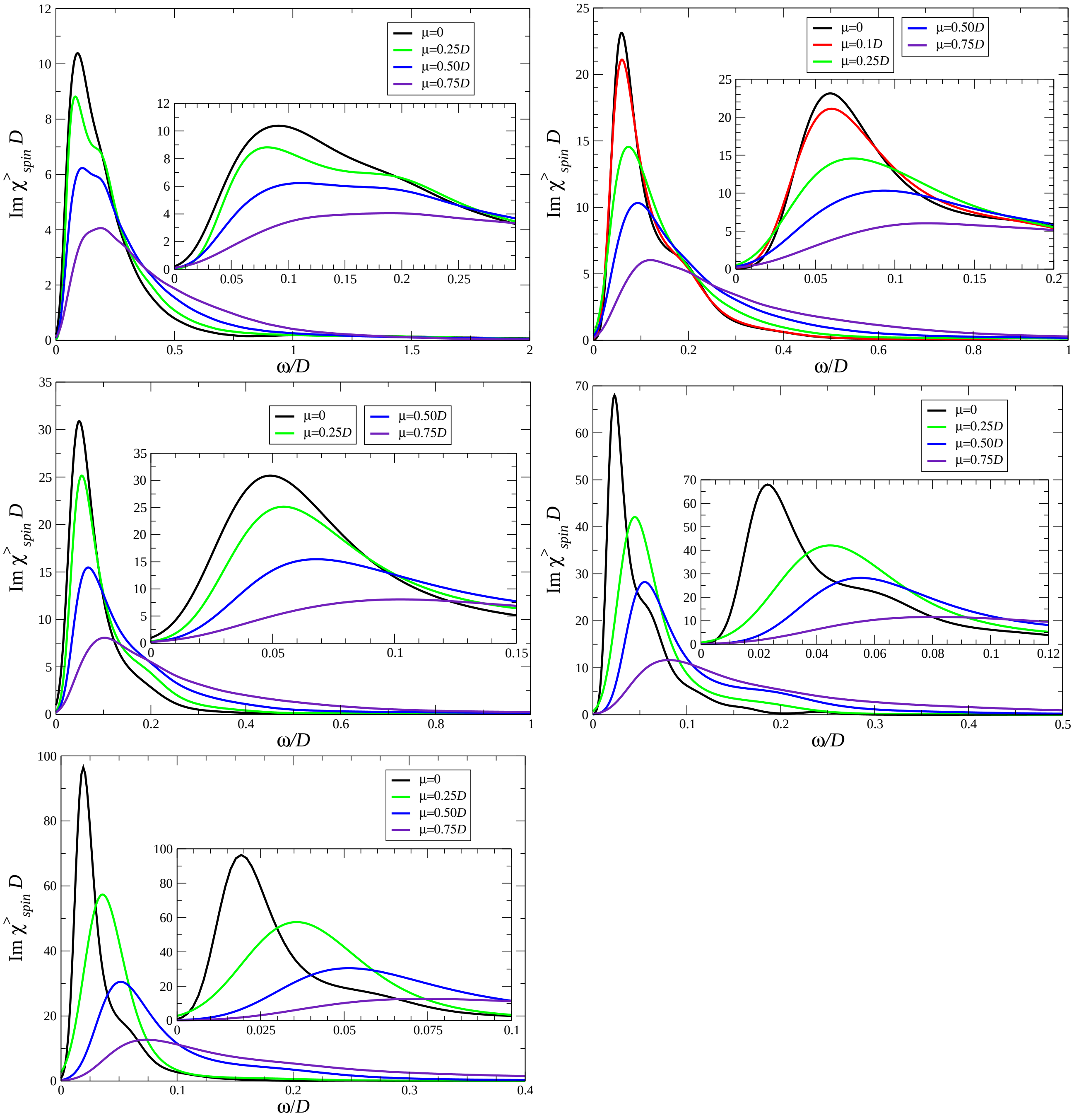

Figure 5.43: Imaginary part of the spin susceptibility $\chi^{>}$ for $U = 2D$ (upper left), $U = 2.3D$ (upper right), $U = 2.5D$ (middle left), $U = 2.7D$ (middle right) and $U = 2.8D$ (lower left) for several values of $\mu$ (see legends). The height of the peak increases with increasing $U$ and decreases with increasing $\mu$.

Next, we discuss the charge susceptibility. For the half-filled case, the local excitation operator reads $d_\uparrow^\dagger d_\uparrow + d_\downarrow^\dagger d_\downarrow - 1$. This operator measures density fluctuations around half-filling; the latter is indicated by $1 = \langle n_\uparrow \rangle + \langle n_\downarrow \rangle$. We still consider the paramagnetic metal, i.e. $\langle n_\uparrow \rangle = \langle n_\downarrow \rangle$ still holds but the sum of both expectation values does not equal one. After having implemented this deviation from the half-filled case, it was tested that for $\mu = 0$ the same charge susceptibilities are obtained as before (not shown). The program passed this test. The results for $\Im\chi^>$ of the charge susceptibility for low values of $U$ are shown in Fig. 5.44. For larger values of $U$, the results are shown in Fig. 5.45 and for fixed filling the results are shown in Fig. 5.46.

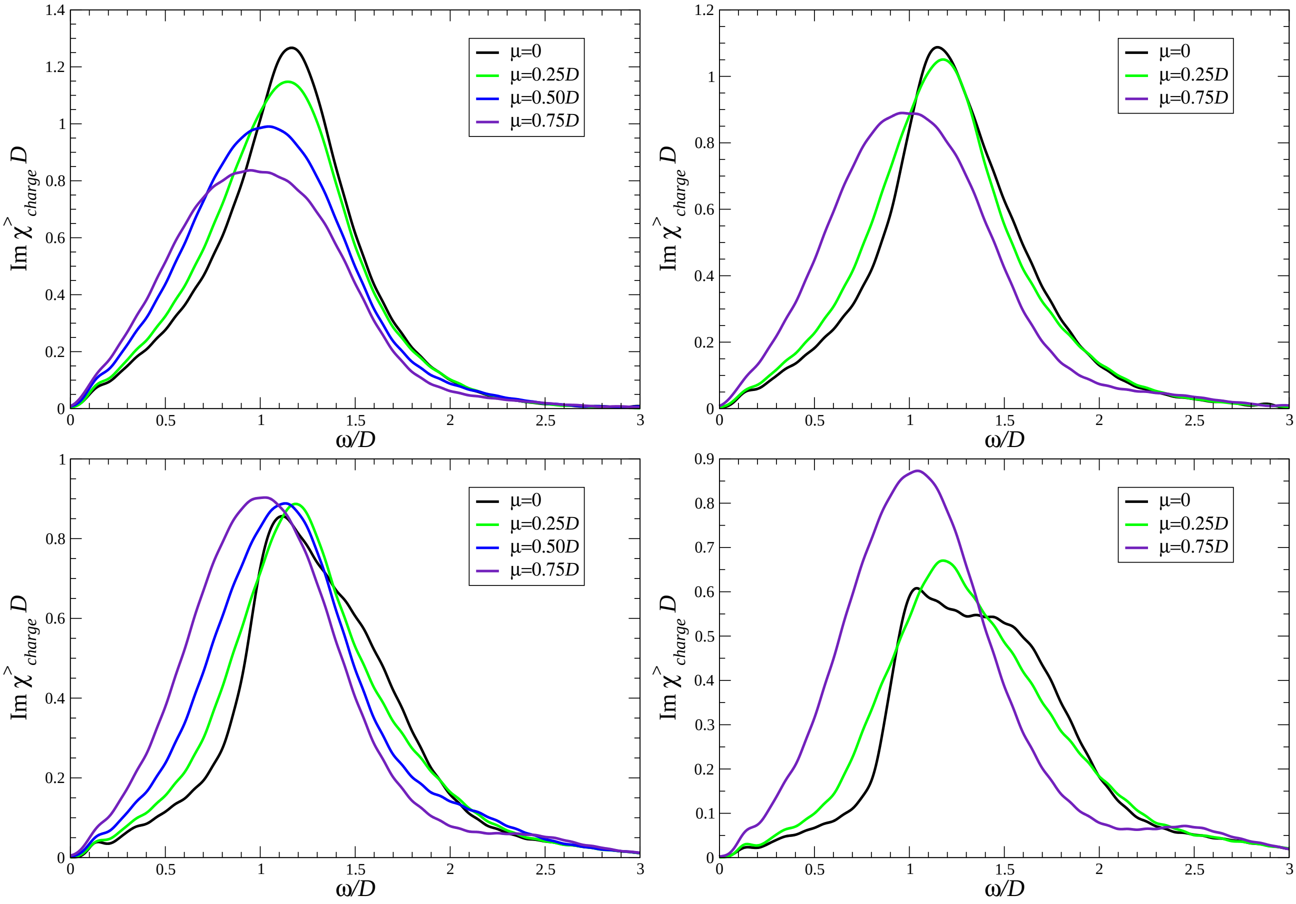

Figure 5.44: Imaginary part of the charge susceptibility $\chi^>$ for $U = D$ (upper left), $U = 1.25D$ (upper right), $U = 1.5D$ (lower left) and $U = 1.75D$ (lower right) for several values of $\mu$ (see legends).

As we saw in the half-filled case, for low repulsion $U$ the charge susceptibility begins with a linear slope up to a maximum after which a more or less monotonous decrease is obtained. For increasing repulsion, the linear slope is suppressed but it can be restored by increasing $\mu$. Roughly speaking, this finding corresponds to the fact that the system becomes more metallic on electron doping.

For larger $U$ and low $\mu$, the charge susceptibility consists mainly of a structure that is similar to the shape and position of the upper Hubbard band. The sharp peak at the inner side of the Hubbard band was also visible in the charge susceptibility for the half-filled case. Even for low values of $\mu$, we see in the charge susceptibility that this feature smears out faster than in the spectral densities $\rho_G$.

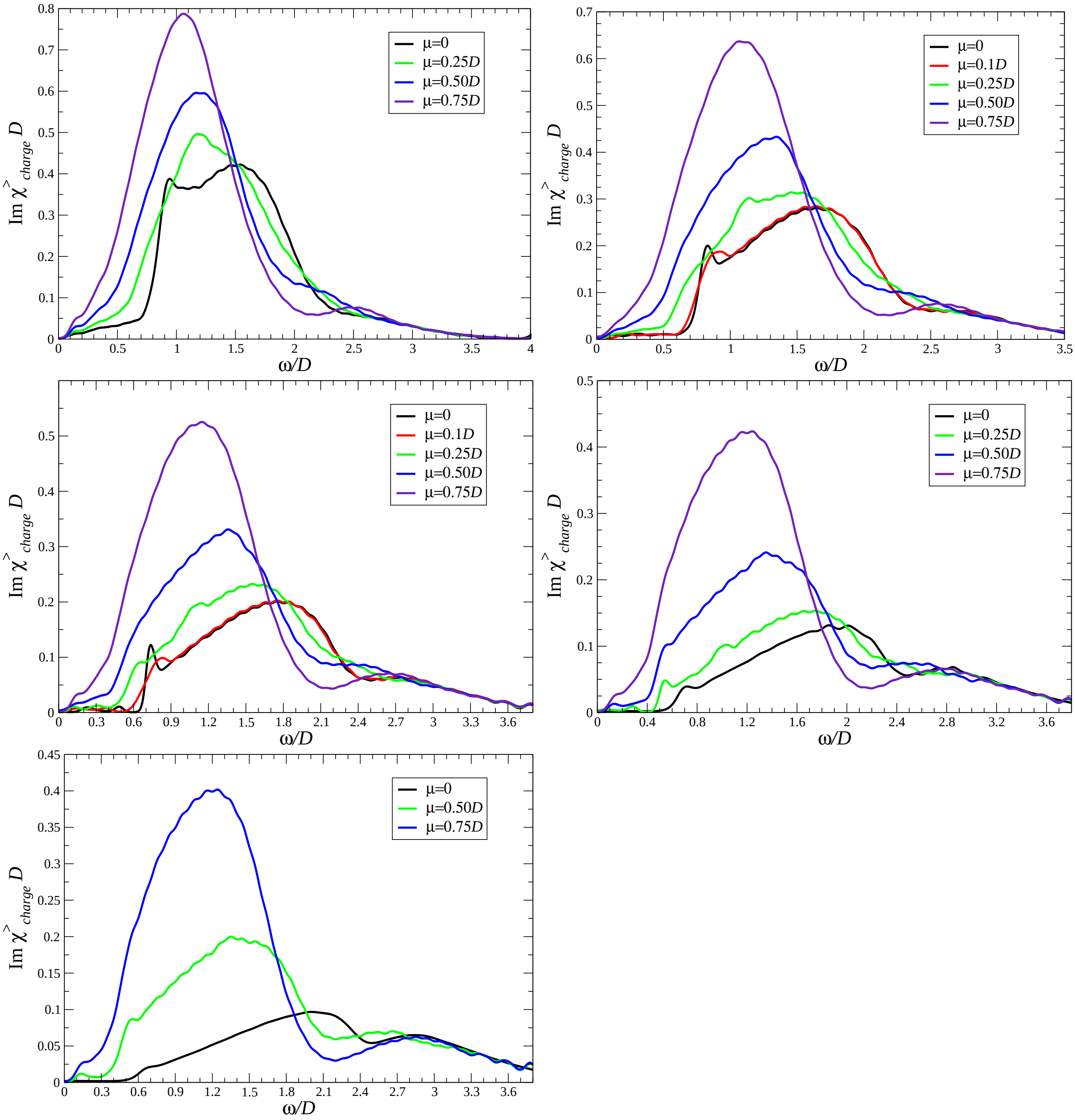

Figure 5.45: Imaginary part of the charge susceptibility $\chi^{>}$ for $U = 2D$ (upper left), $U = 2.3D$ (upper right), $U = 2.5D$ (middle left), $U = 2.7D$ (middle right) and $U = 2.8D$ (lower left) for several values of $\mu$ (see legends).

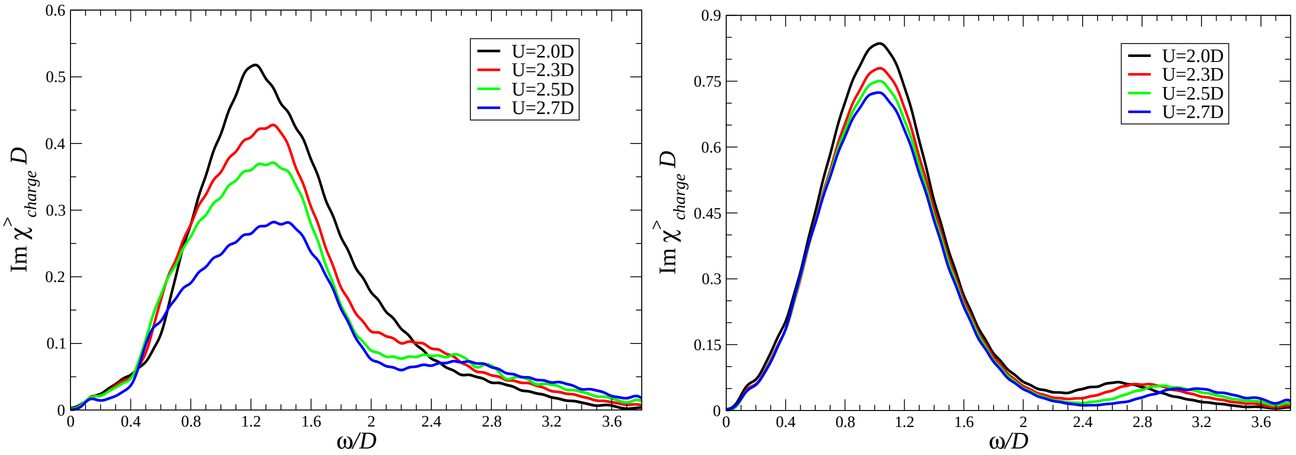

Figure 5.46: Imaginary part of the charge susceptibility $\chi^{>}$ for $n = 0.55$ (left) and $n = 0.65$ (right) for several values of $U$ (see legends).

This statement can be inferred from the charge susceptibility for $U \geq 2.3D$ (upper right panel of Fig. 5.45). For all $\mu \neq 0$, the sharp feature in $\rho_G$ (see upper right panel of Fig. 5.32) is visible but it fades away in the charge susceptibility.

However, the statement that even for large repulsion $U$ the system behaves like a weakly correlated metal (i.e. low repulsion $U$) does not tell the whole story. For energies larger than the broad structure (i.e. $\omega \geq 2.0D$), we see for larger $U$ a small hump in the charge susceptibility that is absent for low repulsions. Hence, there is a physical difference between the electron doped high-repulsion case and the low-repulsion case which we need to explain here. As a first step, we recognize that the position of this hump approximately coincides with the position of the lower Hubbard band. The following analogy can be drawn between $\rho_G$ and the charge susceptibility: For large Coulomb repulsion $U$ and $\mu = 0$, $\rho_G$ exhibits a lower and an upper Hubbard band and the quasi-particle peak. For those cases, the charge excitations for low frequencies are suppressed. For increasing $\mu$, the upper Hubbard band moves towards the quasi-particle peak and merges with it. Roughly speaking and restricted to small frequencies, $\rho_G$ for large $U$ and $\mu$ does not differ very much from the case with low repulsion; i.e. the system behaves like a weakly correlated metal. Hence, we see that the linear slope of the charge susceptibility for small $\omega$, that is suppressed on increasing $U$, can be restored by increasing $\mu$. This statement holds if only low frequencies $\omega$ are considered. But considering a larger frequency range for $\rho_G$, we clearly see a difference between low repulsion $U$ and large $U$ *and* large $\mu$, because the lower Hubbard band occurs. This difference is also seen in the charge susceptibility in the occurrence of the small hump after the large peak.

The physical picture behind the finding described above is the following. Increasing $\mu$ leads to more double occupied sites which enables more electron hopping, i.e. the system becomes more metallic. This leads to more particle-hole excitations at smaller energies which is seen as the increased charge excitation. For increasing $U$, the number of double occupied sites is decreased again, electron hopping is impeded and hence the charge response for low energies is suppressed.

For $n \neq 0.5$, charge and Cooper-pair susceptibility are not identical. Hence, we discuss them separately. For low repulsion $U$, the pair susceptibility is shown in Fig. 5.47.

For low repulsion $U$, the dependencies of the pair susceptibility on $U$ and $\mu$ differs significantly from the dependencies of the charge susceptibility. Whereas the structure in the charge susceptibility

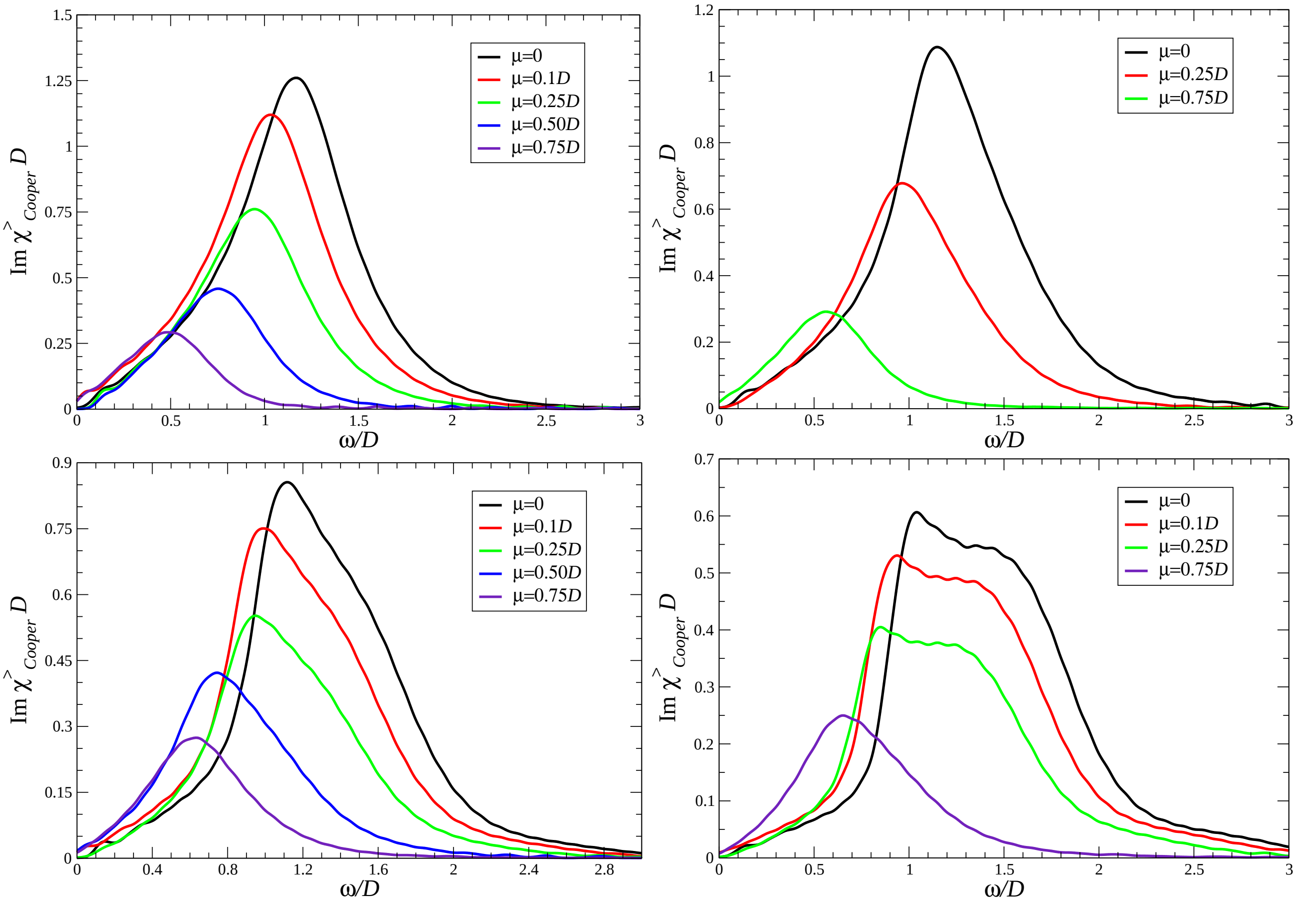

Figure 5.47: Imaginary part of the pair susceptibility $\chi^{>}$ for $U = D$ (upper left), $U = 1.25D$ (upper right), $U = 1.5D$ (lower left) and $U = 1.75D$ (lower right) for several values of $\mu$ (see legends).

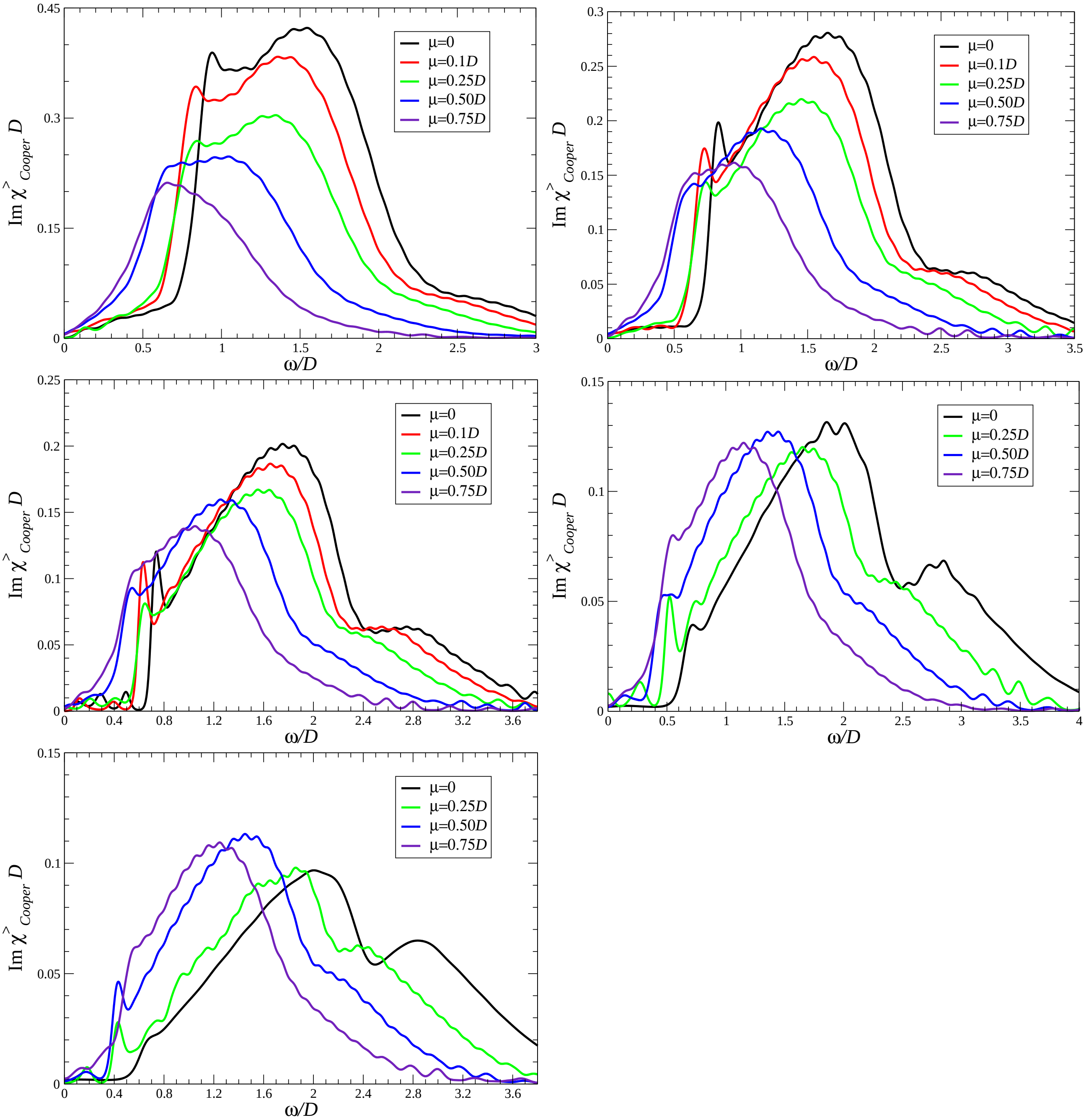

Figure 5.48: Imaginary part of the pair susceptibility $\chi^{>}$ for $U = 2D$ (upper left), $U = 2.3D$ (upper right), $U = 2.5D$ (middle left), $U = 2.7D$ (middle right) and $U = 2.8D$ (lower left) for several values of $\mu$ (see legends).

becomes broader and its height is staying more or less constant, the pair susceptibility peak moves towards smaller energies and is suppressed more clearly for increasing $\mu$. The position of the maximum coincides approximately with the maximum of the upper Hubbard band. The physical explanation for this finding is that the upper Hubbard band corresponds to sites which are occupied by a spin-up and a spin-down electron. Changing the chemical potential $\mu$ directly changes the position of the upper Hubbard band which corresponds to the change of the energy of the pair excitation maximum. At the same time, an increased number of double occupied sites impedes the chance to create a Cooper pair, hence the spectral weight of the pair susceptibility decreases for positive frequencies.

For $U = 1.75D$, we see that the pair excitation for low frequencies is suppressed and precursors of the sharp feature at the inner side of the Hubbard band appear in the pair susceptibility. In contrast to the charge susceptibility, there is no hump in the pair susceptibility for energies larger than the first maximum at low frequencies. For larger energies, the pair susceptibility decreases monotonously.

For larger repulsions $U$ (i.e. $U \geq 2.0D$), we also see that the maximum of the pair excitation follows the maximum of the upper Hubbard band. The pair excitation for low $\mu$ and small frequencies is stronger suppressed than for the charge excitation. For frequencies $\omega \geq 2.4D$, a hump occurs that is completely suppressed on increasing $\mu$. For intermediate frequencies $\omega \in [0.4D, 2.4D]$, the pair susceptibility exhibits a shape similar to the upper Hubbard band. In contrast to the behavior of the charge susceptibility, the sharp feature at the inner side is more persistent. In order to ease a comparison between charge and pair susceptibility, we show examples of both for $U = 1D$ & $U = 2D$ and $\mu = 0.1D$ & $\mu = 0.5D$ together in Fig. 5.49.

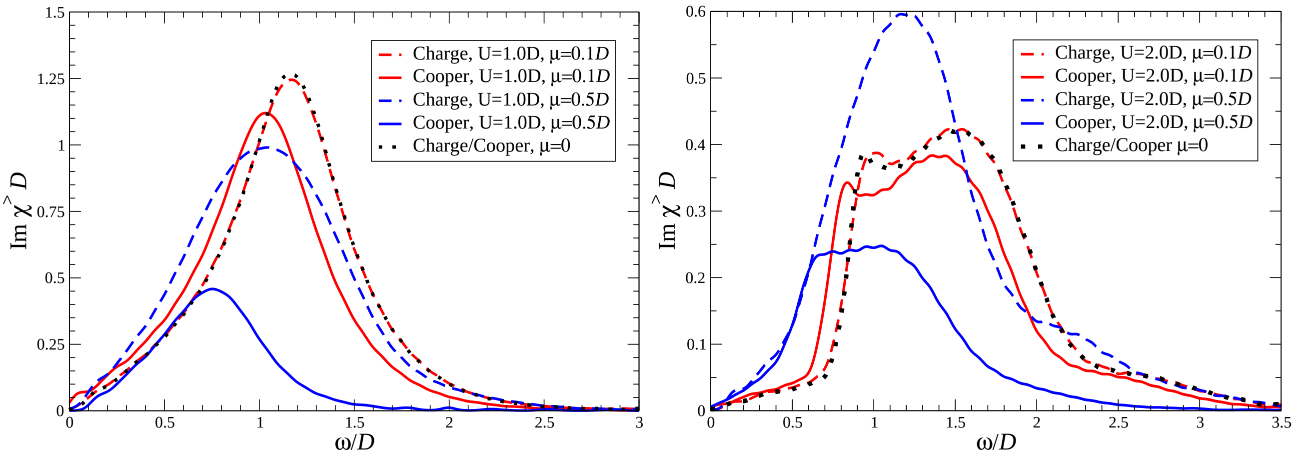

Figure 5.49: Comparison of charge (dashed curves) and pair (solid curves) susceptibility for $U = 1D$ (left panel) and $U = 2D$ (right panel) and $\mu = 0.1D$ (red) and $\mu = 0.5D$ (blue). The dotted curves show the charge/pair susceptibility for the half-filled case.

Comparing charge and pair susceptibility for fixed filling (the pair susceptibility is shown in Fig. 5.50), we obtain that increasing $U$ stronger suppresses the pair excitation than the charge excitation. For $n = 0.55$, the sharp feature at the inner side of the upper Hubbard band in $\rho_G$ is still visible in the pair excitation but not in the charge excitation. Comparing charge and pair susceptibility for $n = 0.65$, we can state that the hump for energies $\omega \geq 2.0D$, which exists in the charge susceptibility, is absent in the pair susceptibility.

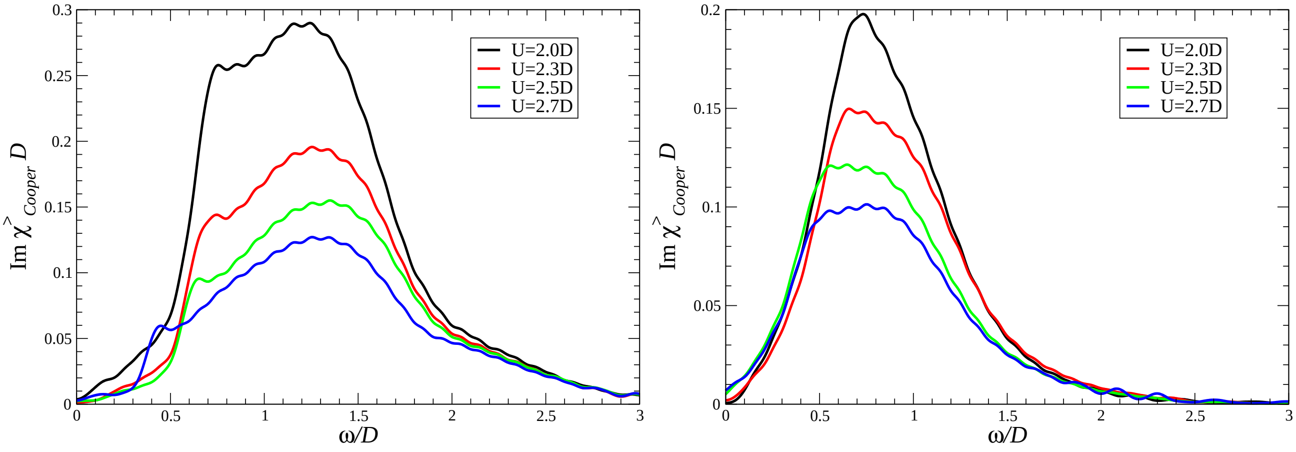

Figure 5.50: Imaginary part of the pair susceptibility $\chi^>$ for $n = 0.55$ (left) and $n = 0.65$ (right) for several values of $U$ (see legends).

### 5.5.5 Kinks and Local Bosonic Excitations away from Half-Filling

The extraction of the kink positions from the real part of the self-energies for the doped case is more complex than for the undoped case. Unfortunately, a fit with an asymmetric version of the fit function (5.16) did not work properly so we had to fit three different linear functions separately (before the left kink, around $\omega = 0$ and after the right kink) and calculate their intersection points. This is exemplified in Fig. 5.51 where we show those fits for $U = 2.3D$ & $\mu = 0.25D$ and $U = 2.3D$ & $\mu = 0.75D$. Fig. 5.51 also shows the increasing difficulty to extract a kink for positive frequencies if $\mu$ is large.

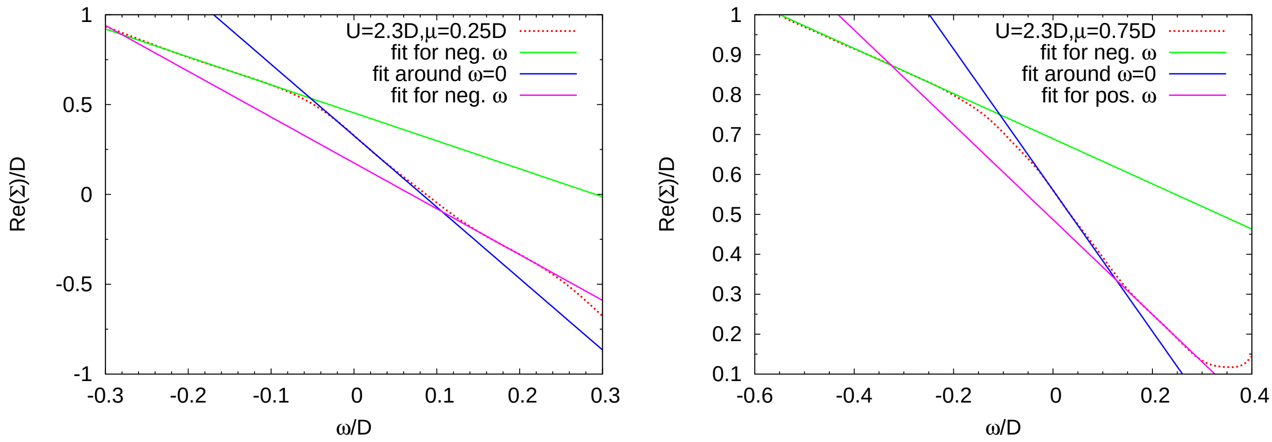

Figure 5.51: Examples ($U = 2.3D$ and $\mu = 0.25D$ (left) and $\mu = 0.75D$ (right)) for the procedure to extract the kinks in $\Re\Sigma$ away from half-filling. The dotted line shows the real part of the self-energy and the solid lines show the three different fits. Although for larger $\mu$ the kink in $\Re\Sigma$ is difficult to see (see upper right part of Fig. 5.38 on page 124), it is still possible to identify the intersection point for positive frequencies.

Also the calculation of the kink positions via the Eqs. (5.13) from Byczuk et al. [31] is more complex than for the symmetric case. In the symmetric case, we just had to calculate the quasi-particle weight

$Z$ and multiply it with $(\sqrt{2}-1)$ which is obviously easier than to calculate the position of the kinks from Eqs. (5.13b) and (5.13c). Away from half-filling, we make a linear fit to the real and imaginary parts of $1/G$ and extract the corresponding parameters for Eqs. (5.13).

Recalling the results of Sec. 5.5.4, it is clear that the spin fluctuations are the candidates for being responsible for the kinks. Here, the question arises whether the maximum of the spin susceptibility coincides with the kink for *positive* or for *negative* frequencies. The imaginary part of the spin susceptibility is for all fillings an anti-symmetric function so the extrema can only coincide with the kink position for positive *or* negative frequencies, not with both. Obviously, this question is hard to answer because the kink positions for positive and negative frequencies do not differ very much. However, from the $\rho_\Sigma$ we see that the trough-like feature is more pronounced for negative frequencies. In addition, the kink in $\Re\Sigma$ can even vanish for $\omega < 0$, see e.g. $U = 2.3D$ with $\mu = 0.75D$. Therefore, we check if the maxima of the spin susceptibility coincide with the kink positions for negative frequencies. This is shown in Fig. 5.52.

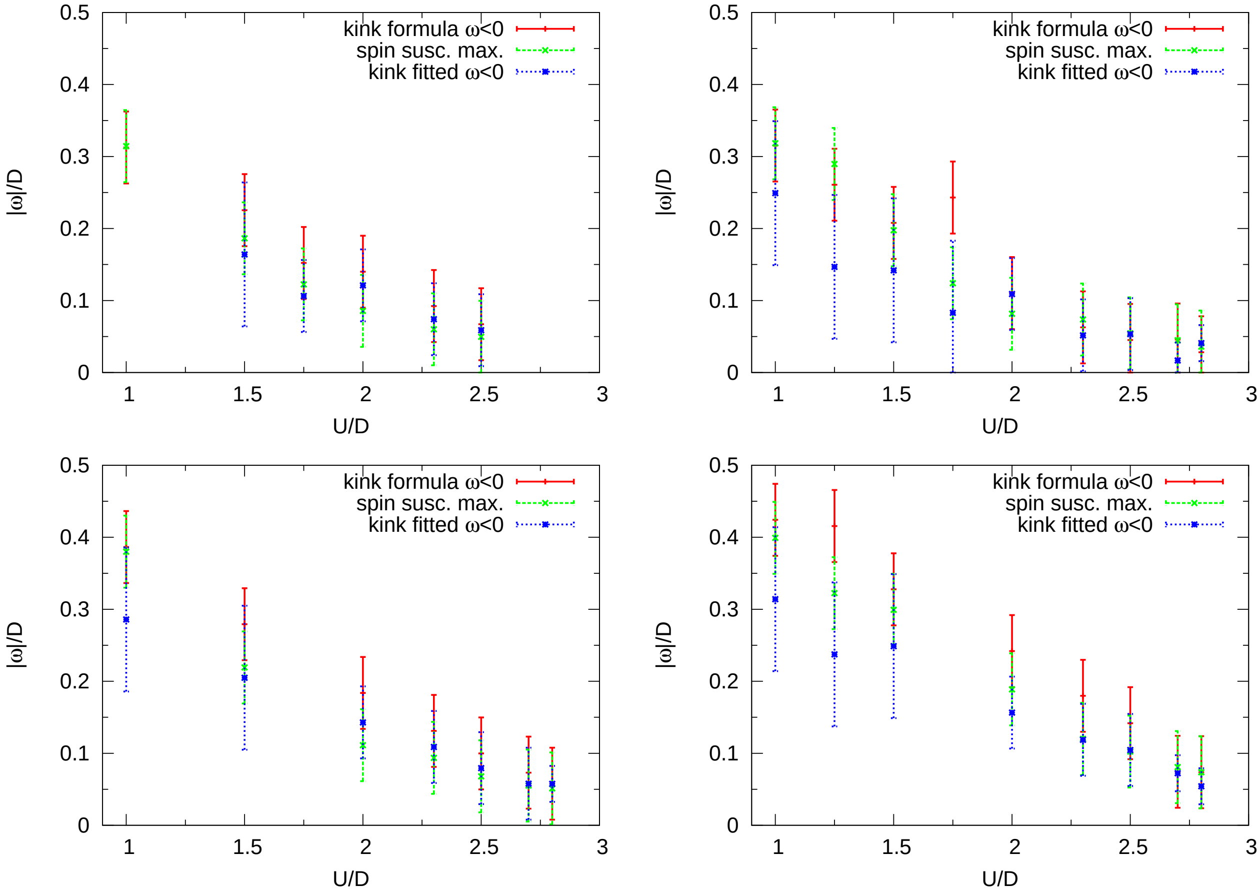

Figure 5.52: Absolute value of the position of the kinks for negative frequencies, maxima of the spin susceptibility and absolute value of the position of the kinks for negative frequencies obtained via Eqs. (5.13) on page 88 for $\mu = 0.1D$ (upper left), $\mu = 0.25D$ (upper right), $\mu = 0.5D$ (lower left) and $\mu = 0.75D$ (lower right). For discussion see text.

From Fig. 5.52 we see that the kink positions for negative frequencies and the position of the maxima of the spin susceptibility coincide. Hence, we conclude that spin fluctuations are also responsible for the kinks at finite $\mu$.

However, one may call into question why the spin susceptibility maxima coincide with the kink position at negative frequencies and not at positive frequencies. For low $\mu$, the data is not conclusive enough since the negative and positive kink positions do not differ very much. Therefore, we compare the spin susceptibility maxima with the positive kink positions for $\mu = 0.75D$ in Fig. 5.53.

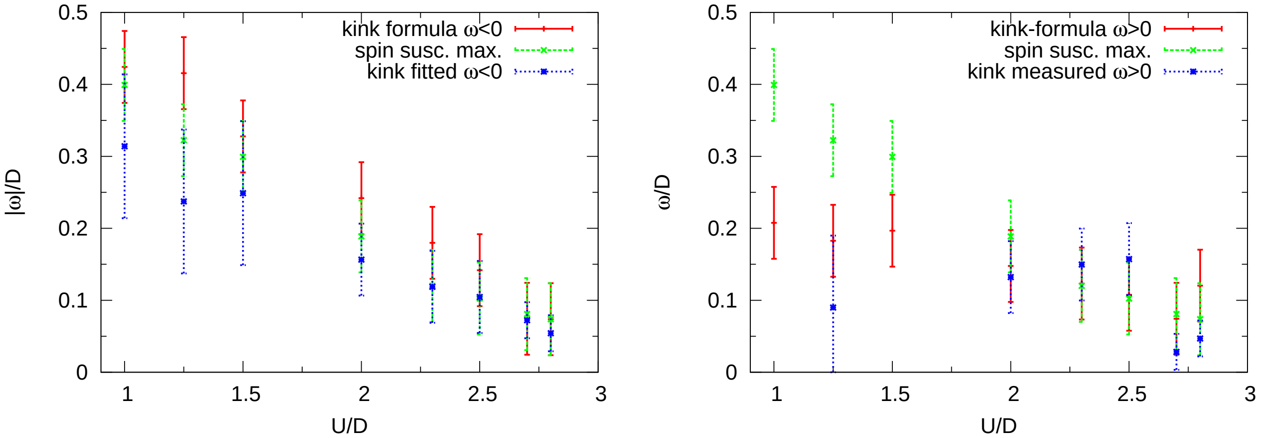

Figure 5.53: Left: Position of the kinks for negative frequencies, maxima of the spin susceptibility and position of the kinks for negative frequencies obtained from Eqs. (5.13) for $\mu = 0.75D$. Right: Position of the kinks for positive frequencies, maxima of the spin susceptibility and position of the kinks for positive frequencies obtained via Eqs. (5.13) for $\mu = 0.75D$. The degree of agreement is better for negative frequencies. Note that for $U \leq 1.5D$, the kink positions for $\omega > 0$ could only be extracted for $U = 1.25D$. In addition, the kink position for $U \leq 1.5D$ calculated from formula (5.13) of Byczuk et al. [31] do *not* coincide within the error bars. For $2.0D \leq U \leq 2.8D$, the extracted kink positions for $\omega < 0$ and the positions of the spin maxima coincide almost exactly whereas larger differences are seen for $\omega > 0$.

From Fig. 5.53, we see that the degree of agreement is better for negative frequencies than for positive frequencies. For $U \leq 1.5D$, the kink positions for $\omega > 0$ could only be extracted for $U = 1.25D$. In addition, for $\omega > 0$ the kink position calculated from formula (5.13) of Byczuk et al. [31] do not coincide within the error bars. For $2.0D \leq U \leq 2.8D$, the extracted kink positions for $\omega < 0$ and the positions of the spin maxima coincide almost exactly whereas larger differences are seen for $\omega > 0$. This is an empiric result but not a sufficient reason. Such a reasoning may be the following line of argument:

First, we should not look at the sign of the frequencies where the kinks are located but on their absolute value. This is reasonable because for $\mu \to -\mu$ we would obtain mirrored spectral densities but the same spin susceptibilities. We should then state that the maximum of the spin susceptibilities coincide with the kink positions at *larger* energies. The position of the maximum of the imaginary part of the spin susceptibility is at $\omega = 0$ for an paramagnetic insulator. For the metal which is driven towards the insulating phase for increasing Coulomb repulsion, this spin susceptibility maximum moves towards $\omega = 0$. Doping leads to less renormalization of the quasi-particle, i.e. the system becomes less interacting and we need a larger repulsion to drive the metal towards the insulating phase. Hence, the maximum of the spin susceptibility is shifted to higher frequencies (which is depicted in Fig. 5.42 and 5.43). Thus, the new decay channel that is indicated by the kink moves to larger frequencies.

However, why is there another kink for positive frequencies? To tackle this question, one should note that we analyze broad structures and not delta peaks in the spin susceptibilities so one should not be surprised about the existence of another kink that is not exactly at the same position. For larger chemical potential $\mu$, there is just one Hubbard band separated from the quasi-particle peak[9], hence just one kink and then the position of the remaining kink coincides with the position of the maxima of the imaginary part of the spin susceptibility.

In addition, one should note that positive $\mu$ shifts the upper Hubbard band towards the quasi-particle peak. The quasi-particle is a many-body effect of single occupied sites. The upper Hubbard band corresponds to the excitation from single occupied sites to double occupied sites. In the spin susceptibility, we see that the quasi-particle couples to a spin mode which set in at a certain frequency (i.e. the position of the maximum of the spin susceptibility). If the energy of the excitation from single to double occupied sites (i.e. the upper Hubbard band) merges with the quasi-particle energy, then the spin fluctuations cannot provide an *additional* decay channel because there is already a decay of the quasi-particle. If there is no additional decay channel for quasi-particle, we do not expect kinks in $\Re\Sigma$. This is the physical reason why the kink for $\omega > 0$ smears out or even vanishes.

On the other hand, electron doping shifts the lower Hubbard band towards larger negative frequencies. The lower Hubbard band corresponds to the excitation from single occupied sites to empty sites. The energy of the quasi-particle and the energy of hole excitations are hence well separated so that the spin fluctuations of the propagating quasi-particle *can* provide an additional decay channel for the quasi-particle. Therefore, we expect kinks in $\Re\Sigma$ for $\omega < 0$. Of course, the spin mode couples to both the particle and the hole. But for electron doping, this spin mode can only provide an additional decay channel for $\omega < 0$ (i.e. for the hole). Hence, the physical picture proposed in this thesis that spin fluctuations provide an additional decay channel for the quasi-particle only applies to $\omega < 0$.

As a conclusion we state that for the electron doped case the spin excitation of the propagating quasi-particle provides an additional decay channel for the quasi-particle for negative frequencies (i.e. for the holes). This additional decay channel is seen as the trough in $\Im\Sigma$ and, due to Kramers-Kronig relations, as the kink in $\Re\Sigma$ for $\omega < 0$. This spin excitation sets in at a certain energy and hence the kink in $\Re\Sigma$ occurs at this particular energy.

---

[9] Note that Byczuk et al. [31] assume that $\rho_G$ exhibits a clear three-peak structure. Hence, their analysis does not apply to cases when e.g. one Hubbard band becomes a shoulder to the quasi-particle peak.

# 6 Conclusion and Outlook

## 6.1 Conclusion

Elucidating the physical mechanisms that are responsible for the properties of solids with strongly correlated electrons is a very complex task. Although the full solid state Hamiltonian (see Eq. (2.6)) is easy to formulate, it is impossible to solve. Simplifications of the general solid state Hamiltonian, specialized analytical tools and numerical methods are needed to gain insights into the physics of strongly correlated electrons.

In this thesis, we analyzed the single-band Hubbard Hamiltonian in the limit of infinite dimension. In this limit, the full lattice Hamiltonian can be mapped on a single-impurity Anderson model which we solved via dynamic density-matrix renormalization (D-DMRG). We analyzed the effect of different weight distributions on the quality of the results for $\rho_G$. We found that the quality of the results is not much affected by the particular choice of the weight distribution. This statement does not apply to the density-matrix correction (DMC) described in Sec. 4.1.5. Although DMC was introduced to improve the results of the ground state energy, we found here that it can also have negative effects on the quality of the results.

We also analyzed the other parts of the self-consistency cycle, i.e. the deconvolution and the extraction of the continued-fraction coefficients (CFCs). We showed how to improve the leas-bias (LB) algorithm to deconvolute self-energies that strictly fulfill FL theory at $\omega = 0$. We found that the extraction scheme for the CFCs applied to data deconvoluted by the LB algorithm is affected by numerical artifacts that the LB algorithm produces. In particular, the convergence of the local $S_z$-fields have to be assured by setting an asymmetric integration interval. In addition, the wiggles in the spectral density $\rho_G$ can cause oscillations of the hopping constants $b_n$ ($n$ is the depth of the continued-fraction). Such oscillations were hitherto interpreted as a sign that the SIAM chain is not large enough. We found that this induction is not compelling.

Let us come to the physical results. With D-DMRG, spectral densities, self-energies and susceptibilities can be calculated with high numerical resolution. We presented those dynamical quantities for the half-filled case at $T = 0$ with the semielliptic, rectangular and triangular DOS and for the semielliptic DOS away from half-filling. We analyzed the physical content of those dynamic quantities, e.g. we calculated the quasi-particle weight, extracted the critical repulsion $U_{c2}$ where the metal-to-insulator transition occurs and we discussed the shift of spectral weight as a function of the repulsion $U$ and the chemical potential $\mu$.

The focus was set on kinks in the real part of the self-energy $\Sigma$ which are found for the metallic solution. Kinks are often interpreted as a hint to the presence of collective bosonic modes or e.g. a coupling between electrons and phonons which both can be responsible for the properties of the correlated metal. An additional interpretation of those kinks was published by Byczuk et al. [31]. They argue that there is *no* need to add any external bosonic mode but that kinks in the real part of the self-energy naturally arise in systems with correlated electrons.

In this thesis, we analyzed this point of view for the single-band Hubbard model. We found that in this model internal spin excitations caused by the propagating quasi-particle are responsible for the kinks in the real part of the self-energy. Both the spin excitations and the kinks occur at the same energy. This statement holds for the half-filled case and away from half-filling. In both cases, emergent collective modes, spin excitations in particular, are responsible for the kinks in the real part of the self-energy.

## 6.2 Outlook

We close this thesis with a short outlook. We focussed on metallic solutions of the single-band Hubbard model because only there kinks in the real part of the self-energy are present. It was shown that the DMFT(D-DMRG)-framework works well and yields spectral densities, self-energies and susceptibilities with good resolution. The next obvious step is to calculate those local quantities for the doped insulator.

The SIAM is actually implemented in Jordan-Wigner language implying that we distinguish between the left and right part of the chain which correspond to different spin orientations. This setup enables calculations of dynamic quantities for the SIAM with a magnetic field.

We found that for all values of the chemical potential spin excitations provide the decay channel of the quasi-particle that cause the kinks in the real part of the self-energy. We restricted ourselves to the single band case. However, the used impurity solver is not restricted to the single-band case and one may extend the program to investigate multiple bands. If $\rho_G$ exhibits a three-peak structure, the argument of Byczuk et al. [31] applies and $\Re\Sigma$ should exhibit kinks. It is worthwhile to analyze this more complex situation and figure out which excitations provide the decay channel in this more complex situation.

It was mentioned that DMRG only works well for one-dimensional systems because the matrix product states (MPS) cannot comprise enough entanglement for more than one spatial dimension. The mentioned projected entangled product states (PEPS) – the generalization of MPS for higher spatial dimensions – are adequate for calculations in higher dimensions. The future will show if PEPS yield dynamic quantities with high quality comparable to D-DMRG in the one-dimensional case. If so, the two-dimensional cuprate planes, which are believed to be highly relevant for high temperature superconductivity, could be analyzed and the long standing problem of the origin of high temperature superconductivity could be solved.

# 7 Bibliography

[1] M. Aichhorn, L. Pourovskii, V. Vildosola, M. Ferrero, O. Parcollet, T. Miyake, A. Georges & S. Biermann, Physical Review B **80**, 085101 (2009)

[2] Y. Aiura, Y. Yoshida, I. Hase, S.I. Ikeda, M. Higashiguchi, X.Y. Cui, K. Shimada, H. Namatame, M. Taniguchi & H. Bando, Physical Review Letters **93**, 117005 (2004)

[3] H. Alloul, J. Bobroff, M. Gabay & P.J. Hirschfeld, Reviews of Modern Physics **81**, 45 (2009)

[4] F.B. Anders, "Die Anderson Modelle – Eine verbesserte störungstheoretische Analyse", Dissertationsschrift Darmstadt 1995

[5] F.B. Anders & N. Grewe, Europhysics Letters **26**, 551 (1994); F.B. Anders, Journal of Physics: Condensed Matter **7**, 2801 (1995)

[6] F.B. Anders & A. Schiller, Physical Review Letters **95**, 196801 (2005)

[7] F.B. Anders & A. Schiller, Physical Review B **74**, 245113 (2006)

[8] P.W. Anderson, Physical Review **124**, 41 (1961)

[9] P.W. Anderson, Science **235**, 1196 (1987)

[10] P.W. Anderson, Science **316**, 1705 (2007)

[11] N. Andrei, Physical Review Letters **45**, 379 (1980)

[12] N. Andrei, K. Furuya & J.H. Lowenstein, Reviews of Modern Physics **55**, 331 (1983)

[13] N.W. Ashcroft & D.N. Mermin, Festkörperphysik, 3. Aufl. Oldenburg Verlag 2007

[14] F.F. Assaad & M. Imada, Journal of the Physical Society of Japan **65**, 189 (1996)

[15] T. Barthel, M.C. Chung & U. Schollwöck, Physical Review A **74**, 022329 (2006)

[16] J.G. Bednorz & K.A. Müller, Zeitschrift für Physik **64**, 189 (1986)

[17] H. Bethe, Zeitschrift für Physik **71**, 205 (1931)

[18] N.E. Bickers, Reviews of Modern Physics **59**, 845 (1987)

[19] C.C. Bidwell, Physical Review **19**, 447 (1922)

[20] S. Biermann, L. de Medici & A. Georges, Physical Review Letters **95**, 206401 (2005)

[21] N. Blümer, Physical Review B **76**, 205120 (2007)

[22] U. Brandt & C. Mielsch, Zeitschrift für Physik **75**, 365 (1989)

[23] U. Brandt & C. Mielsch, Zeitschrift für Physik **79**, 295 (1990)

[24] U. Brandt & C. Mielsch, Zeitschrift für Physik **82**, 37 (1991)

[25] R. Bulla, A.C. Hewson & T. Pruschke, Journal of Physics: Condensed Matter **10**, 8365 (1998)

[26] R. Bulla, Physical Review Letters **83**, 136 (1999)

[27] R. Bulla, T.A. Costi & D. Vollhardt, Physical Review B **64**, 045103 (2001)

[28] R. Bulla, T.A. Costi & T. Pruschke, Reviews of Modern Physics **80**, 395 (2008)

[29] R. Bracewell, “The Hilbert Transform” The Fourier Transform and Its Applications, 3rd ed. New York: McGraw-Hill, 1999.

[30] W.F. Brinkman & T.M. Rice, Physical Review B **2**, 4302 (1970)

[31] K. Byczuk, M. Kollar, K. Held, Y.-F. Yang, I.A. Nekrasov, T. Pruschke & D. Vollhardt, Nature Physics **3**(3), 168 (2007)

[32] M. Byczuk & D. Vollhardt, Physical Review B **77**, 235106 (2008)

[33] M. Byczuk & D. Vollhardt, Annalen der Physik **18**(9), 622 (2009)

[34] M. Caffarel & W. Krauth, Physical Review Letters **72**, 1545 (1994)

[35] C. Callan & F. Wilczek, Physics Letters B **333**, 55 (1994)

[36] T.S. Chihara, Mathematics and Its Applications Vol 13. “An introduction to orthogonal polynomials”, Gordon and Breach Science Publishers Inc., New York 1978

[37] P. Coleman Physical Review B **28**, 5255 (1983); P.Coleman Physical Review B **29**, 3035 (1984)

[38] G. Czycholl, “Theoretische Festkörperphysik”, Vieweg Verlag 2000

[39] A. Damascelli, Z. Hussain & Z.X. Shen, Reviews of Modern Physics **75**, 473 (2003)

[40] E. Demler, W. Hanke & S.-C. Zhang, Reviews of Modern Physics **76**, 909 (2004)

[41] P. Drude, Annalen der Physik **306**, 566 (1900)

[42] F.J. Dyson, Physical Review **75**, 486 (1949)

[43] F.J. Dyson, Physical Review **75**, 1736 (1949)

[44] M.P. Eastwood, F. Gebhard, E. Kalinowski, S. Nishimoto & R.M. Noack, European Physical Journal B **35**, 155 (2003)

[45] E.N. Economou, “Green’s Functions in Quantum Physics”, Springer Series in Solid-State Sciences 7, 2006

[46] F.H.L. Essler, H. Frahm, F. Göhmann, A. Klümper & V.E. Korepin, “The One-Dimensional Hubbard Model”, Cambridge University Press 2005

[47] R. Fassbender, “Spektraldichten und Selbstenergie des Einstörstellen-Anderson-Modells mittels dynamischer Dichtematrixrenormierung”, Diplomarbeit 2005, `http://t1.physik.tu-dortmund.de/uhrig/diploma/diploma_Fassbender_Rolf_2005-04.ps.gz`

[48] M. Feldbacher & F.F. Assaad, Physical Review B **63**, 073105 (2001)

[49] M. Feldbacher, K. Held & F.F. Assaad, Physical Review Letters **93**, 136405 (2004)

[50] M. Feldbacher, K. Held & F.F. Assaad, Physica B **359**, 654 (2005)

[51] A.L. Fetter & J.D. Walecka, “Quantum Theory of Many-Particle Systems”, McGraw-Hill Inc., 1971

[52] R.P. Feynman, Physical Review **76**, 749 (1949)

[53] R.P. Feynman, Physical Review **76**, 769 (1949)

[54] R.P. Feynman, “Statistical Mechanics: A Set of Lectures”, Benjamin, Reading, MA, 1972

[55] J.P. Franck, F.D. Manchester & D.L. Martin, Proceedings of the Royal Society of London Series A **263**, 494 (1961)

[56] J.K. Freericks, T.P. Devereaux, R. Bulla & T. Pruschke, Physical Review B **67**, 155102 (2003)

[57] T. Fujiwara, S. Yamamoto & Y. Ishii, Journal of the Physical Society of Japan **72**, 777 (2003)

[58] E. R. Gagliano & C. A. Balseiro, Physical Review Letters **59**, 2999 (1987)

[59] J. Gaite, Modern Physics Letters A **16**, 1109 (2001)

[60] J. Gaite, "Entanglement entropy and the density-matrix renormalization group", `http://arxiv.org/abs/quant-ph/0301120`

[61] A. Galindo & M.A. Martín-Delgado, Reviews of Modern Physics **74**, 347 (2002)

[62] D.J. García, K. Hallberg & M.J. Rozenberg, Physical Review Letters **93**, 246403 (2004)

[63] D.J. García, E. Miranda, K. Hallberg & M.J. Rozenberg, Physica B **398**, 407 (2007)

[64] D.J. García, E. Miranda, K. Hallberg & M.J. Rozenberg, Physical Review B **75**, 121102 (2007)

[65] W. Gasser, E. Heiner & K. Elk, "Greensche Funktionen in der Festkörper- und Vielteilchenphysik", Wiley-VCH 2001

[66] F. Gebhard, "Springer Tracts in Modern Physics 137: The Mott Metal-Insulator Transition", Springer 1997

[67] A. Georges & G. Kotliar, Physical Review B **45**, 6479 (1992)

[68] A. Georges, G. Kotliar, W. Krauth & M.J. Rozenberg, Reviews of Modern Physics **68**, 13 (1996)

[69] P. Grete & M. Markus, International Journal of Bifurcation and Chaos, **20**, 1459 (2010)

[70] N. Grewe, Zeitschrift für Physik B **52**, 193 (1983)

[71] N. Grewe, Zeitschrift für Physik B **53**, 271 (1983)

[72] N. Grewe, S. Schmitt, T. Jabben & F.B. Anders, Journal of Physics: Condensed Matter **20**, 365217 (2008)

[73] G. Grosso & G.P. Parravicini, Advances in Chemical Physics **63**, 81 (1985); **63**, 133 (1985)

[74] J.E. Gubernatis, M. Jarrell, R.N. Silver & D.S. Sivia, Physical Review B **44**, 6011 (1991)

[75] S.F. Gull, & G.J. Daniell, Nature **272**, 686 (1978)

[76] E. Gull, P. Werner, O. Parcollet & M. Troyer, European Physics Letters **82**, 57003 (2008)

[77] M.C. Gutzwiller, Physical Review Letters **10**, 159 (1963)

[78] H. Hafermann, C. Jung, S. Brener, M. I. Katsnelson, A. N. Rubtsov & A. I. Lichtenstein, Europhysics Letters **85**, 27007 (2009)

[79] K.A. Hallberg, Physical Review B **52**, 9827 (1995)

[80] K.A. Hallberg, Advances in Physics **55**, 477 (2006)

[81] M. Hase, I. Terasaki & K. Uchinokura, Physical Review Letters **70**, 3651 (1993)

[82] K. Haule, Physical Review B **75**, 155113 (2007)

[83] A.C. Hewson, "The Kondo Problem to Heavy Fermions", Cambridge University Press, 1993

[84] J.E. Hirsch & R.M. Fye, Physical Review Letters **56**, 2521 (1986)

[85] J. Hubbard, Proceedings of the Royal Society of London. Series A, Mathematical and Physical **276**, 238 (1963)

[86] J. Hubbard, Proceedings of the Royal Society of London. Series A, Mathematical and Physical **277**, 237 (1964)

[87] J. Hubbard, Proceedings of the Royal Society of London. Series A, Mathematical and Physical **281**, 401 (1964)

[88] M. Imada, A. Fujimori & Y. Tokura, Reviews of Modern Physics **70**, 1039 (1998)

[89] K. Inaba, A. Koga, S. Suga & N. Kawakami, Physical Review B **72**, 085112 (2005)

[90] H. Iwasawa, Y. Aiura, T. Saitoh, I. Hase, S.I. Ikeda, Y. Yoshida, H. Bando, M. Higashiguchi, Y. Miura, X.Y. Cui, K. Shimada, H. Namatame & M. Taniguchi, Physical Review B **72**, 104514 (2005)

[91] J.D. Jackson, "Klassische Elektrodynamik", de Gruyter 2002

[92] V. Janiš, Journal of Physics: Condensed Matter **10**, 2915 (1998)

[93] E.T. Janes, Physical Review **106**, 620 (1957); E.T. Janes, Physical Review **108**, 171 (1957)

[94] M. Jarrell, Physical Review Letters **69**, 168 (1992)

[95] M. Jarrell & T. Pruschke, Zeitschrift für Physik B **90**, 187 (1993)

[96] M. Jarrell & T. Pruschke, Physical Review B **49**, 1458 (1993)

[97] E. Jeckelmann, Physical Review B **66**, 045114 (2002)

[98] S. Jin, T.H. Tiefel, M. McCormack, R.A. Fastnacht, R. Ramesh & L.H. Chen, Science **264**, 413 (1994)

[99] P. Jordan & E. Wigner, Zeitschrift der Physik **47**, 631 (1928)

[100] H. Kajueter & G. Kotliar, Physical Review Letters **77**, 131 (1996)

[101] H. Kajueter, G. Kotliar & G. Möller, Physical Review B **53**, 16214 (1996)

[102] J. Kanamori, Progress of Theoretical Physics **30**, 275 (1963)

[103] M. Karski, "Dynamische Molekularfeldtheorie mittels dynamischer Dichtematrix-Renormierung", Diplomarbeit, Universität zu Köln 2004, `http://t1.physik.tu-dortmund.de/uhrig/diploma/diploma_Karski_Michal_2004-12.ps.gz`

[104] M. Karski, C. Raas & G.S. Uhrig, Physical Review B **72**, 113110 (2005)

[105] M. Karski, C. Raas & G.S. Uhrig, Physical Review B **77** 075116 (2008)

[106] H. Keiter & J.C. Kimball, International Journal of Magnetism **1**, 233 (1971); Journal of Applied Physics **42**, 1460 (1971)

[107] A. Koga, N. Kawakami, T. M. Rice & M. Sigrist, Physical Review Letters **92**, 216402 (2004)

[108] H. Kojima, Y. Kuramoto & M.Y. Tachiki, Zeitschrift für Physik B **54**, 293 (1984)

[109] J. Kondo, Progress in Theoretical Physics **32**, 37 (1964)

[110] H.R. Krishna-murthy, J.W. Wilkins & K.G. Wilson, Physical Review B **21**, 1003 (1980)

[111] H.R. Krishna-murthy, J.W. Wilkins & K.G. Wilson, Physical Review B **21**, 1044 (1980)

[112] T.D. Kühner, "Dynamics with the Density-Matrix Renormalization Group", PhD-thesis, Bonn (1999)

[113] T.D. Kühner & S.R. White, Physical Review B **60**, 335 (1999)

[114] Y. Kuramoto, Zeitschrift für Physik B **53**, 37 (1983)

[115] Y. Kurashige & T. Yanai, Journal of Chemical Physics **130**, 234114 (2009)

[116] L.D. Landau, Soviet Physics JETP **3**, 920 (1956)

[117] J.I. Latorre, E. Rico & G. Vidal, Quantum Information and Computation **4**, 48 (2004)

[118] M. Lee, L. Viciu, Lu Li, Y. Wang, M.L. Foo, S. Watauchi, R.A. Pascal, R.J. Cava & N.P. Ong, Physica B: Condensed Matter **403**, 1564 (2008)

[119] E.H. Lieb & F.Y. Wu, Physical Review Letters **20** 1445 (1968); Erratum: Physical Review Letters **21**, 192 (1968)

[120] A. Liebsch, Physical Review Letters **95**, 116402 (2005)

[121] W. von der Linden, Physics Reports **220**, 53 (1992)

[122] J.M. Luttinger & J.C. Ward, Physical Review **118**, 1417 (1960)

[123] J.M Luttinger, Journal of Mathematical Physics **4**, 1154 (1963)

[124] A.P. Mackenzie & Y. Maeno, Reviews of Modern Physics **75**, 657 (2003)

[125] S. Maekawa, T. Tohyama, S.E. Barnes, S. Ishihara, W. Koshibae & G. Khaliullin, "Solid-State Sciences 144: Physics of Transition Metal Oxides", Springer 2004

[126] Y. Maeno, H. Hashimoto, K. Yoshida, S. Nishizaki, T. Fujita, J.G. Bednorz & F. Lichtenberg, Nature **372**, 532 (1994)

[127] G. Mahan, "Many-Particle-Physics", Plenum Press New York 1981

[128] T. Maier, M. Jarrell, T. Pruschke & M.H. Hettler, Reviews of Modern Physics **77** 1027 (2005)

[129] T.A. Maier, D. Poilblanc & D.J. Scalapino, Physical Review Letters **100**, 237001 (2008)

[130] M. Mathieu, "Funktionalanalysis – Ein Arbeitsbuch", Hochschultaschenbuch, Spektrum Akademischer Verlag 1998

[131] D.C. Mattis & E. H. Lieb, Journal of Mathematical Physics **6**, 304 (1965)

[132] D.B. McWhan, J.P. Remeika, T.M. Rice, W.F. Brinkman, J.P. Maita & A. Menth, Physical Review Letters **27**, 941 (1971)

[133] W. Meissner & B. Voigt, Annalen der Physik **399**, 892 (1930)

[134] N. Metropolis & S. Ulam, Journal of the American Statistical Association **44**, 335 (1949)

[135] W. Metzner & D. Vollhardt, Physical Review Letters **62**, 324 (1989)

[136] W. Meevasana, X.J. Zhou, S. Sahrakorpi, W.S. Lee, W.L. Yang, K. Tanaka, N. Mannella, T. Yoshida, D. H. Lu, Y.L. Chen, R.H. He, H. Lin, S. Komiya, Y. Ando, F. Zhou, W.X. Ti, J.W. Xiong, Z.X. Zhao, T. Sasagawa, T. Kakeshita, K. Fujita, S. Uchida, H. Eisaki, A. Fujimori, Z. Hussain, R.S. Markiewicz, A. Bansil, N. Nagaosa, J. Zaanen, T.P. Devereaux & Z.-X. Shen, Physical Review B **75**, 174506 (2007)

[137] E. Miranda, D.J. García, K. Hallberg & M.J. Rozenberg, Physica B **403**, 1465 (2008)

[138] A. S. Mishchenko, Advances in Condensed Matter Physics **2010**, Article ID 306106 (2010)

[139] K. Miyake, S. Schmitt-Rink & C.M. Varma, Physical Review B **34**, 6554 (1986)

[140] P. Misra, “Heavy Fermion Systems”, Elsevier Science New York 2008

[141] F.J. Morin, Physical Review Letters **3**, 34 (1959)

[142] N.F. Mott, Proceedings of the Physical Society of London A **62**, 416 (1949)

[143] E. Müller-Hartmann, Zeitschrift für Physik B **74**, 507 (1989)

[144] E. Müller-Hartmann, International Journal of Modern Physics B **3**, 2169 (1989)

[145] E. Müller-Hartmann, Zeitschrift für Physik B **76**, 211 (1989)

[146] H.-A. Krug von Nidda, R. Bulla, N. Büttgen, M. Heinrich & A. Loidl, European Physical Journal B **34**, 399 (2003)

[147] M. A. Nielsen & I.L Chuang, “Quantum Computation and Quantum Information”, Cambridge University Press 2000

[148] R.M. Noack & S.R. White, “The Density Matrix Renormalization Group” in Lecture Notes in Physics: “Density-Matrix Renormalization – A New Numercial Method in Physics”, I. Peschel, X. Wang, M. Kaulke & K. Hallberg (Eds.), p. 27-66

[149] W. Nolting, “Grundkurs Theoretische Physik 7 – Viel-Teilchen-Theorie”, Springer 6. Aufl. 2005

[150] W.C. Oliveira & L.N. Oliveira, Physical Review B **49**, 11986 (1994)

[151] T.J. Osborne & M.A. Nielsen, Quantum Information Processing **1**, 45 (2002)

[152] S.G. Ovchinnikov, Physics Uspekhi **46**, 21 (2003)

[153] C.A. Perroni, H. Ishida & A. Liebsch, Physical Review B **75**, 045125 (2007)

[154] I. Peschel, X. Wang, M. Kaulke & K. Hallberg (Eds.), Lecture Notes in Physics: “Density-Matrix Renormalization – A New Numercial Method in Physics”, Springer 1998

[155] D.G. Pettifor & D.L. Weaire, “The recursion method and its applications”, Berlin Springer (1985)

[156] D. Pines & P. Nozières, “The Theory of Quantum Liquids – Volume I: Normal Fermi Liquids”, W.A. Benjamin 1966

[157] M. Potthoff, European Physical Journal B **36**, 335 (2003)

[158] T. Pruschke & N. Grewe, Zeitschrift für Physik B **74**, 439 (1989)

[159] T. Pruschke, D.L. Cox. & M. Jarrell, Europhysics Letters **21**, 593 (1993)

[160] T. Pruschke, D.L. Cox. & M. Jarrell, Physical Review B **47**, 3553 (1993)

[161] T. Pruschke, M. Jarrell & J.K. Freericks, Advances in Physics **44**, 187 (1995)

[162] T. Pruschke & R. Bulla, European Physical Journal B **44**, 217 (2005)

[163] C. Raas, “Dynamic Density-Matrix Renormalization for the Symmetric Single Impurity Anderson Model”, PhD-thesis, Köln, 2005

[164] C. Raas & G.S. Uhrig, Physical Review B **79**, 115136 (2009)

[165] C. Raas, P. Grete & G.S. Uhrig, Physical Review Letters **102**(7), 076406 (2009)

[166] T.V. Ramakrishnan, Current Science **95**, 1284 (2008)

[167] S. Ramasesha, S.K. Pati, H.R. Krishna-Murthy, Z. Shuai & J.L. Brédas, Synthetic Metals **85**, 1019 (1997)

[168] B. Radzimirski & R.J. Wojciechowski, Acta Physica Polonica A **111**, 753 (2007)

[169] A. Rubtsov, V. Savkin & A. Liechtenstein, Physical Review B **72**, 035122 (2005)

[170] O. Sakai & Y. Kuramoto, Solid State Communications **89**, 307 (1994)

[171] S. Sakai, R. Arita, K. Held & H. Aoki, Physical Review B **74**, 155102 (2006)

[172] M. Schiró & M. Fabrizio, Physical Review B **79**, 153302 (2009)

[173] K.P. Schmidt & G.S. Uhrig, Modern Physics Letters B **19**, 1179 (2005)

[174] S. Schmitt, “Excitations, Two-Particle Correlations and Ordering Phenomena in Strongly Correlated Electron Systems from a Local Point of View”, PhD-thesis, Darmstadt 2008

[175] S. Schmitt, T. Jabben & N. Grewe, Physical Review B **80**, 235130 (2009)

[176] S. Schmitt, private communication, 2010

[177] Q. Si, M.J. Rozenberg, G. Kotliar & A.E. Ruckenstein, Physical Review Letters **72**, 2761 (1994)

[178] U. Schollwöck, S. Chakravarty, J.O. Fjærestad, J.B. Marston & M. Troyer, Physical Review Letters **90**, 186401 (2003)

[179] U. Schollwöck, Reviews of Modern Physics **77**, 259 (2005)

[180] U. Schollwöck, Journal of Magnetism and Magnetic Materials **310**, 1394 (2007)

[181] J.R. Schrieffer & P.A. Wolff, Physical Review **149**, 491 (1966)

[182] H.-B. Schüttler & D.J. Scalapino, Physical Review Letters **55**, 1204 (1985)

[183] H.-B. Schüttler & D.J. Scalapino, Physical Review B **34**, 4744 (1986)

[184] F. Schwabl, “Statistische Mechanik”, Springer 2000

[185] F. Schwabl, “Quantenmechanik”, Springer 1998

[186] M. Sigrist, D. Agterberg, T.M. Rice & M.E. Zhitomirsky, Physica C **282**, 214 (1997)

[187] R.N. Silver, J.E. Gubernatis, D.S. Sivia & M. Jarrell, Physical Review Letters **65**, 496 (1990)

[188] D.S. Sivia, “Data Analysis A Bayesian Tutorial”, Clarendon Press Oxford 1996

[189] A. Sommerfeld, Zeitschrift für Physik **47**, 1 (1928) (nowadays found in Zeitschrift für Physik A: Hadrons and Nuclei **47**, 1 (1928))

[190] Z.G. Soos & S. Ramasesha, Journal of Chemical Physics **90**, 1067 (1989)

[191] J. Spałek, Physical Review B **37**, 533 (1988)

[192] J. Spałek, Acta Physica Polonica A **111**, 409 (2007)

[193] F. Steglich, J. Aarts, C.D. Bredl, W. Lieke, D. Meschede, W. Franz & H. Schäfer, Physical Review Letters **43**, 1892 (1979)

[194] G.R. Stewart, Reviews of Modern Physics **56**, 755 (1984)

[195] G.R. Stewart, Reviews of Modern Physics **73**, 797 (2001)

[196] Z. Sun, Y.-D. Chuang, A.V. Fedorov, J.F. Douglas, D. Reznik, F. Weber, N. Aliouane, D.N. Argyriou, H. Zheng, J.F. Mitchell, T. Kimura, Y. Tokura, A. Revcolevschi & D.S. Dessau, Physical Review Letters **97**, 056401 (2006)

[197] M. Suzuki, Progress of Theoretical Physics **56**, 1454 (1976)

[198] K. Takada, H. Sakurai, E. Takayama-Muromachi, F. Izumi, R.A. Dilanian & T. Sasaki, Nature **422**, 53 (2003)

[199] I. Terasaki, Y. Sasago & K. Uchinokura, Physical Review B **56**, R12685 (1997)

[200] J.J. Thomson, Philosophical Magazine **44**, 293 (1897)

[201] Y. Tokura, Y. Okimoto, S. Yamaguchi & H. Taniguchi, Physical Review B **58**, R1699 (1998)

[202] S. Tomonaga, Progress on Theoretical Physics **5**, 544 (1950)

[203] N.-H. Tong, Communications in Theoretical Physics **37**, 615 (2002)

[204] C.C. Tsuei & J.R. Kirtley, Reviews of Modern Physics **72**, 969 (2000)

[205] G.S. Uhrig, private communication, 2009

[206] C.M. Varma, P.B. Littlewood, S. Schmittrink, E. Abrahams & A.E. Ruckenstein, Physical Review Letters **63**, 1996 (1989)

[207] F. Verstraete, D. Porras & J.I. Cirac, Physical Review Letters **93**, 227205 (2004)

[208] F. Verstraete, A. Weichselbaum, U. Schollwöck, I. Cirac, J. von Delft, cond-mat/0504305

[209] F. Verstraete & J.I. Cirac, cond-mat/0407006

[210] F. Verstraete, V. Murg & J.I. Cirac, Advances in Physics **57**, 143 (2008)

[211] S. Viridi, P. Grete & M. Markus, Physics Letters A **372**, 1040 (2008)

[212] V.S. Viswanath, "The recursion method and its application to many body dynamics", Berlin Springer (1994)

[213] J. Voit, Reports on the Progress of Physics **58**, 977 (1995)

[214] W. Weber, Annalen der Physik **19**, 372 (2010)

[215] P. Werner, A. Comanac, L. Medici, M. Troyer & A. Millis, Physical Review Letters **97**, 076405 (2006)

[216] P. Werner, T. Oka & A.J. Millis, Physical Review B **79**, 035320 (2009)

[217] P. Werner, E. Gull & A.J. Millis, Physical Review B **79**, 115119 (2009)

[218] S.R. White & R.M. Noack, Physical Review Letters **68**, 3487 (1992)

[219] S.R. White, Physical Review Letters **69**, 2863 (1992)

[220] S.R. White, Physical Review B **48**, 10345 (1993)

[221] S.R. White, Physical Review Letters **77**, 3633 (1996)

[222] S.R. White & D.J. Scalapino, Physical Review Letters **80**, 1272 (1998)

[223] S.R. White, Physics Reports **301**, 187 (1998)

[224] S.R. White, Physical Review B **72**, 180403(R) (2005)

[225] P.B. Wiegmann, JETP Letters **31**, 364 (1980)

[226] K.G. Wilson, Reviews of Modern Physics **47**, 773 (1975)

[227] E.O. Wollan & W.C. Koehler, Physical Review **100**, 545 (1955)

[228] Y. Yanase, T. Jujo, T. Nomura, H. Ikeda, T. Hotta & K. Yamada, Physics Reports **387**, 1 (2003)

[229] H.-B. Yang, Z.-H. Pan, A.K.P. Sekharan, T. Sato, S. Souma, T. Takahashi, R. Jin, B.C. Sales, D. Mandrus, A.V. Fedorov, Z. Wang & H. Ding, Physical Review Letters **95**, 146401 (2005)

[230] M. Yoshida, M.A. Whitaker & L.N. Oliveira, Physical Review B **41**, 9403 (1990)

[231] R. Žitko & T. Pruschke, Physical Review B **79**, 085106 (2009)

[232] M.B. Zölfl, T. Maier, T. Pruschke & J. Keller, European Physics Journal B **13**, 47 (2000)

[233] M.B. Zölfl, "Stark korrelierte Multiniveau-Elektronensysteme", Dissertation, 2001

# A Appendix

## A.1 Abstract

This work comprise a DMFT analysis of the metallic solutions of the single-band Hubbard model. For solving the involved single-impurity Anderson model, the dynamic density-matrix renormalization (D-DMRG) is used. After an introduction into the field of “strongly correlated electrons” and the approximation “dynamic mean-field theory”, the impurity solver D-DMRG is described and comprehensively validated. D-DMRG allows us to calculate local dynamic quantities such as spectral densities, self-energies and (dynamic) susceptibilities which we analyze for the half-filled case for the semielliptic, the rectangular and the triangular DOS and for the semielliptic DOS with doping. We use D-DMRG in a DMFT framework in order to analyze the origin of the kinks in the real part of the self-energy which occur within the energy range of the quasi-particle peak. The guiding hypothesis throughout this thesis is that those kinks are caused by an additional decay channel of the quasi-particle which is provided by the coupling of the quasi-particle to bosonic excitations. Within a DMFT framework only the local bosonic excitations such as spin-, charge- and pair-excitations are relevant. In all cases it turns out that spin-excitations are the bosonic excitations that provide the new decay channel for the quasi-particle.

## A.2 Kurze Zusammenfassung

Diese Arbeit beschäftigt sich mit der dynamische Molekularfeldtheorie (DMFT) des Ein-Band-Hubbard-Modells im Parameterbereich des stark korrelierten Metalls. Zur Lösung des lokalen Ein-Störstellen-Anderson-Modells wird die dynamische Dichtematrixrenormierung (D-DMRG) benutzt. Nach einer Einführung in das Forschungsfeld der stark korrelierten Elektronen und der benutzten DMFT wird der Störstellenlöser D-DMRG beschrieben und ausführlich geprüft. D-DMRG ermöglicht die Berechnung von lokalen dynamischen Größen wie spektrale Dichten, Selbstenergien und dynamischen Suszeptibilitäten. Die gerade genannten dynamischen Größen werden für die semielliptische, rechteckige und dreieckige freie DOS bei halber Füllung berechnet sowie für die semielliptische DOS abseits halber Füllung. Wir benutzen den DMFT(D-DMRG) Zugang, um den Ursprung der Knicke im Realteil der Selbstenergie aufzuklären, die im Energiebereich des Quasi-Teilchens auftreten. Die Leitidee während der gesamten Arbeit ist, dass diese Knicke durch einen weiteren Zerfallskanal des Quasi-Teilchens zu Stande kommen, der durch die Ankopplung des Quasi-Teilchens an bosonische Anregungen bereit gestellt wird. Innerhalb der DMFT sind nur lokale bosonische Anregungen und zwar Spin-, Ladungs- und Cooper-Paar-Anregungen relevant. Wir haben für alle genannten DOS die benötigten lokalen dynamischen Größen berechnet und heraus bekommen, dass in allen Fällen Spin-anregungen die gesuchten bosonischen Anregungen sind, die den neuen Zerfallskanal für das Quasi-Teilchen bereit stellen.

## A.3 Danksagung

An erster Stelle möchte ich Prof. Dr. Götz S. Uhrig für die Stellung dieses interessanten Themas, die ausgezeichnete Betreuung in Form von Diskussionen und Zeit für Nachfragen und die Hilfe bei der Antragstellung bei der Studienstiftung des deutschen Volkes danken. Ferner möchte ich Dr. Carsten Raas für die Überlassung seines DMRG-Codes, dessen Verbesserung und die Unterstützung meiner Arbeit in Form von Diskussionen danken. Beide Beiträge waren wesentlich für das Zustandekommen dieser Arbeit und können nicht hoch genug von mir geschätzt werden.

Ich möchte der Studienstiftung des deutschen Volkes für das Doktorandenstipendium und für die idelle Förderung danken. Insbesondere möchte ich dem Referenten der Studienstiftung Dr. Rainer Strub-Röttgerding für die hervorragende Betreuung während des Studiums und der Promotion danken.

Ferner möchte ich meinen Bürokollegen Dipl.-Phys. Nils A. Drescher und Dipl.-Phys. Tim Fischer für die gute Zusammenarbeit und motivierende Arbeitsatmosphäre danken. Was sich neben vielen fachlichen Diskussionen an nahezu unbegrenzt vielen Loriot- und Simpsons-Zitaten darbot werde ich vermissen. Ebenso sei allen weiteren Mitgliedern der Lehrstühle T1 und T2 für die gute Arbeitsathmosphäre gedankt.

Insbesondere möchte ich mich bei Nils A. Drescher und Dr. Sebastian Schmitt für die kritische Durchsicht des Manuskripts dieser Dissertation bedanken. Ebenso möchte ich Dr. Sebastian Schmitt für die Bereitstellung der ENCA Daten und für die vielfachen, sehr anregenden und erhellenden Diskussionen danken.

Zudem möchte ich Prof. Dr. Werner P. Weber für die vielen Gespräche beim Kaffee über Klimafragen und das Wissenschaftssystem (um nur zwei Themen zu nennen) danken. Es hat mir viel Freude bereitet, ihm bei seiner ersten Veröffentlichung zur Klimaforschung [214] zu helfen. Außerdem möchte ich Frau Prof. Dr. Dr. Brigitte Falkenburg für die interdisziplinären Gespräche und Zusammenarbeit danken. Ebenso möchte ich Priv.-Doz. Dr. Jürgen Altmann danken, dass ich an einigen Seminaren zum Thema Naturwissenschaft und Abrüstung sowie an einigen Projekten des gleichnamigen Arbeitskreises mitwirken konnte.

Außerdem möchte ich mich bei Prof. Dr. Mario Markus für die wissenschaftliche Zusammenarbeit nach meiner Diplomarbeit bei ihm bedanken, die zu zwei weiteren Veröffentlichungen ([211, 69]) aus meiner Diplomarbeit führte.

Außerhalb der Arbeitsgruppe möchte ich Dr. Malte Schmick für die guten und freundschaftlichen Gespräche beim Mittagessen danken. Außerhalb der Universität möchte ich allen meinen Freunden und dabei insbesondere Michael Blume, Wolfgang Buchhorn, Sabine Dannehl und Norbert Schmidt für die Unterstützung in jeglicher Hinsicht, die vielen nicht-physikalischen Gespräche und generell für Eure Zeit und Begleitung herzlich danken. Ebenso möchte ich mich für die ausgleichenden, nicht-physikalischen Gespräche bei Frank Hahn und Michael Liebig bedanken.

Ferner möchte ich mich sehr herzlich bei meiner Familie bedanken. Insbesondere bei meiner Frau Sabine Grete, die meine nicht seltene Abwesenheit geduldig ertrug und die mich immer wieder zu meiner Arbeit motivierte. Auch bei meiner Mutter Ursula Grete möchte ich mich bedanken, ohne deren finanzielle Unterstützung und Ermunterung zur Aufnahme eines Hochschulstudiums ich diese Arbeit nicht hätte anfertigen können.

## A.4 Erklärung

Hiermit erkläre ich, Patrick Gilbert Grete, an Eides statt, dass ich die vorliegende Dissertation selbstständig verfasst und angefertigt habe, ich keine anderen Hilfsmittel verwendet habe als die angegebenen und dass bisher keine Teile der Dissertation veröffentlicht wurden außer [165].

PATRICK GRETE